Measurement of Cosmic-Ray Magnesium and Aluminum Fluxes with the Alpha Magnetic Spectrometer on the International Space Station

Liu, Zhen

UNIVERSITÉ DE GENÈVE

Département de Physique Nucléaire et Corpusculaire — FACULTÉ DES SCIENCES
Docteur Mercedes Paniccia

Département de Physique Nucléaire et Corpusculaire — FACULTÉ DES SCIENCES
Professeur Xin Wu

Measurement of Cosmic-Ray Magnesium and Aluminum Fluxes with the Alpha Magnetic Spectrometer on the International Space Station

THÈSE

Présentée à la Faculté des sciences de l'Université de Genève
Pour obtenir le grade de Docteurès sciences, physique

Par

Zhen LIU

de

Chine

Thèse N° 5571

GENÈVE

2021

UNIVERSITÉ DE GENÈVE

FACULTÉ DES SCIENCES

DOCTORAT ÈS SCIENCES, MENTION PHYSIQUE

Thèse de Monsieur Zhen LIU

intitulée :

«Measurement of Cosmic-Ray Magnesium and Aluminum Fluxes with the Alpha Magnetic Spectrometer on the International Space Station»

La Faculté des sciences, sur le préavis de Monsieur X. WU, professeur ordinaire et directeur de thèse (Département de physique nucléaire et corpusculaire), Madame M. PANICCIA, docteure et codirectrice de thèse (Département de physique nucléaire et corpusculaire), Madame T. MONTARULI, professeure ordinaire (Département de physique nucléaire et corpusculaire), Monsieur K. BLUM, docteur (Department of Particle Physics and Astrophysics, Weizmann Institute of Science, Rehovot, ISRAEL), autorise l'impression de la présente thèse, sans exprimer d'opinion sur les propositions qui y sont énoncées.

Genève, le 7 juillet 2021

Thèse - 5571 -

Le Doyen

N.B. - La thèse doit porter la déclaration précédente et remplir les conditions énumérées dans les "Informations relatives aux thèses de doctorat à l'Université de Genève".

Résumé

Les noyaux de magnésium dans les rayons cosmiques sont des particules primaires que l'on pense être principalement produites et accélérées dans des sources astrophysiques. Alors que les noyaux d'aluminium dans les rayons cosmiques sont censés être produits à la fois par des sources astrophysiques et par les collisions de noyaux plus lourds avec le milieu interstellaire. La connaissance du comportement précis des spectres en énergie des noyaux de magnésium et d'aluminium est importante pour comprendre l'origine, l'accélération et les processus de propagation des rayons cosmiques dans la Galaxie. Les noyaux d'aluminium dans les rayons cosmiques ont un composant secondaire radioactif : l'isotope ^{26}Al. Les fractions survivantes des isotopes radioactifs tels que ^{10}Be et ^{26}Al dans les rayons cosmiques secondaires fournissent une contrainte sur le temps de résidence des rayons cosmiques dans la Galaxie et permettent de distinguer différents scénarios de propagation des rayons cosmiques. Les fractions survivantes des isotopes ^{10}Be et ^{26}Al peuvent être extraites à partir des rapports des spectres Be/B et Al/Mg mesurés notamment par le détecteur AMS-02 jusqu'au TV, ce qui fournit des informations complémentaires sur la dépendance énergétique du temps de résidence par rapport aux mesures directes de la composition isotopique qui ne sont possible que jusqu'à quelque dizaine de GV.

Dans cette thèse, les mesures de précision des spectres des noyaux de magnésium et d'aluminium dans les rayons cosmiques en fonction de la rigidité allant de 2.15 GV à 3.0 TV sont présentées. Ces mesures se basent sur 2.51 millions de noyaux de magnésium et 0.51 million de noyaux d'aluminium collectés par le détecteur AMS-02 dans ses premières 8.5 années d'exploitation à bord de la station spatiale internationale ISS, du 19 mai 2011 au 30 octobre 2019. Une étude de faisabilité de l'extraction des fractions survivantes des isotopes radioactifs ^{10}Be et ^{26}Al à partir des rapports des spectres Be/B et Al/Mg est également discutée.

Abstract

Magnesium (Mg) nuclei in cosmic rays are primary particles thought to be mainly produced and accelerated in astrophysical sources. While Aluminum (Al) nuclei in cosmic rays are thought to be produced both in astrophysical sources and by the collisions of heavier nuclei with the interstellar medium. Knowledge of the precise behavior of the Mg and Al spectrum are important in understanding the origin, acceleration, and subsequent propagation processes of cosmic rays in the Galaxy. Aluminum (Al) nuclei has secondary components such as ^{26}Al. The surviving fractions of the radioactive isotopes such as ^{10}Be and ^{26}Al in cosmic rays provide constrain on the cosmic-ray residence time in the Galaxy, and allow to distinguish between different cosmic-ray propagation scenarios. The surviving fractions of ^{10}Be and ^{26}Al can be extracted by from the Be/B and Al/Mg flux ratios measured by AMS, allowing to extend direct measurements up to the TV, and thus providing complementary information on the energy dependence of the residence time.

In this thesis, the precision measurements of Mg and Al individual fluxes and their ratio in the rigidity range from 2.15 GV to 3.0 TV based on 2.51 million Mg and 0.51 million Al nuclei collected by the Alpha Magnetic Spectrometer (AMS-02) during its first 8.5 years (May 19, 2011 to October 30, 2019) of operation aboard the International Space Station are presented. A feasibility study of extracting the ^{10}Be and ^{26}Al surviving fractions from Be/B and Al/Mg flux ratios is also discussed.

Acknowledgements

Working in the AMS Collaboration with the University of Geneva group has been the most memorable experience in my life so far. I am grateful for all the help from people I met during my Ph.D. study.

First and foremost, I would like to thank my advisor, Dr. Mercedes Paniccia, for guiding me throughout my Ph.D. journey in these past four years. Without her help and support, this thesis would not be possible.

I would also like to thank my joint advisor, Prof. Xin Wu, for his continuous support and valuable advice and discussions during these years.

I would express my gratitude to Dr. Kfir Blum at the Weizmann Institute of Science for guiding me during the study of cosmic-ray radioactive decay and escape time.

I would also express my gratitude to Dr. Qi Yan at MIT for his valuable suggestions and inspiring discussions about cosmic-ray nuclei analysis.

I want to thank my colleagues from the AMS Nuclei Group, including Dr. Vitaly Choutko at MIT and others. The fruitful discussions with them have accelerated my research.

I also want to thank the jury members for their valuable comments and suggestions on my thesis.

I appreciate the experience I had with my peers in the Geneva group, Dr. Yao Chen and Mr. Jiahui Wei. I have learned a lot about the analysis and codings from them.

I also appreciate the help from my colleagues from AMS during my shifts. In particular, thanks to Dr. Andrey Rozhkov for offering me many transportation help from the AMS POCC to home, which has saved me lots of trouble.

Moreover, I would like to thank Prof. Samuel Ting for offering me the opportunity to join the AMS collaboration, and the China Scholarship Council for providing me the financial support during my Ph.D. study.

Finally, I want to thank my parents for their unconditional love and countless sacrifices.

Table of contents

List of figures

List of tables

Chapter 1

Introduction to Cosmic Rays

1.1 Cosmic rays

Cosmic Rays are energetic particles that originated in outer space. They mainly consist of ionized atomic nuclei, ranging from the proton, helium to the heaviest elements. Cosmic rays also include a small fraction of photons, neutrinos, electrons, positrons, and antiprotons.

Ever since the discovery of cosmic rays by Victor Hess in 1912 [1], an enormous number of experiments have been performed with different techniques, including direct measurements with instruments on balloons (ATIC [2], BESS [3], CREAM [4], TRACER [5]...) satellites (HEAO [6], PAMELA [7], FERMI [8], DAMPE [9] ...), space shuttles (CRN [10], AMS-01 [11]) and space station (CALET [12] and AMS-02), and indirect measurements such as underground-based (BOREXINO [13], GALLEX [14]...) and ground-based experiments (HESS [15], HAWC [16]..).

Historically, cosmic rays led to the discovery of the positron (e^+) [17], muon (μ) [18], pion (π) [19], kaon (K) [20], and many baryons such as Λ [21], and Ξ [22]. Nowadays, cosmic rays are still a unique tool to probe new physics, new phenomena, and to search for unknown particles. Cosmic rays could also reveal the properties of their astrophysical sources, and the interplanetary environment through which they propagated. However, with more than 100 years of effort, the question of cosmic rays production, acceleration, and propagation mechanism remains unresolved.

With the new generation of ongoing and proposed experiments, the mystery of cosmic rays will eventually be revealed in the near future: the multi-messenger astronomy, utilizing signals of electromagnetic, gravitational, weak and strong forces, will probe the physics of transient phenomena in astrophysical sources; the ground-based cosmic-ray measurements from LHAASO [23], Pierre Auger Observatory [24], etc., will allow searching for the new phenomena of cosmic rays in energies from about 100 GeV to above PeV; the space-based

observations from DAMPE, CALET, AMS-02, etc., have been performing the direct and precise measurement of cosmic rays in energies between GeV to TeV.

The Alpha Magnetic Spectrometer (AMS-02) is a multipurpose magnetic spectrometer designed to measure the charge, momentum, rigidity, and flux of charged cosmic rays up to the TeV region. With its long duration and large acceptance, AMS is able to measure the fluxes of cosmic rays with unprecedented precision, and thus shed light on the unresolved questions.

1.1.1 Cosmic-ray spectra

Figure 1.1 shows the differential flux of the all-particle as functions of kinetic energy. As seen, the flux mainly consists of nuclei, which are dominant by proton p (Section 1.1.2). It also has a small fraction from photons (γ), electrons (e^-), positrons (e^+), antiprotons ($\overline{p}$), and neutrinos (ν and $\overline{\nu}$). The energy spectrum spans the energy range from below 1 GeV to above 100 EeV, and intensity range from above $1\text{particle} \cdot cm^{-2} \cdot s^{-1} \cdot sr^{-1}$ (at $\sim 100\,\text{GeV}$) to below $1\text{particle} \cdot km^{-2} \cdot \text{century}^{-1} \cdot sr^{-1}$ (at $\sim 100\,\text{EeV}$). And in the energy region above $\sim 10\,\text{GeV}$, the energy spectrum of the cosmic-ray charged particles can be roughly described by a power-law distribution:

$$\Phi(E) = \frac{\mathrm{d}N}{\mathrm{d}E} \sim E^{-\alpha} \tag{1.1}$$

where α is the spectral index. The spectrum power-law regularity is broken in few regions including the knee at $\sim 3\,\text{PeV}$ and the ankle at $\sim 5\,\text{EeV}$; $\alpha \sim 2.7$ for energy between $\sim 10\,\text{GeV}$ to the knee, $\alpha \sim 3.1$ between the knee and Ankle, and $\alpha \sim 2.6$ beyond the ankle up to $\sim 30\,\text{EeV}$ [26].

At energies below $\sim 10\,\text{GeV}$, cosmic-ray fluxes are distorted and show significant time variations anti-correlated to the solar activity. The phenomenon, known as solar modulation, is due to the fact that the propagation of charged particles near the solar system is impeded by the heliospheric magnetic field carried by the solar wind [27].

At energies above $\sim 100\,\text{TeV}$, cosmic rays can only be measured indirectly since the intensity of cosmic-ray flux is too low. In this range, cosmic rays have enough energy to create cascades by interacting with the atmosphere, therefore they can be measured by the extensive air showers with ground-based experiments. These experiments have revealed that the very-high-energy particles (energy above $\sim$ EeV) certainly originated from extra-galactic sources [28].

This thesis focuses on the energy range between GeV to few TeV, in which cosmic rays are directly measured by stratospheric balloons and space experiments. Cosmic-ray spectra can be directly measured in kinetic energy per nucleon or rigidity, which is defined as

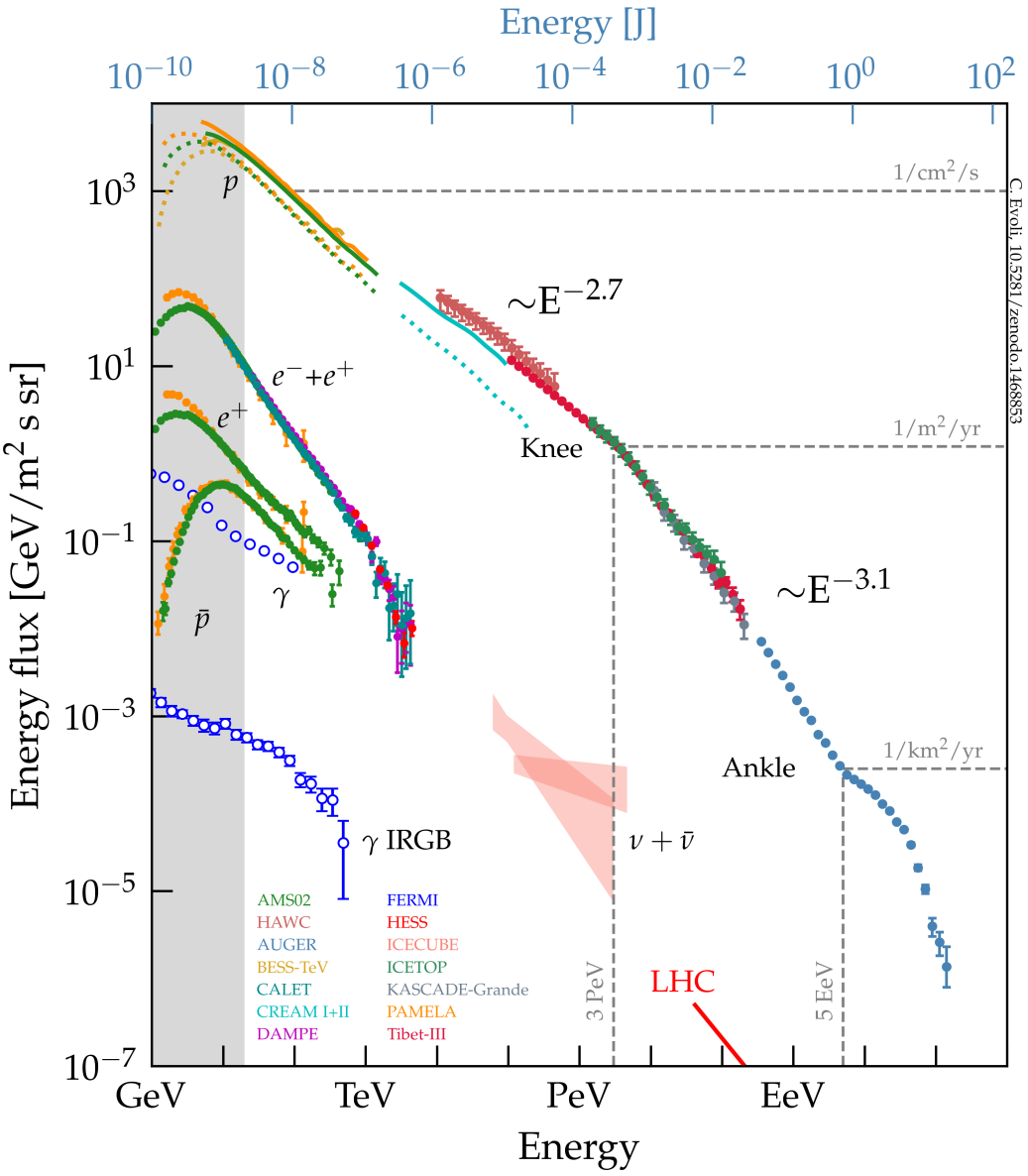

Fig. 1.1 Differential energy spectrum of all cosmic ray particles. Taken from [25]

momentum (p) per unit charge (Z) or the gyroradius (r_L) multiplied by the magnetic field strength (B):

$$R = \frac{p}{Z} = r_L B \tag{1.2}$$

The calorimeter-based detectors such as HEAO and DAMPE measure the spectra in kinetic energy per nucleon, which is approximately conserved during the fragmentation process. While the magnetic spectrometers such as PAMELA and AMS are able to measure the rigidity. The cosmic rays are accelerated and propagated through cosmic magnetic fields. Regardless of species (charge and mass), the relativistic particles (rigidity above a few GVs) with the same rigidity will have the same trajectory in the magnetic field, so measurements of cosmic-ray spectra as a function of rigidity allow a more straightforward extraction of the cosmic-ray key parameters. AMS is currently the only experiment able to directly measure the charged cosmic-ray particles up to nickel nuclei (Z=28) as a function of rigidity and up to few TVs.

1.1.2 Cosmic-ray abundance

Figure 1.2 shows the relative abundances of the elements from H to Cu nuclei in the solar system and in cosmic rays measured by stratospheric balloons and space experiments [29]. Overall, the two distributions have similar odd-even variation structure due to the fact that the odd nuclei are generally less stable than the even ones. However, for Li, Be, B, F and sub-iron nuclei (Sc, Ti, V, Cr, Mn), the relative abundances in cosmic rays are significantly higher than those in the solar system. The phenomenon is attributed to the fact that Li-Be-B, F and sub-iron nuclei are produced by the collisions of heavier elements with the interstellar medium.

Cosmic-ray elements such as p, He, C, O, Ne, Mg, Si and Fe, which are mostly produced by the astrophysical sources, are called primary cosmic rays. While Li, Be, B, F and sub-iron elements, which are produced by the collision of primaries with the Interstellar Medium (ISM), are called secondary cosmic rays. Some other elements such as N, Na and Al are mixtures of primary and secondary cosmic rays [30, 31].

Precise knowledge of the primary and secondary cosmic rays provide important insights into the production, acceleration and propagation mechanism of cosmic rays. Furthermore, the rigidity dependence of some secondary radioactive isotopes such as Beryllium-10 (^{10}Be) and Aluminum-26 (^{26}Al), and the ratio of flux between the decaying nuclei elements and their products, so-called the decaying charge to decayed charge flux ratios, such as Be/B and Al/Mg provide important constraints to current propagation scenarios, which will be discussed in Section 1.3.

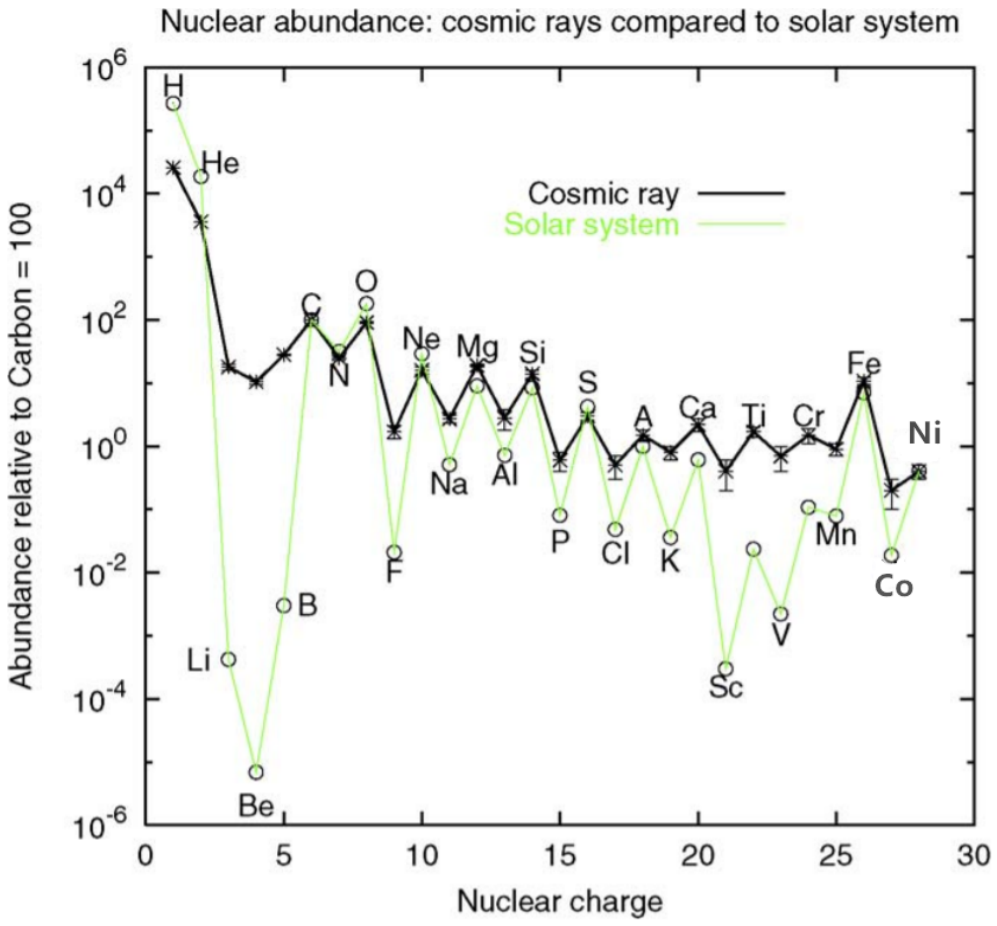

Fig. 1.2 The normalized relative abundances of the elements from H to Cu nuclei in the solar system (open points with green lines) and in cosmic rays (solid points with black lines) measured by stratospheric balloons and space experiments. Taken from [29]

1.2 Cosmic-ray production and acceleration mechanisms

The production and acceleration mechanisms of cosmic rays are still open questions to be solved. By now, the most compelling scenario is that the bulk of the cosmic rays with energy below the 10^{15} eV originates from supernova explosions in the Galaxy, and accelerated by the supernova remnants (SNR).

Cosmic-ray production

While sources like pulsars, gamma-ray bursts and microquasars are possible to contribute to cosmic rays at some level, the supernova is clearly the source of bulk of cosmic rays based on several reasons [32–34]:

- supernovae are the only known source in the Galaxy with sufficient energy to power cosmic rays.
- the ejecta materials of supernovae have similar compositions to cosmic rays.
- observations from X-ray and γ-ray telescopes show that γ-ray emissions are associated with cosmic-ray electrons and ions.
- the observed cosmic-ray fluxes have a spectral index of ~ 2.7, requiring the sources to inject cosmic rays into ISM with a spectral index larger than 2. The SNR acceleration mechanism can naturally produce the particle spectrum following a power-law distribution with a universal slope identical to 2. And given the fact that a fully self consistent scenario of the cosmic-ray acceleration and escaping from SNR shocks is still missing, many explanations can also produce a spectral index larger than 2 within the SNR framework.

Cosmic-ray acceleration

The cosmic rays are believed to be accelerated by the diffusive shock acceleration in Supernova Remnants (SNRs) in the Galaxy [33, 35]. A wealth of observations from the X-ray, γ-ray and Cherenkov telescopes [36–38, 33] has identified the photon radiation produced by the accelerated cosmic ray in SNRs, which makes the SNRs acceleration mechanism the most observationally supported scenario by far.

A SNR is produced by supernova explosion, it consists of material ejected in the explosion itself, and also from the interstellar medium (ISM) which was swept up by the shock wave of the explosion. The evolution of the supernova remnant is divided into three phases [39, 40]:

1. Free expansion phase: the first shock wave produced by the explosion expands in the ISM freely. Behind the shockfront, a shock in the reverse direction is formed.

2. Sedov-Taylor phase: the mass of the ISM swept up by the reverse shock continues to increases, the temperature of interior of the SNR also increase. The atoms are ionized so the ionizing radiation energy loss becomes not possible. The magnetic field inside the SNR shell is also enhanced. At a certain temperature point, heavy elements start to from due to recombination and the shock wave starts to cool down.

3. Cooling phase: the expansion slows down, and with more interstellar gas accumulated, the SNR shell breaks up into clumps.

The cosmic rays are mostly accelerated in the second phase of the SNR evolution [39] by diffusive shock acceleration.

The diffusive shock acceleration, also known as first-order Fermi mechanism, is based on the idea that the charged particles gain energy when scattering by fluctuations in the magnetic field [41, 42]. When a charged particle reflects back and forth between magnetic structures upstream and downstream of the shock, it gains energy as if it was squeezed between converging walls. With multiple reflections, the particle is accelerated rapidly. And the resulting differential energy spectrum follow a single power law $\frac{\mathrm{d}N}{\mathrm{d}p} \propto p^{-\gamma_p}$, where γ_p is the spectral index of the spectrum in momentum which can be calculated from [43]:

$$\gamma_p = \frac{3R_T}{R_T - 1} \tag{1.3}$$

where R_T is the compression ratio of the shock which can be determined from the strength of the shock. For strong shocks, the index of the energy spectrum is calculated as $\gamma_E = 2$ [43].

The diffusive shock acceleration in SNRs naturally produce universal power-law with a spectral index identical to 2. Among all the proposed cosmic rays acceleration mechanisms, it is the most promising one. However, as mentioned, a fully self consistent scenario of the cosmic-ray acceleration and escaping from SNR shocks is still missing and the observation requires SNRs to inject cosmic rays into ISM with a spectral index larger than 2. This discrepancy is possible to be reconciled by adjusting the model within the SNR framework [34].

1.3 Cosmic-ray propagation mechanism

The cosmic-ray production and acceleration mechanism result in a widely accepted paradigm of galactic cosmic rays called *SNR paradigm*. The SNR paradigm describes that the primary cosmic rays are accelerated through the diffusive shock acceleration in SNR, and propagate diffusively through the ISM in the galactic magnetic field. The secondary cosmic rays are produced during collisions of the primaries with ISM, and they also propagate in ISM after being produced.

Models such as diffusion model and leaky box model have been proposed to understand the cosmic-ray transportation mechanism.

1.3.1 Cosmic-ray propagation models

The diffusion model

Cosmic-ray propagation is described as diffusion of energetic charged particles through galactic magnetic fields As shown in Figure 1.3, in this approach, the region where cosmic rays propagate in the Galaxy is a flat halo which has a simple cylindrical geometry with a radius R and height 2×H, the cosmic-ray sources are distributed within a thin flat disk located at the center. The model assumes that charged cosmic rays diffuse in random magnetic fields, which results in a high cosmic-ray isotropy and relatively long confinement time in the Galaxy. And it also assumes that at the boundary of halo (height H of the halo), cosmic rays no longer diffuse but escape freely.

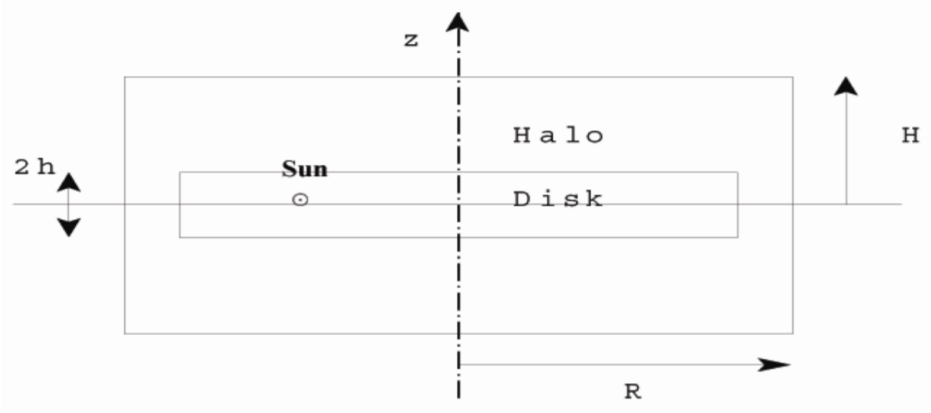

Fig. 1.3 Schematic of cosmic-ray galactic halo with the Sun location indicated. Taken from [44]

The cosmic-ray propagation can be described by a continuity equation which has the following form [45]:

$$\begin{aligned}\frac{\partial\psi(\vec{r},p,t)}{\partial t} &= q(\vec{r},p,t)+\vec{\nabla}\cdot(D_{xx}\vec{\nabla}\psi-\vec{V}\psi)\\ &\quad+\frac{\partial}{\partial p}p^2D_{pp}\frac{\partial}{\partial p}\frac{1}{p^2}\psi-\frac{\partial}{\partial p}[\dot{p}\psi-\frac{p}{3}(\vec{\nabla}\cdot\vec{\nabla}\psi)]-\frac{1}{t_f}\psi-\frac{1}{t_r}\psi \qquad (1.4)\end{aligned}$$

where $\psi(\vec{r},p,t)$ is the density per unit of total particle momentum for a particular cosmic-ray species. The terms on the right hand side include:

- $q(\vec{r},p,t)$ is the source term for both primary and secondary cosmic rays. It consists of contributions from primary, spallation, and decay. Spallation and decay processes also happen during cosmic-ray propagation. As mentioned, the injected spectrum into ISM follows a single power law $\mathrm{d}q/\mathrm{d}p \propto p^{-\gamma_p}$.

- D_{xx} is the spatial diffusion coefficient due the random walk along magnetic filed lines. It is related to the spectrum of interstellar turbulence and can be calculated from $D_{xx} \sim \beta p^{\delta}$, with the spectral index of turbulence δ varies according to model predictions.

- $\vec{V}$ is the convection velocity caused by the galactic wind, and $\vec{\nabla}\cdot\vec{V}$ describes adiabatic momentum gain or loss in the nonuniform gas flow.

- D_{pp} is the momentum-space diffusion coefficient which determines the diffusive re-acceleration. The diffuse re-acceleration is due to the particles gaining or losing momentum during the spatial diffusion in ISM. Therefore, D_{pp} is related to D_{xx} by $D_{pp}D_{xx} \propto p^2$.

- $\dot{p}$ is the momentum gain or loss due to interactions such as ionization, bremsstrahlung, synchrotron, inverse compton and so on.

- t_f is the timescale for loss by fragmentation, it depends on the energy-dependent spallation cross sections and ISM density.

- t_r is the timescale for radioactive decay

the boundary condition $\psi = 0$ is assumed at the boundary of the galactic halo ($z =\mid H \mid$).

The calculation of the transport equation involves hundreds of isotope fragmentation and transformation channels describing the interactions with the ISM during cosmic-ray propagation. Many efforts have been made to solve the equation analytically in some simplified cases [44, 46, 47]. Some full-scale numerical or semi-analytical models such as GALPROP

[48], DRAGON2 [49], Picard [50] and USINE [51] have been developed to solve the Galactic cosmic-ray propagation. Among these, GALPROP [48] code can numerically solve the transport equation using model in three dimension with cylindrical symmetry in the Galaxy, and provide a unified framework for interpretations of many types of cosmic-ray data [52].

Leaky box model

The leaky box model is an extremely simplified version of the diffusion model. It assumes that the boundary of the cosmic-ray propagation volume has a strong reflection, and the cosmic-ray particle has finite probability per unit time ($1/t_{esc}$) to escape during the encounter with the boundary. Therefore, in this model cosmic rays oscillate in the fixed volume and have a uniformly distribution, and they slowly leak out from the boundary.

The leaky box model uses a steady-state formalism ($\partial\psi/\partial t = 0$) and replace the diffusion term in Equation 1.4 with a phenomenological mean path length (λ_{esc}) through the ISM for the escape of cosmic rays [53]. This model can be analyzed analytically and it is characterized only by λ_{esc} which is to be determined by experimental data. The cosmic-ray residence time (or cosmic-ray age, confinement time) t_{esc} in the galaxy , i.e. the time the cosmic rays spend in the Galaxy before escape, is calculated as

$$t_{esc} = \frac{\lambda_{esc}}{M \cdot n_{ISM} \beta c} \tag{1.5}$$

where M is the mean atomic weight of the ISM, n_{ISM} is the mean ISM number density, βc is the velocity of galactic cosmic rays in the ISM.

The leaky box model is a good approximation to the diffusion model for stable nuclei. However, the two types of models give different results for some cosmic-ray properties such as the residence time t_{esc} [54, 55]. Experimentally, t_{esc} can be extracted from the surviving fractions of radioactive cosmic rays. Thus the survival fractions of radioactive cosmic rays obtained from data can be used to distinguish between different propagation models.

1.3.2 Cosmic-ray residence time and radioactive cosmic rays

Cosmic-ray residence time is estimated to be of the order of Myr. Some of the secondary cosmic-ray isotopes created by fragmentation during the propagation of primary cosmic rays are radioactive. Among these, as shown in Table 1.1, ^{10}Be, ^{26}Al, ^{36}Cl, and ^{54}Mn , the so-called cosmic-ray clocks, have half-lives of the same order of magnitude as the cosmic-ray residence time. Comparing the measured survived fraction of these isotopes with what would

Table 1.1 Decay half-lives of the cosmic-ray clocks [56]

Nucleus	Daughter	Decay mode	Half-life (error)
$^{10}_{4}$Be	$^{10}_{5}$B	β^-	1.51Myr(0.06)
$^{26}_{13}$Al (*)	$^{26}_{12}$Mg	e capture	4.08Myr(0.15)
	$^{26}_{12}$Mg	β^+	0.91Myr(0.04)
$^{36}_{17}$Cl (*)	$^{36}_{16}$S	e capture	15.84Myr(0.11)
	$^{36}_{18}$Ar	β^-	0.307Myr(0.002)
$^{54}_{25}$Mn	$^{54}_{24}$Cr	e capture	312.3d(0.4)
	$^{54}_{26}$Fe	β^-	0.494Myr(0.006)

(*) the e capture decay mode can be neglected for ^{26}Al and ^{36}Cl

be expected if these isotopes were stable, the cosmic-ray residence time t_{esc} can be derived within the context of cosmic-ray propagation models.

Figure 1.4 shows the compilations of measurements of ^{10}Be/^{9}Be and ^{26}Al/^{27}Al flux ratios [57, 58]. The isotopic fluxes are measured below 1 GeV/n with statistical error typically larger than 25%. In this limited situation, the residence time t_{esc} calculated from ^{10}Be/^{7}Be and ^{26}Al/^{27}Al flux ratios yield $t_{esc} = 15.0 \pm 1.6$ Myr within a leaky box model interpretation [59], and $t_{esc} \sim 100$ Myr within diffusion models interpretation [45, 60].

Present-day experimental techniques can't yet provide sufficient mass resolutions for the measurements of cosmic-ray isotopes such as ^{10}Be and ^{26}Al at energy above $\sim$ 10 Gev/n. Therefore the energy dependence of the residence time can't be obtained with the isotopic ratios. However, this experimental limitation can be overcome extracting the surviving fraction of ^{10}Be and ^{26}Al, from the Be/B and Al/Mg decaying charge to decayed charge flux ratios, allowing to extend direct measurements up to TV, and thus providing complementary information on the energy dependence of the residence time. Chapter 5 will focus on this topic.

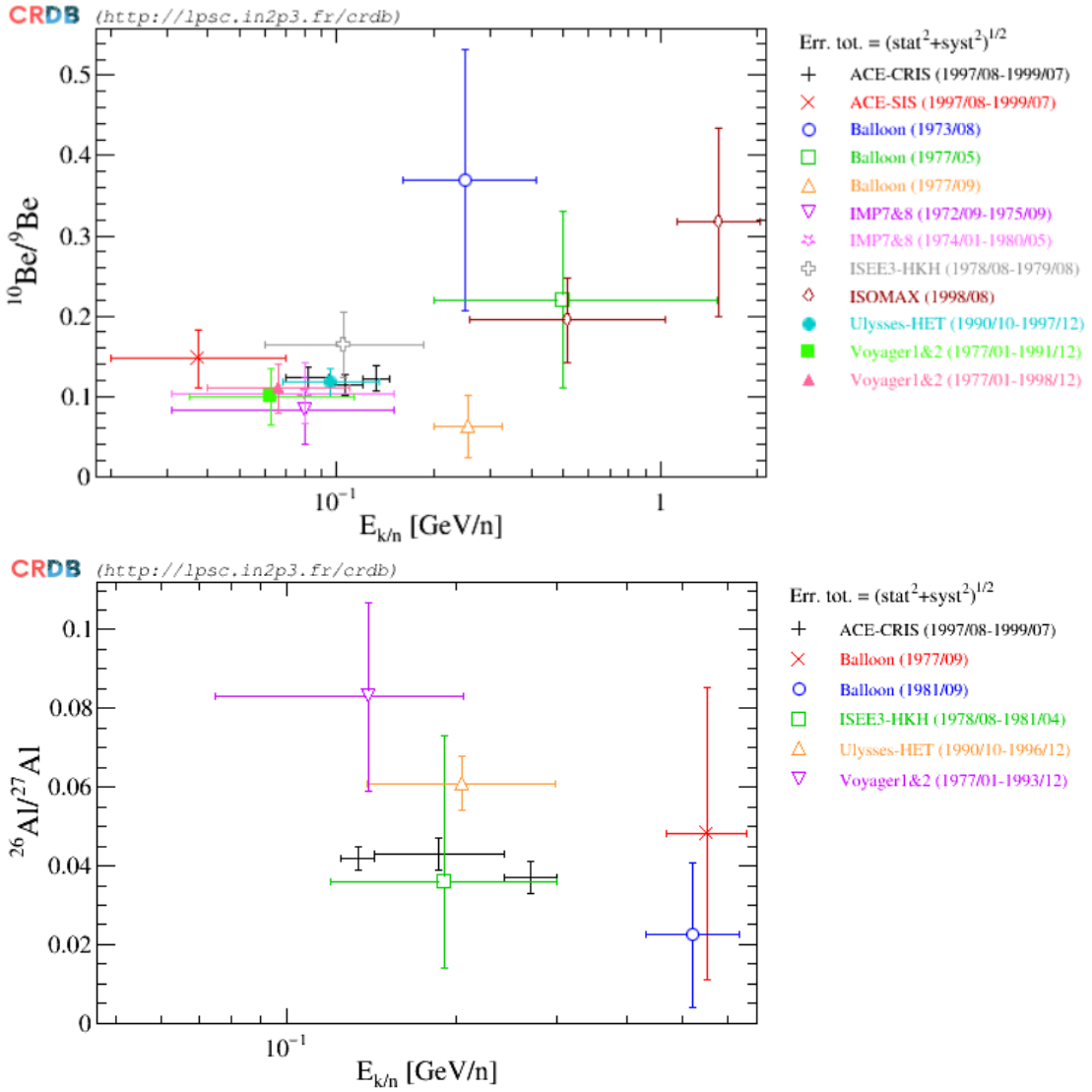

Fig. 1.4 Current measurements of Beryllium-10 to Beryllium-9 (^{10}Be/^{9}Be, top plot) and Aluminum-26 to Aluminum-27 (^{26}Al/^{27}Al, bottom plot) flux ratios. Taken from Cosmic-Ray DataBase (CRDB) [57, 58]

1.4 AMS measurements

Recent space-based experiments such as AMS have measured many different types of cosmic rays with significantly reduced uncertainties, which are pushing cosmic-ray physics in the GeV to TeV range into a precision era. The AMS data have revealed several new and unexpected features in the cosmic-ray spectrum, challenging the widely accepted cosmic ray paradigm.

Several results published by AMS related to this thesis will be introduced.

1.4.1 Positron and antiproton fluxes

AMS has measured the spectra of anti-particle positron e^+ and antiproton $\bar{p}$ in cosmic rays with unprecedented accuracy [61–65]. Figure 1.5 shows the AMS positron and antiproton spectrum scaled by $\widetilde{E}^3$ as a function of energy $\widetilde{E}$. Positron flux shows distinctive properties [64, 65]: it deviates from a single power law and has a significant excess in the energy above ~ 25 GeV, it is well described by the sum of a diffuse term at low energies and a new source term at high energies, the cutoff of the new source term has a significance of more than 4σ. By comparing with the antiproton flux, the positron flux is found to have similar behavior at high energies. These observations may indicate the existence of a new source of high energy positrons.

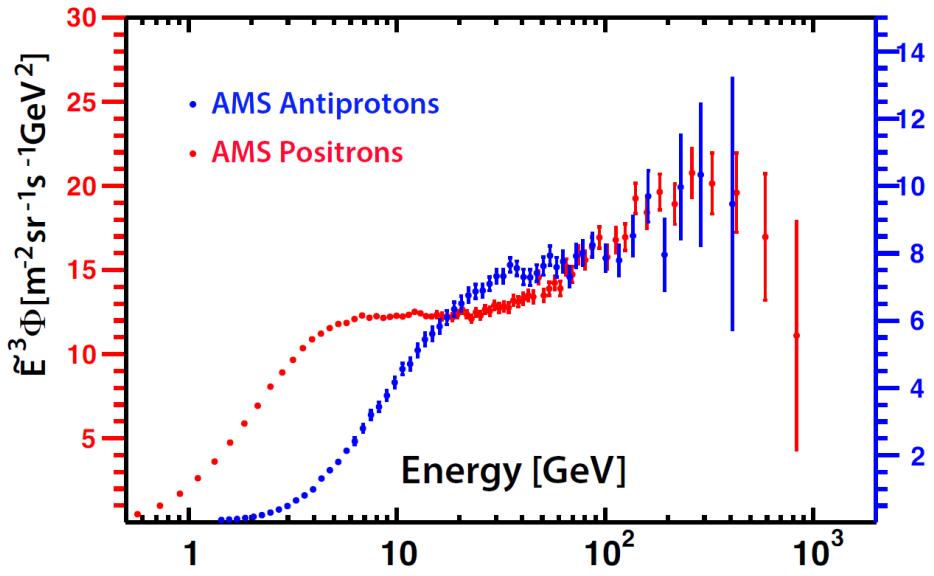

Fig. 1.5 The AMS positron (red points) and antiproton (blue points) spectrum scaled by $\widetilde{E}^3$ as a function of energy. Taken from [65]

The excess of positron flux at high energies is not compatible with the predictions of the traditional cosmic-ray paradigm and has brought out numerous new physics models. To generate the excess positrons, three possible explanations have been proposed:

1. annihilating or decaying dark matter particles
2. the new astrophysical sources such as pulsars
3. traditional source (SNR) with the modification in the acceleration or propagation mechanism.

The dark matter explanations have become less likely [66]. The most favored dark matter candidate is weakly interacting massive particle (WIMP). To explain the excess positrons, a much larger WIMP annihilation cross section value is needed, comparison to the reference one constrained from experiments such as LUX [67], Panda-X [68], IceCube [69], Super-K [70], etc. Moreover, the observation that the antiproton flux does not show an high-energy excess would require a leptophilic WIMP, most dark matter models have been ruled out. In addition, observations from γ-ray telescope such as Fermi [71] and H.E.S.S. [72] are also incompatible with most of dark matter models.

The leading explanation for the excess of positron flux is the new astrophysical sources such as pulsars. Pulsar is a rapidly spinning, highly magnetized neutron star which gradually converts its energy into γ-ray emission and e^- e^+ pairs. Pulsars have long been known as one of the γ-ray point sources, and some of them have been detected nearby. Photons with energies above the threshold for pair production (1.02 MeV) are believed to be produced by high energy e^- e^+ pairs. The positron excess can be easily explained by pulsars [73]. Studies [74, 75] have shown that the nearby pulsars such as Geminga and Monogem, could produce positrons to explain the AMS positron observations. However, this explanation has been challenged. The indirect measurement of the positron emission from the High-Altitude Water Cherenkov (HAWC) experiment [76] revealed that the contributions of the positron flux by nearby pulsars are much smaller than previously assumed, making pulsars unlikely to be the source of positron excess. The future γ-ray instruments such as the Cherenkov Telescope Array (CTA) [77], has improved angular and energy resolutions, which will allow studying cosmic-ray sources in more details, and therefore, test the pulsar hypothesis [34].

The third possible explanation is that the traditional source (SNR) with the modification in the acceleration or propagation mechanism can account for the observed excess. Several variants of traditional cosmic-ray propagation models have been proposed. For example, Reference [78] proposed that secondaries positrons might be produced by the collision between protons in the same region where cosmic rays are accelerated, and they are accelerated

by SNR before escaping into ISM. Reference [79] explains the observation by taking into account the phenomena that a fraction secondaries can be produced within the acceleration region and particles can be re-accelerated during propagation. And reference [80] proposed that a propagation model can coincidentally explain the secondary origin of positrons, in which the radiative losses can be neglected. Considering that secondary nuclei species are also accelerated in SNR just like positrons, these cosmic-ray propagation models can be examined with the secondaries to primaries fluxes ratios.

1.4.2 Cosmic-ray nuclei fluxes

Before the measurement of primary Mg flux in 2020, AMS has released the measurements of Helium (He), Lithium (Li), Beryllium (Be), Boron (B), Carbon (C), Oxygen (O) and Nitrogen (N) in the rigidity range $\sim$ 2 GV to $\sim$ 3 TV with unprecedented accuracy [81–83, 65]. Among these, He, C, O are the most abundant primary cosmic ray nuclei, Li, Be, B are the most abundant secondary cosmic ray nuclei, while N contains both primary and secondary components.

Figure 1.6 shows the AMS results on the primary He-C-O, and secondary Li-Be-B fluxes multiplied by $\widetilde{R}^{2.7}$ as functions of rigidity above 30 GV. Several new properties of cosmic rays have been observed: all the fluxes deviate from a single power law, exhibiting a spectral hardening above 200 GV. The spectra of primary cosmic rays He C and O have identical rigidity dependence above 60 GV. The spectra of secondary cosmic rays Li Be and B also show identical rigidity dependence above 30 GV, but the rigidity dependences of primary cosmic rays and of secondary cosmic rays are distinctly different.

Results form the precise measurements of the primary He-C-O, and secondary Li-Be-B fluxes have challenged the widely accepted SNR paradigm (discussed in Section 1.2), in which both the cosmic-ray spectra injected into the ISM (source term in Equation 1.4) and the diffusion effect imposed on the spectra (diffusion coefficient in Equation 1.4) follow the single power law. The spectral breaks at around 200 GV can originate either from the source or during the propagation. The two competing scenarios can be examined with the secondary to primary flux ratios since the secondaries are produced by the spallation of primaries during the propagation [84]. However, due to the limitation of flux errors, large uncertainties in spallation cross sections and limited knowledge of cosmic-ray propagation parameters such as cosmic-ray escape time, which origin dominates the spectral break phenomena is not clear yet. Reducing the flux uncertainties and obtaining precision measurements from more cosmic-ray species will help to improve the understanding of Galactic cosmic rays [84].

Figure 1.7 shows AMS Nitrogen (N) flux together with the fit with the weighted sum of two components: one describing the the primary contribution and the other describing the

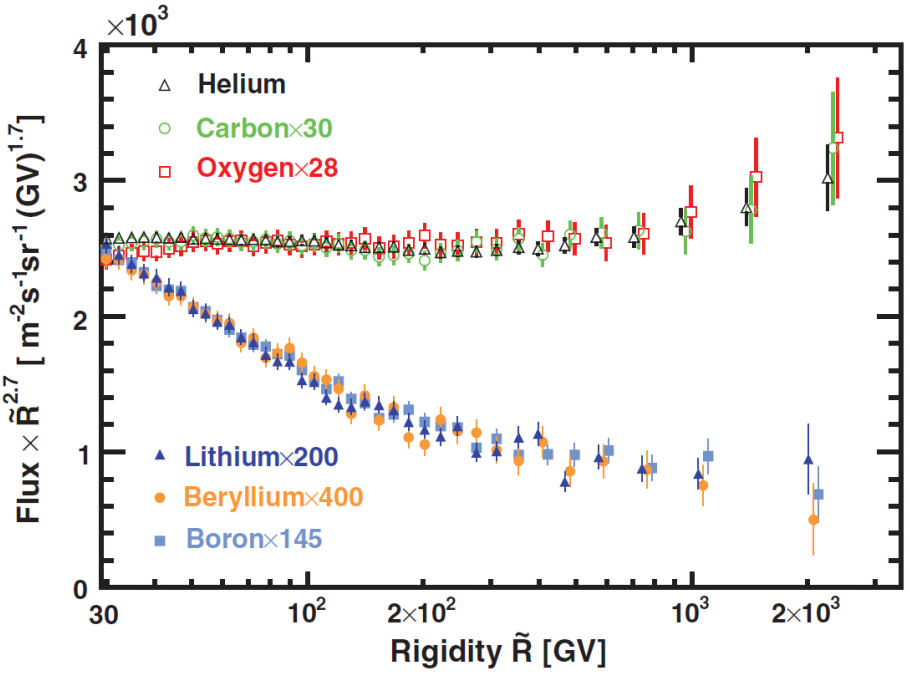

Fig. 1.6 AMS results on the primary He-C-O, and secondary Li-Be-B fluxes multiplied by $\widetilde{R}^{2.7}$ as functions of rigidity above 30 GV. The fluxes were rescaled as indicated. Taken from [82]

the secondary contribution. The AMS measured Oxygen (O) and Boron (B) spectra have been used as characteristic primary and secondary component respectively. As seen, N flux is well described by the sum of a primary and a secondary component in the entire rigidity range.

Magnesium (Mg) along with Neon (Ne) and Silicon (Si) are mostly primary cosmic-ray nuclei heavier than Oxygen. And similar to Nitrogen (N), Aluminum (Al) nuclei are expected to be a mixture of primary and secondary cosmic rays. Based on the new properties observed from the precision measurements of light nuclei by AMS, one would wonder if the heavier nuclei have similar behavior. Observations for Ne, Mg, and Si will be discussed in Section 3.9 of Chapter 3, and observation for Al will be discussed in Section 4.5 of Chapter 4.

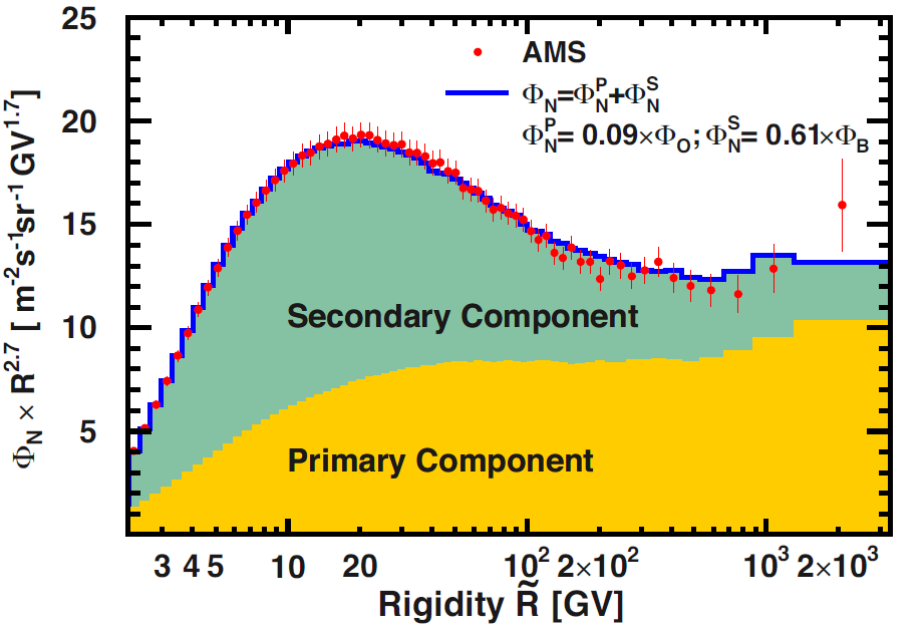

Fig. 1.7 The AMS Nitrogen flux together with the fit of the weighted sum of the primary Oxygen and secondary Boron fluxes over the entire rigidity range (2.2 GV to 3.3 TV). Taken from [65]

Chapter 2

The Alpha Magnetic Spectrometer

The Alpha Magnetic Spectrometer (AMS) is a multipurpose particle physics detector installed on the International Space Station (ISS) on May 19, 2011. As a unique magnetic spectrometer in space, AMS has been continuously taking data and will operate on the ISS for its entire lifetime. The physics objectives of AMS include the precise study of cosmic-ray properties, searching for dark matter, antimatter as well as the exploration of new phenomena.

2.1 The AMS-02 detector

The AMS-02 instrument consists of several sub-detectors to redundantly identify particles (e^-, e^+, p, $\overline{p}$), nuclei, and anti-nuclei in space.

As seen in Figure 2.1, the AMS detector includes a permanent magnet, an array of Anti-Coincidence Counters (ACC) and a series of sub-detectors to independently measure particle charge (Z), energy (E), and momentum (P) or rigidity (R=P/Z). The sub-detectors include

- a Transition Radiation Detector (TRD),
- four planes of Time of Flight counters (TOF), of with two are placed above the magnet (Upper TOF) and the other two are below the magnet (Lower TOF)
- a Ring Imaging Cherenkov counter (RICH)
- an Electromagnetic Calorimeter (ECAL)
- nine layers of Silicon Tracker, the first layer placed at the top of the detector, the second just above the magnet and below the Upper TOF, six layers inserted inside the magnet bore, and the last placed between RICH and ECAL.

The AMS coordinate system is concentric with the center of the magnet. The x axis is parallel to the main component of the magnetic field (Section 2.1.1), y axis points to the bending direction and z axis points to vertically.

The detector weighs 7.5 tons and has the dimensions of 5 m × 4 m × 3 m.

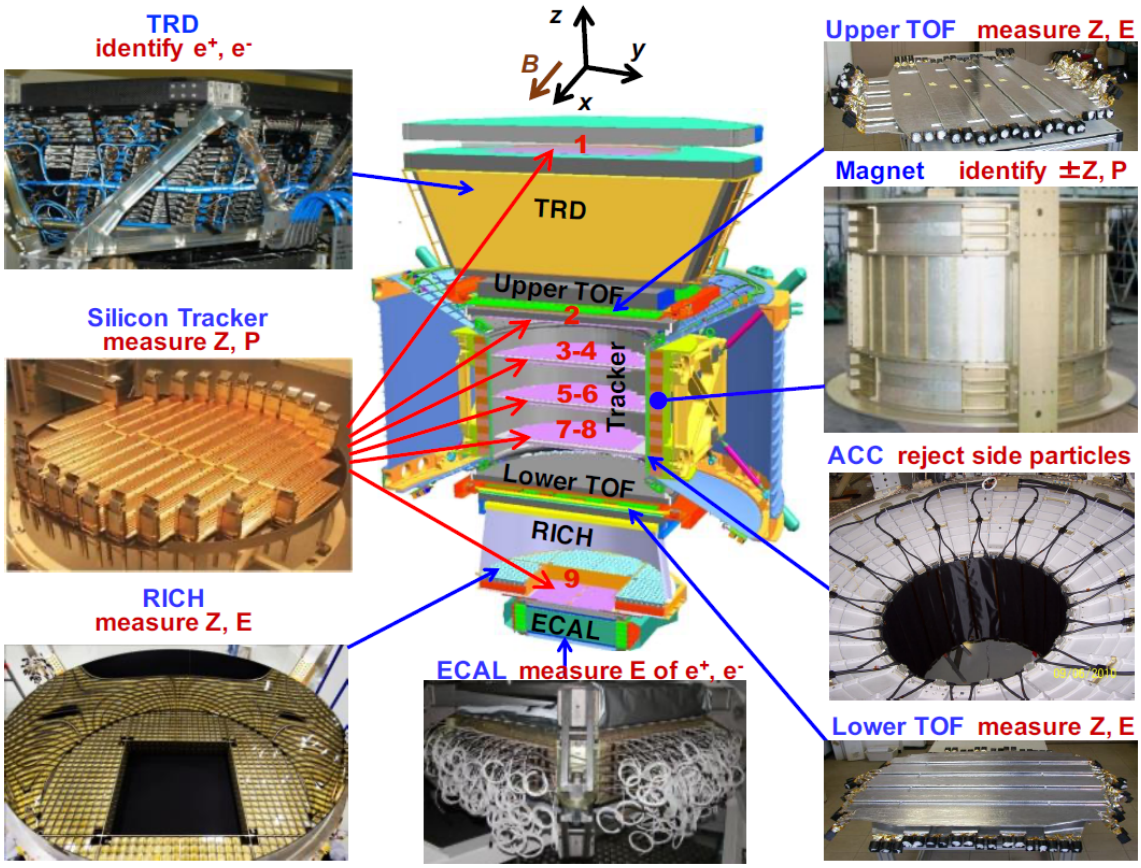

Fig. 2.1 The layout of AMS detector and its main elements and their functions, taken from[65]. The sub-detectors including Tracker, TOF, RICH and ECAL independently measure particle charge (Z), energy (E) and momentum (P) or rigidity (R=P/Z). The ACC counters are used to reject particles entering the detector from the side. The AMS coordinate system, concentric with the magnet, is also shown.

2.1.1 Permanent Magnet

The heart of the detector is the magnetic spectrometer, made by the permanent magnet and seven Silicon Tracker layers inside magnet bore.

The permanent magnet consists of 64 high-grade Nd-Fe-B permanent magnet sectors assembled in a cylindrical shell with the diameter of 1.1m and height of 0.8m. As seen

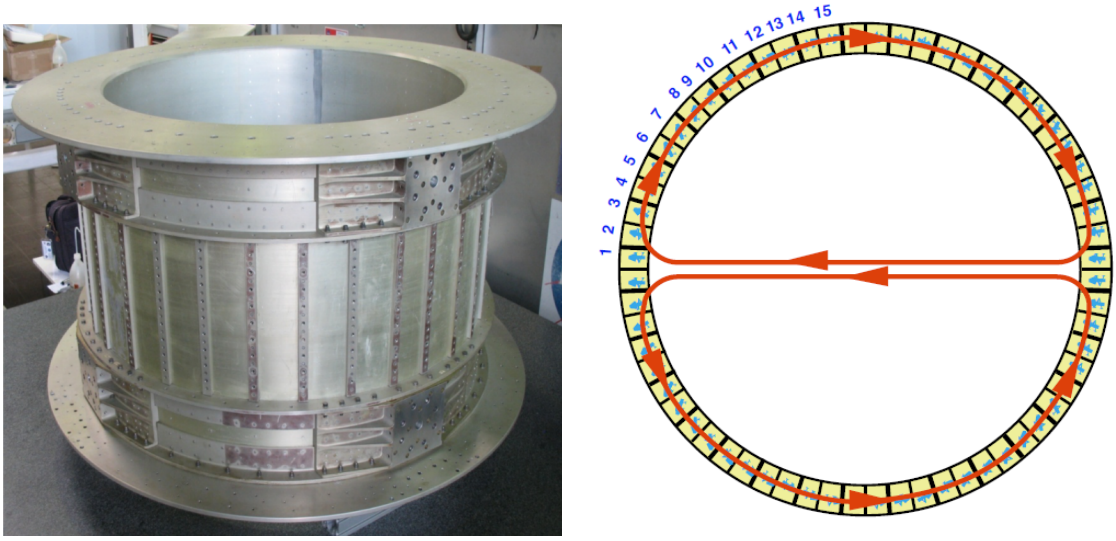

Fig. 2.2 A picture of the magnet (left plot) which has a cylindrical shell structure of 0.8 m long with an inner diameter of 1.115 m. And the arrangement of the AMS magnet and the magnetic field direction produced by the 64 permanent magnets sectors (right plot). Taken from [65].

in Figure 2.2, the arrangement produces a field of 1.4kG at the center of the magnet and negligible dipole moment and field leakage outside the magnet. Together with nine layers of Silicon Tracker, the magnet provides a maximum detectable rigidity (i.e., the maximum rigidity that the detector can discriminate) of 2 TV for protons and 3.2-3.7 TV for nuclei [65, 85].

The AMS coordinate system is naturally defined according to the geometry of the magnetic field, as mentioned, in which y axis points to the bending direction and z axis points to vertically.

2.1.2 Silicon Tracker

The Silicon Tracker, together with the permanent magnet, measures particle charge (Z), momentum (P) and rigidity (R) which is the momentum divided by charge.

The Silicon Tracker consists of 9 tracker layers, each layer is made of 16 to 26 ladders composed of double sided microstrip silicon sensors, readout electronics, and mechanical support [86, 87]. As shown in Figure 2.3a, six layers (L3 to L8) are mounted on 3 support planes placed inside the magnet bore. One layer, L2, is mounted on a support plane placed just above the magnetic. Two Additional layers (L1 and L9), each mounted on its own support plane are placed at the top (above TRD) and at the bottom (below ECAL) of the detector respectively. L2-L8 is called the Inner Tracker. The stability of the planes of

the Inner Tracker are monitored by 20 IR laser beams, and the positions of Tracker L1 and L9 are aligned using cosmic ray protons every 2 minutes. Figure 2.3b and 2.3c show the alignment stability of L1 and L9 over seven years. As seen, the alignment stability is 2.2 μm for Tracker L1 and 2.3 μm for Tracker L9.

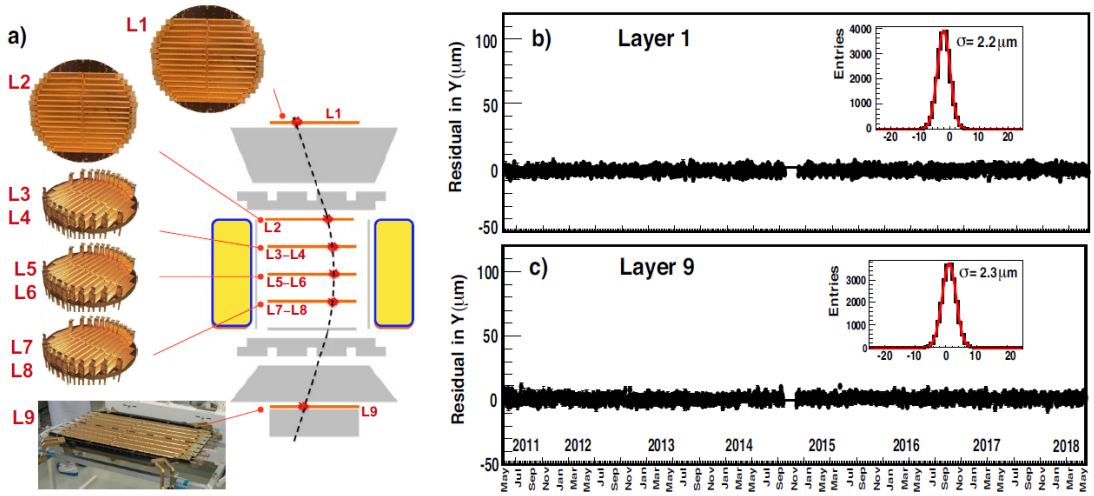

Fig. 2.3 (a) Schematic of the AMS tracker. The alignment stability of (b) Tracker L1 and (c) Tracker L9 over seven years. Taken from [65].

The Silicon Tracker accurately determines the particle trajectory and charge by multiple measurements of the coordinates and energy losses. The particle trajectory determines the particle gyroradius. And the rigidity is determined by the particle gyroradius multiplied by the magnetic field strength.

Figure 2.4 shows the schematic of the measurement principles in a double-sided micro-strip sensor. With a biasing voltage applied on the sensor, a charged particle traversing the sensor creates electron/hole pairs due to ionizing radiation. The electrons and holes are then collected by n^+ strip (defined as the x-side in AMS convention), and p^+ strip (defined as the y-side) receptively. The AMS-02 silicon double-sided micro-strip sensors are 300 μm thick with the dimensions of $72.045 \times 41.360\,\mathrm{mm}^2$. The signal collection depends on the implantation and readout pitches which are placed on the surfaces of both x-side and y-side strips. For the y-side strips, the implantation pitch is 27.5 μm, and the readout pitch is 110 μm, i.e., every three intermediate strips separate two readout strips. While for the x-side strips, the implantation pitch is 104 μm, and the readout pitch is 208 μm, i.e., every two intermediate strips separate two readout strips. The x (non-bending) and y (bending) coordinates are measured simultaneously by the sensor.

The y-side strips have a much finer implantation pitch compared to the x-side, which allows a more accurate coordinate measurement in the bending direction (y direction), and

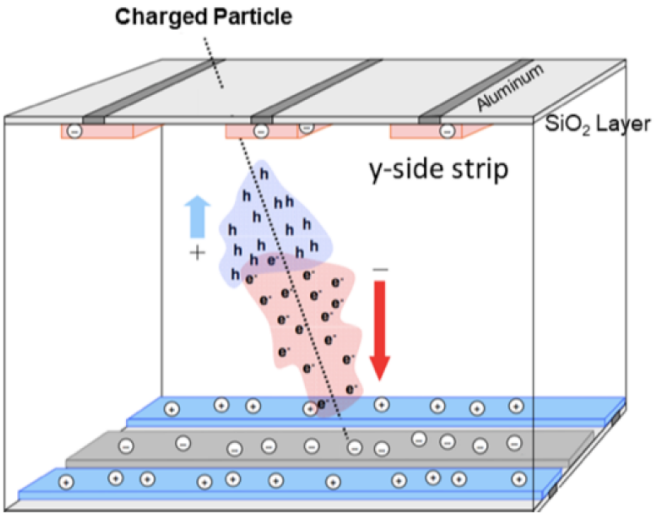

Fig. 2.4 Schematic of the measurement principles of double-sided micro-strip sensor. Taken from [88].

thus better determination of the rigidity. The spatial resolution is $5-10\,\mu$m in the bending plane (y-z plane) and $13-20\,\mu$m in the non-bending plane (x-z plane) [89].

Moreover, the ionization energy losses deposited in the sensor are proportional to the square of charge, hence the absolute value of charge is constructed from the deposited energy measured by x- and y- side strips independently. By combining the charge measured by both x- and y- sides, each layer has charge resolution ($\Delta Z/Z$) of 2.9% for Z=12 (Mg) and 3.0% for Z=13 (Al) nuclei in the region $R > 7$ GV. And then by combining the charge measured by the six layers of Inner Tracker, the overall resolution is 1.1% for Z=12 (Mg) and 1.3% for Z=13 (Al) nuclei [88].

The performance of Silicon Tracker resolution has been studied with both pre-flight at test beams and in-flight calibrations [65]. Before the launch, AMS was extensively calibrated at the CERN with 180 and 400 GeV proton test beams and 10 to 290 GeV positron, electron, and pion test beams. The upper plot of Figure 2.5 shows the comparison between the Data and MC of the inverse rigidity measured by the tracker for 400 GeV protons. The distribution is centered at zero and shows that the Tracker performance is precisely reproduced by MC both in the core and in the tails. During flight, the Tracker performance can be studied by comparing the inverse rigidity measured with the Tracker L1 to L8, with that measured with Tracker L2 to L9. The lower plot of Figure 2.5 shows the comparison between the inverse rigidities measured with the Tracker L1 to L8 and Tracker L2 to L9 for the cosmic ray proton for Data and MC in the rigidity between 1130 GV and 1800 GV. As seen, Data and MC are in a good agreement.

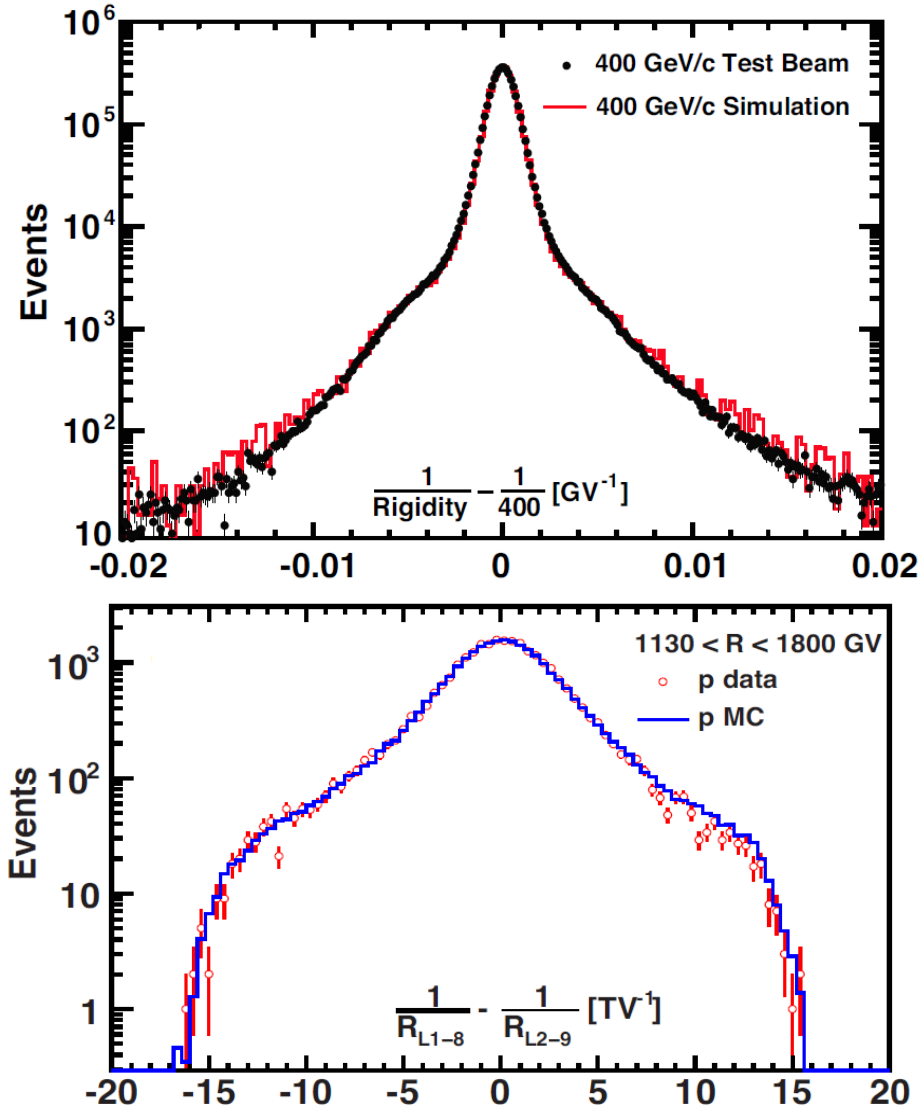

Fig. 2.5 Comparison of the Data and MC tracker resolution measured by the Silicon Tracker with 400 GeV test beam protons (upper plot). Comparison of the Data and MC tracker resolution measured with the Tracker L1 to L8 and Tracker L2 to L9 for the cosmic ray proton in the rigidity between 1130 GV and 1800 GV (lower plot). Taken from [65].

The shift in the absolute rigidity scale due to the residual tracker misalignment and Tracker magnetic field map measurement results in the inaccuracy of the calibration of rigidity. The uncertainty of the absolute rigidity scale is one of the primary sources of the systematic error of the cosmic-ray nuclei fluxes measured by AMS, which will be discussed in Section 3.8.1 of Chapter 3.

2.1.3 Time of Flight counters (TOF)

The Time of Flight counters (TOF) are composed of four layers of scintillator counters. Two layers (Upper TOF) are placed above the magnet, and the other two layers (Lower TOF) are placed below the magnet. As shown in Figure 2.6, each layer consists of 8 or 10 scintillating paddles, readout by 2 or 3 Photo-Multiplier Tubes (PMTs) on each side to efficiently detect the traversing particle. To avoid geometrical inefficiencies, neighboring scintillating paddles with length of length of 110 $\sim$ 135 cm and thickness of 1 cm are assembled with 0.5 cm overlap.

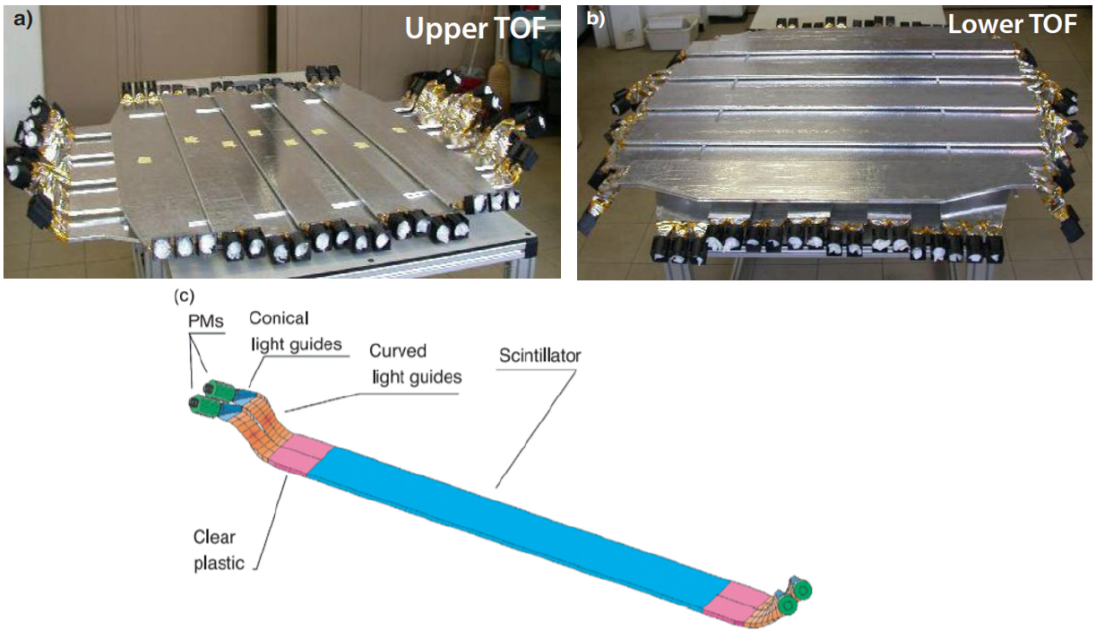

Fig. 2.6 Time of Flight counters (TOF): (a) Upper TOF layer, (b) Lower TOF layer, (c) one TOF scintillating paddle. Taken from [65, 90]

TOF measures the direction and velocity of particles by measuring the time difference between different scintillator layers when the particle passes through the detector. The velocity β (i.e., v/c) of incoming particle is determined from the time of flight, and the upward-going and downward-going particles can be distinguished with the time sequence of the signal

produced in Upper TOF and Lower TOF. Charge can also be constructed from deposited energy measured by four TOF layers. The TOF charge resolution ($\Delta Z/Z$) was measured to be $\sim$ 1.8% for Al and Mg nuclei in the region $R > 20\,\mathrm{GV}$. Matching of charge measured by TOF and Tracker allows the precision measurement of all nuclei fluxes up to and beyond nickel (Z = 28). Figure 2.7 shows the nuclei charge measured simultaneously by TOF and Tracker.

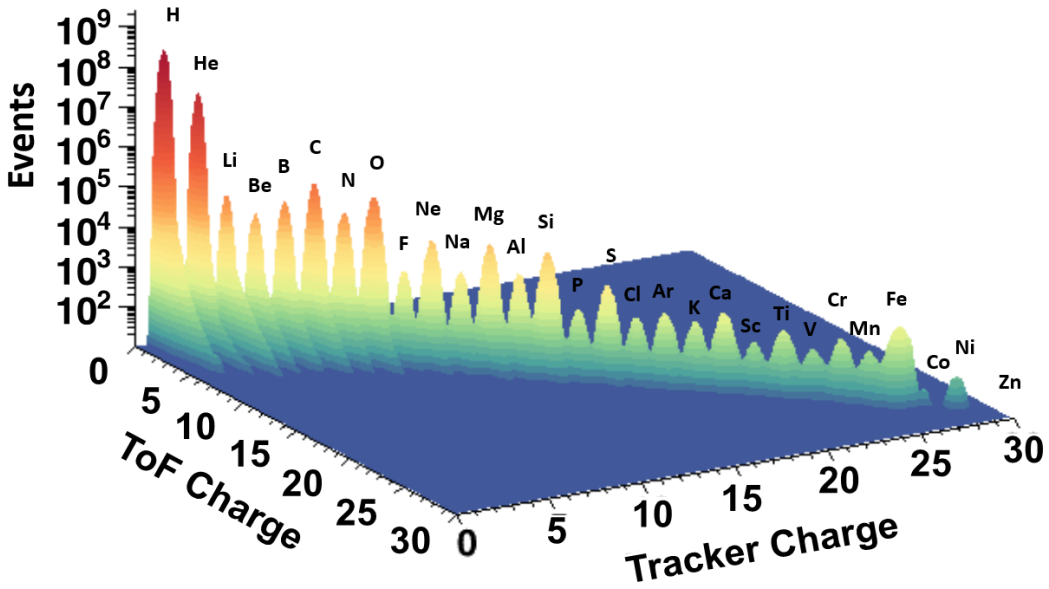

Fig. 2.7 Charge measured by TOF and Tracker. Taken from [65]

TOF covers the detector's geometrical acceptance, the coincidence of signals from all four layers delivers the main trigger to the detector (Section 2.2).

2.1.4 Transition Radiation Detector (TRD)

The Transition Radiation Detector (TRD) is placed at the top of the AMS detector between Tracker L1 and the Upper TOF. It is mainly used to distinguish positrons from protons and electrons and antiprotons from electrons with the transition radiation effect.

The TRD is composed by 20 layers of fleece radiator and proportional tube counters filled with mixture of Xe and CO_2 gas of a total 230 L volume. The proportional tubes run along x direction in eight of the 20 layers, and run along y direction in the remaining 12 layers. Figure 2.8 shows the schematic of the TRD working principle. For electron and positron, the transition radiation is produced in a 20 mm thick fiber fleece radiator, and then collect by the tubes filled with a 90% Xe and 10% CO_2 gas mixture. Xe gas is used to capture the transition radiation X-ray and CO_2 is used as quencher to ensures stable operation of the tubes. While for proton and antoproton passing through TRD with the same energy as electron and positron, they produces energy loss signal by ionizing the gas in the tube and won't produce transition radiation, because proton's γ factor is around 2000 times smaller. In order to separate the light from the heavy particles having the same charge sign, i.e., identify positrons from proton and electrons from aniptotons, signals from the 20 layers of TRD are combined. Figure 2.9shows the proton rejection power of the TRD. At 90% $e^{\pm}$ efficiency, the proton rejection is above 1000 in the energy range from 2GeV/c to 200 GeV/c [65]. And the rejection power at high rigidity can be further improved by tightening the $e^{\pm}$ efficiency to 65%.

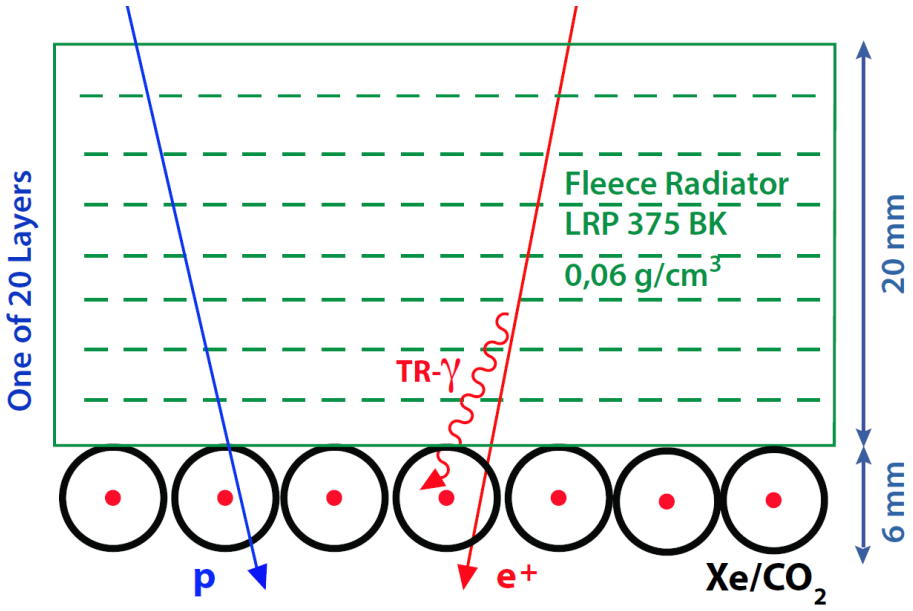

Fig. 2.8 Schematic of the TRD working principle. Taken from [65]

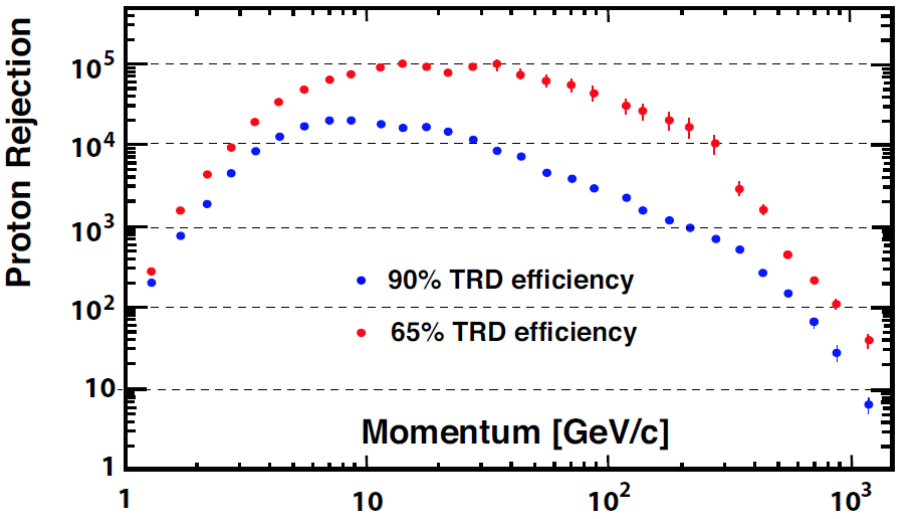

Fig. 2.9 Proton rejection power of the TRD measured on orbit at 90% (blue) and 65% (red) electron and positron efficiency. Tightening the $e^{\pm}$ efficiency to 65% improves the proton rejection power. Taken from [65]

2.1.5 Ring Imaging Cherenkov counter (RICH)

The Ring Imaging Cherenkov (RICH) detector measures the velocity and charge of the relativistic particle by the Cherenkov effect. The AMS RICH is placed below the Lower TOF.

The Cherenkov effect occurs when a charged particle passes through an optically transparent medium. If the speed of the particle is greater than the speed of light in the medium, a cone of light, so-called Cherenkov radiation, is produced. The angle of the light cone is determined by the relativistic velocity of the particle, and the intensity of photons is determined by the energy loss. As shown in Figure 2.10, the AMS RICH is composed of a NaF/ aerogel radiator plane, an expansion volume surrounded by a conical reflector, and a photo-detection plane composed by 680 photo-multiplier for a total of 10,880 pixels.

The radiator plane is composed by two material regions: NaF region, which has a square shape at the center, with refractive index n =1.33, and silica aerogel at the surrounding area with refractive index n=1.05. The Cherenkov radiation is produced with an inclination angle θ, only when the velocity of the incoming particle exceeds the threshold velocity 1/n. The refractive index of NaF is higher than that of aerogel, allowing the detector to cover the velocity (β) range above 0.75 with the NaF radiator, and 0.953 with the aerogel radiator. The velocity is reconstructed from θ, with the charge measured from the intensity of the emitted photons. The velocity resolution for $|Z|>1$ is better than 0.1% at $\beta \sim 1$ [65].

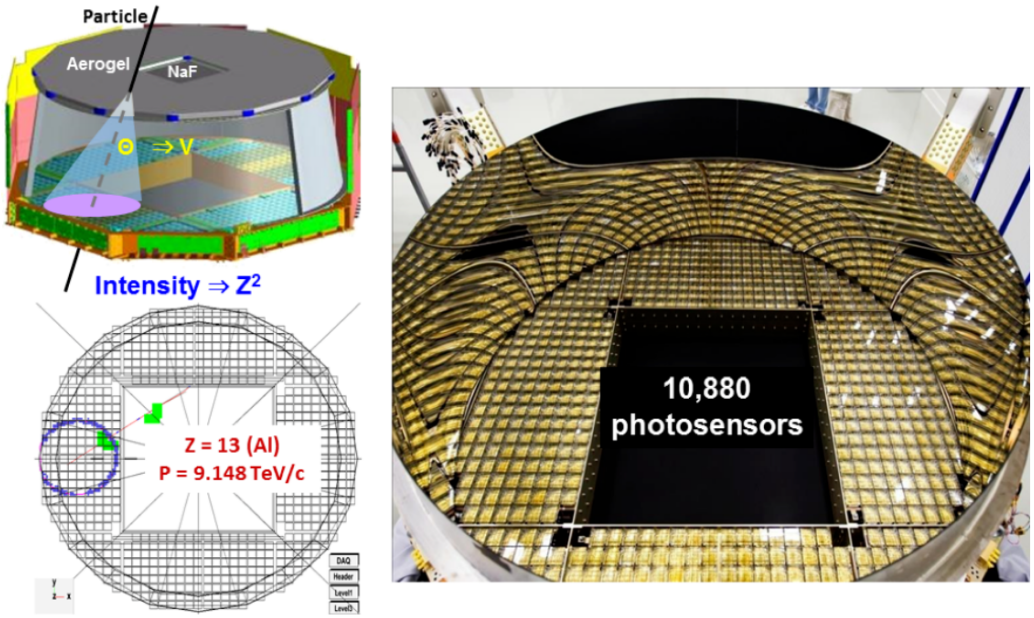

Fig. 2.10 The AMS RICH detector, taken from [65]. The top left plot shows the schematic of the RICH detection principle, the bottom left plot shows an event display of Al nuclei event with momentum of 9.148 TeV/c, and the right plot shows a picture of the AMS RICH.

2.1.6 Electromagnetic Calorimeter (ECAL)

The Electromagnetic Calorimeter (ECAL) is a thick lead-scintillating fiber sampling calorimeter, which performs the 3D reconstruction of electromagnetic showers. It is the critical detector for the measurement of the energy of electrons and positrons, and adding further e/p rejection power.

As shown in Figure 2.11, ECAL consists of a multilayer sandwich of lead and scintillating fibers with an active area of 648×648 mm^2 and a thickness of 166.5 mm corresponding to 17 radiation lengths. The calorimeter is composed of 9 superlayers with each each superlayers composed of 2 layers . To achieve the three-dimensional reconstruction of electromagnetic showers, the scintillating fibers in the superlayers are stacked alternately in x and y directions. The fibers are read out on one end by 324 photomultiplier tubes (PMT), with each PMT reading 4 cells. The cell with the size of 9 mm $\times$ 9 mmis an active area of the superlayer.

ECAL provides an accurate energy measurement for electrons and positrons up to multi-TeV. And the ECAL energy resolution [91] obtained with CERN electron and positron test beams is parametrized by $\sigma(E)/E = (10.4 \pm 0.2)\%/\sqrt{E\,(\mathrm{GeV})} \oplus (1.4 \pm 0.1)\%$. ECAL is also powerful in separating electrons and positrons from protons. By matching between the energy measured by ECAL and the momentum measured by the Silicon Tracker, i.e. $E/P > 0.7$, and discriminating the different 3D shower shapes produced by leptons and

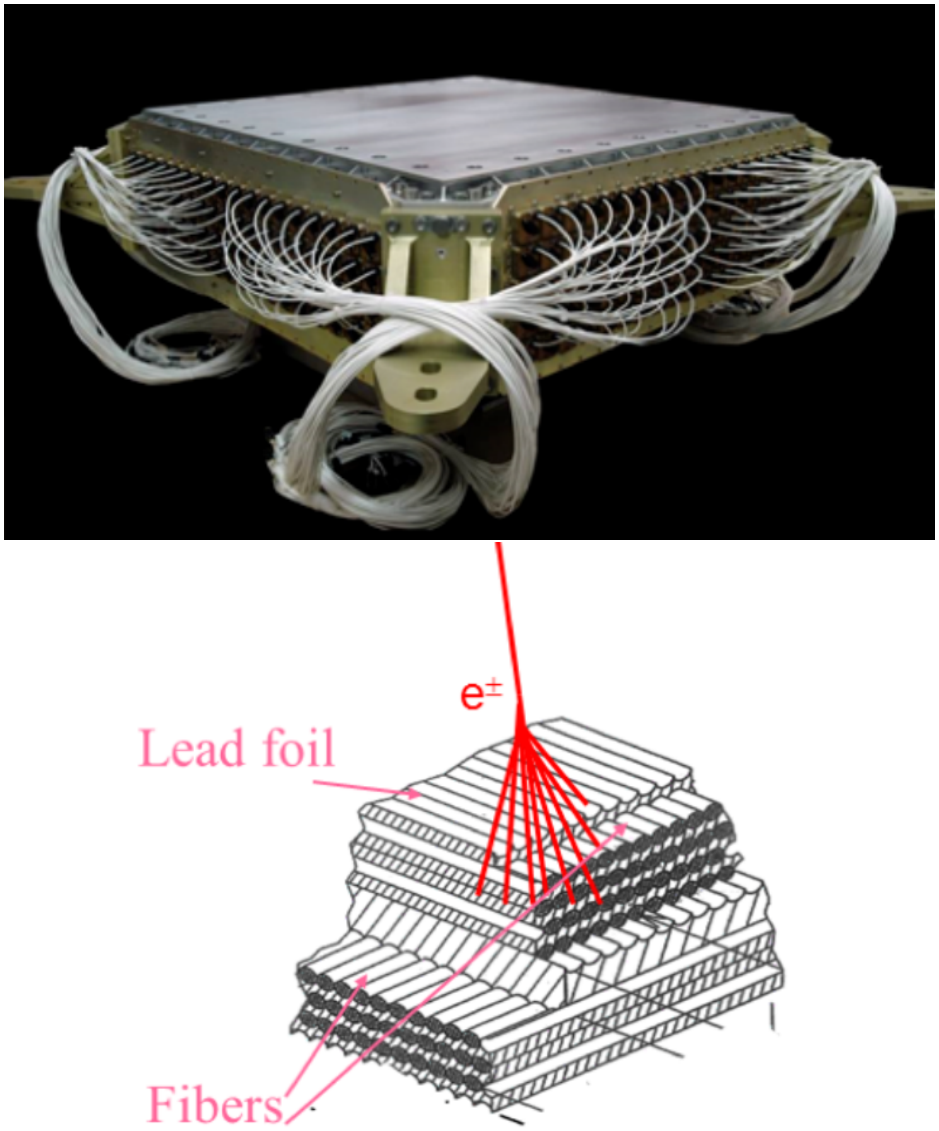

Fig. 2.11 A picture of ECAL and the schematic of the ECAL structure. Taken from [65]

protons, the proton proton rejection is above 10'000 in the energy range above 2 GeV/c at at 90% $e^{\pm}$ efficiency [65].

2.1.7 Anti-Coincidence Counters (ACC)

The Anti-Coincidence Counters (ACC) surround the Inner Tracker and are inside the magnet bore. It is used to veto the particles entering the Inner Tracker from the sides, and also to reject the events with large fragmentation due to interactions of incoming particles with the materials above the Inner Tracker. The veto function of ACC is an important part of the trigger logic, which will be discussed in the following section.

As shown in Figure 2.12, ACC consists of 16 curved scintillation panels with a thickness of 8 mm and height of 800 mm which are assembled into a cylinder with the diameter of 1.1 m [65, 92]. The wavelength shifting fibers are embedded in the panels to collect scintillation light. The wavelength shifted light is then transported by the clear fiber cables and finally collected by the PMT box.

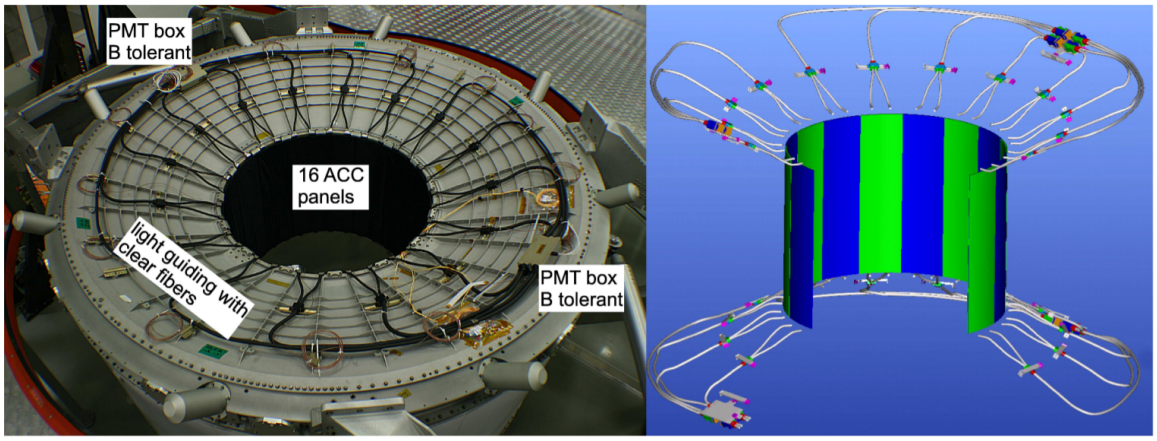

Fig. 2.12 A picture of ACC system (left) and the cutaway view of the ACC. Taken from [92]

Long duration tests of the ACC show that the counters have an efficiency of 0.99999 [92].

2.2 Trigger logic

The AMS-02 trigger logic has been designed to take a fast and efficient decision to start the data acquisition of the signals of interest.

The AMS trigger system uses the combined signal information coming from the TOF, ACC, and ECAL. The trigger logic is based on a complex decision tree architecture with three

levels including Fast trigger (FT), Level-1 trigger and Level-3 trigger. For data acquisition, only the Fast trigger and the Level-1 trigger are used.

Considering that AMS detects particles with a wide range of charge, mass, and energy, different signals can be produced in the sub-detectors of the trigger system. In each level, a set of sub-trigger logic is set up according to the characteristic of particles, with the different combinations of the sub-detectors' signals.

2.2.1 Fast trigger (FT)

The Fast Trigger (FT) is the first trigger activated and is designed to make extremely fast decisions. The next level will be activated only if the Fast Trigger logic is fulfilled.

FT used the signals from ToF and ECAL. TOF signals are classified into three categories:

1. Charged Particle (CP): signal with energy observed in TOF over the high threshold for minimum-ionizing particle (HT). CP signals on TOF layer from 0 to 3 are defined as CP(0) to CP(3) respectively.

2. Charged Particle in Tracker Acceptance (CT): signal with energy observed in TOF over HT and inside the Tracker acceptance

3. High-charge Particle (BZ-TOF): signal with energy observed in TOF over the super high threshold for minimum-ionizing particle (SHT)

On each ECAL superlayer, two signals (ECAL-F) are produces based on signal detected in x or y direction. ECAL signals from 6 out of 9 superlayers excluding the first one and the last two superlayers are used [93]. ECAL-F in x and y directions are combined with logic OR and logic AND to provide another set of signals called ECAL-F-OR and ECAL-F-AND.

The ToF and ECAL signals are then combined in different logic to produce three different FT sub-triggers, FT is formed from the logic OR of the three sub-triggers:

1. FTC (using CP and CT signals from TOF) for all cosmic rays: at least 3 out of 4 TOF layers have CP or CT signals

2. FTE (using energy signals from ECAL) for electrons, positrons and photons: a combination of ECAL-F-OR and ECAL-F-AND

3. FTZ (using BZ-TOF signals) for slow particles such as strangelets: all the 4 TOF layers have BZ-TOF signals and the coincidence of signals is within the time window of 640 ns

2.2.2 Level-1 trigger

Level-1 trigger is after Fast trigger. It contains 15 types of signal and requires 1 μs decision time. The 15 signals are constructed from TOF, ECAL and ACC, including

1. Charged particle signals: after FT, a 240ns gate is opened to latch charged particles signals CP and CT from 4 TOF layers. For FTCP and FTCT, each has two combinations:
   (a) FTCP0: CP signals from at least 3 out of 4 TOF layers
   (b) FTCP1: CP signals from 4 TOF layers
   (c) FTCT0: CT signals from at least 3 out of 4 TOF layers
   (d) FTCT1: CT signals from 4 TOF layers
2. ACC signals: after FT, a 240ns gate is opened to latch ACC signals to count number of ACC. Two signals are produced according to the thresholds of the number of fired ACC ($< N_{tr}$).
   (a) ACC0: number of fired ACC is 0, i.e. $NACC = 0$
   (b) ACC1: number of fired ACC less than a threshold N_{tr1}, i.e. $NACC < N_{tr1}$. Note, N_{tr1} was set to 5 at the beginning of the mission in May 2011, and after February 26, 2016, N_{tr1} was set to 8 to loose the setting and increase the trigger efficiency for heavy nuclei.
3. BZ signals: after FT, a 240ns gate is opened to latch BZ-TOF signals from 4 out of 4 TOF layers.
4. ECAL-F signals: a 240ns gate is opened to latch ECAL-F signals. Same as FT, ECAL-F-OR and ECAL-F-AND are used in Level-1 trigger logic
5. ECAL-A signals: a 240ns gate is opened to latch ECAL-A signals. ECAL-A constructed from the ECAL Shower detected in x or y direction by superlayers. Same as ECAL-F, ECAL-A-OR and ECAL-A-AND are used in Level-1 trigger logic.
6. EXT-GATE signals: a 240ns gate is opened to latch external gate signals including EXT-GATE0 and EXT-GATE1. The two types of signals are not used during flight.

Together with FTE and FTZ, a total of 15 signals from TOF, ECAL, and ACC have been produced. The signals are then combined in different logic to produce eight Level-1 subtrigger. During flight, 7 of the sub-trigger are used to form the Level-1 trigger with the logic OR:

1. Unbiased charged (FTCP0): at least 3 out of 4 TOF signals above HT. Unbiased trigger is not related to physics, and only 1 out of 100 events are stored to reduce the trigger rate.

2. Single charged (ACC0&FTCT1): 4 out of 4 TOF layers signals above HT and number of fired ACC is 0 (NACC=0)

3. Normal Ions (BZ&ACC1): 4 out of 4 TOF layers signals above SHT and $NACC < N_{tr1}$, with $N_{tr1} = 5$ before February 26, 2016, and $N_{tr1} = 8$ after.

4. Slow Ions (FTZ): 4 out of 4 TOF layers signals above SHT and the coincidence of signals is within the time window of 640ns

5. Electrons (ECAL-F-AND&FTCT1): 4 out of 4 TOF layers signals above HT and ECAL signals detected in both x and y direction

6. Photons (ECAL-F-AND): ECAL shower detected in both x and y direction

7. Unbiased EM (ECAL-F-OR): ECAL shower detected in at least on of the direction, only 1 out of 100 events are stored to reduce the trigger rate.

In Level-1 trigger, the Normal Ions sub-trigger is important for heavy nuclei analysis. For heavy nuclei, sizable fragmentation can happen above the Inner Tracker, and a small threshold of number of fired ACC has a non-negligible possibility to reject heavy nuclei events. To avoid the loss of heavy nuclei events, as mentioned previously, the threshold of ACC1 signal was loosed from 5 to 8 after February 26, 2016. The Unbiased trigger events, which are pre-scaled by a factor of 100, are not related to physics and are used to measure the physics trigger efficiency. The trigger efficiency for Mg and Al will be discussed in Section 3.5.6 of Chapter 3 and Section 4.2.2 of Chapter 4, respectively.

2.3 Data acquisition (DAQ)

Figure 2.13 shows the DAQ architecture, which has a tree-like structure [94]:

- The trigger processor (JLV1) collects signals from Fast trigger (FT) ans distributes them to all the sub-detectors to start their readout cycles.

- All the sub-detectors are equipped with dedicated Front-End electronics. Signals from the Front-End electronics are collected and reduced by around 300 data reduction computers (xDR, with x specifying a sub-detector, e.g., TDR stands for Tracker data re-

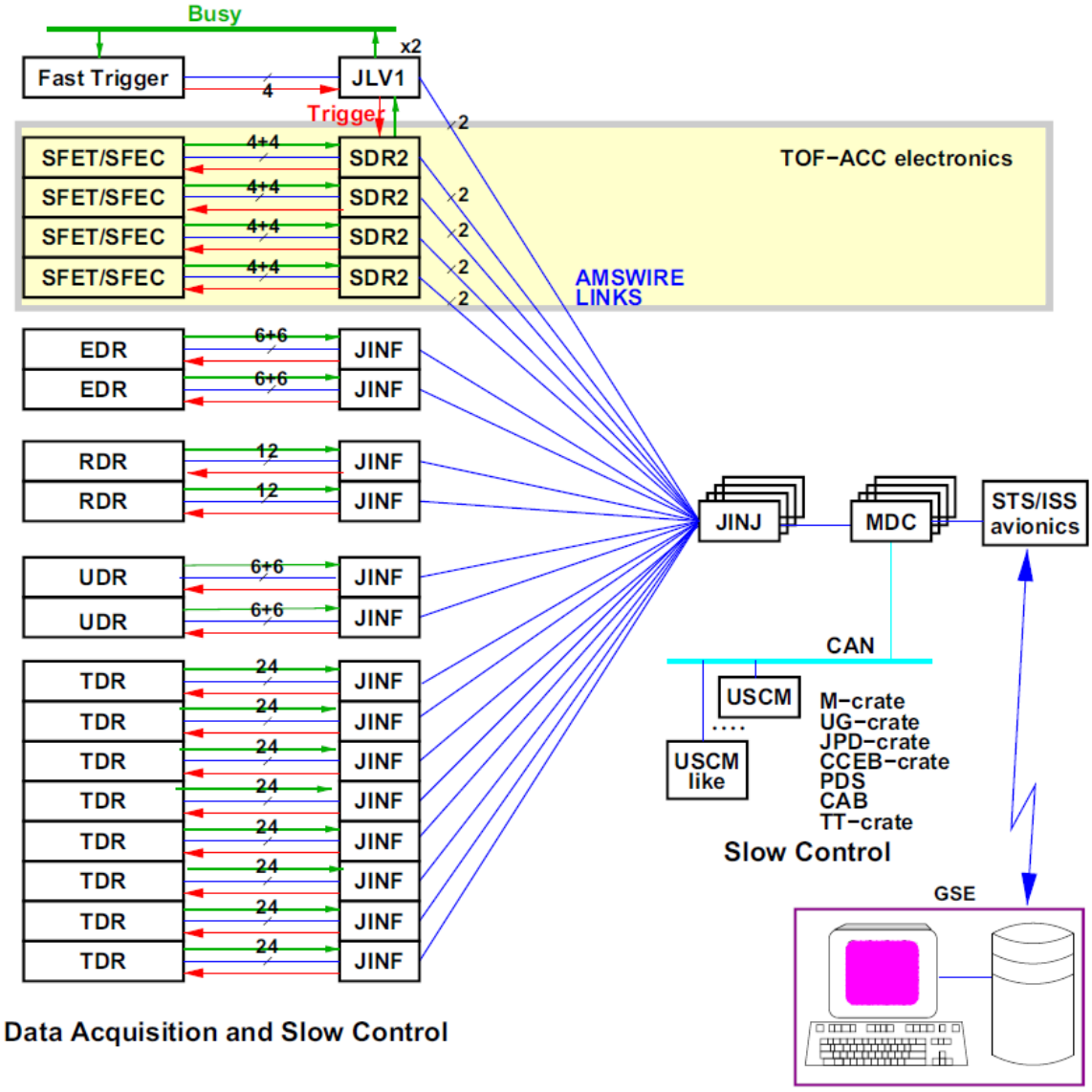

Fig. 2.13 AMS data acquisition (DAQ) system. Taken from [94]

duction computers). The Data from xDR are then processed by readout computers (JINF).

- Signals from TOF and ACC systems are processed by 40 TOF Front-End computers (SFET) and 8 TOF data reduction computers (SDR).
- After collection and reduction, data from JINF, SDR, and JLV1 are combined in DAQ computers (JINJ). Four JINJ are equipped for redundancy. One of the four JINJ was used before February 26, 2016, and two are used after.
- JINJ computers send data to, and receive commands from four redundant main data computers (JMDC). JMDC collects the physics data and then format, compress, reconstruct, buffer the data and send them to the ground. It also has a large buffer to store data of around one day to avoid data loss during the transmission between ISS and ground. Moreover, it also interfaces with ISS Avionics, and executes commands from the AMS Payload Operations Control Centre (POCC) at CERN. Finally, it also handles the monitoring data.

Heavy nuclei with high energy produce large data sizes in DAQ. As mentioned, before February 26, 2016, only one of the four JINJ was used to process data. And due to the limitation of JINJ buffer size (24500 bytes), events with large data size have a non-negligible probability to be truncated. To avoid event truncation for heavy nuclei analysis, 2 JINJ are used since February 26, 2016. The DAQ efficiency evaluates the probability of event truncation, which will be discussed in Section 3.3.3 of Chapter 3

2.4 The AMS Operation in Space

AMS onboard the ISS circles the Earth in roughly 93 minutes at an average altitude of 400 km with an inclination of 51.6 $^\circ$ with respect to the equator.

Thermal control, effects due to the geomagnetic field, and data transfer during the operation will be introduced in this section.

2.4.1 Thermal control

The instrument is subject to drastic thermal variations due to its direction variation to the Sun, Earth, ISS Solar Array, attitude variation of the ISS, etc. To avoid thermal damage to the detector, a system of 298 thermostatically controlled heaters and 1118 temperature monitoring sensors equip the electronics and the sub-detectors to ensure they all work within

their safe thermal limits. The Silicon Tracker is also equipped with an active thermal control systems. The Silicon Tracker produces most of the heat, and its operational range is $-20\,^{\circ}\mathrm{C}$ and $40\,^{\circ}\mathrm{C}$. The temperature of the Silicon Tracker was controlled by the TTCS (Tracker Thermal Control System), which is a mechanically pumped two-phase CO_2 cooling system. And it is able to maintain the temperature range of the Tracker between $-10\,^{\circ}\mathrm{C}$ and $25\,^{\circ}\mathrm{C}$ [95].

Between November 2019 to January 2020, the TTCS was replaced by UTTPS (Upgraded Tracker Thermal Pump System) with four spacewalks carried out by ESA and NASA astronauts. The newly installed UTTPS will enable AMS to continue to operate throughout the lifetime of the ISS.

2.4.2 The Earth's magnetic field

The Earth's magnetic field (geomagnetic field) is approximated by a dipole magnetic field with its axis offset by about 11 degrees from the Earth's rotational axis. The Lorentz force of the geomagnetic field is at its maximum at the geomagnetic equator and at its minimum at the poles. The dipolar magnetic field changes slowly with time and accounts for around 80–90% of the total field in most locations. And together with the effect of the solar wind, the geomagnetic field varies with locations and time. A widely used geomagnetic field model is the International Geomagnetic Reference Field (IGRF) model [96, 97].

AMS orbits at 51.6 degrees inclination and crossing several geomagnetic latitudes, Charged cosmic ray particles of low rigidity ($\lesssim 30\,\mathrm{GV}$), are affected by the Earth's magnetic field.

Geomagnetic cutoff

The geomagnetic field deviates the trajectories of charged particles due to the Lorentz force. For charged particles entering the magnetosphere at the same geomagnetic position, direction, and arrival time, those with the rigidity below a certain threshold value, so-called the geomagnetic cutoff, are shielded by the geomagnetic field. Therefore, particles with rigidity below the cutoff are secondaries coming from inside the Earth's magnetosphere, and need to be rejected in the cosmic-ray analysis.

In the AMS data analysis offline software, the cutoff is calculated by back-tracing [98] particles from the top of AMS out to 50 Earth's radii using the recent IGRF model (the 12th generation) [96, 97]. At each position of the ISS, the maximum value, i.e., the maximum geomagnetic cutoff, for all the directions within the 40° AMS field of view is used in the analysis to reject secondaries. Figure 2.14 shows the maximum geomagnetic cutoff as a function of geographic latitude and longitude over a period of more than 70 days, between

March and May 2012. As seen, the geomagnetic cutoff is higher at lower latitude where it reaches about 30 GV.

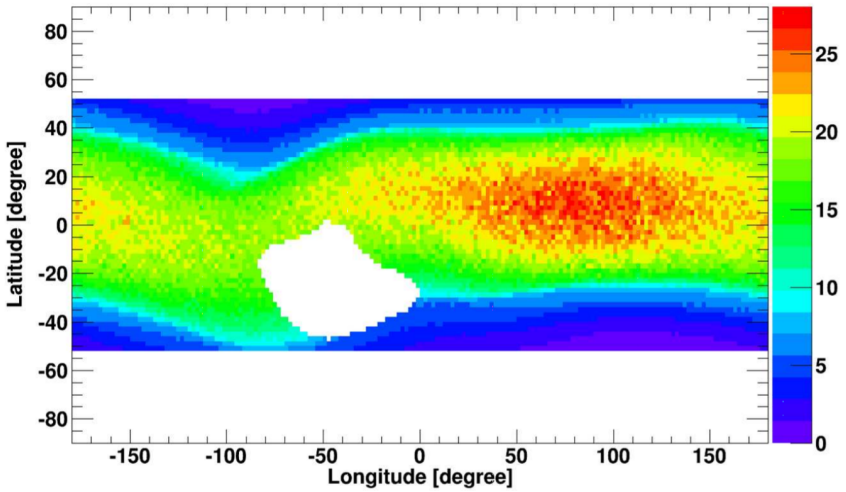

Fig. 2.14 The maximum geomagnetic cutoff within the 40° AMS field of view as a function of geographic latitude and longitude over a period of more than 70 days, between March and May 2012. The blank area indicates the SAA (South Atlantic Anomaly). Taken from [99]

SAA (South Atlantic Anomaly)

Populations of relativistic electrons and protons can be trapped by the geomagnetic field in an inner region of Earth's magnetosphere called the Van Allen radiation belts [100]. The Van Allen radiation belt has a two zone structure: the inner belt at low altitude and the outer belt at high altitude. Due to the slight offset between the geographical center and the geomagnetic center of the Earth, the lower bound of the Inner Van Allen Belt reaches an altitude of around 200 km above the Earth's surface in the South Atlantic geographical region. This area is called SAA (South Atlantic Anomaly), inside it the particle rate is exceptionally high for the AMS DAQ. Data collected inside SAA are not used in the analysis.

2.4.3 AMS operation and data transmission

AMS is operated by its own onboard computers and operations are monitored mainly at the AMS Payload Operation and Control Center (POCC) at CERN.

First, data collected by AMS are transmitted from ISS to the Tracking and Data Relay Satellite System (TDRSS) with an average rate of 10Mbit/s, and then collected by the Space to Ground Link Terminal at White Sands Ground Terminal in New Mexico. And to avoid data dropout during transmission, data for up to two months are stored in the AMS Laptop

onboard ISS. Second, the data are transmitted from White Sands to the Marshall Space Flight Center (MSFC) via NASA networks and then reach at the AMS POCC. After pre-processing, the data are used to monitor the detector status. The data are also transmitted from the AMS POCC at CERN to the AMS Asia POCC in Taiwan, allowing to monitor the status of AMS 24 hours every day. Commands can also be sent from the POCC to AMS follow the same path in reverse. Science data are further processed for data analysis at the AMS Science Operation Center at CERN.

2.5 Monte Carlo simulation (MC)

The AMS Monte Carlo (MC) simulated events are produced by a dedicated program developed by the collaboration [101, 102] based on the GEANT4-10 package [103–105]. The MC simulation is based on the precise knowledge of the detector, including its geometrical dimensions, material composition, characteristics of the electronics, etc. The program simulates the interactions of particles in the AMS material and generates detector responses. More than 8.3 billion simulated magnesium events and 8.7 billion simulated aluminum events and were produced, the simulated raw events then undergo the same reconstruction software as used for the data to reconstruct objects such as particle charge, rigidity, β (velocity), track, etc.

The downward-going MC simulated events are generated uniformly on a 3.9m×3.9m plane above Tracker L1 at 1.95m above the center of the magnet. Two sets of MC simulations have been produced:

- L1 focused MC, the generated particle track is within the Tracker L1 to L8 geometry fiducial volume, and the generated rigidity ranges from 1 GV to 2 TV
- L19 focused MC, the generated particle track is within the the Tracker L1 to L9 geometry fiducial volume, and the generated rigidity ranges from 2 GV to 8 TV

The generated particle spectrum as a function of generated rigidity (R_{gen}) follows a single power-law with the spectral index of -1 (R_{gen}^{-1}). In many cases, the MC generated spectrum needs to be reweighted to have the same energy spectrum features of the Data, which will be discussed in Section 3.1 of Chapter 3.

Chapter 3

Cosmic-ray magnesium nuclei flux measurement with the AMS experiment

As mentioned in Chapter 1, cosmic-ray magnesium (Mg) nuclei are mostly primary cosmic rays produced and accelerated in astrophysical sources. Precise knowledge of their spectra in the GV-TV rigidity range provides important information on the origin, acceleration, and propagation processes of cosmic rays in the Galaxy.

Before this measurement, there have been no measurement of Mg flux as functions of rigidity. And over the last 60 years, earlier measurements (Figure 3.1) were done in kinetic energy per nucleon (Ek/n), however, these measurements have errors larger than 20% at kinetic energy per nucleon 50 GeV/n.

In this Chapter, the precision measurement of the Mg flux in the rigidity range from 2.15 GV to 3.0 TV based on data collected by AMS-02 during its first 7 years of operation on the ISS (from May 19, 2011 to May 26, 2018), and published in [106] will be presented, together with the updated result based on 8.5 years AMS data collected up to October 30,2019.

AMS has been continuing acquiring data, the 8.5 years of data is the current available dataset. The analysis based on 8.5 years AMS data will be presented in detail.

3.1 Analysis framework

3.1.1 Flux formula

Mg flux Φ in the ith rigidity bin $(R_i, R_i + \Delta R_i)$ is computed using the following equation:

$$\Phi(R_i) = \frac{(N_{count}(R_i) - N_{bkg}) \times (1 - \sum_{Z>12} \delta)}{A^{MC}_{\text{effective}}(R_i) \prod \varepsilon_{Data/MC}(R_i) \varepsilon_{DAQ} \varepsilon_{L1Q} \Delta T(R_i) \Delta R_i} \tag{3.1}$$

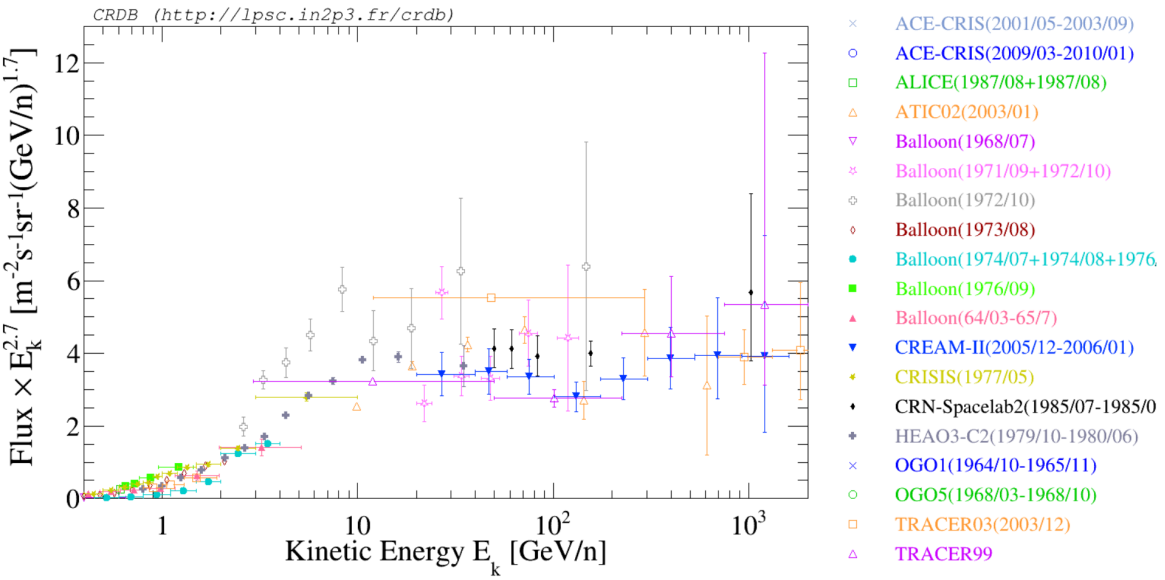

Fig. 3.1 Mg flux as functions of kinetic energy per nucleon (Ek) multiplied by $Ek^{2.7}$, measured by earlier experiments. Data is taken form CRDB [57, 58]

where

- R_i is the rigidity in GV measured by the Silicon Tracker. In this thesis, the fluxes were measured in 66 rigidity bins from 2.15 GV to 3.0 TV, with bin widths chosen according to the tracker rigidity resolution;

- N_{count} is the number of Mg events counts, N_{bkg} is the residual background from nuclei fragmentation occurred between Tracker L1 and L2, $\sum_{Z>12}\delta$ is the top of the instrument background fraction due to fragmentation of heavier nuclei (nuclei with charges Z larger than 12) occurring above Tracker L1, ε_{DAQ} is data acquisition efficiency evaluated from DATA , ε_{L1Q} is the Data L1 charge inefficiency which describes the Mg event loss for Data due to the charge cut on the Tracker L1. The product of these terms (the number of events subtracted by the background contamination, and corrected by DAQ efficiency and L1 charge inefficiency) is also corrected by the bin-to-bin migration resulting from the limited rigidity resolution;

- $A^{MC}_{\text{effective}}$ is the MC effective acceptance including geometric acceptance, event reconstruction and selection efficiencies, and inelastic interactions of nuclei in the AMS materials. To obtain a flux measurement with percent accuracy, small discrepancies between data and MC simulation are accounted by the Data/MC efficiency ratios ($\varepsilon_{Data/MC}$);

- ΔT is the exposure time in seconds, it represents the amount of time that the detector collects data during nominal operating status and has access to the above geomagnetic cutoff particles.

3.1.2 AMS Data and MC

Data

In about 10 years of operation onboard the International Space Station, the AMS detector has collected more than 175 billion cosmic ray events. For each event, 0.46 MB of raw data are produced by 300,000 readout channels of the AMS electronics system. The raw data is then reconstructed with the AMS offline reconstruction software developed by AMS collaboration over the last decades. After that, high-level reconstructed objects such as particle charge, rigidity, β (velocity), track, etc. are stored in the reconstructed data set. This analysis has been performed on the most updated AMS reconstructed data set available, which is based on the first 8.5 years of operations. This data set has been processed with the latest version of the AMS offline reconstruction software (*ISS B1130_pass7*).

MC

The Mg MC simulated raw events, as introduced in Section 2.5 of Chapter 2, undergo the same reconstruction software as used for Data. The latest version of Mg MC simulated events (version *B1220*) is used.

As mentioned, the MC generated particle spectrum as a function of generated rigidity (R_{gen}) follows a single power-law. To evaluate the small discrepancies between data and MC simulation with Data/MC efficiency ratios ($\epsilon_{Data/MC}$) in the flux equation 3.1, the Mg MC generated spectrum is reweighted according to the shape of the Mg flux to produce the same energy spectrum features of the Data. The MC reweighting is done with an iteration method:

1. Mg MC generated spectrum is reweighted with Mg raw flux (flux without efficiency and bin-by-bin migration correction)
2. a preliminary Mg flux is computed
3. MC spectrum is then reweighted with the updated flux

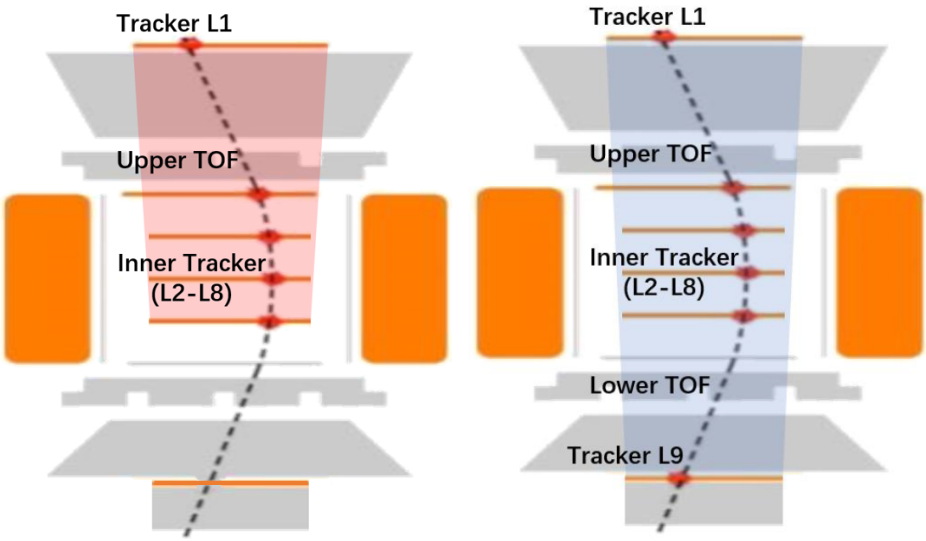

(a) L1Inner (b) FS

Fig. 3.2 Schematic view of the L1Inner (left) and FS (right) geometries

3.1.3 Acceptance geometries

To maximize the statistics of Mg sample and extend the flux measurement to the maximum detectable rigidity (MDR), two detector geometries are used in the analysis (Figure 3.2):

- L1Inner Geometry (L1Inner), requiring particle track passing through Tracker L1 to L8, which has the maximum geometrical acceptance and the MDR for Mg nuclei of ~ 1.3 TV;
- Full Span Geometry (FS), requiring particle track passing through Tracker L1 to L9, which has the MDR of ~ 2.8 TV for Mg nuclei, but has the geometrical acceptance ~ 6 times smaller than L1Inner.

The data sample selected according to the L1Inner geometry is used for the flux measurement below 1.3 TV, and above the FS geometry is used.

3.2 Exposure time

To count the exposure time, a set of standard selection criteria is applied to ensure the detector is in good operational status, and also has access to the above geomagnetic cutoff particles.

Firstly, the time periods when the detector was not in nominal configuration need to be rejected. The AMS runs are named after the UTC time and recorded with Unix Time format, among which the bad runs include:

1306219312, 1306219522, 1306233745, 1307125541-1307218054, 1321198167, and 1434801178-1434841341

Secondly, as mentioned in Section 2.4.2 of Chapter 2, the periods when the International Space Station was inside of the SAA (South Atlantic Anomaly) also need to be cut out.

Moreover, only the seconds when DAQ was away from saturation and having at least one good reconstructed particle are kept. At this purpose, the following data quality selection developed by AMS collaboration is applied on the Real Time Information (RTI):

1. a set of cuts on the triggered events (N_{trig}), reconstructed events (N_{evt}), absent events (N_{err}), and the number of reconstructed particle (N_{par}) to reject events collected during the DAQ closing to saturation and select good reconstructed particle, including:
   - $N_{trig}/N_{evt} > 0.98$
   - $N_{err}/N_{evt} < 0.1$
   - $N_{part}/N_{trig} > 0.07/1600 \times N_{trig}$ && $N_{part}/N_{trig} < 0.25$
2. data acquisition life time (t_l) is greater than 0.5 to avoid DAQ saturation
3. at least one reconstructed particle selected by $N_{par} > 0$ and redundant cut $N_{evt} < 1800$
4. AMS z-axis pointing within 40° of the local zenith to avoid to have the detector looking at the Earth's limb
5. good RTI status to reject duplicate events, event number flip, event missing at the beginning or the end of second, or the second at the beginning or the end of run
6. agreement between bending coordinate obtained from two independent alignment algorithms

Finally, the measured rigidity is required to be greater than a safety factor of 1.2 times the maximum geomagnetic cutoff R_c within the 40° AMS field of view. Systematic uncertainty due to the choice of the safety factor will be checked by varying it from 1.0 to 1.4 in Section 3.8.4. As a result, to count the the seconds of the exposure time(α_t) , $\alpha_t = t_l \times N_{evt}/(N_{evt} + N_{err})$ is accumulated in the rigidity bin whose lower bin edge is larger than $1.2 \times R_c$.

The AMS-02 8.5 years (May 19, 2011 to October 30, 2019) exposure time as a function of rigidity is shown in Figure 3.3. Due to the effect of the geomagnetic field, the exposure time increases with rigidity and reaches a plateau value of $\sim 1.97 \times 10^8$ s for rigidity above 30 GV.

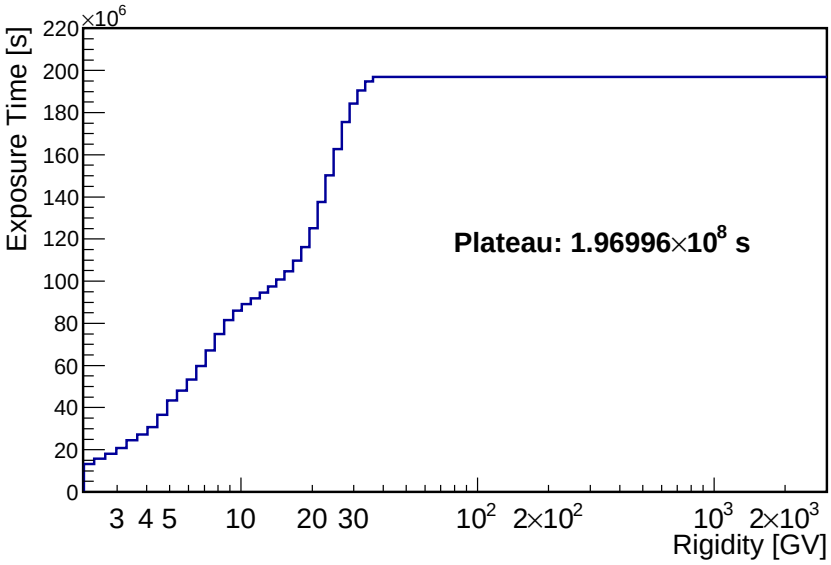

Fig. 3.3 The AMS-02 8.5 years (May 19, 2011 to October 30, 2019) exposure time as a function of rigidity

3.3 Event Selection and Event Counts

3.3.1 Event selection

As mentioned in section 3.2, the selection applied to the exposure time includes bad runs removal, SAA cut, data quality cut, and geomagnetic cutoff. Moreover, regardless of nuclei species, physical trigger selection should also be applied in the analysis.

Since L1Inner and FS are used for the nuclei measurements, the sub-detectors involved are the TOF detector, Inner Tracker, external layers of Tracker (L1, L9). Selections on TOF, Inner Tracker, Tracker L1, and Tracker L9 (for FS study) are applied to have good reconstruction.

TOF reconstruction selection

- A velocity β is well reconstructed, and $\beta > 0.4$ to make sure the particle is downward going

- The unbiased TOF track (i.e. track reconstructed without requiring the Silicon Tracker) extrapolated to L8 for L1Inner geometry and to L9 for FS is reacquired to be within the Silicon Tracker fiducial volume:
  - the extrapolation of the unbiased TOF track to Tracker layers L2 to L8 (Inner Tracker) is within the fiducial volume of at least 5 of these layers
  - as mentioned in Section 2.1 of Chapter 2, the Inner Tracker L3 to L8 are installed on three support planes, with each plane equipped with 2 layers of detector on both sides, while L1, L2 and L9 are installed on three distinct planes. So for L1Inner analysis, the unbiased TOF track extrapolation is required to be within L1 and all the Inner Tracker support planes ($L1\,\&\,L2\,\&\,(L3 \mid L4)\,\&\,(L5 \mid L6)\,\&\,(L7 \mid L8)$)
  - Similarly for FS analysis, the unbiased TOF track extrapolation is required to be within all the support planes ($L1\,\&\,L2\,\&\,(L3 \mid L4)\,\&\,(L5 \mid L6)\,\&\,(L7 \mid L8)\,\&\,L9$)

Inner Tracker track reconstruction selection

- The reconstructed track is required to have at least five hits on Inner Tracker layers in the bending direction coordinate (y)
- The reconstructed track is required to have at least one hit on all the Inner Tacker support planes ($L2\,\&\,(L3 \mid L4)\,\&\,(L5 \mid L6)\,\&\,(L7 \mid L8)$) in y coordinate
- Inner Tracker track fitting quality $\chi^2_{Inner}/d.f. < 10$ in y coordinate is applied

External Tracker Layer reconstruction selection

- Tracker Track has both x- and y-side hits on L1
- for FS study, x- and y-side hits on L9 is required
- for L1Inner study, L1+Inner Tracker track fitting quality $\chi^2_{L1Inner,Y}/d.f. < 10$ and $(\chi^2_{L1Inner,Y} - \chi^2_{Inner,Y}) < 10$ are required. While for FS study, L1+Inner+FS fitting quality $\chi^2_{L1InnerL9,Y}/d.f. < 10$ is required

Charge selection

Magnesium nuclei events are identified by requiring that the charges measured by TOF, Inner Tracker, Tracker L1 and, for FS analysis, L9 are compatible with charge Z=12. The Charge

selection for Mg was carefully determined [101, 107, 108] to minimize the contamination from neighboring charges and maximize the Mg statistics:

- L1 charge
  - L1 Q[10.6309 , 12.7818] for Data, and L1 Q>10.6309 for MC. The L1 charge upper cut is applied only to Data to minimize the charge contamination form heavier nuclei such as Al and Si. However, with the upper charge cut, Mg events with reconstructed charge Q>12.7818 are lost. A correction to the number of event counts that takes this into account will be discussed in subsection 3.3.2
  - difference between L1 x- and y-side measured charge $\mid Q_{L1,x} - Q_{L1,y} \mid /(Q_{L1,x} + Q_{L1,y}) < 0.2$
  - L1 good charge status, i.e. $(Q_{status}\&0x10013D) == 0$, which is required to select the charge signal that is produced only at the active area of the Silicon Tracker ladders
- Inner charge Q[11.5502 , 12.4498]
- UTOF Q[11.3075 , 13.5]
- LTOF Q>11.3075 for FS analysis
- L9 charge for FS analysis
  - L9 Q[11.3353 , 13.3691]
  - L9 Q asymmetry cut $\mid Q_{L9,x} - Q_{L9,y} \mid /(Q_{L9,x} + Q_{L9,y}) < 0.2$

Event counts

With all the mentioned selection criteria applied, AMS-02 collected more than 2.5 million Mg nuclei events during the first 8.5 years operation. Figure 3.4 shows the Mg events counts and event rates for L1Inner and FS geometries.

3.3.2 Background

The event selection yields a Mg sample purities larger than 97% over the entire rigidity range. The impurities come from the following two sources:

- below L1 background, which is a residual background from the interactions of heavier nuclei such as Al and Si in the material between Tracker L1 and L2

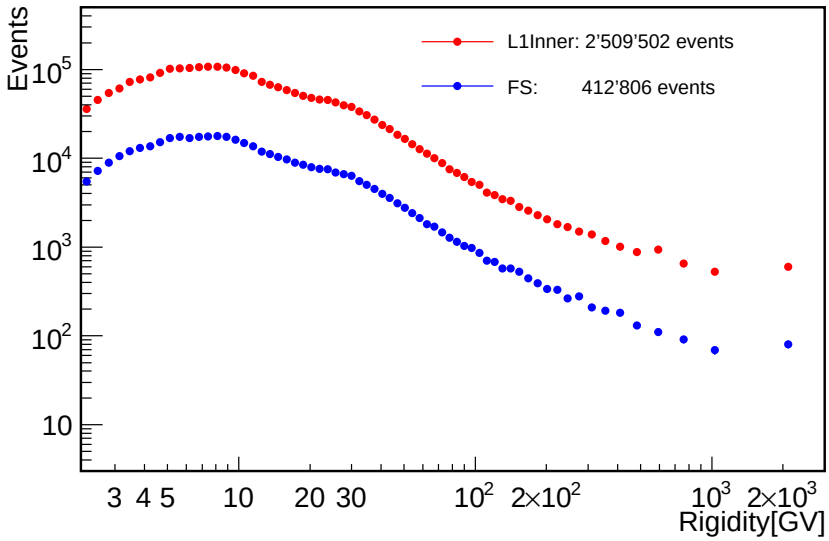

(a) Mg event counts

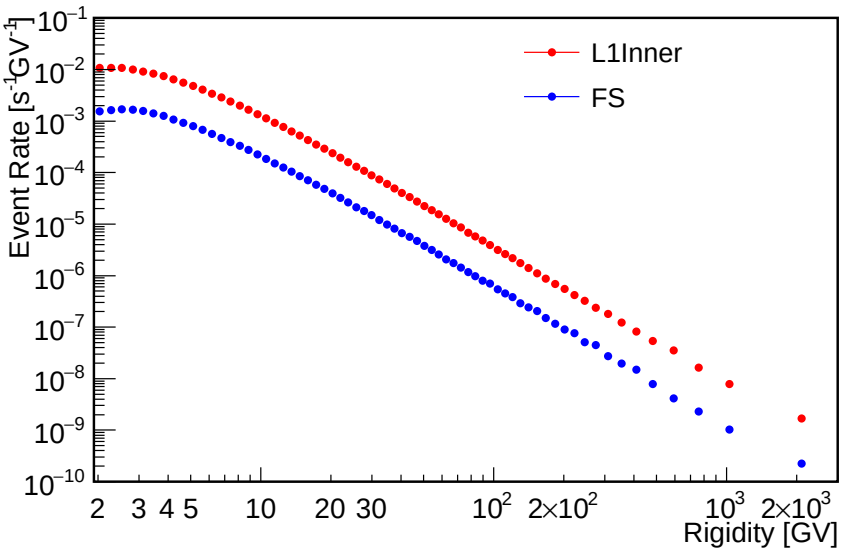

(b) Mg event rate

Fig. 3.4 The AMS-02 8.5 years Mg event counts(top) and event rates(bottom) as functions of rigidity for the L1Inner (red points) and FS (blue points) geometries.

- top of instrument background, which arises from fragmentation of heavier nuclei such as Si and S interacting in materials above Tracker L1 (thin support structures made of carbon fiber and aluminum honeycomb [101]).

Below L1 background

Below L1 background is evaluated by fitting the Mg L1 charge distribution with charge templates of Mg, Al, and Si nuclei. The charge templates can be constructed from L2 charge distributions. Because on the one hand, L1 and L2 have the same detector response as L1 and L2 modules are mechanically and electrically identical, on the other hand, L2 non-interacting samples can be obtained with L1, UTOF, L3-L8 (Inner Tracker without L2), and LTOF selections.

To obtain the pure L2 Mg(Z=12), Al(Z=13), and Si(Z=14) non-interacting samples, the following tight selections have been applied:

- L1 charge Q[Z-0.5, Z+0.5], $| Q_{L1,x} - Q_{L1,y} | /(Q_{L1,x} + Q_{L1,y}) < 0.2$, L1 good charge status $((Q_{status} \& 0x10013D) == 0)$
- UTOF charge Q[Z-0.5, Z+0.5], TOF L1 and L2 charge difference smaller than 1.2 ($| Q_{L1} - Q_{L2} | < 1.2$)
- Tracker Track has both x- and y-side hits on L2, L2 has good charge status
- L3-L8 charge (calculated by the truncated mean) Q[Z-0.5, Z+0.5],
- LTOF charge Q[Z-0.5, Z+0.5], TOF L3 and L4 charge difference smaller than 1.2 ($| Q_{L3} - Q_{L4} | < 1.2$)
- 4 TOF layers have good Path Length Status to cut out the TOF signals produced in the overlap region of the scintillating paddles

Mg, Al and Si charge templates are obtained from the L2 charge distributions converted to probability density functions (PDF) using *RooKeysPdf* method provided by the *RooFit* library [109] in the *ROOT* analysis framework [110]. The events are divided into 42 rigidity bins between 2.15 GV and 3 TV. Figure 3.5 shows examples of Mg and Al L2 charge distribution and their PDFs in one of the rigidity bins.

To study the L1 charge residual background, the L1 charge distribution obtained applying the standard UTOF and Inner Tracker charge cuts mentioned in Section 3.3, is fitted with Mg, Al and Si charge templates. Figure 3.6 shows an example of Mg template fit result in

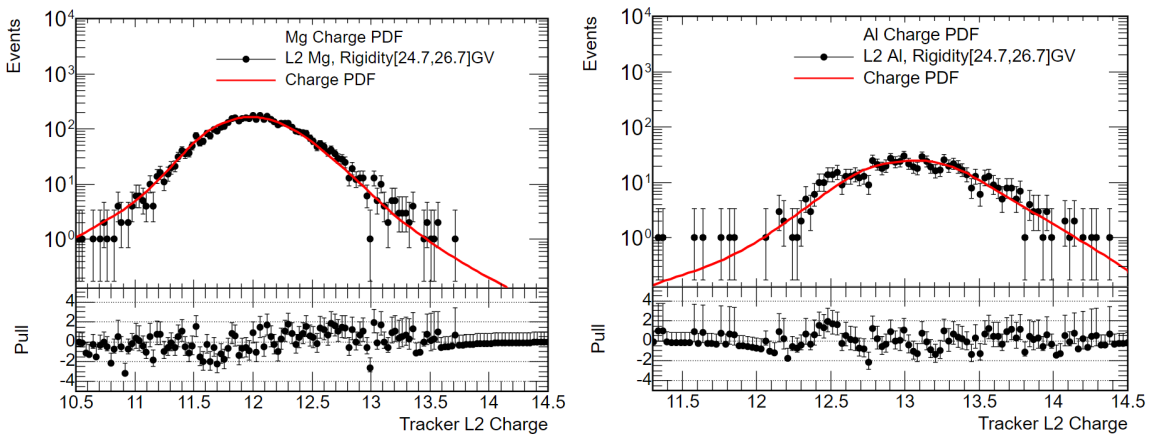

(a) Mg (b) Al

Fig. 3.5 L2 charge distributions for Mg (left) and Al (right) events selected by the L1, UTOF, L3-L8, LTOF in the rigidity range between 24.7 and 26.7 GV (black points). The solid red curves show the PDFs constructed from L2 charge distributions.

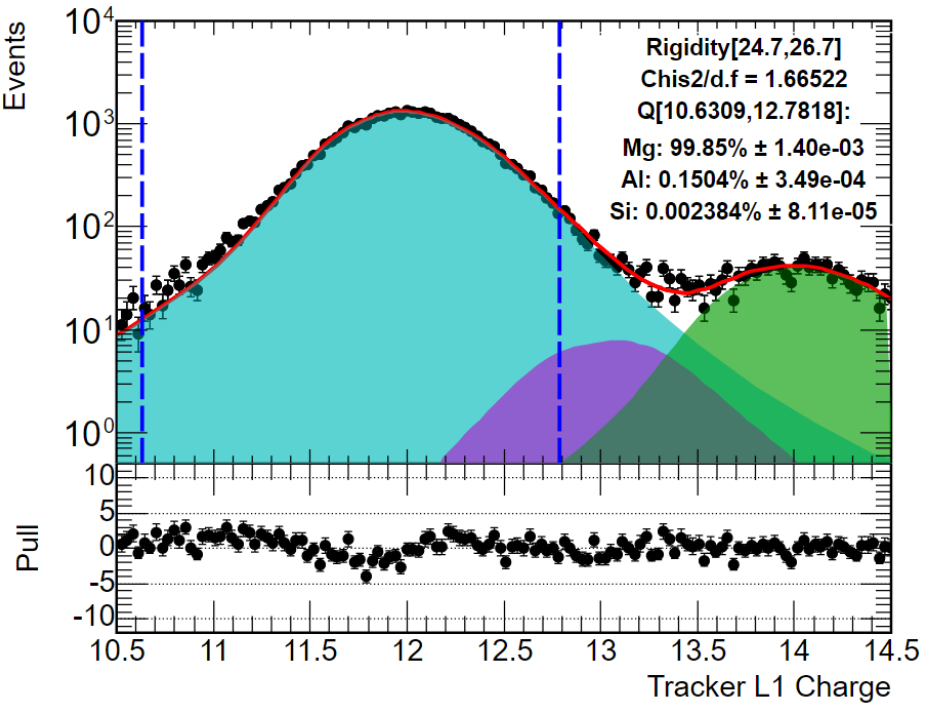

Fig. 3.6 Mg L1 charge distribution in the rigidity range between 24.7 and 26.7 GV (black points). The solid red curve shows the fit using Mg, Al, and Si charge templates obtained from L2 charge distributions. The vertical dashed lines show the charge selection applied on L1 charge. The below L1 background in this rigidity bin is $\sim 0.15\%$.

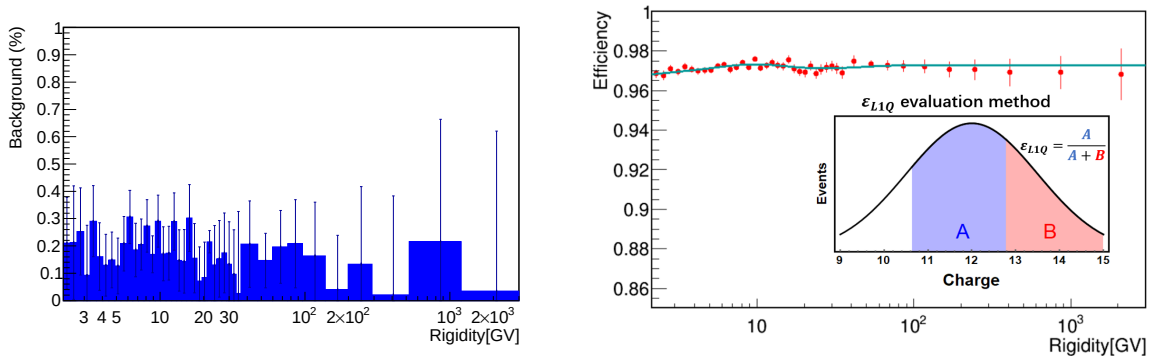

(a) Mg below L1 background

(b) Data L1 charge cut inefficiency

Fig. 3.7 Mg below L1 background (left) and Data L1 charge cut inefficiency ε_{L1Q}(right) as a functions of rigidity. The below L1 background is found to be negligible (less than $\sim 0.3\%$) over the entire rigidity range. ε_{L1Q} is calculated from Mg charge template as shown in the right plot inset.

one rigidity bin. The Mg charge residual background over the entire rigidity range is shown in figure 3.7a; as seen, it's less than 0.3%.

The Data L1 charge cut inefficiency ε_{L1Q} can be evaluated directly by the ratio between the integral of Mg charge template in the L1 charge selection range (Q[10.6309, 12.7818]) and the integral of Mg charge template in the charge range above the L1 lower cut (Q>10.6309), as illustrated in the inset of Figure 3.7b.

Top of the instrument background

Considering that heavier nuclei can interacting in materials above L1 and produce Mg nuclei, the measured Mg events N'_{Mg} contains both genuine cosmic-ray Mg N_{Mg} and Mg events from fragmentation $N_{X\to Mg}$. Therefore, the genuine cosmic-ray Mg flux obtained as follows:

$$\begin{aligned}
\Phi_{Mg} &= \frac{N_{Mg}}{A_{Mg}\Delta T\Delta R} = \frac{N'_{Mg} - \sum N_{X\to Mg}}{A_{Mg}\Delta T\Delta R} \\
&= \frac{N'_{Mg}}{A_{Mg}\Delta T\Delta R}(1 - \frac{\sum N_{X\to Mg}}{N'_{Mg}}) = \Phi'_{Mg}(1 - \sum \frac{\Phi_X}{\Phi'_{Mg}}\frac{A_{X\to Mg}}{A_{Mg}}) \\
&= \Phi'_{Mg}(1-\delta)
\end{aligned} \tag{3.2}$$

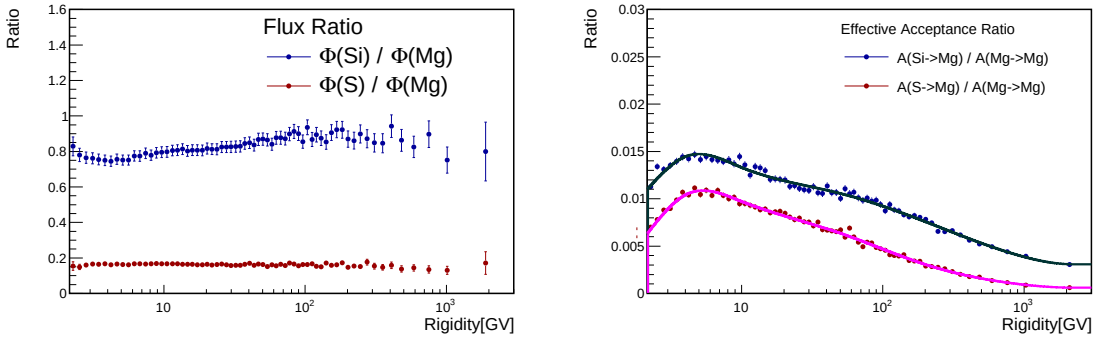

(a) Flux ratios

(b) Effective acceptance ratios

Fig. 3.8 Ratios of Si and Si fluxes to Mg background contaminated flux Φ_{Si}/Φ'_{Mg} and Φ_S/Φ'_{Mg} (left) and effective acceptance ratios $A_{Si\to Mg}/A_{Mg}$ and $A_{S\to Mg}/A_{Mg}$ (right). The blue points shows the ratio between Si and Mg, red points shows the ratio between S and Mg.

where $A_{X\to Mg}$ is the the effective acceptance of heavier nuclei X fragmenting to Mg, Φ_X is the flux of heavier nuclei X, and Φ'_{Mg} is the background contaminated Mg flux. As a result, the top of instrument background correction δ is calculated as $\sum \frac{\Phi_X}{\Phi'_{Mg}} \frac{A_{X\to Mg}}{A_{Mg}}$.

The background contaminated Mg flux Φ'_{Mg} is calculated without considering top of the instrument background. To compute this correction, only the most abundant heavier nuclei nearby Mg are used that is Si and S. The AMS published Si nuclei flux and the AMS preliminary S nuclei flux have been used. Figure 3.8a shows the flux ratios Φ_{Si}/Φ'_{Mg} and Φ_S/Φ'_{Mg} . The effective acceptance will be introduced in Section 3.4. For the top of instrument background evaluation, Mg, Si and S L1Inner geometry effective acceptance can be obtained from the corresponding MC, as shown in Figure 3.8b.

Figure 3.9 shows the top of the instrument background result as a function of rigidity. The background mainly comes from fragmentation of Si, which contribute less than 1.5% over the entire rigidity range.

3.3.3 Data Acquisition (DAQ) efficiency

As mentioned in Section 2.3 of Chapter 2, before February 2016, only 1 JINJ was used in the Data Acquisition (DAQ) system. The collected events, especially for the high charge and high rigidity events, might be truncated during DAQ process due to the limited JINJ size (24500 bytes). The total truncated events taken in time period 1 (before February 2016) $N^1_{>24500}$ can be classified into the following two categories:

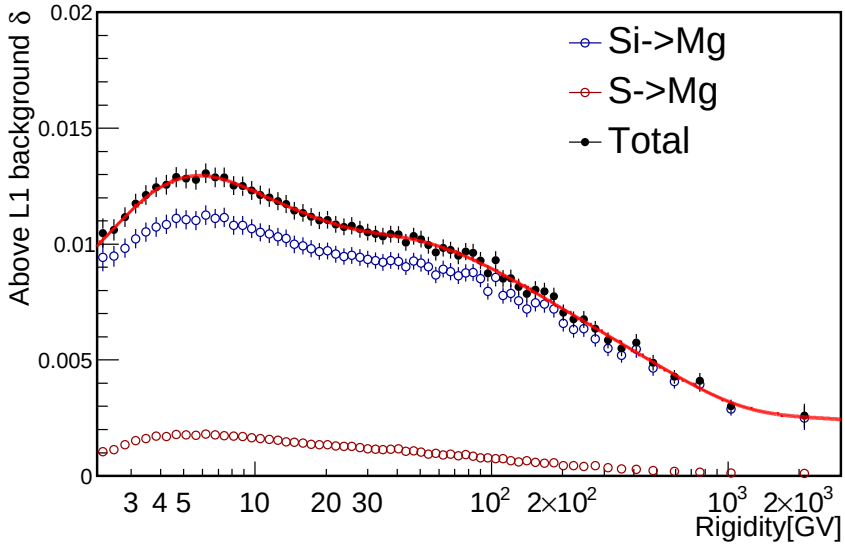

Fig. 3.9 Mg top of the instrument background as a function of rigidity. The blue points show the background from Si, red points show the background from S, black points show the total background, and the red solid curve shows the spline fit to the total background.

- N_{error}: the real event truncation. The primary particle's information of key detectors such as Tracker and TOF is lost by truncation. Therefore, these events will not pass the event selection, because of missing or incomplete information in detectors used in the nuclei analysis.

- N_{irr}: irrelevant event truncation. The information lost concern only delta ray (secondary particle) or detectors such as TRD, RICH and ECAL, which is not used in nuclei event selection.

So the DAQ efficiency in time period 1 (before February 2016) ε^1_{DAQ} can be calculated by:

$$\varepsilon^1_{DAQ} = 1 - \frac{N_{error}}{N^1_{\leq 24500} + N^1_{>24500}} = \frac{N^1_{\leq 24500} + N_{irr}}{N^1_{\leq 24500} + N^1_{>24500}} \tag{3.3}$$

However, in the denominator of equation 3.3, the number of truncated events ($N^1_{>24500}$) is much less than the number of complete events ($N^1_{\leq 24500}$). While in the time period 2 (after February 2016), two JINJ has been used, there is no event truncation and both $N^2_{\leq 24500}$ and $N^2_{>24500}$ are complete events. Thus, the truncated events $N^1_{>24500}$ can be estimated with events collected during time period 2 by assuming the ratio between events with size less

and lager than 1 JINJ size (24500 bytes) are the same for the 2 periods:

$$\frac{N^1_{\leq 24500}}{N^1_{>24500}} = \frac{N^2_{\leq 24500}}{N^2_{>24500}} \tag{3.4}$$

With equation 3.3 and 3.4, the DAQ efficiency for 8.5 years (May 19, 2011 to October 30, 2019) analysis, can be calculated by:

$$\begin{aligned} \epsilon^{total}_{DAQ} &= \frac{N^1_{\leq 24500} + N_{irr} + N^2_{\leq 24500} + N^2_{>24500}}{N^1_{\leq 24500} + N^1_{>24500} + N^2_{\leq 24500} + N^2_{>24500}} \\ &= \frac{N^1_{\leq 24500} + N_{irr} + N^2_{\leq 24500} + N^2_{>24500}}{N^1_{\leq 24500} + \frac{N^2_{>24500}}{N^2_{\leq 24500}} N^1_{\leq 24500} + N^2_{\leq 24500} + N^2_{>24500}} \end{aligned} \tag{3.5}$$

Figure 3.10 shows the Mg DAQ efficiency estimated on Data for 8.5 years analysis.

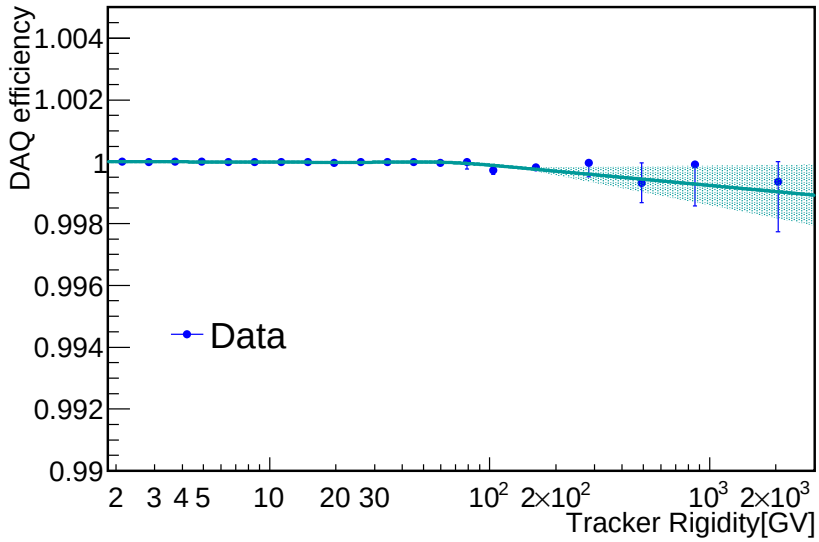

Fig. 3.10 Mg 8.5 years DAQ efficiency as a function of rigidity (blue solid points). The light green curve and band shows the spline fit to the DAQ efficiency and 68% C.L. interval respectively.

3.4 Effective acceptance

The effective acceptance $A_{\text{effective}}$ is estimated from MC simulated Mg nuclei events, which includes the geometrical acceptance, event reconstruction and selection efficiencies, and inelastic interactions of nuclei in the AMS materials. It is then corrected for small differences between Data and MC response.

As mentioned in Section 2.5 of Chapter 2, MC simulated events are generated uniformly on a 3.9m × 3.9m plane at 1.95m above the center of the Magnet. The MC effective acceptance $A^{MC}_{\text{effective}}$ is calculated as:

$$A^{MC}_{\text{effective}} = A_0 \times \frac{N_{sel}}{N_{gen}} \tag{3.6}$$

where A_0 is the geometric factor of the MC event generation plane, N_{sel} is the number of events passing the Mg event selection, and N_{gen} is the number of MC generated events.

Geometric factor

The geometric factor is given by

$$\begin{aligned} A_0 &= \int_\Omega \mathrm{d}\omega \int_S \mathrm{d}\sigma\, \hat{\mathrm{r}} = \int_\Omega \int_S \cos\theta \mathrm{d}\sigma \mathrm{d}\phi \mathrm{d}\cos\theta \\ &= \int_S \pi \mathrm{d}\sigma = \pi \times 3.9^2\,\mathrm{m}^2\mathrm{sr} \approx 47.78\,\mathrm{m}^2\mathrm{sr} \end{aligned} \tag{3.7}$$

where θ is the colatitude and ϕ is the longitude angle, $\mathrm{d}\omega = \mathrm{d}\phi\mathrm{d}\cos\theta$ is the element of solid angle Ω, $\mathrm{d}\sigma$ is the element of surface S.

MC generated events

As mentioned, the MC events are generated with a 1/R spectrum in the rigidity range of 1 GV to 2 TV for L1 focused MC, and 2 GV to 8 TV for L19 focused MC. The total number of MC generated events (N_{gen}) is counted directly from full MC simulation and then distributed into the rigidity bins following 1/R. For the latest version of Mg MC (version *B1220*), the number of MC generated events is 8'427'980'800 for for L1 focused MC, and 8'335'462'400 for L19 focused MC.

The number of generated events is a crucial element for the calculation of effective acceptance. A cross-check of the value of N_{gen} has been performed inverting the formula $A_{geom} = A_0 \times N_{geom}/N_{gen}$, where N_{geom} is the number of generated events passing through

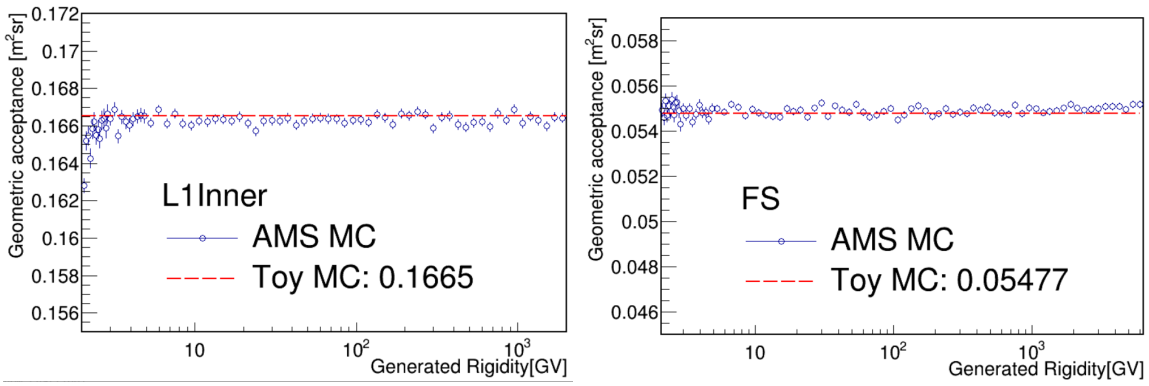

Fig. 3.11 The geometric acceptance calculated from AMS Mg MC (blue points) and toy MC (red line) for L1Inner (left) and FS (right) geometries respectively.

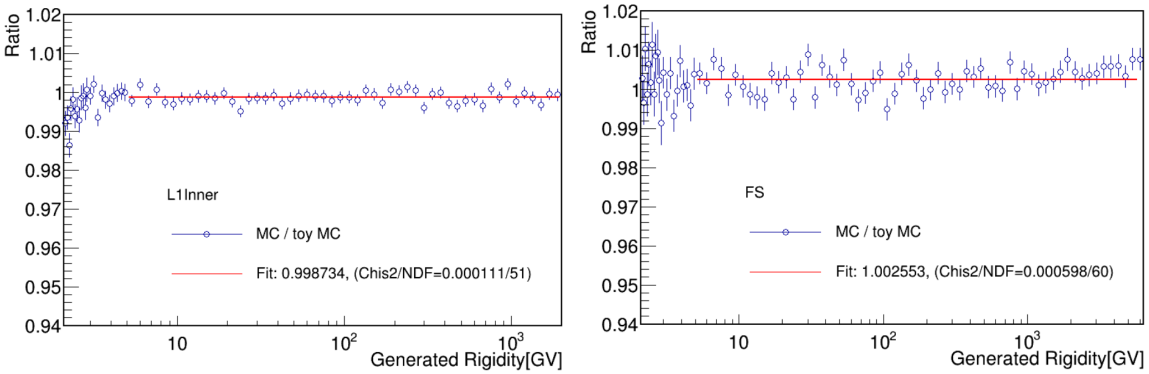

Fig. 3.12 Ratio of the geometric acceptance between AMS Mg MC and toy MC for L1Inner (left) and FS (right). The red line shows a constant fit to the ratio.

the detector fiducial volume. And the MC geometric acceptance A_{geom} can be obtained from a toy MC.

The toy MC events are generated in the same way as AMS MC, i.e. the events are randomly and uniformly generated on the 3.9m×3.9m plane with $\cos^2\theta$ and ϕ uniformly distributed. In the toy MC, 1 billion events were generated, with 0.348504% passed the L1Inner fiducial volume, and 0.114613% passed the FS fiducial volume. So the geometric acceptance result calculated form toy MC is $A_{geom} = A_0 \times 0.114613\% \approx 0.1665\,\mathrm{m^2sr}$ for L1Inner and $A_{geom} \approx 0.05477\,\mathrm{m^2sr}$ for FS. Figure 3.11 shows the geometric acceptance calculated from AMS Mg MC and toy MC, Figure 3.12 shows the ratio between the two calculation results, the two results agrees within 0.3%.

MC effective acceptance

The number of Mg events can be obtained by requiring Mg event selection, with the number of MC generated events verified, MC effective acceptance can be evaluated with equation 3.6. Figure 3.13 shows MC effective acceptance for L1Inner geometry and FS geometry.

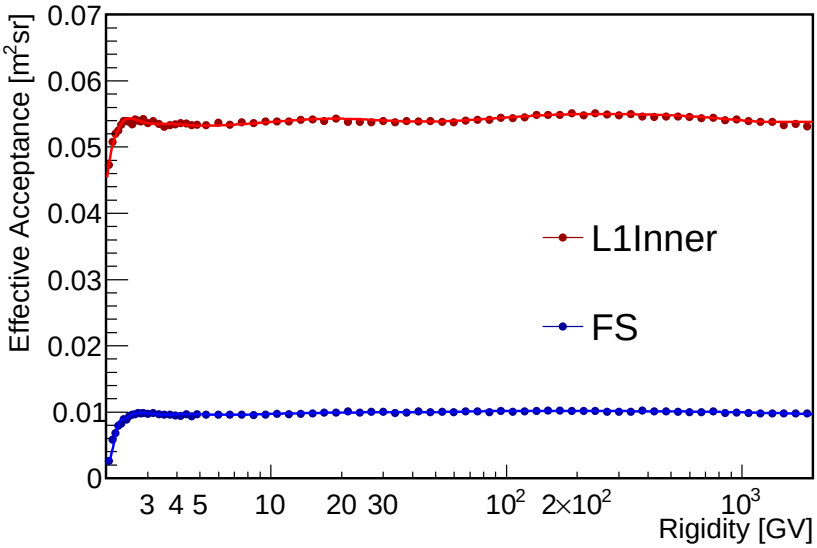

Fig. 3.13 Mg MC effective acceptance as a function of rigidity for L1Inner (red points) and FS (blue points) geometries. The red and blue solid curves show the spline fit to L1Inner and FS results respectively.

3.5 Data/MC corrections

The efficiency of a given cut is computed from the events passing the cut and the sample before applying this cut, by the following formula

$$\varepsilon(R) = \frac{N_{\text{selected}}(R)}{N_{\text{sample}}(R)} \tag{3.8}$$

where ε is the efficiency of a given cut for a specific subdetector; N_{sample} is the number of the sample events which is selected with a set of subdetectors other than the one under study, and without applying this cut; N_{selected} is the number of events passing the cut applied on the sample; the uncertainty of the efficiency is estimated by the binomial error.

Thanks to the redundancy of the AMS detector, the samples used to study the selection and reconstruction efficiencies of a specific subdetector can be defined without requiring this

sub-detector. Therefore, the selection and reconstruction efficiencies can be derived not only from MC but also from the flight Data.

Due to the imperfect MC simulation, the small discrepancies between data and MC simulation need to be accounted for the evaluating of the MC effective acceptance. The MC effective acceptance are corrected by the Data/MC efficiency ratios ($\prod \varepsilon_{Data/MC}$) including

1. Tracker L1 big charge (BZ) efficiency
2. Tracker L1 pick-up efficiency;
3. Inner tracker efficiency;
4. ToF charge efficiency;
5. Tracker L9 efficiency (for FS study).
6. trigger efficiency

3.5.1 L1 BZ efficiency

L1 big charge (BZ) efficiency evaluates the probability that the event has both x- and y-side hits on Tracker L1, with the L1 measured charge greater than 10.63.

To study the L1 BZ efficiency, a sample of Mg nuclei event is selected by requiring the charge measured by a set of sub-detectors except the Tracker L1 to be compatible with Mg nuclei, and without requiring any information about the Tracker L1 hits.

To obtain the sample (denominator of efficiency), the following cuts have been applied

- bad runs removal, SAA cut, RTI cut, and geomagnetic cutoff
- events passing physical trigger
- good reconstructed TOF
- good reconstructed Inner tracker track for L1Inner study and Inner+L9 track for FS study, and the extrapolated track within the Tracker L1 fiducial volume.
- Mg nuclei charge cuts applied on Inner, TOF and L9 (for FS study only)

The detailed description of the listed selections has been discussed during the introduction of the event selection in Section 3.3.

Additional cuts including Tracker L1 hits, L1 big charge (BZ), and L1 unbiased charge status are applied on the sample (to obtain the numerator of the BZ efficiency) to evaluate

the L1 BZ efficiency. The L1 hit with the largest charge, which is not necessarily attached to the Inner tracker track, is called unbiased hit. The selection on the sample is listed as the following:

- both x- and y-side unbiased hits on Tracker L1, which can be applied by requiring the L1 x- and y-side unbiased charge greater than 0
- good unbiased charge status
- the x- and y-side combined unbiased charge greater than 10.6309

For the L1 efficiency study, since the Tracker L1 cannot be used in the sample selection, the rigidity measured by Inner Tracker (for L1Inner study) and Inner Tracker + L9 (for FS study) is used. The MC efficiency as function of the generated rigidity is also done and used as a reference. Figure 3.14 shows the Mg L1 BZ efficiency for Data and MC, and their ratio. The spline fit has been applied to parameterize the Data/MC efficiency ratio. In the high rigidity range, the ratio is parameterized as a constant, and the slope of the efficiency in the MC generated rigidity is taken into account in the evaluation of the error of the Data/MC efficiency ratio parametrization. As seen in the figure, the difference between the Data and MC efficiency is less than 1%, and it does not depend on rigidity.

3.5.2 L1 pick-up efficiency

L1 pick-up efficiency evaluates the probability that a L1 hit is attached to the Inner tracker track and its charge is compatible with Mg nuclei.

The sample to study the L1 pick-up efficiency is selected with the same selection as the L1 BZ efficiency to which is added a tighter upper cut on the combined L1 x- and y-side unbiased charges (L1 unbiased Q<12.5).

Additional cuts are applied to this sample to obtain the numerator of the L1 pick-up efficiency, including

- both x- and y- side L1 reconstructed hits are attached to the Inner tracker track
- good L1+Inner (for L1Inner study) or L1+Inner+L9 (for FS study) reconstructed tracker track, i.e. track fitting quality cuts $\chi^2_{L1Inner,Y}/d.f. < 10$ and $(\chi^2_{L1Inner,Y} - \chi^2_{Inner,Y}) < 10$ for L1Inner study, and $\chi^2_{L1InnerL9,Y}/d.f. < 10$ for FS study
- Tracker L1 charge greater than 10.63, and good L1 charge status

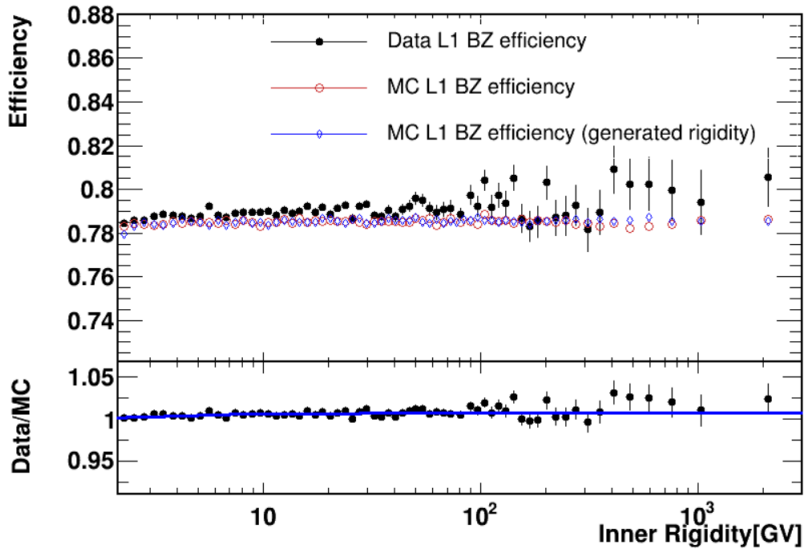

(a) L1Inner

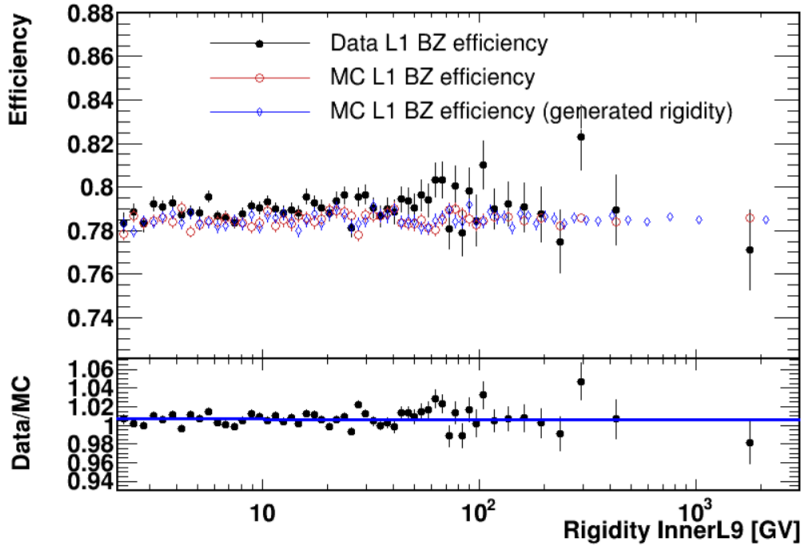

(b) FS

Fig. 3.14 L1 BZ efficiency for Mg nuclei as function of rigidity for L1Inner (upper panel of the plot a) and FS (upper panel of the plot b) geometries obtained from Data (black full circles) and MC (red open circles) as function of the reconstructed rigidity. MC efficiency as function of the generated rigidity is also shown (blue circles). The lower panel shows the ratio between Data and MC efficiencies (black points) and the spline fit of the efficiency ratio (blue line) with its 68% C.L intervals (blue shed). Above 200 GV, the error band of the spline fit is calculated from the slope of the MC efficiency as function of generated rigidity.

Same as the L1 BZ efficiency study, the rigidity measured by Inner Tracker (for L1Inner study) and Inner Tracker + L9 (for FS study) is used for L1 pick-up efficiency. Figure 3.15 shows the Mg L1 pick-up efficiency for Data and MC, and their ratio. The spline fit has been applied to parameterize the Data/MC efficiency ratio. In the high rigidity range, the ratio is parameterized as a constant, and the slope of the efficiency in the MC generated rigidity is take into account as the error of the Data/MC efficiency ratio parametrization. As seen in the figure, the pick-up efficiency increases with increasing rigidity, which is due to the elastic scattering energy dependence. For rigidity above 200 GV, L1Inner and FS efficiencies show different behavior, this is because different track fitting quality cuts in L1Inner and FS study, and the maximum detectable rigidity for Inner Tracker geometry is smaller than Inner Tracker + L9 . As seen in the figure, the difference between the Data and MC efficiency results is less than 1% for rigidity above $\sim$ 10 GV.

3.5.3 Inner Tracker efficiency

Inner tracker efficiency is the probability that the event has well reconstructed Inner Tracker track, with the charge measured by tracker compatible with Mg nuclei.

Rigidity Estimator: TOF β and the geomagnetic rigidity cutoff

In the Inner Tracker efficiency study, Inner Tracker can't be used in the sample selection, instead, a TOF standalone reconstruction is performed using the track from TOF and TRD. To obtain the rigidity dependence of the efficiency, particle's rigidity is estimated from TOF β and the geomagnetic rigidity cutoff.

The β (velocity) measured by TOF is converted to rigidity as

$$R = \frac{Am_p\beta}{Z\sqrt{1-\beta^2}} \tag{3.9}$$

where A=24 and Z=12 are the mass number and the charge of Mg nuclei assuming Mg nuclei are mainly composed by ^{24}Mg, m_p is the proton mass. Due to the limited TOF β resolution, the estimated rigidity is valid below $\sim$ 6.4 GV corresponding to $\beta < 0.96$. Figure 3.16 shows the rigidity estimator constructed from β versus the tracker rigidity: they are in good agreement for $R \lesssim 6.4$ GV.

As mentioned in section 3.2, the maximum geomagnetic rigidity cutoff R_c has a rigidity dependence below few tens of GV, thus can be used to estimate particle's rigidity. Figure 3.17 shows maximum geomagnetic rigidity cutoff versus Tracker rigidity and the edge of maximum geomagnetic rigidity cutoff versus Tracker rigidity. A straight fit is applied to

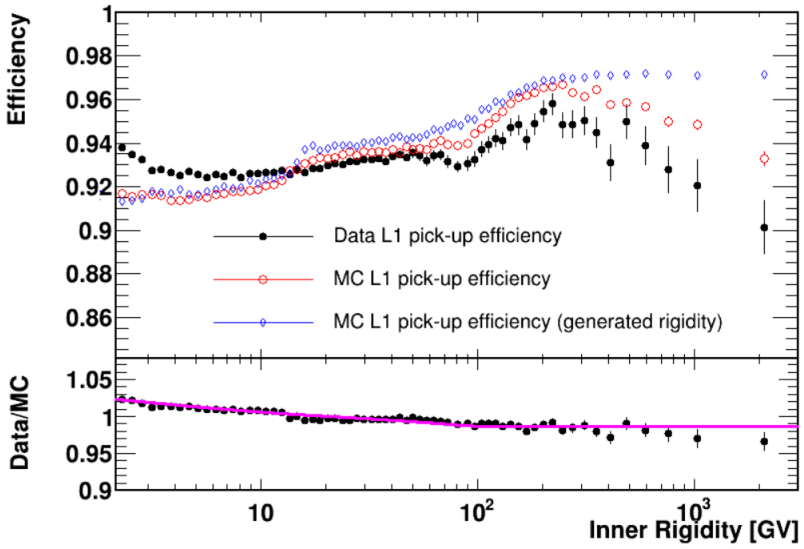

(a) L1Inner

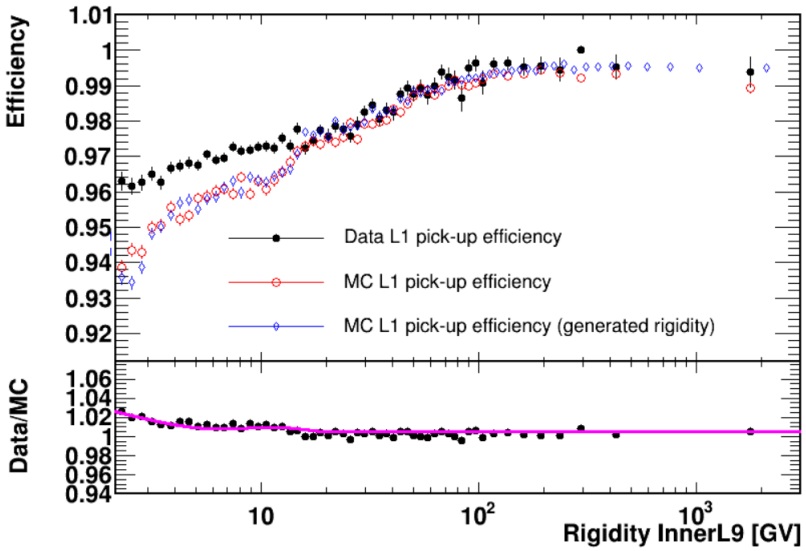

(b) FS

Fig. 3.15 L1 pick-up efficiency for Mg nuclei as function of rigidity for L1Inner (upper panel of the plot a) and FS (upper panel of the plot b) geometries obtained from Data (black full circles) and MC (red open circles) as function of the reconstructed rigidity. MC efficiency as function of the generated rigidity is also shown (blue circles). The lower panel shows the ratio between Data and MC efficiencies (black points) and the spline fit of the efficiency ratio (magenta line) with its 68% C.L intervals (magenta shed). Above 200 GV, the error band of the spline fit is calculated from the slope of the MC efficiency as function of generated rigidity.

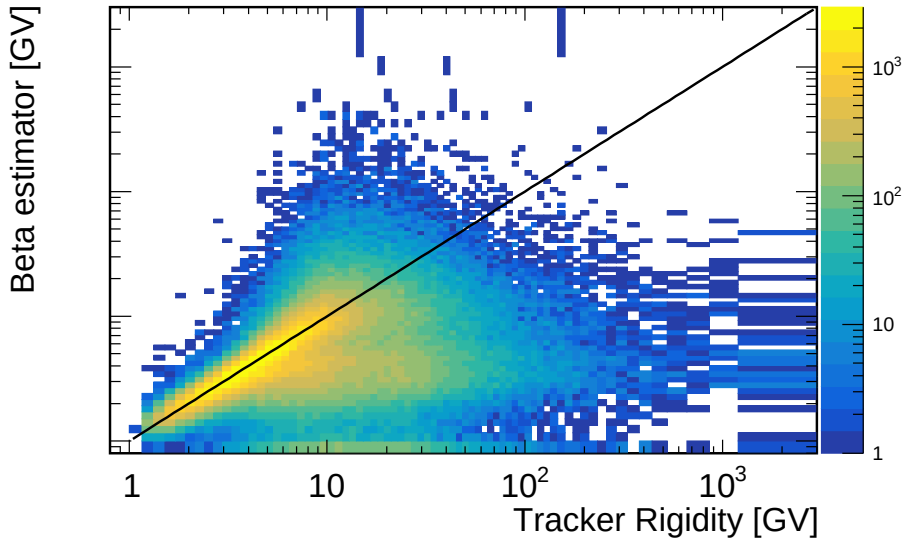

Fig. 3.16 Rigidity estimator constructed from TOF β vs tracker rigidity. The black straight line has a slope of +1, showing that the estimated rigidity and Tracker rigidity are in good agreement for $R \lesssim 6.4$GV

the edge of the maximum geomagnetic rigidity cutoff, and used to estimate particle's rigidity between 6.4GV and 20 GV.

Inner Tracker efficiency selection and result

The sample to estimate the Inner Tracker efficiency is selected with the following cuts:

- bad runs removal, SAA and Data quality cut, physical trigger
- TOF standalone track matching TRD Track
- good unbiased TOF β
- TOF and TRD track extrapolation within the tracker L1-L9 fiducial volume
- Unbiased L1 x- and y- side hits on L1 and L9 (for FS study)
- tight charge cuts on the unbiased charge of 4 TOF layers
- tight charge cuts on the unbiased charge of L1 and L9 (for FS)

The reconstructed Inner Tracker track and the Charge measured by the Inner Tracker is applied to the sample to evaluate the Inner Tracker efficiency. The selection includes

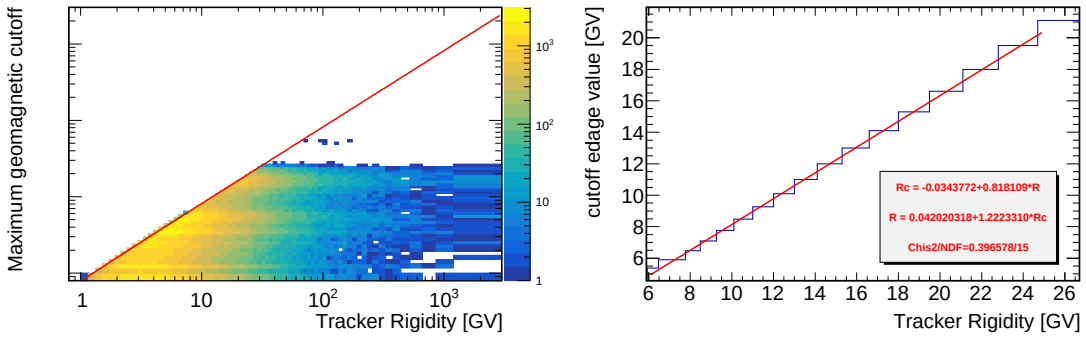

Fig. 3.17 Maximum geomagnetic rigidity cutoff versus Tracker rigidity (left) and the edge of maximum geomagnetic rigidity cutoff versus Tracker rigidity (right). The right line shows the straight fit to edge of R_c, which is used to estimate Tracker rigidity for rigidity between 6.4GV and 20 GV.

requiring the Inner Tracker to have well reconstructed track, Inner track matching with TOF track, and charge measured by Inner tracker within the Mg charge cut range.

Figure 3.18 shows the Inner Tracker efficiency as function of the estimated particle's rigidity for L1Inner and FS, the Data to MC efficiency ratio is calculated with β estimator for R< 6.4 GV, and R_c estimator for rigidity between 6.4 GV and 20 GV. Since the estimator is only valid up to 20 GV, the ratio is assumed to be constant at higher rigidity, and the error band of the parametrization result is calculated from the slope of the MC generated efficiency as function of the generated rigidity.

3.5.4 TOF charge efficiency

TOF charge efficiency evaluates the efficiency of TOF charge reconstruction and selection cuts. This efficiency is evaluated on a sample of Mg nuclei events selected without using information from the TOF detector. The sample is selected by the Inner Tracker and the Tracker external layers including L1 and L9 (for FS study) where the Tracker external layers charge cut has also been tightened to obtain a clean sample to avoid charge contamination from neighboring charges. The TOF charge efficiency is then obtained counting the events that pass UTOF and LTOF (for FS study) charge cuts.

Firgure 3.19 show the TOF charge efficiency for Mg nuclei evaluated from Data and MC, and their ratio. The corresponding Data/MC efficiency correction is obtained by parameterizing the Data/MC with a spline fit. In the high rigidity range, the ratio is parameterized as a constant, and the slope of the efficiency as function of the MC generated rigidity is taken into account as the error of the Data/MC efficiency ratio parametrization. The Data/MC correction for TOF charge efficiency is less than 1%.

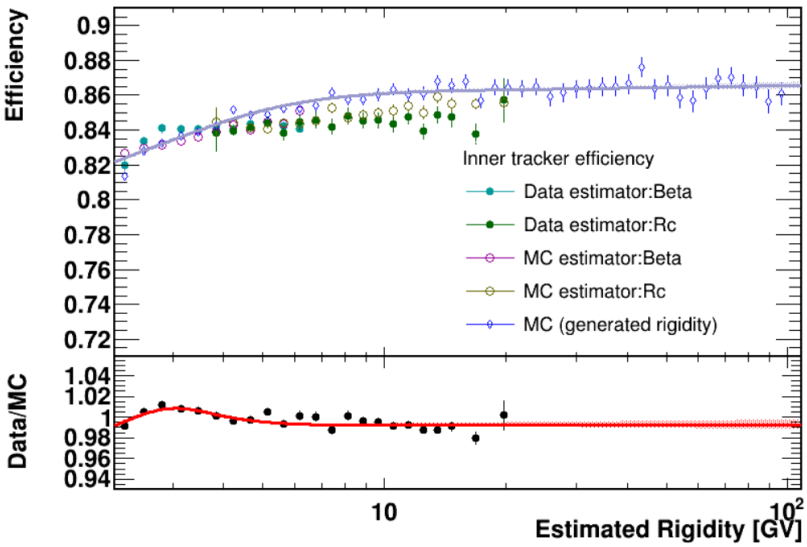

(a) L1Inner

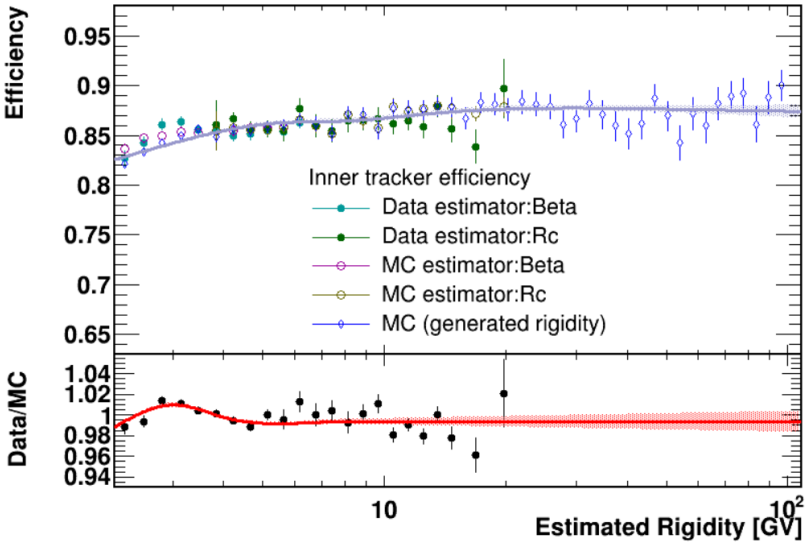

(b) FS

Fig. 3.18 Inner Tracker efficiency as function of rigidity for Mg nuclei for L1Inner (upper panel of the plot a) and FS (upper panel of the plot b) geometries obtained from Data (full circles) and MC (open circles), using the rigidity estimators TOF β (cyan full circles and red open circles) and geomagnetic rigidity cutoff R_c (green full circles and yellow open circles) respectively. MC efficiency as function of the generated rigidity is also shown (blue circles). The lower panel shows the ratio between Data and MC efficiencies (black points) and the spline fit of the efficiency ratio (red line) with its 68% C.L intervals (red shed). Above 200 GV, the error band of the spline fit is calculated from the slope of the MC efficiency as function of generated rigidity. The ratio is calculated with β estimator for R$<$ 6.4 GV , and R_c estimator for rigidity between 6.4 GV and 20 GV.

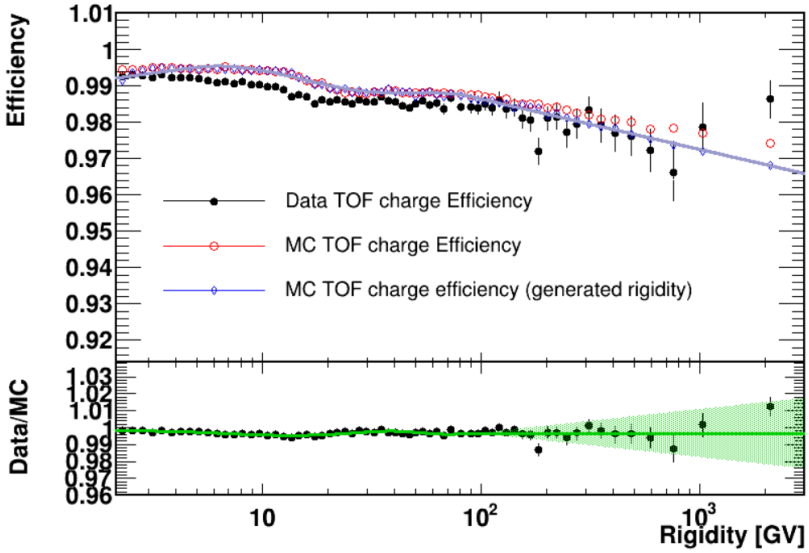

(a) L1Inner

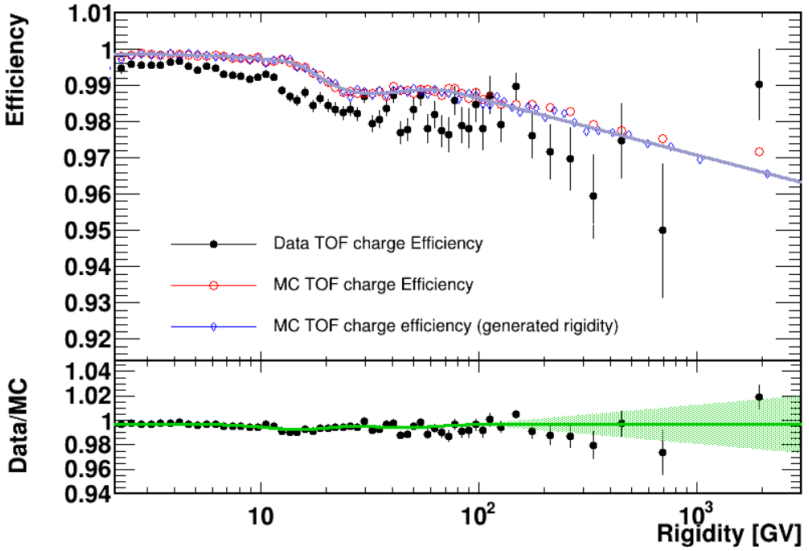

(b) FS

Fig. 3.19 TOF charge efficiency for Mg nuclei as function of rigidity for L1Inner (upper panel of the plot a) and FS (upper panel of the plot b) geometries obtained from Data (black full circles) and MC (red open circles) as function of the reconstructed rigidity. MC efficiency as function of the generated rigidity is also shown (blue circles). The lower panel shows the ratio between Data and MC efficiencies (black points) and the spline fit of the efficiency ratio (green line) with its 68% C.L intervals (green shed). Above 200 GV, the error band of the spline fit is calculated from the slope of the MC efficiency as function of generated rigidity.

3.5.5 L9 efficiency (for FS study)

For FS analysis, LTOF and Tracker L9 are used in addition to L1, UTOF and Inner Tracker. The L9 efficiency evaluates the probability that the event which has a well reconstructed L1+Inner Tracker track has good hits on L9 x- and y-sides, the track attached to the Inner Tracker track, and the charge measured by L9 is compatible with Mg nuclei. Thus, the L9 efficiency includes survival probability from Tracker L8 to L9, L9 track reconstruction efficiency, and L9 charge selection efficiency.

The L9 efficiency is is evaluated on a sample selected requiring the Mg nuclei event selection except the LTOF charge, L9 track and L9 charge selection cuts. Tighter cuts on L1 and UTOF charge have been applied to increase the purity of the sample. The L9 efficiency is then obtained from the percentage of events having L9 x- and y-side hits, good L1+Inner+L9 tracks, and L9 charge compatible with Mg nuclei.

As shown in Figure 3.20, the L9 efficiency for Data and MC is lower than 0.6 because it contains the survival probability from Tracker L8 to L9 in addition to the L9 reconstruction and selection efficiencies. The Data and MC results have a difference of around 10% for rigidity above 10 GV. The difference mainly comes from the discrepancy of the L9 Charge selection efficiency and survival probability between Data and MC. The Tracker L8 to Tracker L9 survival probability will be discussed in Section 3.7.

3.5.6 Trigger efficiency

The trigger efficiency evaluates the probability that a particle entering the detector is triggered by Trigger system. The trigger logic used has been described in Section 2.2 of Chapter 2.

For MC, the trigger efficiency ε_{MC} can be calculated by

$$\varepsilon_{MC} = \frac{n_{physical}}{n_{tot}} = \frac{n_{physical}}{n_{physical} + n_{ub}} \tag{3.10}$$

where $n_{physical}$ is the number of events passing the physical trigger pattern, n_{ub} is the number of events passing the unbiased trigger.

For Data, as mentioned in Section 2.2 of Chapter 2, during time period 1 (before February 2016), NACC<5 was required for BZ trigger, so the physical events is just the NACC<5 events ($n^{(1)}_{physical} = n^{(1)}_{NACC<5}$). Afterwards the BZ trigger setting was loosen by requiring NACC<8, the physical events contains both NACC<5 and the NACC>5 events ($n^{(2)}_{physical} = n^{(2)}_{NACC<8}$). With the loosed trigger setting, the trigger efficiency is ~ 1 are recorded. Considering that only 1 out of 100 events triggered by the unbiased trigger pattern are recorded,

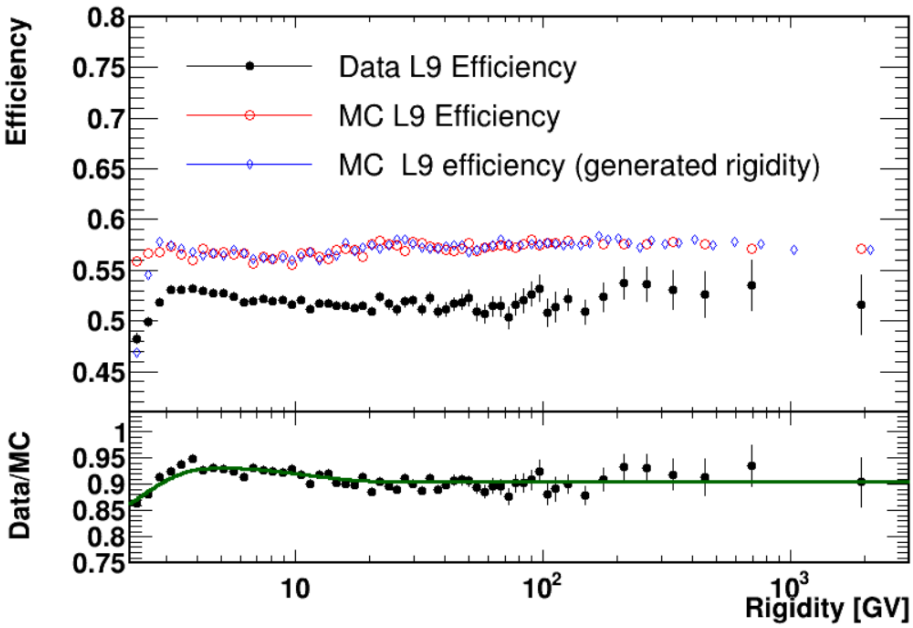

Fig. 3.20 L9 efficiency for Mg nuclei as function of rigidity for FS geometry (upper panel) obtained from Data (black full circles) and MC (red open circles) as function of the reconstructed rigidity. MC efficiency as function of the generated rigidity is also shown (blue circles). The lower panel shows the ratio between Data and MC efficiencies (black points) and the spline fit of the efficiency ratio (dark green line) with its 68% C.L intervals (dark green shed). Above 200 GV, the error band of the spline fit is calculated from the slope of the MC efficiency as function of generated rigidity.

the unbiased events have to be re-scaled by a factor of 100. The trigger efficiency for total time period (8.5 years) can be calculated by

$$\begin{aligned}
\varepsilon^{total}_{trig_Data} &= \frac{(n^{(1)}_{NACC<5} + n^{(2)}_{NACC<8})}{n^{(1)}_{tot} + n^{(2)}_{tot}} \\
&= \frac{(n^{(1)}_{NACC<5} + n^{(2)}_{NACC<8})}{(n^{(1)}_{NACC<5} + n^{(1)}_{ub} \times 100) + (n^{(2)}_{NACC<8} + n^{(2)}_{ub} \times 100)} \\
&= \frac{n^{(1)}_{NACC<8} + n^{(2)}_{NACC<8}}{n^{(1)}_{tot} + n^{(2)}_{tot}} \times \frac{(n^{(1)}_{NACC<5} + n^{(2)}_{NACC<8})}{n^{(1)}_{NACC<8} + n^{(2)}_{NACC<8}}
\end{aligned} \tag{3.11}$$

where $n^{(1)}_{NACC<5}$ is the number of physical events collected in time period 1 (before February 2016) with tight BZ trigger setting (NACC<5), and $n^{(2)}_{NACC<8}$ is number of the physical events collected after February 2016 with loose BZ trigger setting (NACC<8). $n^{(1)}_{NACC<8}$ is the inferred number of physical events by assuming time period 1 running with NACC<8.

If in the time period 1 the same trigger setting (NACC<8) as time periods 2 were used, it is reasonable to assume that the trigger efficiencies in the two time periods would be the same:

$$\frac{n^{(1)}_{NACC<8} + n^{(2)}_{NACC<8}}{n^{(1)}_{tot} + n^{(2)}_{tot}} = \frac{n^{(2)}_{NACC<8}}{n^{(2)}_{tot}} = \varepsilon^{(2)}_{trig\_Data} \approx 1 \tag{3.12}$$

plugging the above equation into equation 3.11, the total trigger efficiency can be calculated by

$$\begin{aligned}
\varepsilon^{total}_{trig_Data} &= \varepsilon^{2}_{trig_Data} \times \frac{(n^{(1)}_{NACC<5} + n^{(2)}_{NACC<8})}{n^{(1)}_{NACC<8} + n^{(2)}_{NACC<8}} \\
&\approx \frac{(n^{(1)}_{NACC<5} + n^{(2)}_{NACC<8})}{n^{(1)}_{NACC<8} + n^{(2)}_{NACC<8}}
\end{aligned} \tag{3.13}$$

Similar to the derivation of the DAQ efficiency in Section 3.3.3, by assuming the ratio between events with NACC<5 and NACC<8 settings are the same for the 2 periods (i.e. $n^{(1)}_{NACC<5}/n^{(1)}_{NACC<8} = n^{(2)}_{NACC<5}/n^{(2)}_{NACC<8}$) , the total trigger trigger efficiency during 8.5 years (May 19, 2011 to October 30, 2019) of operation can be evaluated from time period 2 :

$$\varepsilon^{total}_{trig\_Data} \approx \frac{(n^{(1)}_{NACC<5} + n^{(2)}_{NACC<8})}{n^{(1)}_{NACC<5} \times \frac{n^{(2)}_{NACC<8}}{n^{(2)}_{NACC<5}} + n^{(2)}_{NACC<8}} \tag{3.14}$$

Figure 3.21, shows the 8.5 years total trigger trigger efficiency for Mg nuclei events evaluated from time period 2. The discrepancy between Data and MC is less than 1%.

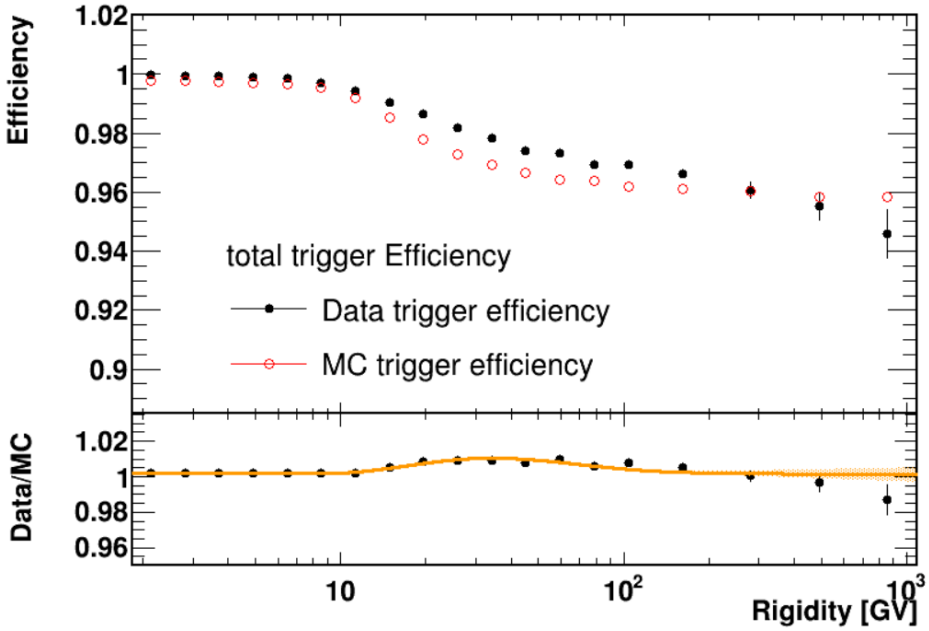

Fig. 3.21 The AMS trigger efficiency for Mg nuclei as function of rigidity for the first 8.5 years of operation (upper panel) obtained from Data (black full circles) and MC (red open circles). The lower panel shows the ratio between Data and MC efficiencies (black points) and the spline fit of the efficiency ratio (orange line) with its 68% C.L intervals (orange shed).

3.5.7 Overall correction

The overall Data/MC efficiency correction ($\prod \varepsilon_{Data/MC}$) for Mg nuclei is less than 2% for L1Inner, and around 10% for FS, as shown in Figure 3.22.

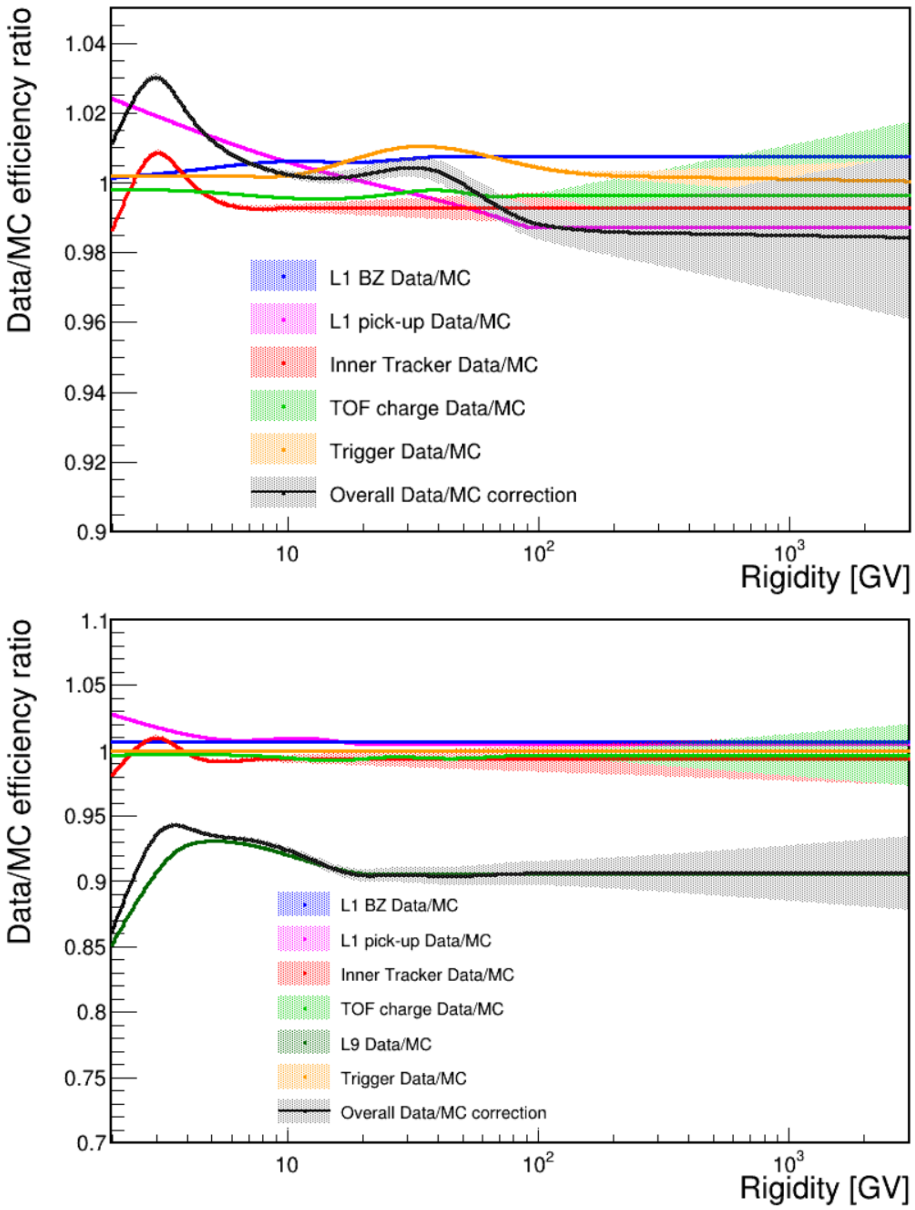

Fig. 3.22 Mg nuclei overall Data/MC efficiency correction (black curve) as a function of rigidity for L1Inner (top) and FS (bottom,) geometries, together with its break-down in L1 BZ, L1 pick-up, Inner Tracker, TOF charge, and L9 (for FS) corrections.

3.6 Rigidity resolution unfolding

With the ingredients mentioned in previous sections, the Mg raw flux can be calculated with equation 3.1. Figure 3.23 shows the Mg nuclei raw fluxes for FS and L1Inner geometries and their ratio. The raw fluxes are distorted by bin-to-bin event migration due to the finite rigidity resolution.

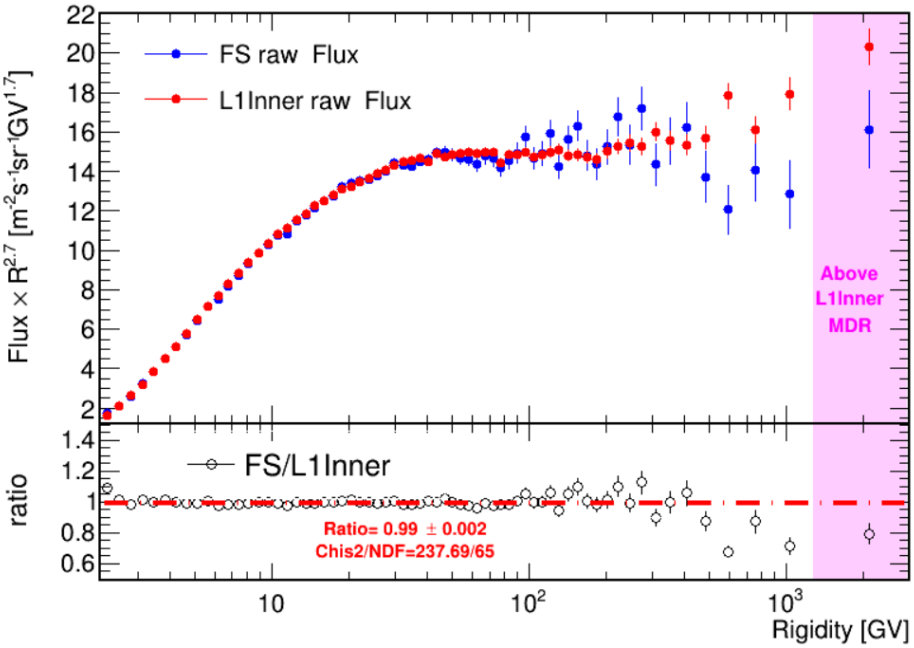

Fig. 3.23 Mg raw flux with statistical error as functions of rigidity multiplied by $R^{2.7}$ for L1Inner (red points) and FS (blue points). The lower panel shows the ratio between FS and L1Inner raw flux (black points), and a fit to a constant value (red dashed line). The magenta shaded area is the rigidity region above L1Inner maximum detectable rigidity (MDR).

The bin-to-bin event migration is corrected applying the forward unfolding method simultaneously to L1Inner and FS raw fluxes. The mathematical foundation of the unfolding is an inverse problem, whose goal is to construct a kernel function to transform the measured distribution to the true distribution. In the flux analysis, the kernel function is the rigidity resolution function which describes the detector resolution effects.

3.6.1 Rigidity resolution function

In MC, for each events, both the reconstructed rigidity (R_{rec}) and the MC generated rigidity (R_{gen}) are known, and the rigidity resolution can be constructed from the difference between the inverse of reconstructed rigidity and generated rigidity ($1/R_{rec} - 1/R_{gen}$). The distribution

of $1/R_{rec} - 1/R_{gen}$, i.e. $f(1/R_{rec} - 1/R_{gen})$ in each generated rigidity bin has a pronounced Gaussian core, and it also has a small right side tail in the low rigidity range.

The MC events are splitted in 80 even-log generated rigidity bins form 0.5 GV to 6 TV. In each bin, $f(1/R_{rec} - 1/R_{gen})$ is parameterized by two Gaussian functions and one positive skewed Exponentially Modified Gaussian (EMG) [111]. One of the two Gaussian functions describes the pronounced Gaussian core of $f(1/R_{rec} - 1/R_{gen})$, and is called the core Gaussian. The positive skewed EMG function with same mean (μ_G) as the core Gaussian can be described 3 parameters:

$$\begin{aligned} \mathrm{EMG}(1/R_{rec} - 1/R_{gen}; \mu_G, \sigma, \tau) &= \mathrm{EMG}(1/R_{rec} - 1/R_{gen}; \mu_G, \sigma, \tau) \\ &= \frac{1}{2\tau}\exp[(\frac{\sigma}{\sqrt{2}\tau})^2 - \frac{x-\mu_G}{\tau}]\mathrm{erfc}[\frac{\sigma}{\sqrt{2}\tau} - \frac{x-\mu_G}{\sqrt{2}\sigma}] \end{aligned} \tag{3.15}$$

where erfc is the error function, μ_G is the mean of core Gaussian, σ describes the width of the distribution, and τ describes the exponential tail. To avoid the arithmetic overflow, for the cases when $\sigma/\tau > 10$, the EMG is set to degenerates to a Gaussian.

$f(1/R_{rec} - 1/R_{gen})$ can be described by 8 parameters:

1. f_0: the normalization factor
2. μ_G: mean of the core Gaussian, and the other two distributions are assigned to have the same mean as the core Gaussian
3. σ_1: width of the core Gaussian
4. σ_2: width of the second Gaussian
5. σ_3: width of the EMG
6. τ: tail of the EMG (τ)
7. f_1: fraction of the core Gaussian with respect to the total distribution
8. f_2: fraction of the second Gaussian with respect to the total distribution

Since there are 8 parameters involved in the fit, the software (*ROOT*) can't achieve a good fit in one go. To obtain a robust fit result, an iterative fit method has been applied as following:

step 1 Gaussian fit to determine the mean and width of the core Gaussian

step 2 the initial step of the iterative fit: setting a set of rough range limits for the 5 fit parameters (σ_2/σ_1, σ_3/σ_1, τ/σ_3, f_1, f_2)

step 3 for each parameter range: divide into several (7) sub-ranges

step 4 iterative fit (total steps: $7^5 = 16'807$) with the sub-ranges for each rigidity bin

step 5 by comparing $\chi^2/d.f.$, find the best fit for each rigidity bin

Figure 3.24 shows $f(1/R_{rec} - 1/R_{gen})$ and its parametrization in one of the generated rigidity bin.

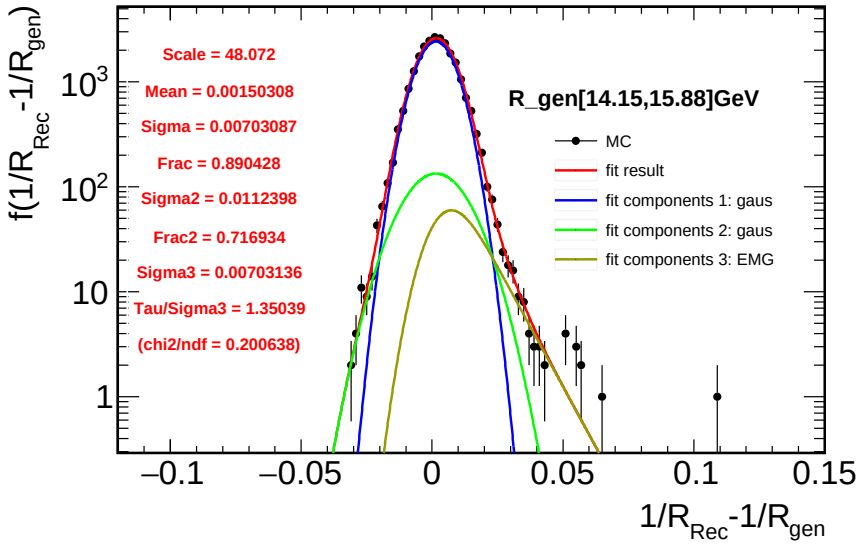

Fig. 3.24 Rigidity resolution function $f(1/R_{rec} - 1/R_{gen})$ for Mg nuclei in on of the 80 generated rigidity bins ($R_{gen} \in [14.15, 15.88]$ GV). The black points show the MC distribution, the red curve shows the parametrization with two Gaussians and one EMG, while the blue, green and brown curve show the components of the parametrization.

To construct the 2D resolution function $R(1/R_{gen}, 1/R_{rec} - 1/R_{gen})$ from $f(1/R_{rec} - 1/R_{gen})$, the 8 fit parameters are then parameterized as functions of the generated rigidity. Figure 3.25 shows the rigidity dependence of the σ_1 of core Gaussian as an example. The σ_1 of the core Gaussian describe the width of the distribution, when it equals to 1/R, the resolution reaches 100%. As shown in the figure, the Maximum Detectable Rigidity (MDR) is found to be 1.28 TV for L1Inner and 2.79 TV for FS.

3.6.2 The L1Inner and FS combined forward unfolding

The true distribution of rigidity $f_{gen}(R_{gen})$ can't be directly obtained. Due to the limitation of the finite rigidity resolution, $f_{gen}(R_{gen})$ is transformed into the distorted but measurable distribution of reconstructed rigidity $f_{rec}(R_{rec})$. Since the rigidity resolution function is

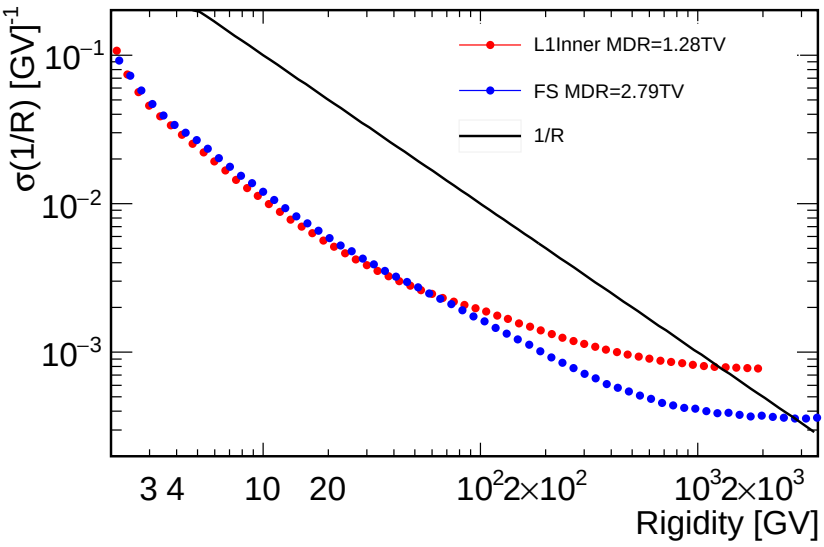

Fig. 3.25 σ_1 of the core Gaussian as function of the generated rigidity for L1Inner (red points) and FS (blue points). The black line shows the 1/R function. The intercept between the 1/R and the σ_1 gives the MDR, which is found to be 1.28 TV for L1Inner and 2.79 TV for FS respectively.

determined in the inverse rigidity space, the distribution of the inverse reconstructed rigidity $f_{rec}(1/R_{rec})$ can be described by

$$f_{rec}(1/R_{rec}) = \int R(1/R_{gen}, 1/R_{rec}) f_{gen}(1/R_{gen}) \mathrm{d}\frac{1}{R_{gen}} \tag{3.16}$$

where the $R(1/R_{gen}, 1/R_{rec})$ is the rigidity resolution function obtained from $f(1/R_{rec} - 1/R_{gen})$.

For the Mg nuclei event distribution $N(R)$, the number of events in i_{th} rigidity bin is calculated as

$$N_i = \int_{\Delta R_i} \Phi(R) \times A(R) \times \Delta T(R) \mathrm{d}R \tag{3.17}$$

On one hand, by putting the above two equations (equation 3.16 and 3.16) together and assuming the true flux $\Phi(R_{gen})$ is known, the folded rate f^{cal} can be calculated convoluting the rigidity resolution function $R(1/R_{gen}, 1/R_{rec} - 1/R_{gen})$ and true flux in 1/R space (i.e.

$\Phi(1/R_{gen})$) as shown in the following formula

$$\begin{aligned} f_i^{cal} &= f_{rec}^{cal}(\frac{1}{R_{rec}}, \frac{1}{R_{rec}+\Delta R_{rec}}) \\ &= \int_{\Delta}\frac{1}{R_{rec}}\left\{\int_0^{\infty} R(1/R_{gen}, 1/R_{rec}-1/R_{gen})R_{gen}^2\Phi'(\frac{1}{R_{gen}})A(\frac{1}{R_{gen}})\mathrm{d}\frac{1}{R_{gen}}\right\}\mathrm{d}\frac{1}{R_{rec}} \end{aligned} \tag{3.18}$$

On the other hand, the folded rate can also be obtained from Data (f^{Data}) with equation 3.1 as

$$f_i^{Data} = (N_{count} - N_{bkg})\prod(1-\sum\delta)\prod\varepsilon_{MC/Data}\times\varepsilon_{DAQ}\times\varepsilon_{L1Q}/\Delta T(R_{rec}) \tag{3.19}$$

The assumed flux model $\Phi'(R_{gen})$ in equation 3.18 is parameterized by the spline function, which can be varied by adjusting the spline nodes. By minimizing the difference between f^{cal} and f^{Data}, $\Phi'(R_{gen})$ will approach to the true flux $\Phi(R)$. The minimization is done with *ROOT:: Minuit2:: Minuit2Minimizer* toolkit, by minimizing the χ^2 defined as

$$\chi^2 = \sum(\frac{f_i^{Data}-f_i^{cal}}{\sigma_i})^2 \tag{3.20}$$

where the σ_i is the statistical error of f_i^{cal} in i_{th} rigidity bin.

Considering that both the Mg L1Inner and FS analysis should yield the same Mg flux, the L1Inner and FS can be unfolded together with the combined χ^2 defined as

$$\chi^2 = \chi^2_{L1Inner} + \chi^2_{FS} = \sum(\frac{f^{Data}_{L1Inner,i}-f^{cal}_{L1Inner,i}}{\sigma_{L1Inner,i}})^2 + \sum(\frac{f^{Data}_{FS,i}-f^{cal}_{FS,i}}{\sigma_{FS,i}})^2 \tag{3.21}$$

where only bins below the MDR are used, that is for FS, the χ^2_{FS} is summed from rigidity 2.15 GV to 3 TV, while for L1Inner, the $\chi^2_{L1Inner}$ is summed from 2.15 GV to 1.2 TV. With this formula, the Mg flux is determined from both L1Inner and FS for rigidities below 1.2 TV (L1Inner MDR), and FS only for rigidities above 1.2 TV.

Figure 3.26 shows the folded rates f^{Data} and f^{cal} for L1Inner and FS after minimization. As seen the difference between f^{Data} and f^{cal} is smaller than 2% for rigidity below 100 GV.

The the unfolding factor is defined as the ratio between the raw and unfolded event counts, in which the unfolded event counts are obtained by plugging the flux model $\Phi'(R_{gen})$ after minimization into equation 3.17. Figure 3.27 shows the unfolding factor result. At rigidities below about 2.5 GV, the unfolding is invalid for FS because it's acceptance close to 0. For

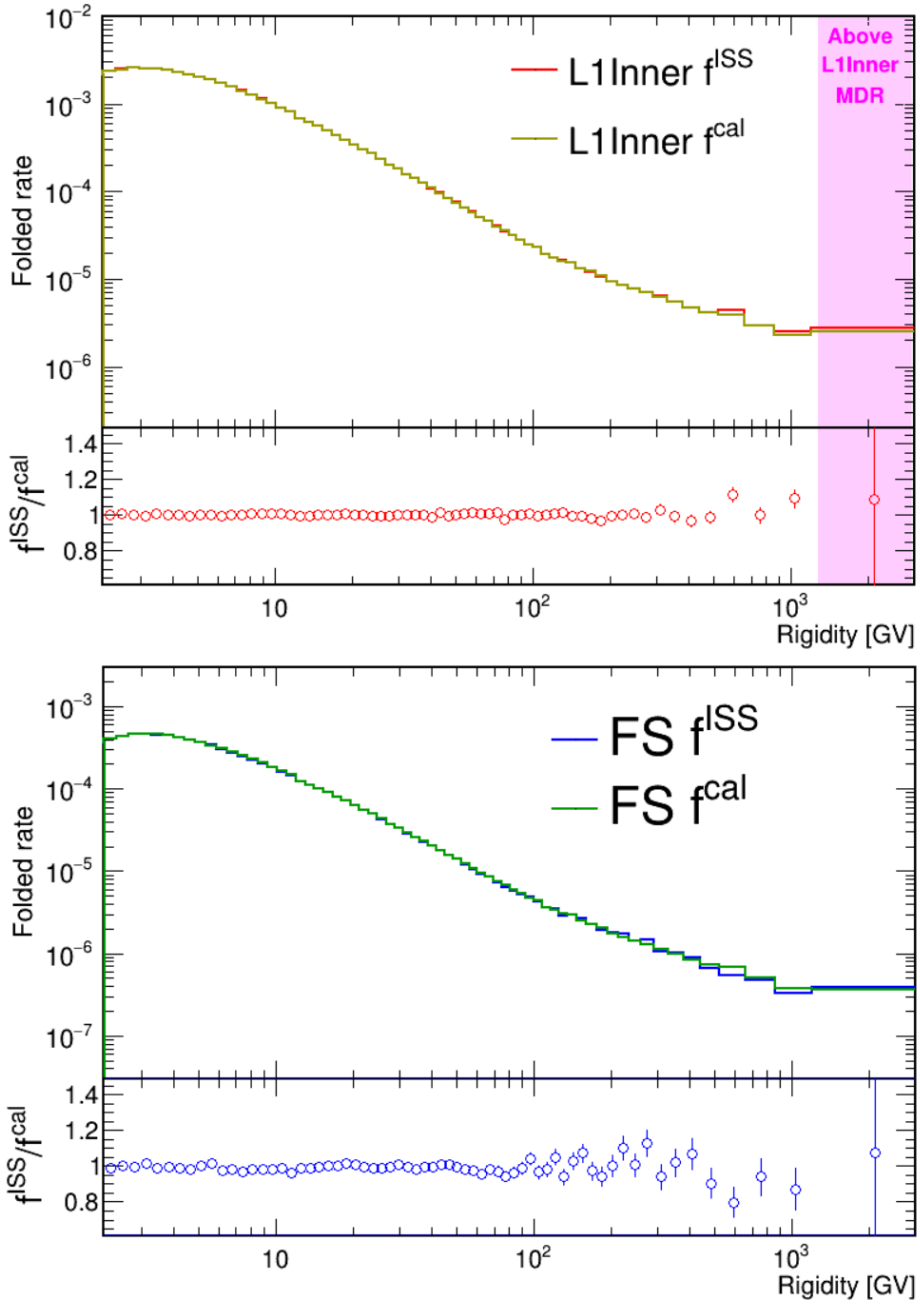

Fig. 3.26 The Mg folded rate after minimization for L1Inner (left) and FS (right). The blue and red histograms show the folded rate from Data (f^{Data}) for L1Inner and FS, the yellow and green histograms show the folded rate obtained from the minimization calculation (f^{cal}) for L1Inner and FS. The lower panels show the ratio of the folded rate from Data to the folded rate from the minimization.

rigidities below about 20 GV, the unfolding gives >10% correction, due to the multiple-scattering effect. While at high rigidities, the unfolding correction is smaller than 5% for FS due to the improved rigidity resolution and larger MDR.

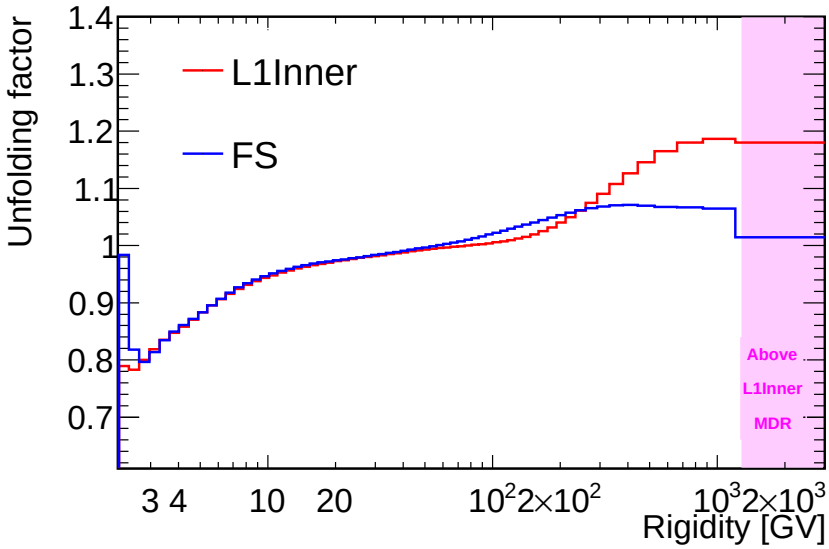

Fig. 3.27 Mg unfolding factor as a function of the generated rigidity for L1Inner (red) and FS (blue). The shaded magenta area is the rigidity region above L1Inner MDR.

3.6.3 Mg unfolded flux

The Mg nuclei flux is obtained after the unfolding is shown in Figure 3.28 for L1Inner and FS. The ratio between FS and L1Inner shows FS and L1Inner fluxes have good agreement.

To obtain more statistics and extend the analysis to TV, the final Mg nuclei flux is a combination of L1Inner and FS fluxes, whose last point above L1Inner MDR is taken from the FS result and the others are taken from the L1Inner result.

3.7 Mg nuclei survival probability

The precise knowledge of nuclear interactions with the detector materials can be evaluated with the nuclei survival probabilities [101, 102]. The cross section model in MC has been tuned based on Data Data [102]. The small remaining discrepancy of the survival probabilities between Data and MC can be accounted as a correction to the flux normalization. Thanks to the MC tuning, this correction is not rigidity dependent, therefore it can be ap-

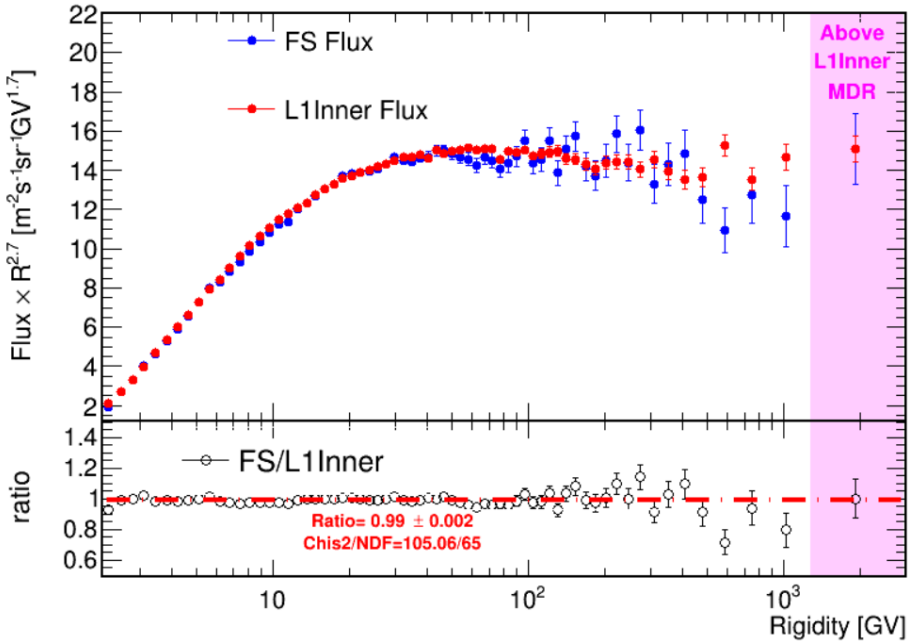

Fig. 3.28 Mg nuclei unfolded flux as functions of rigidity multiplied by $R^{2.7}$ for L1Inner (red points) and FS (blue points). Only the statistical errors are shown. The lower panel shows the ratio between FS and L1Inner unfolded flux (black points), and a fit to a constant value (red dashed line). The magenta shaded area is the rigidity region above L1Inner Maximum Detectable Rigidity (MDR).

plied to the flux after unfolding. The uncertainties in the evaluation of MC to Data survival probability ratios are one of the main source of the acceptance systematic error.

The material traversed by nuclei from the top of AMS to Tracker L9 is composed primarily by weight of 67% carbon and 21% aluminum [107]. The discrepancy between the MC and Data survival probabilities between the top of AMS and Tracker L9 can be evaluated studying the survival probabilities from Tracker L1 to Tracker L2 (L1-L2) and from Tracker L8 to Tracker L9 (L8-L9).

3.7.1 L1-L2 survival probability

The survival probabilities between Tracker L1 and Tracker L2 for Mg nuclei can be evaluated with rigidity above ~ 8 GV due to large energy transfer in the materials for low rigidity Mg events. Tracker L1 is used to selected the incoming beam, Mg nuclei in this case, TRD and Upper TOF are used as target, and the outgoing particles are identified by the Inner Tracker (L2 to L8).

To perform the measurement, a sample is selected by requiring the event to have the charge measured by Tracker L1 compatible with Mg ($Q_{L1} \in [11.5, 12.5]$), a well reconstructed Inner Tracker track, and the measured velocity $\beta > 0$ (downward-going particle) in the TOF. Due to nuclear interactions in the material between Tracker L1 and Tracker L2, the events detected by the Inner Tracker will have charge value less or equal to that measured by Tracker L1. L1-L2 survival probability is extracted from the Inner Tracker charge distribution.

Figure 3.29 shows the Inner Tracker charge distribution for events selected as Mg nuclei by L1 charge for Data and MC. With the sample selected by Mg nuclei L1 charge ($Q_{L1} \in [11.5, 12.5]$), the events with the charge measured by Inner tracker in Mg nuclei selection range $Q_{Inner} \in [11.5, 12.5]$ can be written as:

$$N^{Inner} = N_{Mg}^{Inner} + N_{Al \to Mg} + (N_{Na}^{Inner} + N_{Al}^{Inner}) \tag{3.22}$$

where N^{Inner} is the events in the Inner tracker Mg nuclei charge selection range ([11.5,12.5]). N_{Mg}^{Inner} is the Mg survived events, $N_{Al \to Mg}$ is the fragmented events from heavier nuclei Al contaminating the incoming beam due to finite L1 charge resolution, and $(N_{Na}^{Inner} + N_{Al}^{Inner})$ is the neighboring nuclei contaminating the outgoing beam due to finite Inner charge resolution.

Considering that Mg is ~ 6 times more abundant than the neighboring nuclei Na and Al, contributions from neighboring nuclei are are found to be negligible. The above equation is

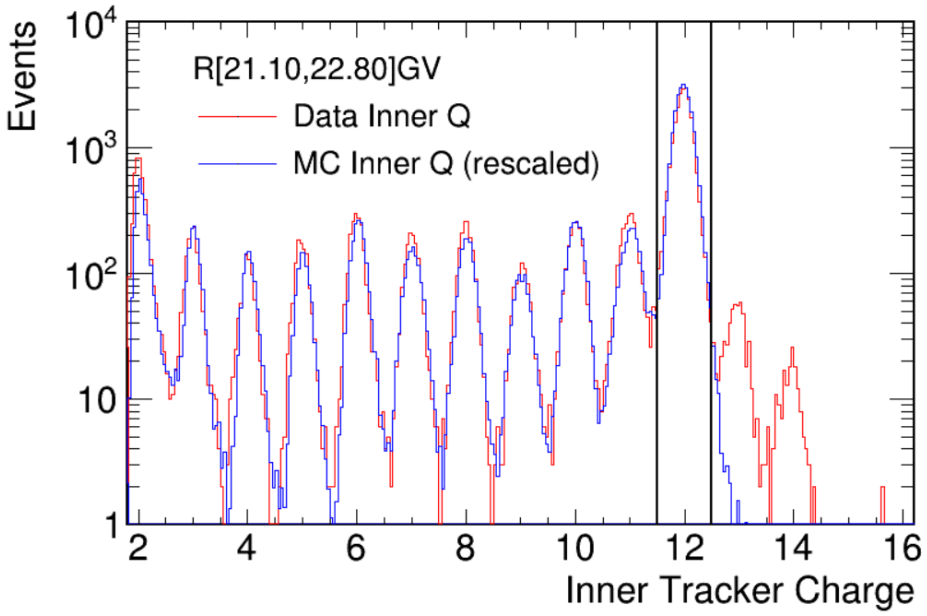

Fig. 3.29 The Inner Tracker charge distribution with L1 charge selection for Data (red) and MC (blue) in the rigidity range form 21.1 GV to 22.8 GV. The MC distribution has been re-scaled according to the Data distribution at charge 12. The black vertical lines show the Mg Inner charge cut range for L1-l2 survival probability study.

then simplified as:

$$N^{Inner} \approx N_{Mg}^{Inner} = \varepsilon_{Mg}^{sur} f_{Mg}^{L1} N^{tot} \tag{3.23}$$

where ε_{Mg}^{sur} is the Mg L1-L2 survival probability, N^{tot} is the number of nuclei in the incoming beam, f_{Mg}^{L1} is the purity of the incoming beam.

The purity of the incoming beam is estimated with the L1 charge template fit method. As shown in Figure 3.30, similar to the below L1 background estimation discussed in Section 3.3.2, the L1 charge distribution without any charge selection cuts is fitted by the O (Z=8) to S (Z=16) charge templates constructed from L2 clean and non-interacting samples.

Figure 3.31 shows the contamination in Mg L1 charge section range, the total contamination is around 6%, therefore the purity ofthe incoming beam (f_{Mg}^{L1}) is around 94%.

From these results, and from the Inner Tracker charge distribution of the outgoing beam, the Mg L1-L2 survival probability is calculated as

$$\varepsilon_{Mg}^{sur} = \frac{N_{Mg}^{Inner}}{f_{Mg}^{L1} N^{tot}} \tag{3.24}$$

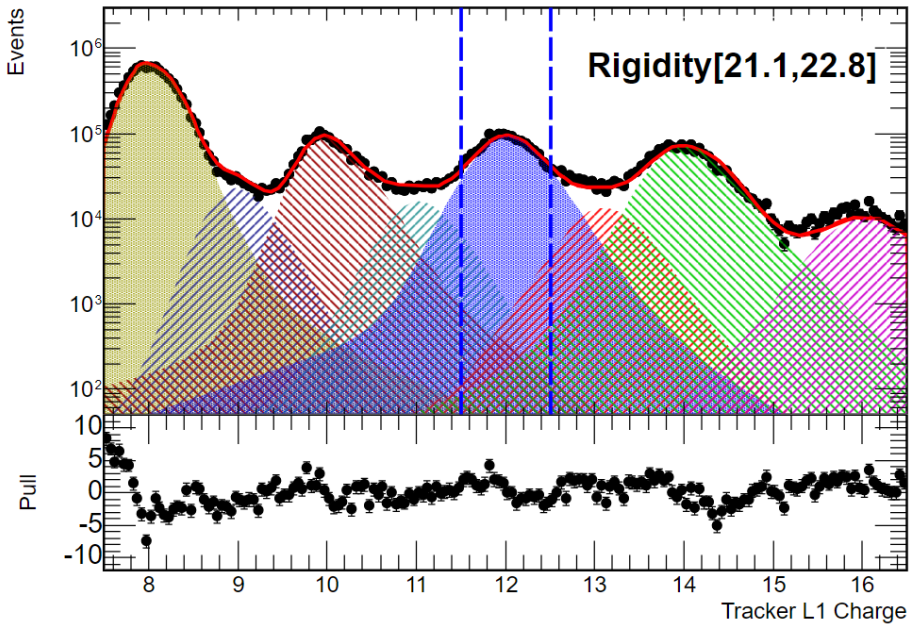

Fig. 3.30 The L1 charge distribution for samples from Z=8 to Z=16 in the rigidity range form 21.1 GV to 22.8 GV. The red curve shows the fit to the L1 charge distribution with L2 templates. The templates are constructed from O (Z=8) to S (Z=16) L2 non-interacting samples. The blue vertical lines show the Mg L1 charge cut range for L1-L2 survival probability study.

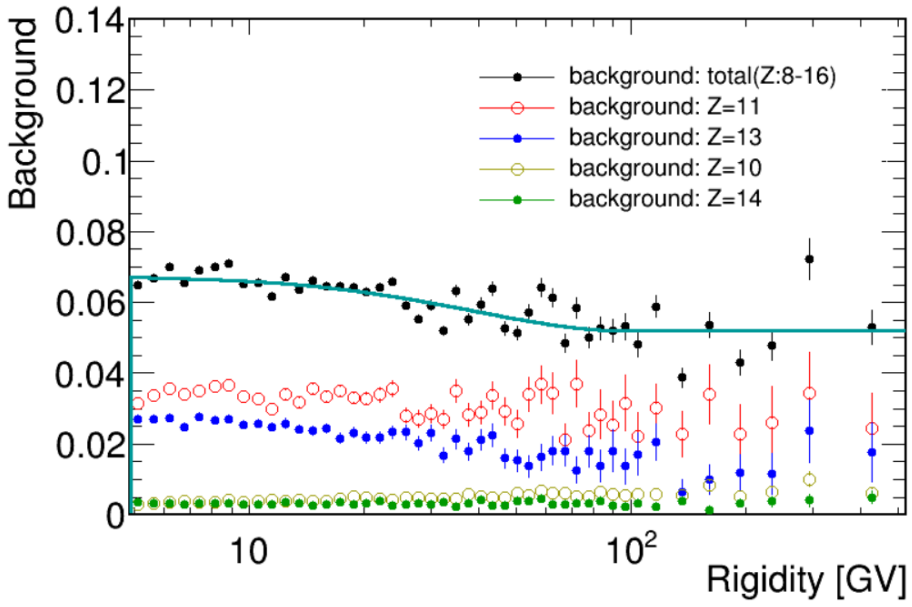

Fig. 3.31 The contamination from Ne (Z=10, yellow points), Na (Z=11, red points), Al (Z=13, blue points), and Si (Z=14, green points) in Mg L1 charge section range as functions of rigidity. The black points show the total contamination, and the solid curve shows the parameterization of the total contamination result

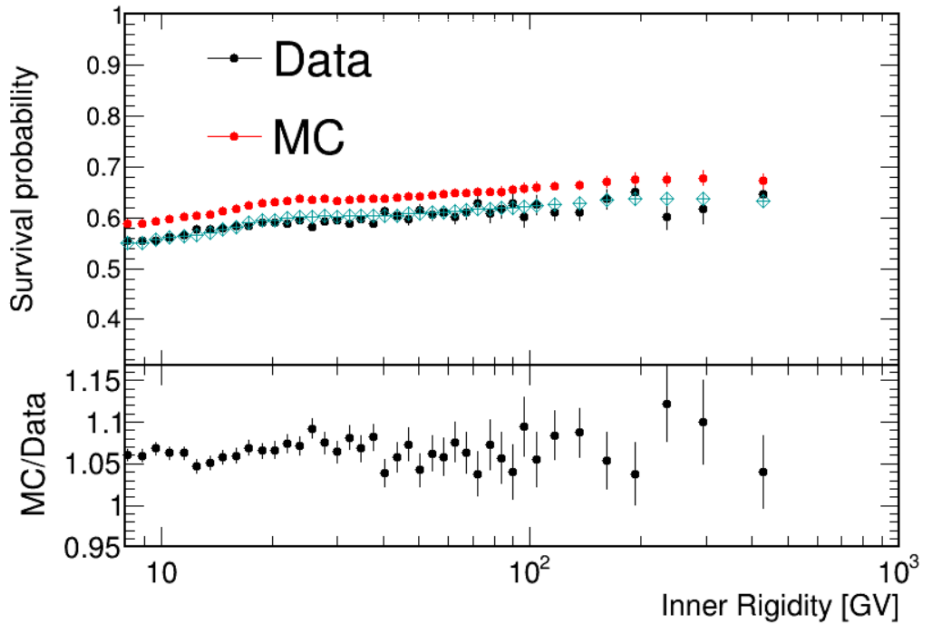

Fig. 3.32 Mg L1-L2 survival probability for MC (red) and Data (black) as functions of rigidity measured by Inner Tracker below the Inner Tracker MDR ($\sim$ 800 GV).

Figure 3.31 shows Mg L1-L2 survival probability for MC, Data and their ratio as functions of rigidity measured by Inner Tracker. Since the events that fragmented between L1 and L2 can be lost in the old trigger setting period (before February 2016), only the new trigger setting period is used for Data sample in the calculation. As seen in the figure, the discrepancy between MC and Data is around 6%, which will be also verified by L8-L9 survival probability as discussed in the next subsection.

3.7.2 L8-L9 survival probability

Evaluation method

The Tracker L8 to Tracker L9 survival probability measures the probability that cosmic-ray nuclei, Mg in this case, traverse the material which constitute the LTOF and RICH detectors without undergoing fragmentation. In this study, Tracker L1, UTOF and Inner Tracker (Tracker L2-L8) are used to selected the incoming beam, LTOF and RICH are used as target, and the outgoing particles are identified by the Tracker L9. The impurity of the outgoing beam is evaluated with the ECAL below Tracker L9.

Two sets of samples are used to evaluate Mg nuclei survival probabilities between Tracker L8 and Tracker L9.

- L1Inner sample: events are required to have charges measured by L1, UTOF and Inner Tracker compatible with Mg nuclei, a well reconstructed Inner Tracker track, the velocity $\beta > 0$ measured by TOF (downward-going particles), and the track extrapolation within the fiducial volume of Tracker L9 and the first layer of ECAL.

- ECAL MIP sample: in addition to the selection for L1Inner sample, a series of ECAL cuts is also applied to select events for which the energy deposition in ECAL is compatible with a Minimum Ionizing Particle (MIP)..

Different downstream selections are required on the two samples to extract the L8-L9 survival probability.

For the L1Inner sample, the Mg nuclei downstream selection is applied on the unbiased Tracker L9 hits and charges, that is without requiring that those hits are attached to the L1-Inner Tracker track. The downstream selection requires the following cuts:

- X- and Y-side unbiased hits on L9

- distance between unbiased L9 hit and L1-Inner Tracker track extrapolation less than 1cm

- unbiased L9 charge compatible with Mg: Q_{L9} greater than 11.5

- L9 charge asymmetry cut: $\mid Q_{L9,x} - Q_{L9,y} \mid /(Q_{L9,x} + Q_{L9,y}) < 0.2$

- good L9 charge status

The ratio between the number of Mg nuclei from the downstream selection, N_{L9}^{sel}, and the number of Mg nuclei in the incoming beam from the L1Inner selection, $N_{L1Inner}^{tot}$, can be written as:

$$\frac{N_{L9}^{sel}}{N_{L1Inner}^{tot}} = \varepsilon^{sur} \cdot \varepsilon^{det} \cdot \varepsilon^{sel} \tag{3.25}$$

where ε^{det} and and ε^{sel} are the L9 detection and selection efficiencies for Mg nuclei respectively. Lighter nuclei events such as Na (Z=11) fragmented from Mg can also enter the L9 selection, but their contribution is negligible because the Mg→Na breaking-up probability and the probability to select Na applying the Mg charge selection are both small.

For the MIP sample, by requiring MIP in ECAL, only the events which are not fragmented from top to the bottom of the detector are kept. Therefore the L8-L9 survival probability does not enter in the expression of the ratio between the number of incoming and

outgoing Mg nuclei, which can be written as:

$$\frac{N_{L9}^{sel}}{N_{MIP}^{tot}} = \varepsilon^{det} \cdot \varepsilon^{sel} \cdot P \tag{3.26}$$

where N_{MIP}^{tot} and N_{L9}^{sel} are the number of incoming and outgoing Mg nuclei respectively. P is the purity of the incoming beam which is discussed next after giving more details on the MIP selection.

MIP selection

To obtain the non-fragmented events below L8, while maximize statistics, the first layer of ECAL is required to select MIP events. In each layer, the cell with the maximum deposited energy is identified, and its deposited energy is called S1. The sum of S1 and the deposited energy in its two adjacent cells (if they exist) is called S3. Similarly, S5 is defined from S3 and its two adjacent cells (if they exist). A signal induced in ECAL by MIP is expected to be concentrated in few cells, that is, and S3/S5> 0.98. The details of ECAL MIP selection are listed below:

- the extrapolation of the Tracker track is required to be within the fiducial volume of the first ECAL layer, defined removing the two outermost cells from each side;
- events for which the maximum deposited energy is on the 2 outermost cells of the first ECAL layer are rejected;
- the maximum deposited energy cell and the deposited energy center of gravity cell of the first ECAL layer are required to be less than 2 cells away;
- S3/S5> 0.98 for the first ECAL layer

Figure 3.33 shows the unbiased L9 charge distribution for for Mg nuclei in the L1Inner and MIP samples. MIP selection is able to suppress, although not eliminate, the charge fragmentation. The purity of sample needs to be estimated.

Proved for light nuclei (Z≤9) by previous studies [112, 113], MIP deposited energy in ECAL has a nonlinear dependence on the square of integer charge (Z^2), which can be described as:

$$\frac{\mathrm{d}E}{\mathrm{d}x} = \frac{A_0 Z^2}{1 + k_0 \arctan\left(\frac{k_b}{k_0} Z^2\right)} \tag{3.27}$$

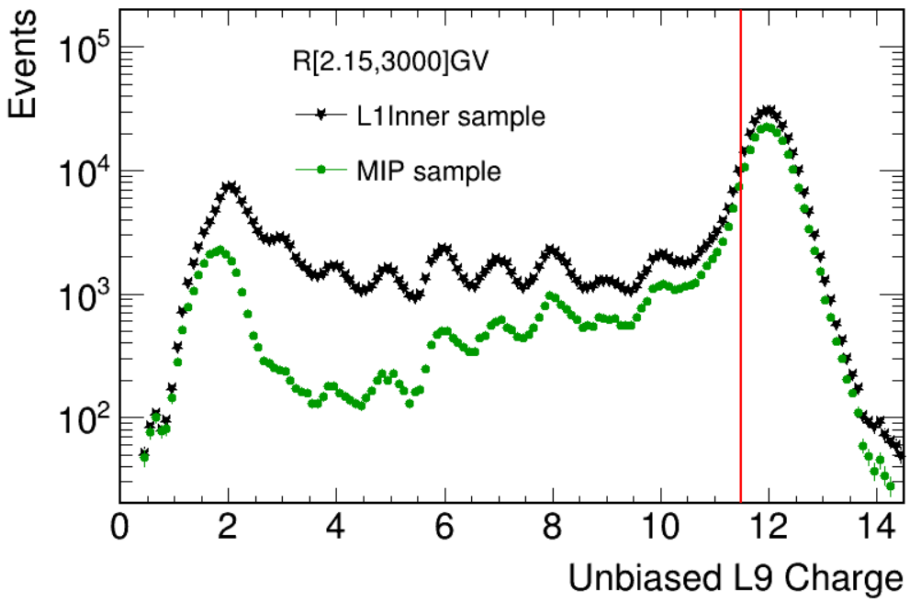

Fig. 3.33 Unbiased L9 charge distribution for Mg nuclei selected by L1Inner outgoing (black) and MIP selection (green) respectively. The red vertical line shows the charge cut to select outgoing Mg nuclei.

where dE/dx is the deposited energy in ECAL layers obtained by requiring MIP selection for charge Z nuclei. A_0, k_0 and k_b are parameters determined by fit.

To further verify that the MIP selection used in this analysis is able to select good MIP sample, similar studies have been done for nuclei from He (Z=2) to Si (Z=14) and the fit results have been compared to those obtained by the previous AMS study on light nuclei [114]. Figure 3.34 shows the deposited energy in the first ECAL layer versus Z^2 for nuclei from He to Si, and its fit. The fit result shows a good agreement with previous light nuclei study.

Purity of MIP sample

The purity of MIP sample in equation 3.26 needs to be evaluated to obtain the L8-L9 survival probability. Considering the events in MIP sample as shown in Figure 3.33, in Mg unbiased L9 charge cut range ($Q_{L9} > 11.5$), both Mg and lighter nuclei events such as Na (Z=11) can be selected. Therefore the number of events after $Q_{L9} > 11.5$ selection can be computed as:

$$N_{Q>11.5} = N^{tot}_{MIP}(P \cdot \varepsilon^{sel}_{Z=12} + (1-P) \cdot \varepsilon^{sel}_{Z<12}) \tag{3.28}$$

where N^{tot}_{MIP} is total number of events in the MIP sample, $N_{Q>11.5}$ is the number of events in the MIP sample that pass the $Q_{L9} > 11.5$. $\varepsilon^{sel}_{Z=12}$ and $\varepsilon^{sel}_{Z<12}$ are the selection efficiencies

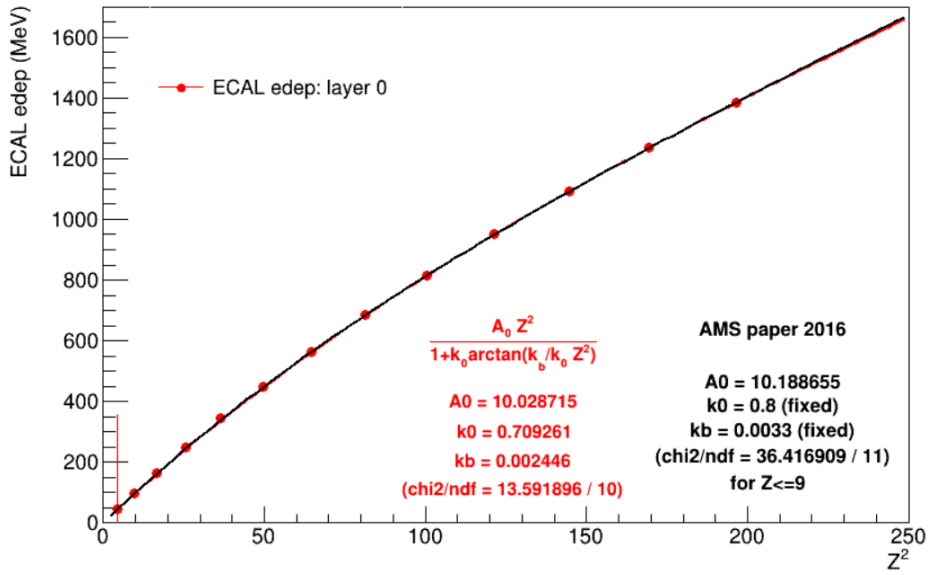

Fig. 3.34 Deposited energy in the first ECAL layer vs Z^2 for nuclei He (Z=2) to Si (Z=14). The red curve shows the fit result, while the black curve shows the parametrization result from the previous AMS study [114]. The two results are in good agreement.

of $Q_{L9} > 11.5$ cut for Mg nuclei and lighter nuclei respectively. Considering both $(1-P)$ and $\varepsilon^{sel}_{Z<12}$ are much smaller than P and $\varepsilon^{sel}_{Z=12}$, the second term can be neglected. So the purity can be estimated as:

$$P \approx \frac{N_{Q>11.5}}{N^{tot}_{MIP}} / \varepsilon^{sel}_{Z=12} \tag{3.29}$$

$N_{Q>11.5}/N^{tot}_{MIP}$ can be directly obtained from the unbiased L9 charge distribution of MIP sample, as shown in Figure 3.35.

Considering that L1, L2, and L9 have the same detector response, the charge selection efficiency of $Q > 11.5$ (i.e. $\varepsilon^{sel}_{Z=12}$) can be estimated from cleaner charge distributions such as those obtained by L1 and L2. In this analysis, four sets of charge distributions are used independently to calculate $\varepsilon^{sel}_{Z=12}$ and survival probability, the discrepancy is take into account as one of the source of the systematic error:

- L1 charge distribution obtained by requiring Inner tracker and 4 layers of TOF, the L1 good charge status is also required
- L1 charge distribution obtained by requiring Inner tracker and 4 layers of TOF, the L1 good charge status is not required
- L2 charge distribution obtained by requiring L1, Inner tracker L3-L8 and 4 layers of TOF, the L2 good charge status is also required

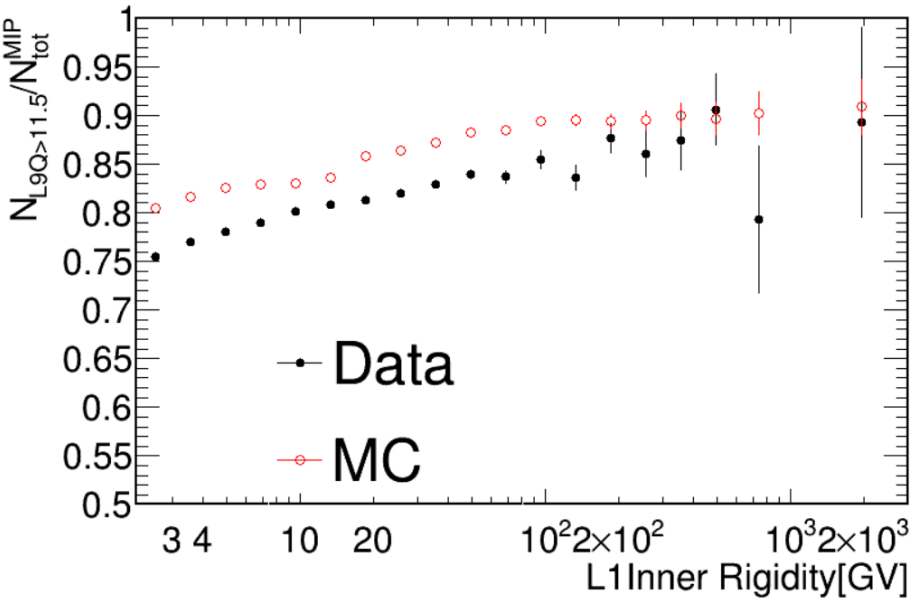

Fig. 3.35 Ratio between the the number of events in the MIP sample that pass the $Q_{L9} > 11.5$, $N_{Q>11.5}$, and the total number of events in the MIP sample, N_{MIP}^{tot}, for Data (black) and MC (red).

- L2 charge distribution obtained by requiring L1, Inner tracker L3-L8 and 4 layers of TOF, the L2 good charge status is not required

Figure 3.36 shows $Q_{L9} > 11.5$ charge selection efficiency ($\varepsilon_{Z=12}^{sel}$) for Data and MC obtained form 4 sets of L1, L2 charge distributions. The discrepancy in the $Q_{L9} > 11.5$ will result in discrepancy in the MC/Data survival probability ratio, which will be one of the source of the systematic error.

L8-L9 survival probability calculation

With the MIP selection well defined, and the purity of ECAL MIP sample obtained, the L8-L9 survival probability for Mg nuclei can be evaluated combing equation 3.25 and equation 3.26. Firstly, the ratio between the number of incoming and outgoing Mg nuclei for L1Inner and MIP samples (Equations 3.25 and 3.26) are evaluated, as shown in Figure 3.37.

With the L9 efficiencies evaluated from MIP sample and the MIP sample purity, the detection and selection efficiency $\varepsilon^{det} \cdot \varepsilon^{sel}$ can be extracted. Finally, with $\varepsilon^{det} \cdot \varepsilon^{sel}$ and the L9 efficiencies evaluated from L1Inner sample, the L8-L9 survival probability for Mg nuclei can be obtained. Because 4 sets of L1 and l2 charge distribution have been independently used to estimate the purity, therefor 4 sets of survival probability results are obtained cor-

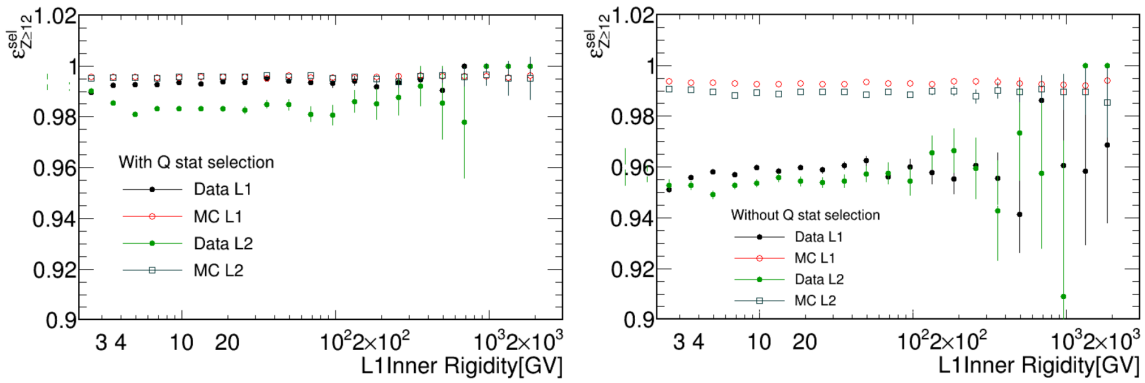

Fig. 3.36 The selection efficiency of $Q > 11.5$ (i.e. $\epsilon^{sel}_{Z=12}$) calculated from L1 and L2 charge distributions with (left) and without (right) applying charge status selection. Black points show Data L1 result, red points show MC L1 result, blue points show Data L2 result, cyan points show MC L2 result.

respondingly. Figure 3.38 shows the Mg L8-L9 survival probability for MC and Data, and their ratio. The MC truth result is also shown as reference.

Since the survival probability are calculated from 4 independent purity estimation methods, the final MC/Data survival probability ratio is calculated from the average of the four results, as shown in Figure 3.39.

The error on the MC/Data L8-L9 survival probability ratio comes from several sources:

- statistical error, calculated in rigidity from 2.15 GV to ~80 GV, and then extrapolated to high rigidity
- since the ratios are calculated from 4 independent purity estimation methods, the maximum deviation to the average is accounted in the error
- at low rigidity, larger energy transfer might vary the result, the error is accounted from the slope of MC truth result.
- at high rigidity (above ~80 GV), MC/Data survival probability ratio is assumed to be constant. The error due to this assumption is estimated from the slope of MC truth result.

Figure 3.40 shows the error on the Mg MC/Data L8-l9 survival probability ratio. The total error on the MC/Data ratio is 3% to 4%, which also contributes to the systematical error of Mg flux.

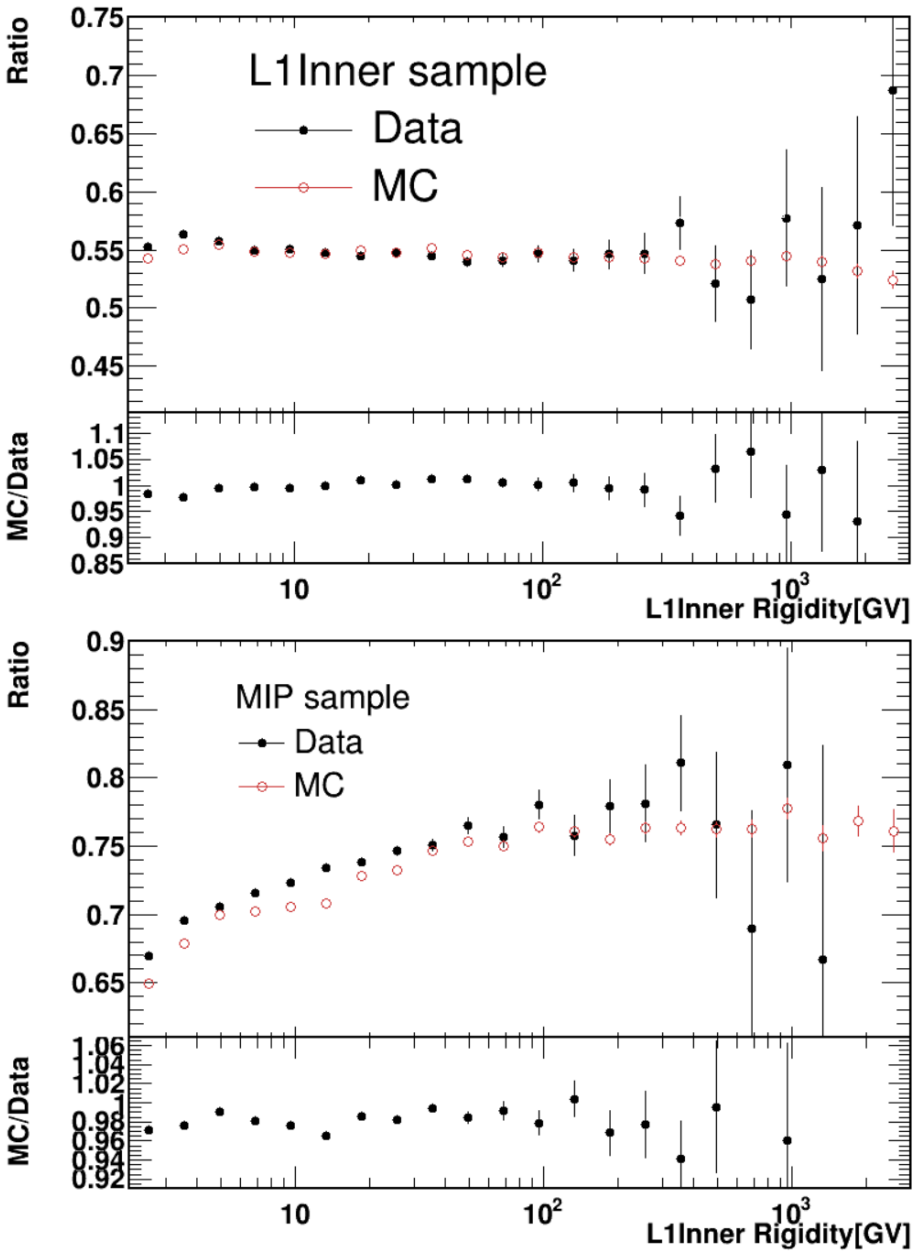

Fig. 3.37 The ratio between the number of incoming and outgoing Mg nuclei for L1Inner (left) and MIP samples (right) evaluated with Equation 3.25 and equation 3.26. In the upper panels, black points show Data results, red points show MC results. Black points in lower panels shows the ratio of MC and Data ratio results

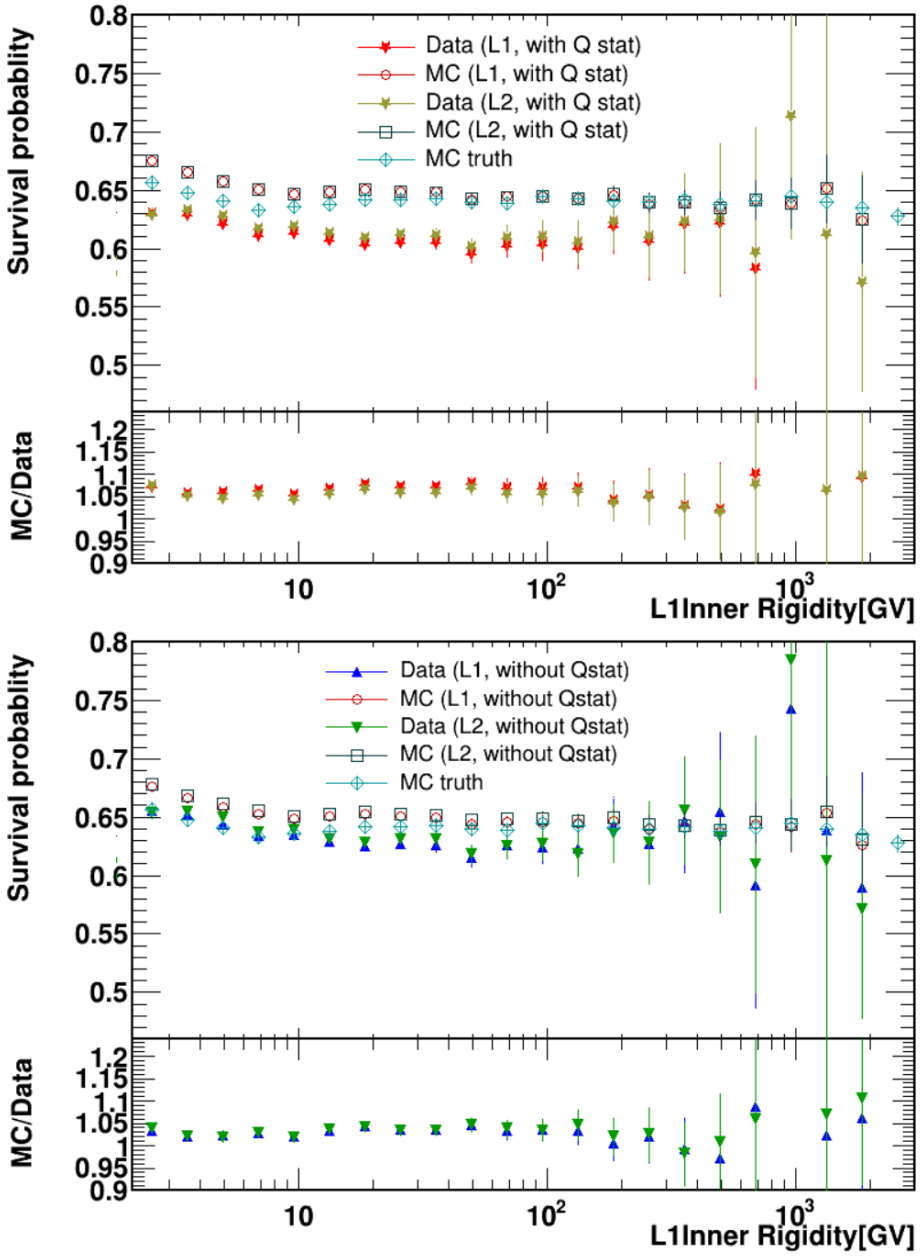

Fig. 3.38 Mg L8-L9 survival probability for MC and Data, and their ratio. Survival probabilities are calculated with 4 independent purity estimation methods. The MC truth result (cyan Diamond points) are also shown.

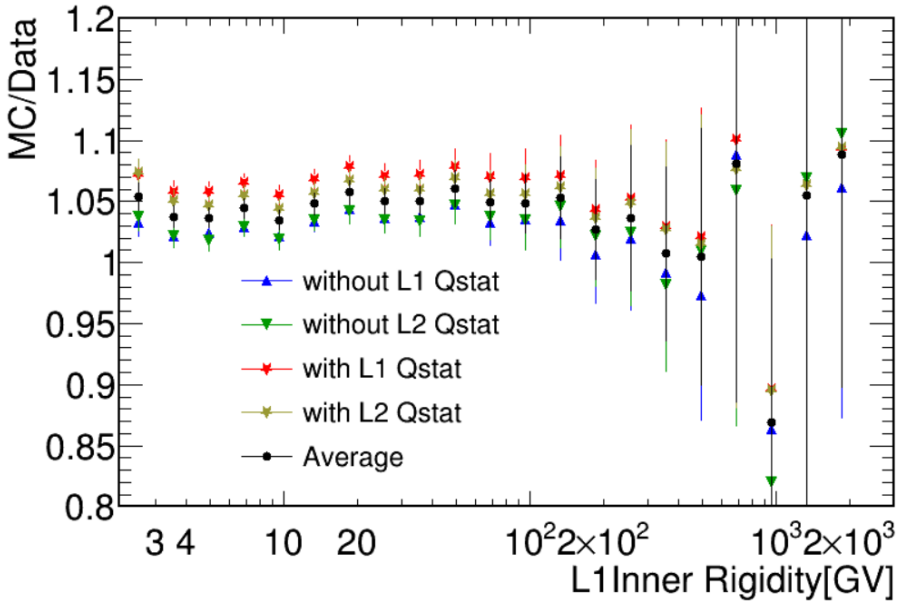

Fig. 3.39 Mg MC/Data survival probability ratios calculated from 4 independent purity estimation methods. Black points show the average of the results.

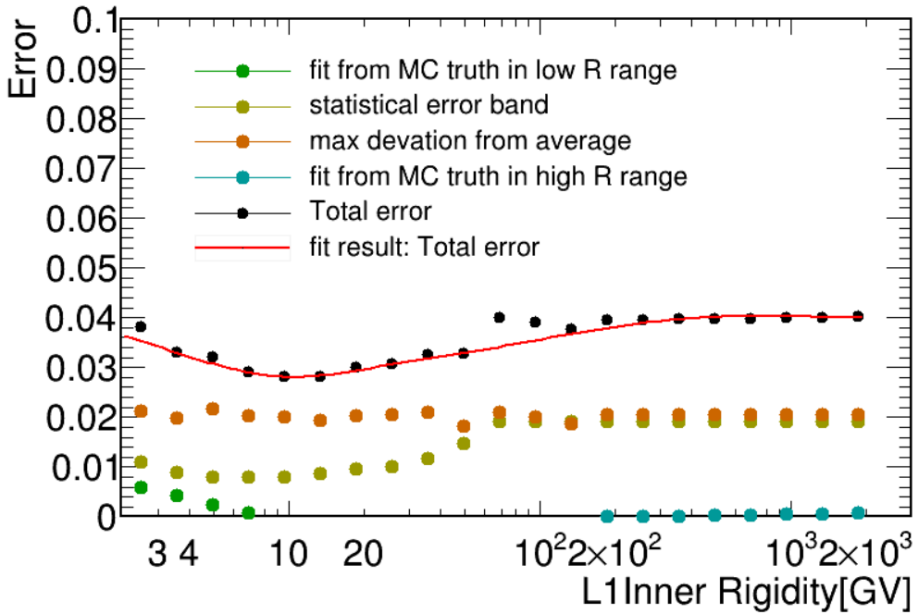

Fig. 3.40 Error on the Mg MC/Data L8-l9 survival probability ratio. Black points shows the total error, the red curve shows its parametrization.

3.7.3 Flux normalization correction

The MC/Data ratios of L1-L2 and L8-L9 survival probability for Mg nuclei deviate from 1 by around 5%, which suggests a discrepancy in the description of inelastic interactions of Mg nuclei with the AMS materials in MC simulation. Since the L8-L9 survival probability is included in the L9 efficiency, it is is already corrected by the MC/Data L9 efficiency correction. Therefore only the discrepancy in the survival probability between the top of the instrument (above L1) and L8 ($\varepsilon_{\rightarrow L8}$) needs to be corrected.

The survival probability between the top of the instrument (above L1) and L8 ($\varepsilon_{\rightarrow L8}$) for Data can't be directly estimated. Instead, the ratio between MC and Data (i.e. $\varepsilon^{MC}_{\rightarrow L8}/\varepsilon^{Data}_{\rightarrow L8}$) can be estimated from the ratios of L1 to L2 and L8 to L9 survival probabilities. And the discrepancy between Data and MC survival probabilities originates from the imperfect MC cross-section model. The survival probability ε depends on the amount of materials and the interaction cross sections:

$$\varepsilon = e^{-n\sigma} \tag{3.30}$$

where n is the number of the target nuclei per area, σ is the interaction cross section on target nuclei. The difference between interaction cross section in different part of the detector are neglected, because detector material compositions are very similar [102].

To estimate $\varepsilon^{MC}_{\rightarrow L8}/\varepsilon^{Data}_{\rightarrow L8}$, information on the material amount n is needed. The ratio of material amounts between different part of the AMS detector can be evaluated from MC survival probabilities:

$$\frac{\log\varepsilon_1}{\log\varepsilon_2} \approx \frac{n_1}{n_2} \tag{3.31}$$

Figure 3.41 shows the survival probabilities between different part of the AMS detector calculated from MC truth. With the above equation, the ratios of material amounts are calculated by the ratios of the logarithms of the survival probabilities, as shown in Figure 3.42.

Then the MC survival probability between the top of the instrument (above L1) to L8 (i.e. $\varepsilon^{MC}_{\rightarrow L8}$) can be estimated from the L1 to L2 or L8 to L9 survival probabilities as:

$$\varepsilon^{MC}_{\rightarrow L8} = e^{-\sigma n_{\rightarrow L8}} = e^{-\sigma \frac{n_{\rightarrow L8}}{n_{L8\rightarrow L9}} n_{L8\rightarrow L9}} = (\varepsilon^{MC}_{L8\rightarrow L9})^{\frac{n_{\rightarrow L8}}{n_{L8\rightarrow L9}}} \tag{3.32}$$

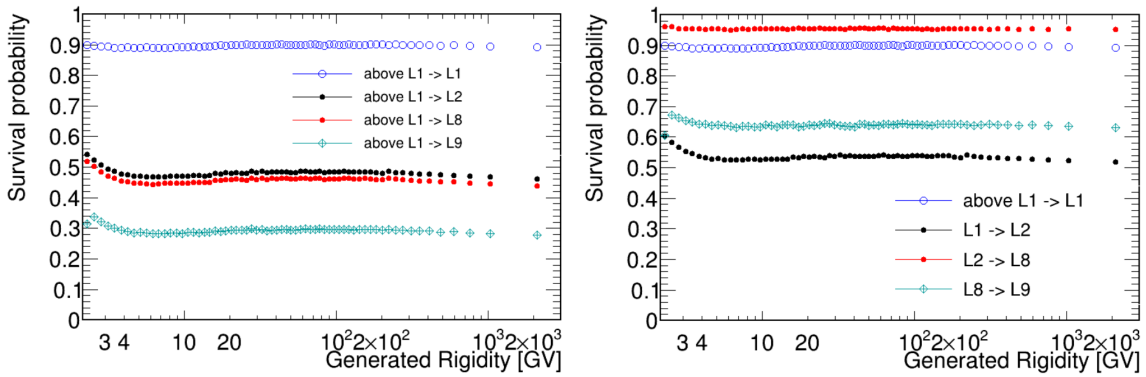

Fig. 3.41 Survival probabilities between different part of the AMS detector evaluated from MC truth. Left: survival probabilities between the top of the instrument (above L1) and different tracker layers. Right: survival probabilities between different tracker layers.

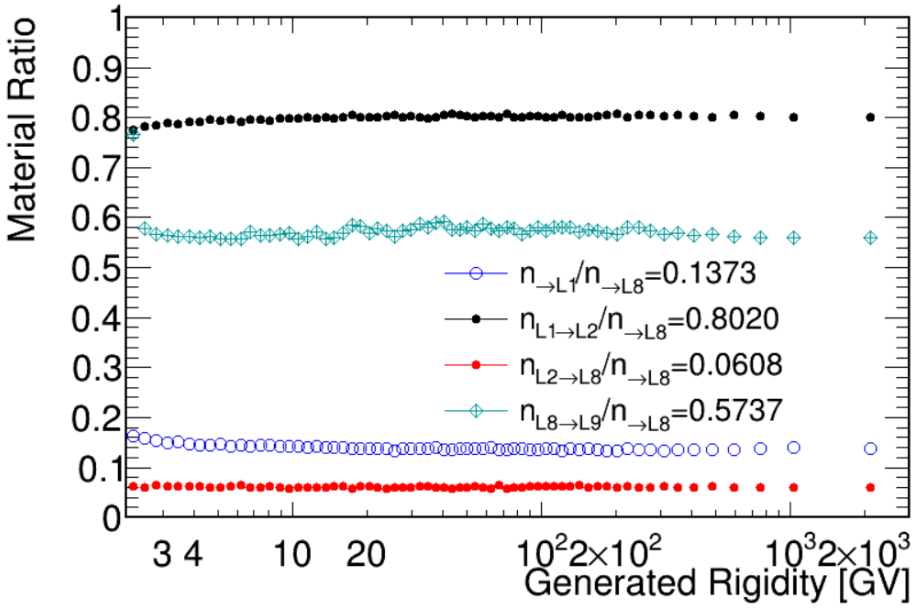

Fig. 3.42 The ratios of material amounts between different part of the AMS detector.

The material amounts are well described by MC. And the ratios of material amounts between different part of detector for MC and Data can be assumed as the same:

$$\frac{n^{MC}_{\rightarrow L8}}{n^{MC}_{L8\rightarrow L9}} \approx \frac{n^{Data}_{\rightarrow L8}}{n^{Data}_{L8\rightarrow L9}} \tag{3.33}$$

Finally, the MC and Data ratio of the survival probability between the top of the instrument and L8 (i.e. $\varepsilon^{MC}_{\rightarrow L8}/\varepsilon^{Data}_{\rightarrow L8}$) is rescaled from the ratios of L1 to L2 or L8 to L9 survival probabilities:

$$\frac{\varepsilon^{MC}_{\rightarrow L8}}{\varepsilon^{Data}_{\rightarrow L8}} = (\frac{\varepsilon^{MC}_{L8\rightarrow L9}}{\varepsilon^{Data}_{L8\rightarrow L9}})^{\frac{n^{MC}_{\rightarrow L8}}{n^{MC}_{L8\rightarrow L9}}} = (\frac{\varepsilon^{MC}_{L1\rightarrow L2}}{\varepsilon^{Data}_{L1\rightarrow L2}})^{\frac{n^{MC}_{\rightarrow L8}}{n^{MC}_{L1\rightarrow L2}}} \tag{3.34}$$

Similarly, MC and Data ratio of L1 to L2 survival probability can also be re-scaled from that of L8 to L9 survival probability. Figure 3.43 shows MC and Data L1 to L2 survival probability ratio, and the result rescaled from L8 to L9 survival probability ratio. The two results are in good agreement.

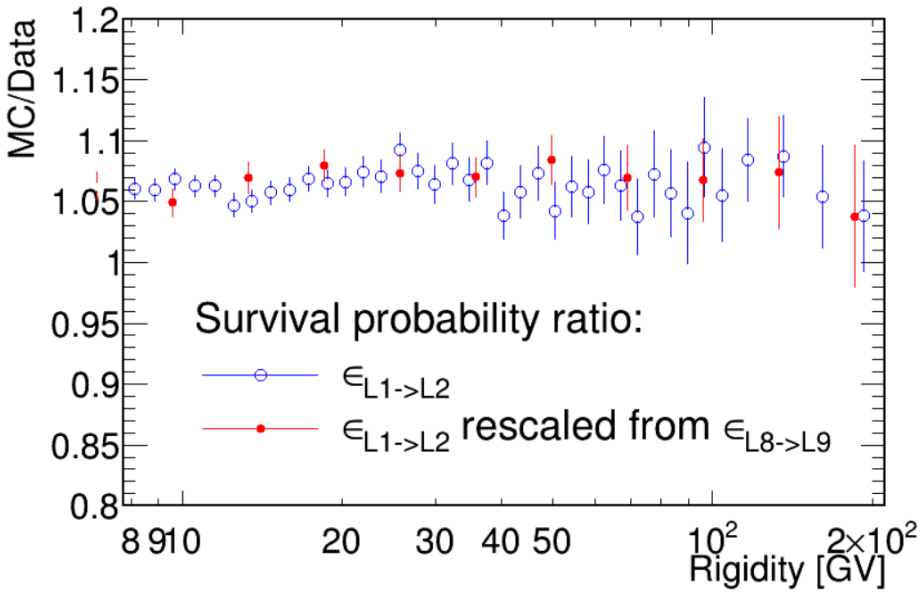

Fig. 3.43 Ratio of MC to Data L1 to L2 survival probability for Mg nuclei as estimated from particles traversing the material between Tracker L1 and L2 without fragmenting (blue open circles) and obtained by rescaling the L8-L9 survival probability ratio.

Considering that L8 to L9 survival probability have better measurement, the MC and Data ratio of between above L1 to L8 survival probability is rescaled from L8 to L9 survival probability ratio. Figure 3.44 shows the Mg above L1 to L8 survival probability ratio. The

bias between MC and Data is found to be 1.067, which will be taken as a flux normalization correction. Its uncertainty contributes to the total systematic error of the flux.

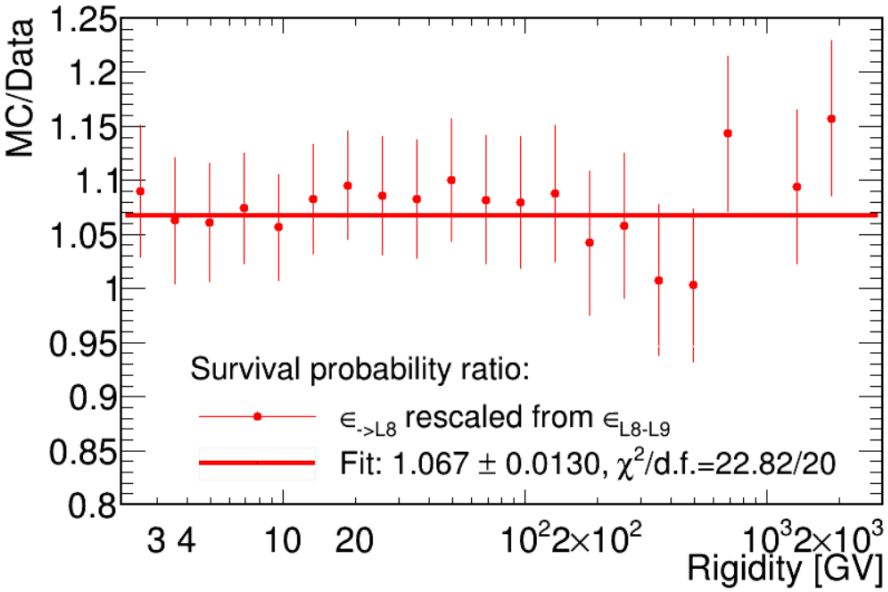

Fig. 3.44 MC to Data ratio of top-of-the-instrument (above L1) to L8 survival probability for Mg nuclei (red points). The red line shows a constant fit to the ratio.

3.8 Systematic errors

Extensive studies were made of the systematic errors which include the uncertainties due to the absolute rigidity scale, rigidity resolution function, unfolding procedure, geomagnetic cutoff, the acceptance calculation, and the DAQ and L1 charge efficiencies. The acceptance errors include uncertainties coming from Data and MC efficiencies and the Mg nuclei survival probabilities due to interactions in AMS materials for Data and MC.

3.8.1 Absolute rigidity scale

The shift in the absolute rigidity scale results in inaccuracy of the calibration of rigidity, there are two contributions to the systematic uncertainty on the rigidity scale [107].

The first is due to residual tracker misalignment. The misalignment happened at the micron level during the assembling of the detector, and the AMS launch into space due to vibrations and accelerations. And it also happens during the operation, because L1, Inner Tracker and L9 work in different thermal environments. The misalignment has been estimated by comparing the ratio between the energy measured with the ECAL and the rigidity

measured with the tracker for electrons and positrons [115]. After the correction of the misalignment, the residual uncertainty was found to be $1/30\,\mathrm{TV}^{-1}$.

The second uncertainty on the absolute rigidity scale arises from the Tracker magnetic field map measurement and its temperature corrections [107]. The uncertainty was found to be 0.27%.

The absolute rigidity scale shift causes the shift of the rigidity resolution function. Therefore it can be studied by varying the mean of the rigidity resolution function

- to estimate the error due to residual tracker misalignment: the mean of the core Gaussian of the rigidity resolution function has been shifted by $\pm(1/30)\,\mathrm{TV}^{-1}$
- to estimate the error due to the uncertainty of magnetic field map measurement: the mean of the core Gaussian has been shifted by by $\pm 0.27\%$, i.e. $(\frac{1}{R_{rec}(1 \pm 0.27\%)} - \frac{1}{R_{rec}})\,\mathrm{TV}^{-1}$

Then repeat the unfolding procedure. The systematic error due to the absolute rigidity scale is then obtained from the ratio between the obtained Mg nuclei fluxes and the original Mg nuclei fluxes. The result is shown in Figure 3.45.

3.8.2 Resolution function

The parametrization of rigidity resolution function also contributes to the flux uncertainty. Similar to the study of the systematic error arising from the uncertainty on the absolute rigidity scale, the error is obtained by varying the width of the Gaussian core of the rigidity resolution function by 5% and by independently varying the amplitude of the non-Gaussian tails by 10% according to the measured Silicon Tracker bending coordinate accuracy [81]. Figure 3.46 shows the systematic error due to the parametrization of the rigidity resolution function for both FS and L1Inner geometries. The FS error is smaller than L1Inner error in the high rigidity range, because FS has better resolution and higher MDR.

3.8.3 Unfolding procedure

As discussed in Section 3.6.2, the unfolding procedure is performed as an iterative procedure that minimizes the difference between the measured folded event rate and the folded rate calculated from a prior flux model. The flux model is parameterized by a series of node points (x_1, y_1; x_2, y_2; ...; x_n, y_n;). And the positions of the nodes are determined when the minimized iteration is finished. The systematic error arising from the unfolding procedure comes from the minimization procedure and the parametrization of the flux model (i.e. the

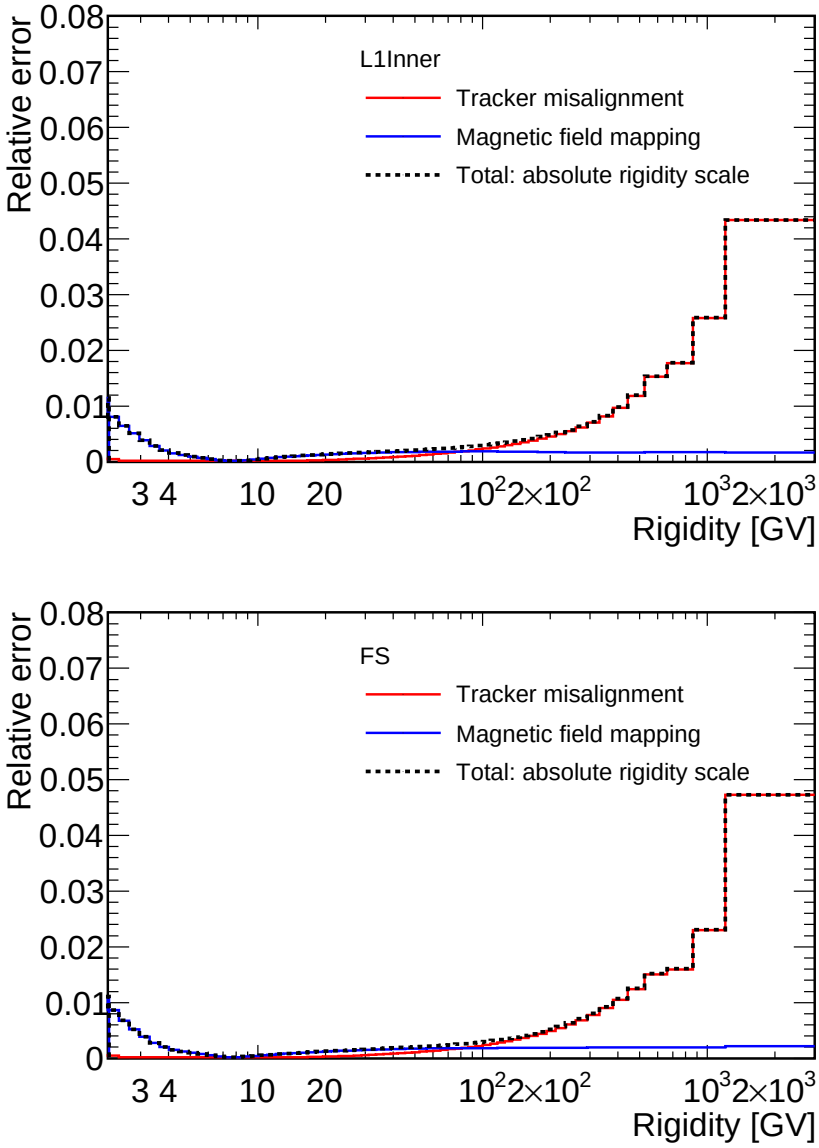

Fig. 3.45 Relative systematic error due to the uncertainty on the absolute rigidity scale for L1Inner (top) and FS (bottom) geometries (black dashed line) calculated summing in quadrature of the contributions from the tracker misalignment (red line) and the magnetic field map measurement (blue line).

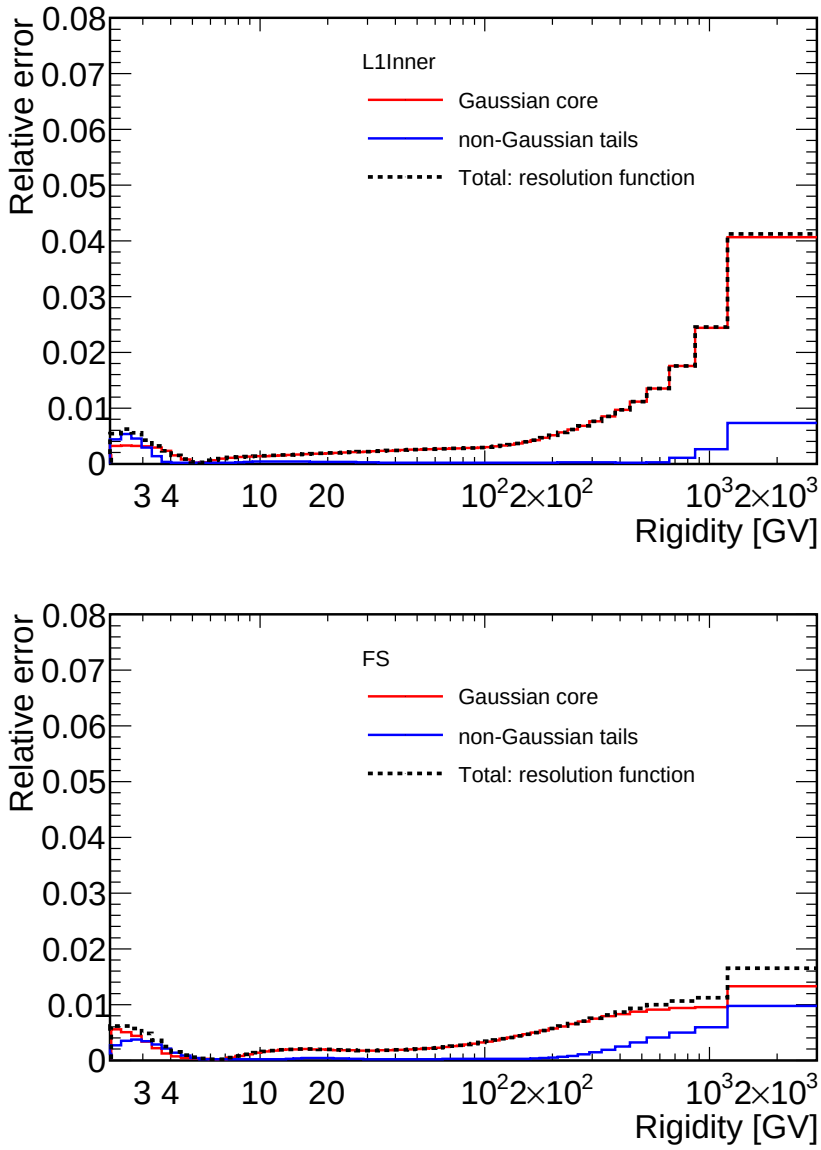

Fig. 3.46 Relative systematic error due to the rigidity resolution function for L1Inner (top) and FS (bottom) geometries (black dashed line) calculated summing in quadrature of the contributions from the width of the Gaussian core (red line) and the amplitude of the non-Gaussian tails (blue line).

positions of the nodes). It can be evaluated by varying the nodes of the spline function to redefine the flux model and then repeating the unfolding procedure until the minimization converge.

The x- positions of the nodes have been shifted by 20% independently, and the number of nodes has also been varied by adding or removing one of the x-nodes. The y- positions have been varied within the statistical error of the Mg nuclei flux. The unfolding procedure has been repeated using the flux model resulting by repeatedly adjusting the spline fitting function. The error due to the unfolding procedure has been obtained from the ratio between the resulting Mg nuclei fluxes and the original Mg nuclei flux. Figure 3.47 shows the systematic error due to the unfolding procedure.

3.8.4 Geomagnetic cutoff

As mentioned in Section 3.2, a safety factor of 1.2 is applied to the maximum geomagnetic cutoff in the particle measured rigidity cut to make sure that the selected particle is a cosmic-ray coming from outside the Earth's magnetosphere. The geomagnetic cutoff factor has been varied from 1.0 to 1.4 to evaluate the resulting uncertainty. By varying the safety factor, the number of collected events and the exposure time for rigidities below 30 GV will change, Figure 3.48 shows a comparison between Mg nuclei raw fluxes obtained varying the safety factor from 1.0 to 1.4. As seen in the figure, for rigidities below 30 GV, the error due to geomagnetic cutoff safety factor is negligible.

3.8.5 Acceptance calculation

The effective acceptance includes geometric acceptance, event reconstruction and selection efficiencies, and inelastic interactions of nuclei in the AMS materials.

As discussed in Section 3.4, by checking the geometric acceptance with a toy MC, the error due to the geometric acceptance calculation is negligible (less than 0.3%). The error due to the discrepancy of event reconstruction and selection efficiencies between Data and MC is evaluated from the error of the parametrization of Data/MC efficiency ratios.

The error due to the discrepancy of inelastic interactions of nuclei in the AMS materials between Data and MC is evaluated from the uncertainty of the Mg nuclei survival probability.

Parametrizations of Data/MC efficiency ratios

The error due to the parametrization are already evaluated during the Data/MC efficiency ratio calculations. As discussed in Section 3.5. The uncertainty in the parametrization comes from two sources

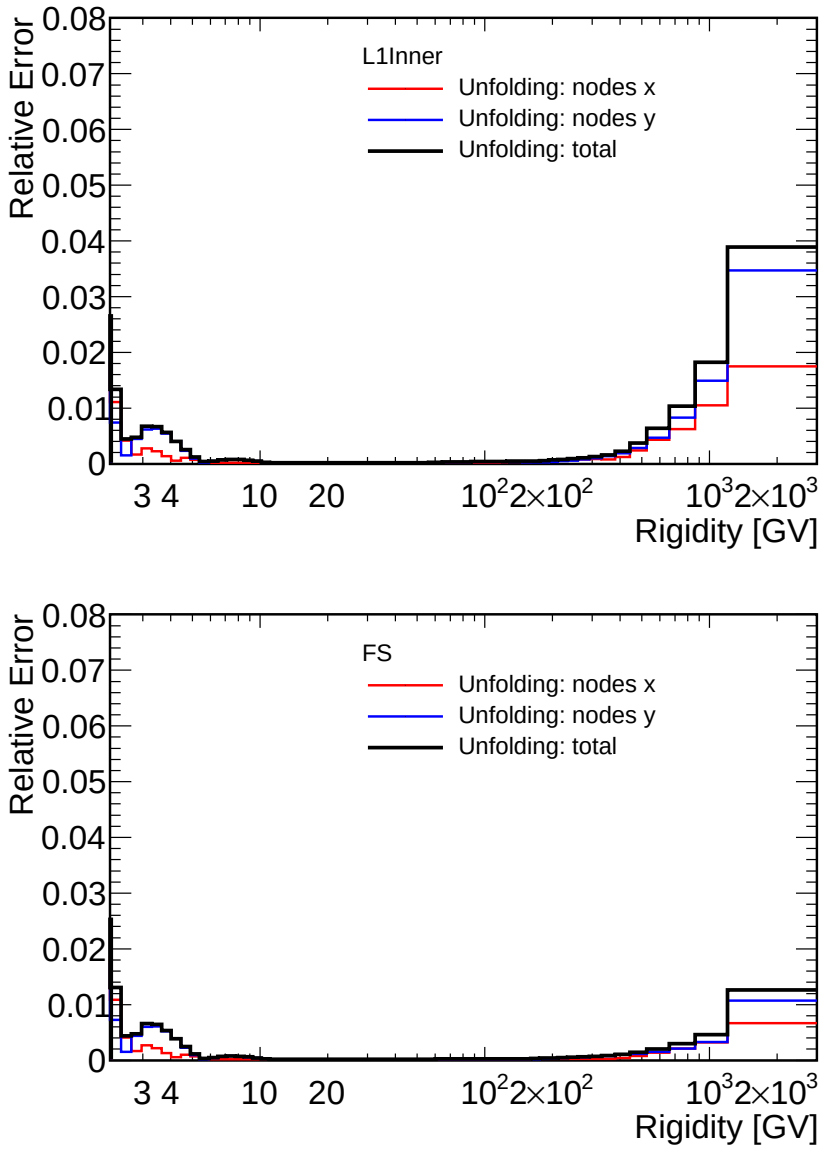

Fig. 3.47 Relative systematic error due to the unfolding procedure for L1Inner (top) and FS (bottom) geometries (black line) calculated summing in quadrature of the error obtained by adjusting x-node (red line) and the error obtained by varying y-node within the statistical error of the Mg flux (blue line).

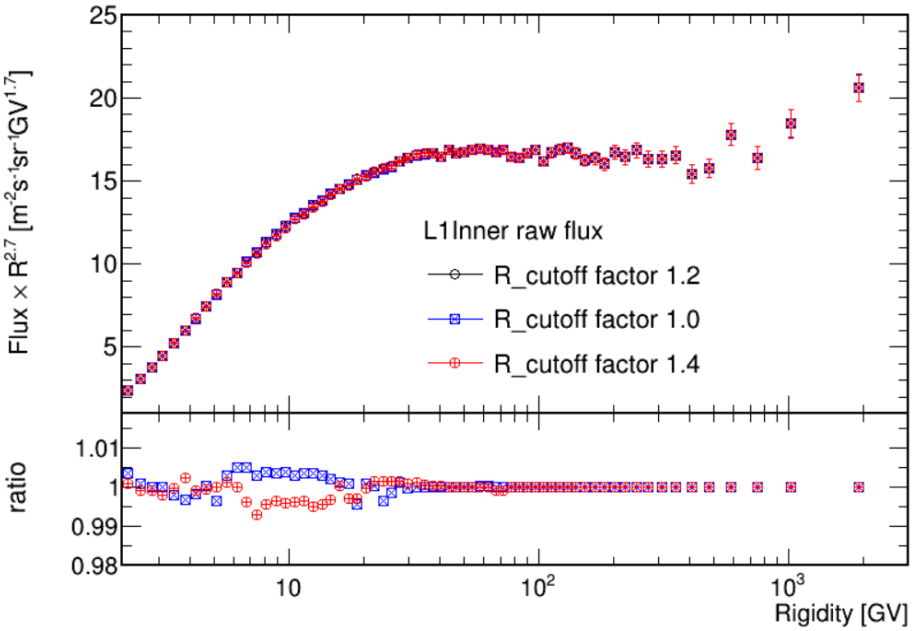

Fig. 3.48 Mg nuclei L1Inner raw fluxes (top panel) obtained with different geomagnetic cutoff safety factor values: 1.2 (black), 1.0 (blue), and 1.4 (red), and ratios (bottom panel) to the original flux (safety factor 1.2) for the fluxes obtained with safety factors 1.0 (blue points) and 1.4 (red points).

1. the spline fit error, which is determined by the 68% CL interval;
2. the assumption of the shape in the high rigidity range. In order to smooth out the statistical fluctuation, the Data/MC efficiency ratio is assumed and parameterized to be a constant at high rigidity. The error is calculated from the slope of the MC efficiency in the generated rigidity.

Figure 3.49 shows the error due the parametrization of Data/MC efficiency ratio extracted from the Data/MC overall correction of Figure 3.22 of Section 3.5.

Survival probability

The systematic error due to the discrepancy in the description of inelastic interactions of Mg nuclei in the AMS materials between Data and MC has been evaluated from the uncertainty of the Mg nuclei survival probabilities. Extensive studies have been done to evaluate the uncertainty as shown in Figure 3.40 in Section 3.7. The relative uncertainty arising from the Mg nuclei survival probability is found to be between 3%-4% in the entire rigidity range.

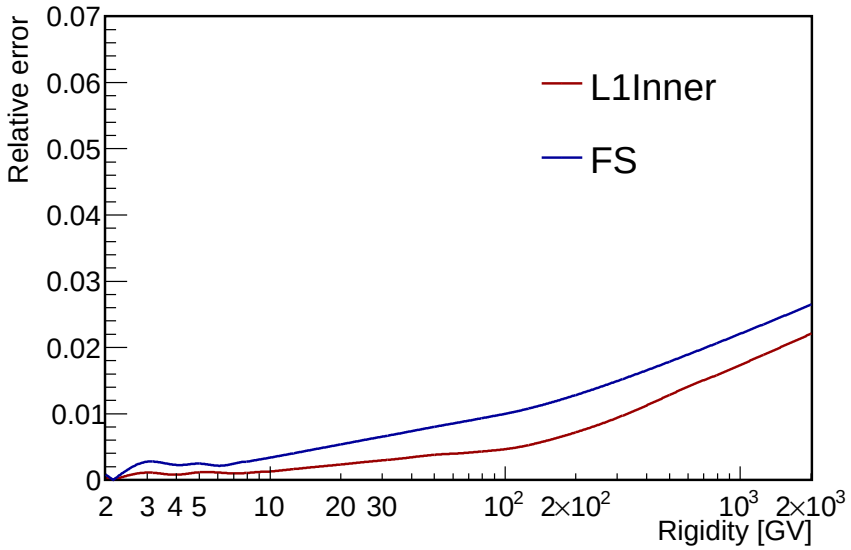

Fig. 3.49 The systematic error due the parametrization of Data/MC efficiency ratio for L1Inner (red), and FS (blue), extracted from the Data/MC overall correction of Figure 3.22 of Section 3.5

3.8.6 Total error of Mg nuclei flux

Error form DAQ efficiency and L1 charge cut inefficiency, as shown in Section 3.3.3 and Section 3.3.2, evaluated with the same method as other efficiency uncertainties, have <1% contributions to the total flux error. The contribution of individual sources of the systematic error are added in quadrature to arrive at the total systematical error. To obtain the final flux error, the last bin is taken from FS, the other bins are taken form L1Inner, the statistical errors are taken accordingly. Figure 3.49 shows the total error of Mg nuclei flux and its error break down. At 100 GV, the Mg nuclei flux has around 4% relative error.

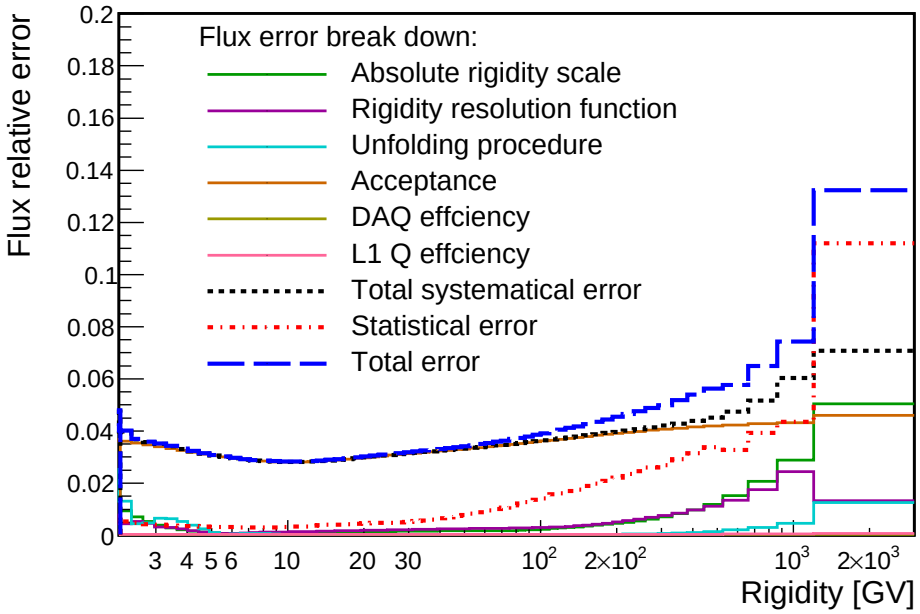

Fig. 3.50 Mg nuclei flux error break down including total error (blue dashed line), statistical error (red dashed line), total systematic error (black dashed line), and the components of systematic error (solid lines).

3.9 Mg nuclei flux result

3.9.1 8.5 years Mg nuclei flux

The Mg nuclei flux (multiplied by $R^{2.7}$) and its spectral index in the rigidity range from 2.15 GV to 3 TV with 2.5 million Mg nuclei events collected by AMS during the first 8.5 years operation from May 19, 2011 to October 30, 2019 are shown in Figure 3.51. The points of flux are placed along the abscissa at rigidity R calculated for a flux $\propto R^{-2.7}$ [116]. The spectral index is used to examine the rigidity dependence of the fluxes, it has been calculated in model independent way as

$$\gamma = \mathrm{d}[\log(\Phi)]/\mathrm{d}[\log(R)] \tag{3.35}$$

over non-overlapping rigidity intervals bounded by 7.09, 12.0, 16.6, 28.8, 45.1, 80.5, 192.0, 441.0, and 3000 GV.

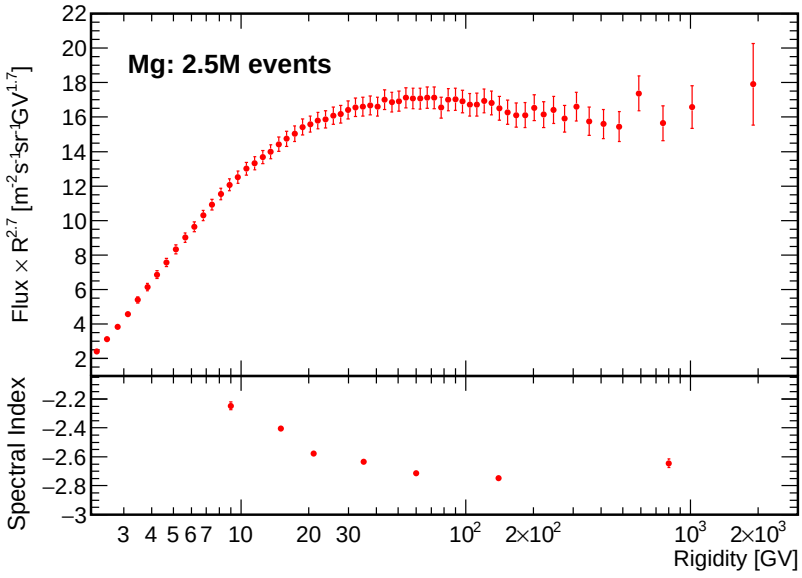

Fig. 3.51 Mg nuclei flux in the rigidity range from 2.15 GV to 3 TV with 2.5 million Mg nuclei events collected by AMS during the first 8.5 years operation from May 19, 2011 to October 30, 2019. The upper panel shows the flux multiplied by $R^{2.7}$, the lower panel shows the spectral index.

As seen in Figure 3.51, the Mg flux deviates from a single power law, and the spectral index hardens with increasing rigidity above ~200 GV.

AMS Mg nuclei flux is the first and the only measurement in rigidity. As mentioned in Section 3, previous experiments have measured the the Mg flux as function of kinetic energy

per nucleon E_k. To compare the AMS result to earlier measurements, the rigidity measured by AMS is converted to kinetic energy per nucleon as

$$E_k = (\sqrt{Z^2R^2 + M^2} - M)/A \tag{3.36}$$

where Z, M, and A are the charge, mass, and atomic mass number of a Mg nucleus. By assuming Mg nuclei incosmic rays are mainly ^{24}Mg [57, 58, 117], Z=12, M=24, A=24 have been used in the calculation.

Figure 3.52 shows the Mg nuclei flux as a function of kinetic energy per nucleon E_k multiplied by $E_k^{2.7}$ together with earlier measurements [57, 58]. Earlier measurements have errors larger than 20% at 50 Gev/n), while the total error of the AMS 8.5 years Mg flux is $\sim$ 4% at 100 GV ($\sim$ 50 Gev/n).

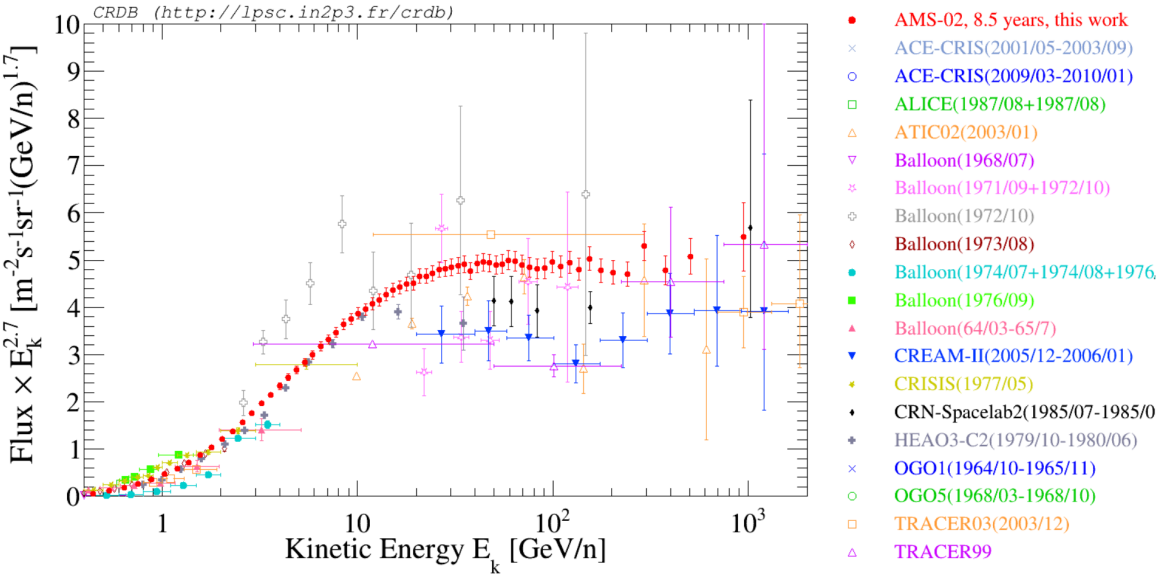

Fig. 3.52 Mg nuclei flux as a function of kinetic energy per nucleon E_k multiplied $E_k^{2.7}$ together with earlier measurements [57, 58]

3.9.2 Comparison to the published result

The work presented in the previous section is an update of a previous analysis based on 7 years of data which has been published in May 2020 [106].

Figure 3.51 shows the Mg flux (multiplied by $R^{2.7}$) based on 7 years of data and its spectral index.

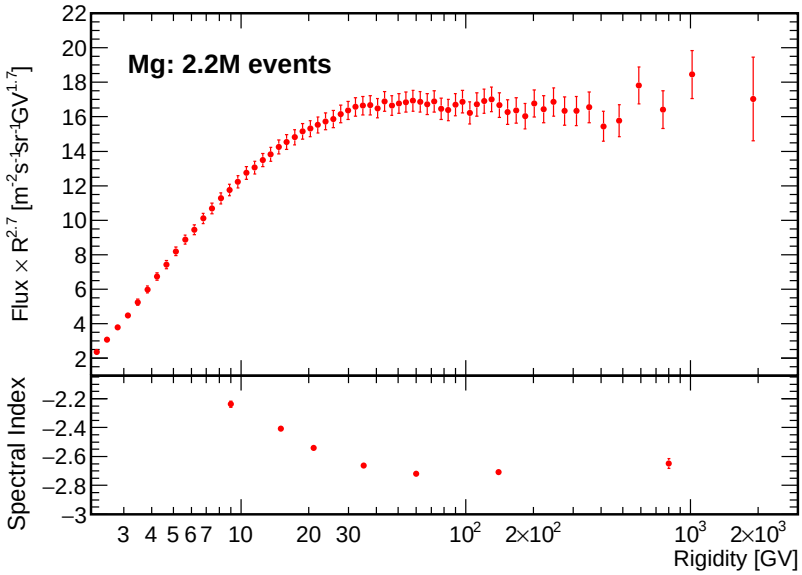

Fig. 3.53 Mg nuclei flux in the rigidity range from 2.15 GV to 3 TV with 2.2 million Mg nuclei events collected by AMS during the first 7 years operation from May 19, 2011 to May 26, 2018. The upper panel shows the flux multiplied by $R^{2.7}$, the lower panel shows the spectral index.

Figure 3.54 shows a comparison of Mg flux between 8.5 years and 7 years results. As seen, the two results are in good agreement, and the effect caused by solar modulation is not visible.

Three independent analyses were performed on the 7 years of data within the AMS collaboration by groups from the University of Geneva (this work), MIT, and CIEMAT and Bologna University. As shown in Figure 3.55, the three results were consistent within the systematic uncertainty.

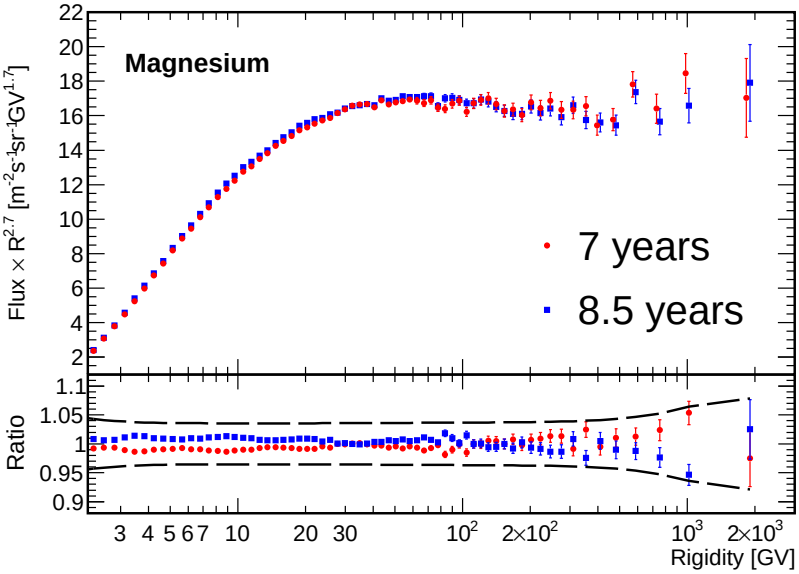

Fig. 3.54 Mg fluxes as functions of rigidity based on 7 years (red) and 8.5 years (blue) of data. The lower panel shows the ratio between each result and the average. The error of the ratio is calculated from statistical error subtracting ∼10% correlation. The black dashed band is the average of systematical error subtracted by the acceptance error.

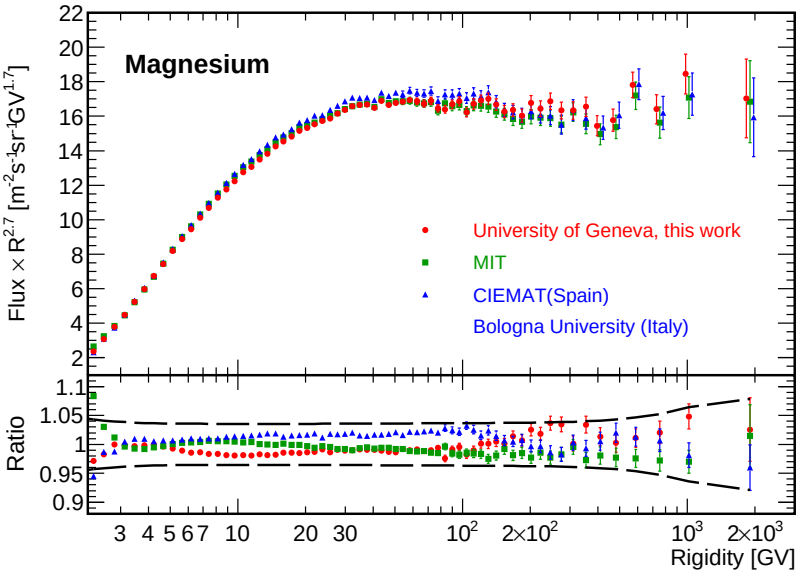

Fig. 3.55 Comparison of 7 years Mg flux resulting from independent analysis performed at the University of Geneva (this work, red points), MIT (green squares), and CIEMAT and Bologna University (blue triangles). The lower panel shows the ratio between each result and the average, together with the average of systematical error band.

3.9.3 Discussion of the Mg nuclei flux result

Primary and secondary components in Mg nuclei flux

As mentioned, the cosmic-ray Mg nuclei are mainly primary. To obtain the fractions of the primary Φ^P_{Mg} and secondary Φ^S_{Mg} components in Mg nuclei flux $\Phi_{Mg} = \Phi^P_{Mg} + \Phi^S_{Mg}$, a fit of Φ_{Mg} to the weighted sum of a heavy primary cosmic ray flux and of a heavy secondary cosmic ray flux was performed above 5 GV. The Si flux (Φ_{Si}) and the F flux (Φ_F) are used as templates for the primary and secondary components respectively.

As shown in Figure 3.56, the fit yields $\Phi^P_{Al} = (0.980 \pm 0.021) \times \Phi_{Si}$ and $\Phi^S_{Al} = (2.32 \pm 0.21) \times \Phi_f$ with $\chi^2/d.f = 4.06/39$. The contribution of the secondary component in Mg nuclei flux decreases with increasing rigidity, and found to be smaller than 10% in rigidities above $\sim$ 100 GV.

Comparison between Mg and Si fluxes

The Mg flux rigidity dependence is compared to that of other primary cosmic-ray nuclei of similar mass, Ne and Si, and to light primary cosmic-ray O nuclei. In this study, O and Si fluxes have been measured from the same AMS dataset (8.5 years) by the University of Geneva group.

To examine the difference in rigidity dependence of the heavy primary nuclei fluxes, the Si/Mg flux ratios were computed. Figure 3.57 shows Mg, Si fluxes and Si/Mg flux ratio. The flux ratios rise with rigidity up to a certain rigidity R_0 and then reach a plateau (Figure 3.58). To establish the rigidity intervals where the fluxes have identical rigidity dependence, the Si/Mg flux ratios have been fitted with the function:

$$\frac{\Phi_{Si}}{\Phi_{Mg}} = \begin{cases} k(R/R_0)^{\Delta} & R \leqslant R_0 \\ k & R > R_0 \end{cases} \tag{3.37}$$

The fit to the Si/Mg flux ratio yields: $k^{Si/Mg} = 0.901 \pm 0.007$, $\Delta^{Si/Mg} = 0.056 \pm 0.004$, $R_0^{Si/Mg} = 85.5 \pm 15.5$, with $\chi^2/d.f = 22.85/53$. The fit result shows that the Si and Mg fluxes have an identical rigidity dependence above 86.5 GV (upper edge of the rigidity bin containing 85.5 GV).

Additional study with the fit to the Ne/Mg flux ratio [106] shows that the Ne and Mg fluxes have an identical rigidity dependence above 3.65 GV. From the fit results, it can be concluded that Ne, Mg, and Si fluxes have an identical rigidity dependence above 86.5 GV. This is a unique observation of the properties of cosmic-ray Ne, Mg, and Si nuclei.

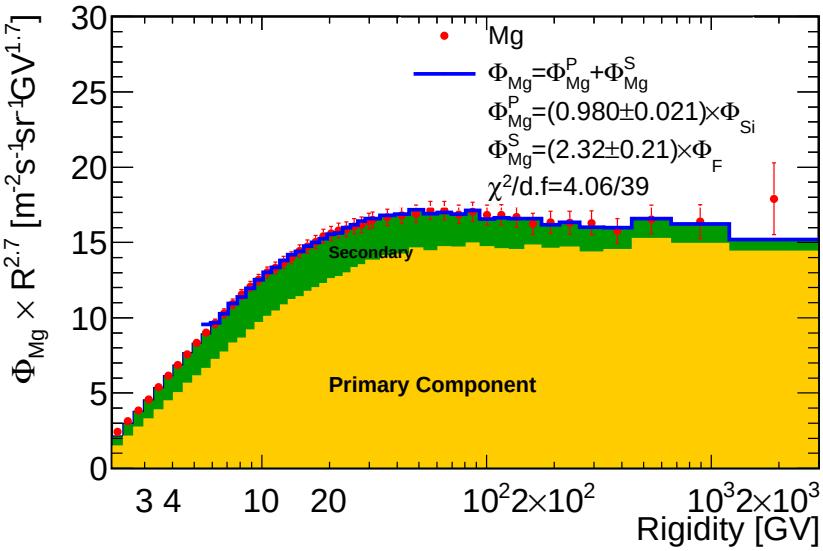

(a) Mg nuclei flux fit to the weighted sum of Si nuclei flux Φ_{Si} and F nuclei flux

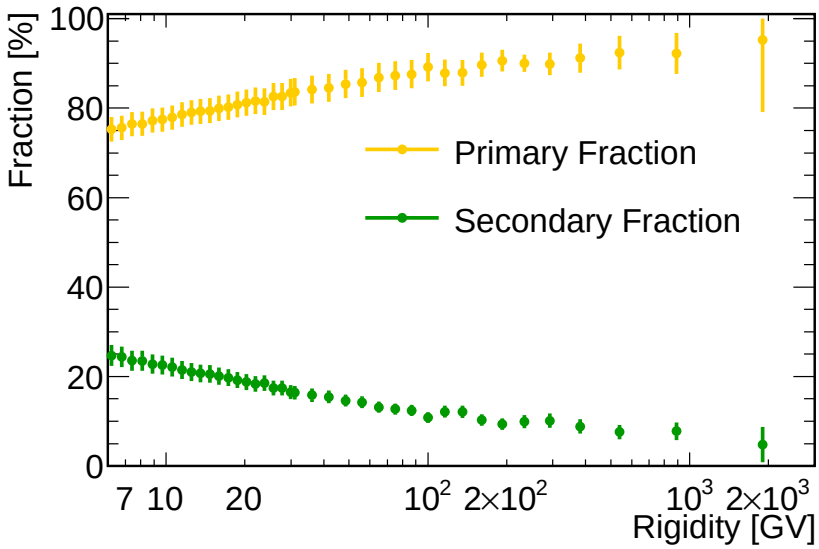

(b) The fractions of primary and secondary components of Mg flux

Fig. 3.56 Mg nuclei flux Φ_{Mg} fit to the weighted sum of Si nuclei flux Φ_{Si} and F nuclei flux Φ_F above 5 GV, i.e. $\Phi_{Mg} = \Phi^P_{Mg} + \Phi^S_{Mg}$ (top plot), with the yellow shaded area showing the contribution of the primary component, the green area showing the contribution of the secondary component. And the fractions of primary (yellow line) and secondary (green line) components of Mg flux (bottom plot) obtained from the fit. To reduce statistical fluctuations, for rigidity above 28.8 GV, every two bins have been merged into one bin.

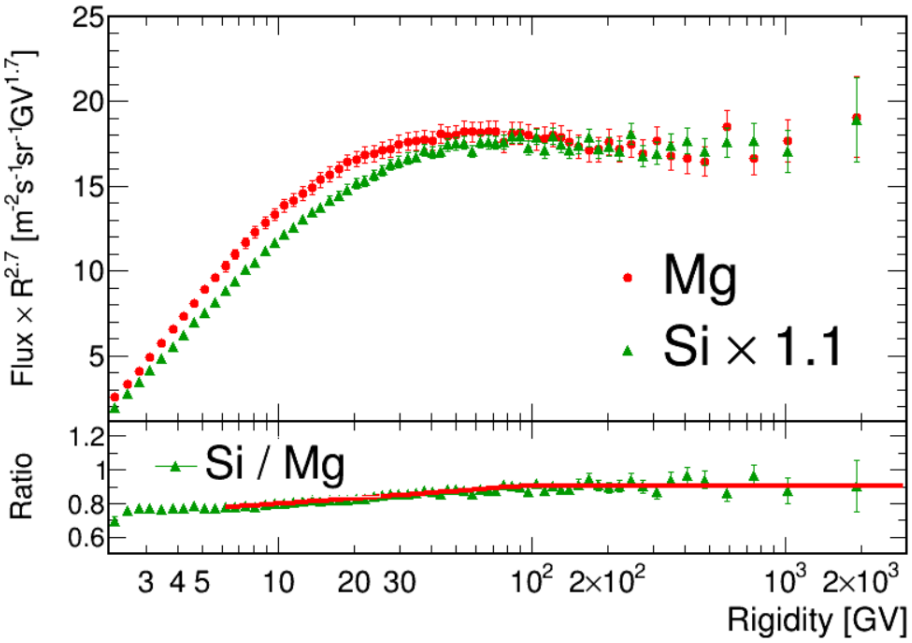

Fig. 3.57 Comparison between Si and Mg (upper panel) nuclei fluxes, and their ratio (lower panel). The fluxes have been multiplied by $R^{2.7}$. For display purposes only, the Si flux was rescaled as indicated. The solid curves show the fit results with equation 3.37, the fit range is above 6 GV.

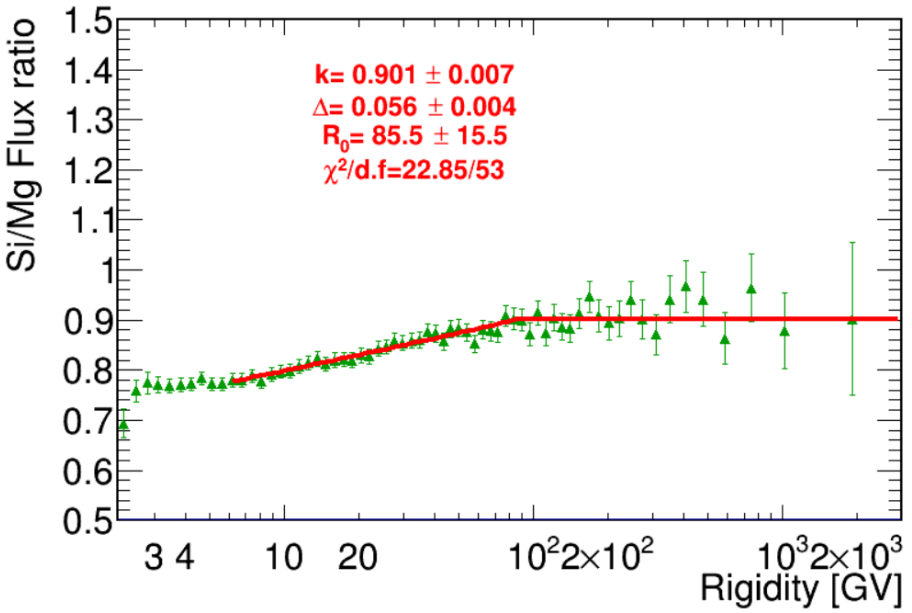

Fig. 3.58 The Si/Mg flux ratio with its total errors as functions of rigidity. The solid curve show the fit result with equation 3.37. As seen, the Si and Mg fluxes have identical rigidity dependence above 86.5 GV.

Comparison between Mg and O fluxes

As introduced in Section 1.4 of Chapter 1, the previous AMS results on lighter primary cosmic rays He, C, and O [81] show that they have identical rigidity dependence above 60 GV. Figure 3.59 shows Mg and O fluxes and their ratio.

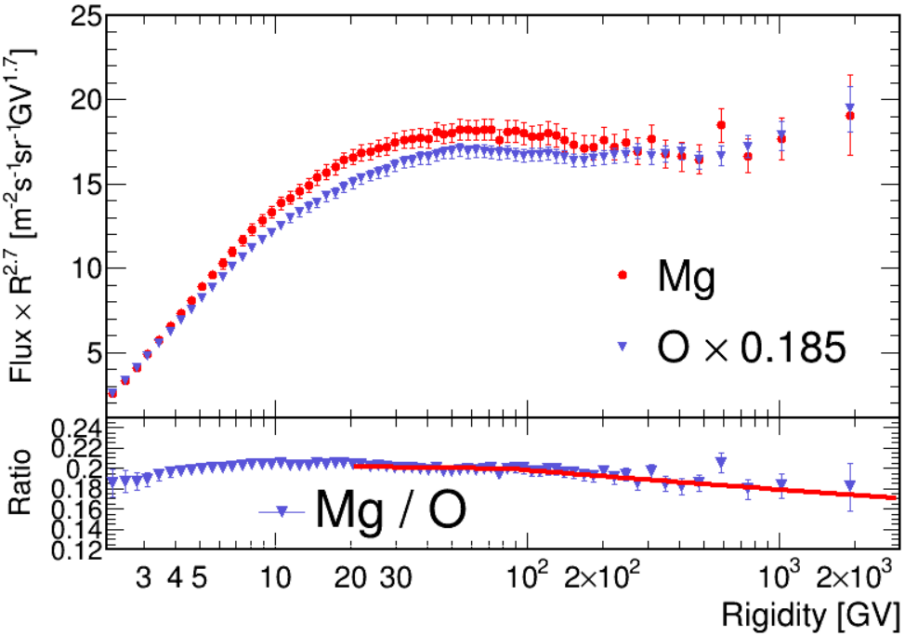

Fig. 3.59 Mg (red points) and O (blue points) fluxes multiplied by $R^{2.7}$ (top panel) and Mg/O flux ratio (bottom panel) with their total errors as functions of rigidity. For display purposes only, the O flux has been rescaled as indicated. The solid red curve shows the fit results with equation 3.38.

As seen, in high rigidity range, the Mg/O flux ratio (Figure 3.60) decreases with increasing rigidity. To examine the rigidity dependence, Mg/O is fitted to the double power law:

$$\frac{\Phi_{Mg}}{\Phi_O} = \begin{cases} C(R/86.5\,\mathrm{GV})^{\Delta} & R \leqslant 86.5 \\ C(R/86.5\,\mathrm{GV})^{\delta} & R > 86.5 \end{cases} \tag{3.38}$$

The fit yields $C^{Mg/O} = 0.199 \pm 0.001$, $\Delta^{Mg/O} = -0.008 \pm 0.008$, $\delta^{Mg/O} = -0.044 \pm 0.017$, with $\chi^2/d.f = 14.41/53$. The fit result shows that the Mg and O have different behavior in rigidity above 86.5 GV. Additional studies with the fit to Ne/O, and Si/O [106] show that the fits yield the $\delta^{Ne/O}$, $\delta^{Mg/O}$ and $\delta^{Si/O}$ are fully compatible with each other and different from zero by more than 5σ.

It can be concluded that, above 86.5 GV, the rigidity dependence of primary cosmic ray Ne, Mg and Si is fluxes is different from the rigidity dependence of lighter primary cosmic

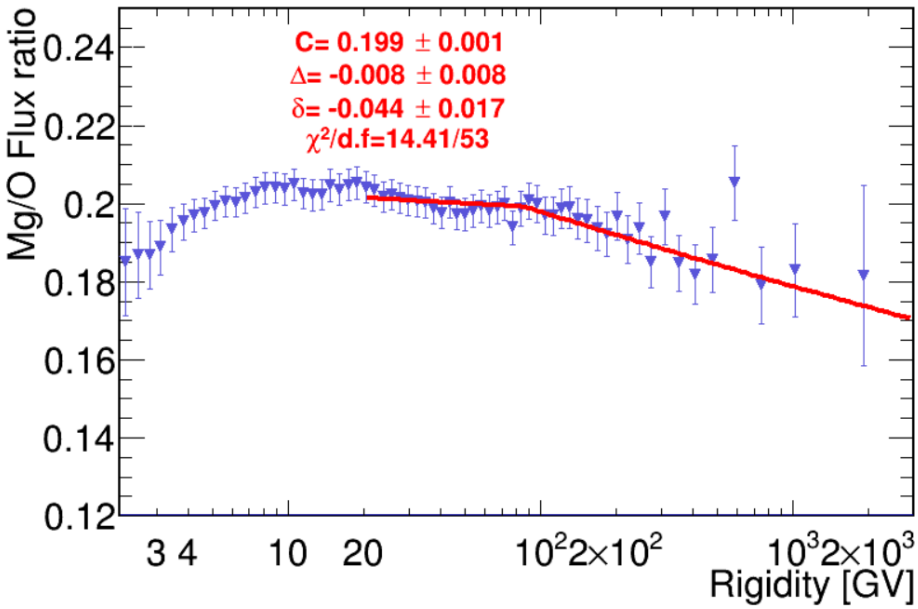

Fig. 3.60 Mg/O flux ratio with its total errors as function of rigidity. The solid curves show the fit results with equation 3.38. The fit result shows that the O and Mg fluxes have different rigidity dependence from rigidity above 86.5 GV

ray He, C, and O. This shows that the Ne, Mg, and Si and He, C, and O are two different classes of primary cosmic rays.

Chapter 4

Cosmic-ray Aluminum nuclei flux measurement

Aluminum (Al) nuclei in cosmic rays are thought to be produced both in astrophysical sources and by the collisions of heavier nuclei with the interstellar medium [118, 119, 45]. Precise knowledge of the rigidity dependence of the Al flux provides important information on the cosmic ray production and propagation. And as mentioned in Section 1.3 of Chapter 1, with the Al/Mg flux ratio, the energy dependence of the cosmic-ray residence time can be quantitatively examined. The Aluminum nuclei flux as a function of rigidity has been measured using the same rigidity binning and data set that were used for the measurement of the Mg nuclei flux to obtain the Al/Mg flux ratio.

In this chapter, the precision measurement of the Al flux in the rigidity range from 2.15 GV to 3.0 TV based on 0.5 million Al nuclei collected by AMS-02 during its first 8.5 years (May 19, 2011 to October 30, 2019) of operation aboard the International Space Station will be presented.

4.1 Event Selection and Event Counts

Same as the Mg analysis, the latest version of reconstructed Data (version *B1130 pass7*) and Al MC (version *B1220*) are used in this analysis.

Event Selection

The event selection for Al is based on the same set of cuts used for Mg, with only the charge cuts adapted to select nuclei compatible with Z=13:

- Tracker L1 charge Q[11.5326 , 13.8379] for Data, and L1 Q>11.5326 for MC

- Inner Tracker charge Q[12.52 , 13.48]
- UTOF Q[12.285 , 14.5]
- LTOF Q>12.285 for FS analysis
- Tracker L9 charge [12.2876 , 14.4674] for FS analysis only

Event counts and rates

Given that the Al nuclei are collected in the same time period (8.5 years, from May 19, 2011 to October 30, 2019) as Mg, the Al exposure time is also the same as Mg shown in Section 3.2 of Figure 3.3.

During the first 8.5 years of operation, the AMS-02 detector has collected 0.5 million Al nuclei events. Figure 4.1 shows the Al raw event counts and rates for L1Inner and FS geometries.

Below L1 background and L1 charge cut inefficiency

Similar to the Mg nuclei analysis discussed in Section 3.3.2 of Chapter 3, the below L1 background for Al nuclei is a residual background from the interactions of heavier nuclei such as Si, S and P in the material between Tracker L1 and L2, which is evaluated by fitting the Al L1 charge distribution with charge templates of Si, S and P nuclei. Compared to Mg, the major challenge in the Al nuclei measurement is the background evaluation because the neighboring nuclei Mg and Si are around 6 times more abundant than Al, and may contaminate the Al sample.

Figure 4.2 and 4.3 shows the Al Tracker L1 charge template fit result in one of the 42 rigidity bins and the below L1 background for Al as a function of rigidity. The residual background from the interactions of Si in the material between Tracker L1 and L2 is between 7%-15%. While as discussed in Section 3.3.2, the below L1 background for Mg is negligible (less than $\sim 0.3\%$) over the entire rigidity range.

The L1 charge cut inefficiency for Al nuclei ε_{L1Q} was estimated on Data using the same method applied to Mg, from Al L2 non-interacting samples. The result is shown in Figure 4.4, and it is found to be similar to the Mg result ($\sim 97\,\%$).

Top of the instrument background

In the case of Al nuclei, the top of the instrument background is due to nuclei heavier than Al, mainly Si and S, interacting in materials above Tracker L1. Similar to the evaluation for

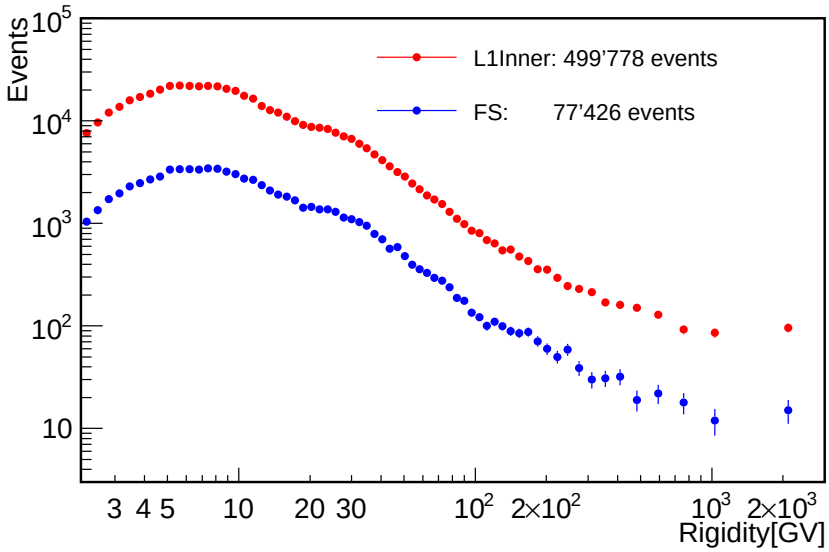

(a) Al event counts

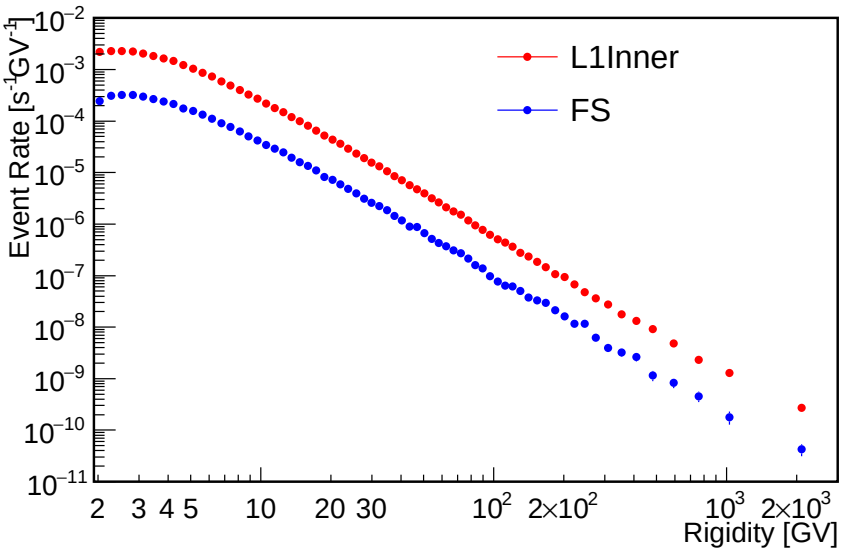

(b) Al event rate

Fig. 4.1 The AMS-02 8.5 years Al event counts (top) and event rates (bottom) as functions of rigidity. The red points show L1Inner result, the blue points show FS result.

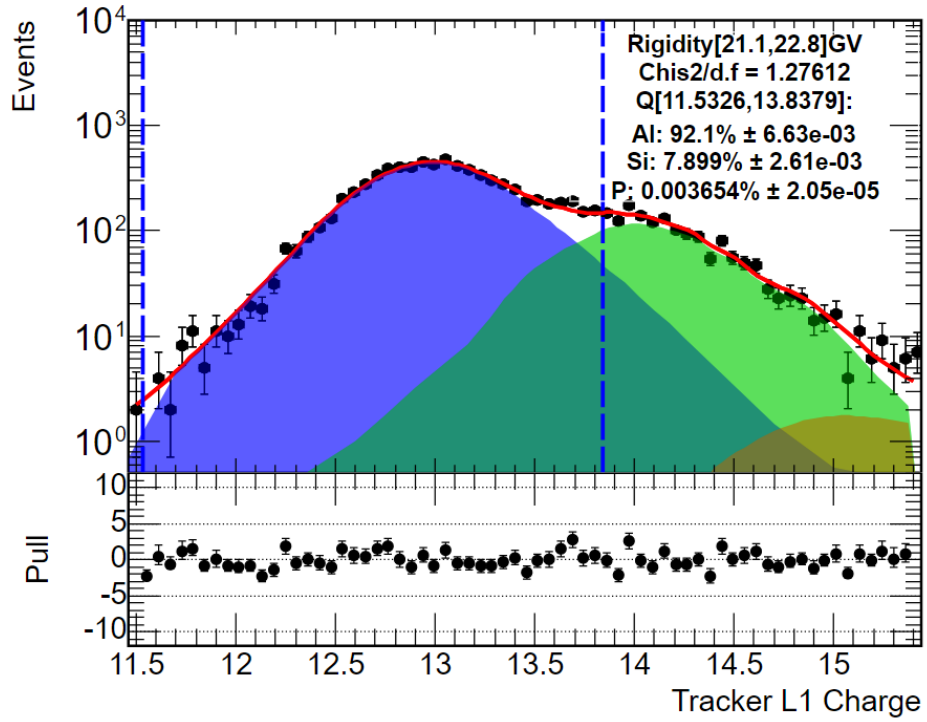

Fig. 4.2 Tracker L1 charge distribution for charge Z=13 sample selected using UTOF and Inner Tracker in the rigidity range between 21.1 and 22.8 GV (black points). The solid red curve shows the fit using Al, Si, and P PDFs. The PDF templates are obtained from L2 non-interacting samples. The vertical dashed lines show the charge selection cuts applied to L1. In this rigidity range, the below L1 background arising from Si nuclei contaminating the Al sample is 7.899%.

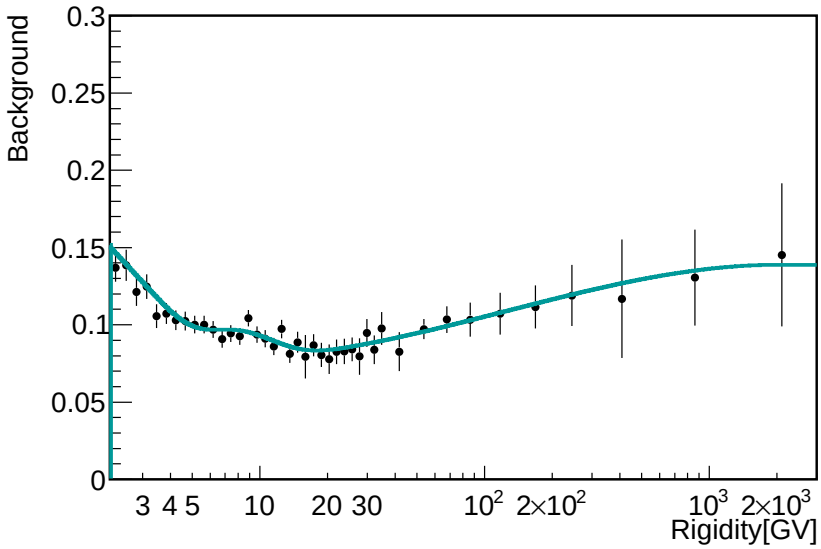

Fig. 4.3 Al below L1 background due to the interactions of heavier nuclei in the material between Tracker L1 and L2 as a function of rigidity. This background varies smoothly from $\sim 9\%$ at 10 GV to $\sim 15\%$ at 2 GV and 3 TV.

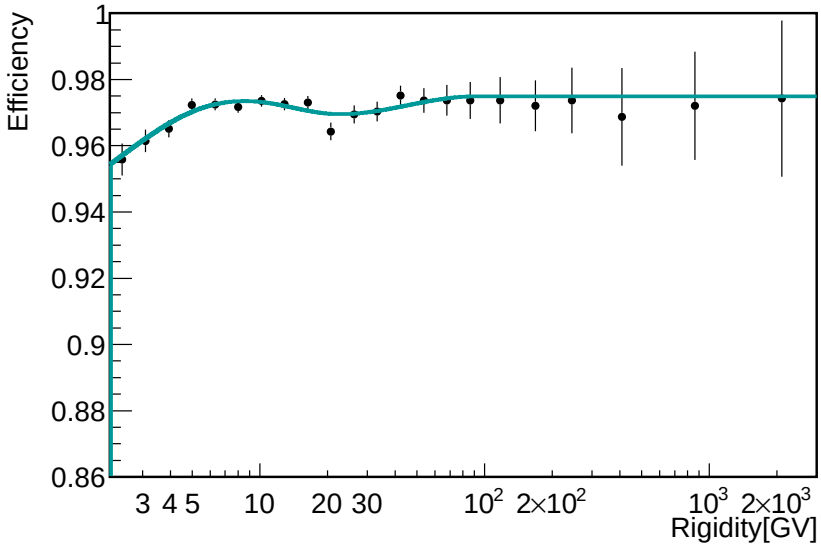

Fig. 4.4 Al Data Tracker L1 charge cut inefficiency ε_{L1Q} as a function of rigidity. ε_{L1Q} is calculated from Al L2 charge template obtained from the Tracker L2 charge distribution of unfragmented Al sample.

Mg nuclei discussed in Section 3.3.2 of Chapter 3, the the top of the instrument background correction for Al nuclei is evaluated by $\sum_{\mathrm{Si,S}} \frac{\Phi_X}{\Phi'_{\mathrm{Al}}} \frac{A_{X\to\mathrm{Al}}}{A_{\mathrm{Al}}}$, where Φ'_{Al} is the background contaminated Al flux, Φ_X is the flux of heavier nuclei X such as Si and S, A_{Al} is the Al effective acceptance, and $A_{X\to\mathrm{Al}}$ is the the effective acceptance of heavier nuclei X fragmenting to Al.

This background (Figure 4.5) is found to be $\sim$ 6 % at 100 GV which is around 6 time larger compared to the result form Mg.

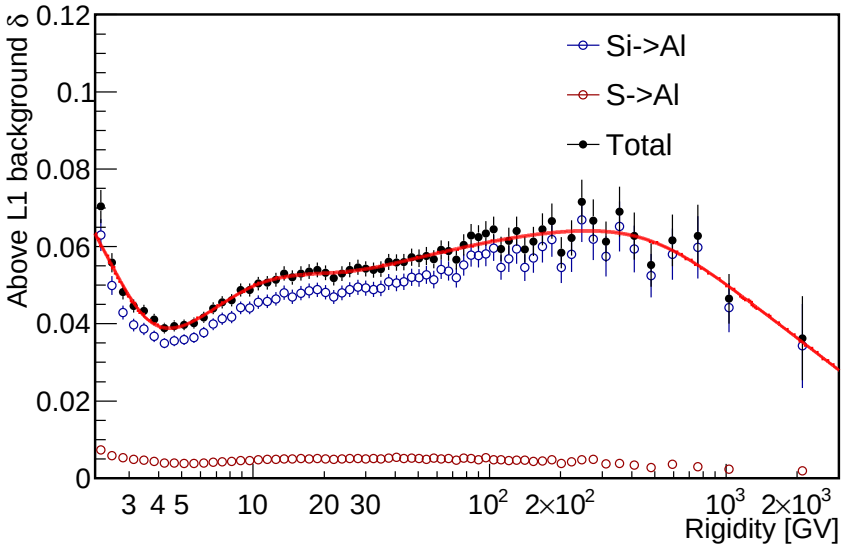

Fig. 4.5 Al top of the instrument background as a function of rigidity (black points) arising from interaction of nuclei heavier than Al with the thin material above Tracker L1. The main contributions come from Si (blue points) and S (red points) nuclei interactions. The red solid curve shows the spline fit to the total background.

DAQ efficiency

Al and Mg have similar charge and mass, and they create similar event size in DAQ system, so the DAQ efficiency results are similar. But the Al result has large error due to the statistics (Figure 4.6).

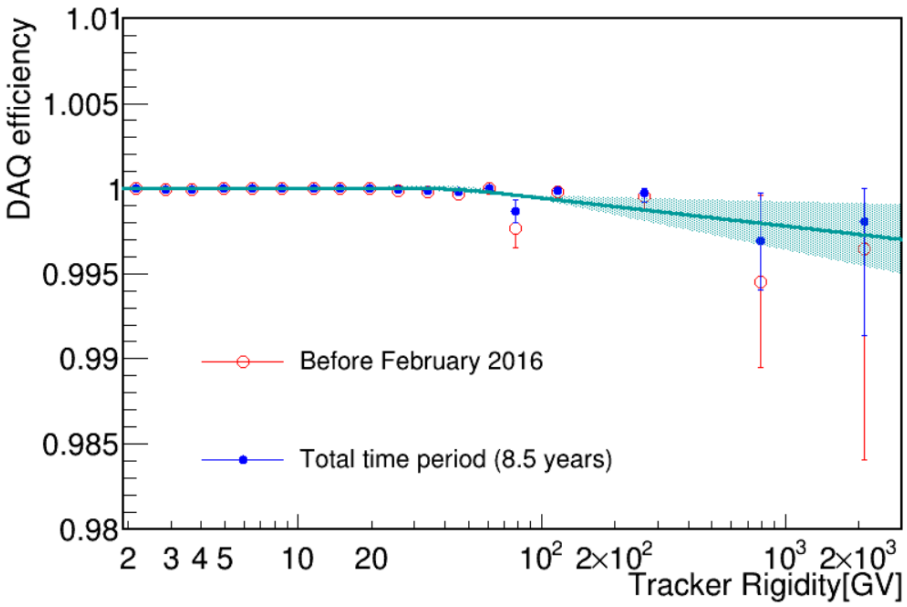

Fig. 4.6 Al 8.5 years DAQ efficiency as a function of rigidity (blue solid points) and its parametrization (light green curve). For reference, the red points show the DAQ efficiency before February 2016 with the old DAQ setting.

4.2 Effective acceptance

4.2.1 MC effective acceptance

Similar to the Mg analysis, the total number of MC generated events is counted directly from full MC simulation and then distributed into the rigidity bins following 1/R. For the latest version of Al MC (version B1220), the number of MC generated events is 8'709'578'752 for L1 focused MC, and 8'932'601'856 for L19 focused MC. Figure 4.7 shows the Al MC effective acceptance for L1Inner and FS geometries.

4.2.2 Data/MC corrections

Inner tracker efficiency

For Mg study, the Inner tracker reconstruction and charge efficiencies are evaluated together. While for Al, without requiring 7 layers of Inner Tracker, the contamination from Mg and Si in the sample could be large and bias the efficiency estimation.

To avoid the bias from contamination, reconstruction and charge efficiencies are evaluated separately.

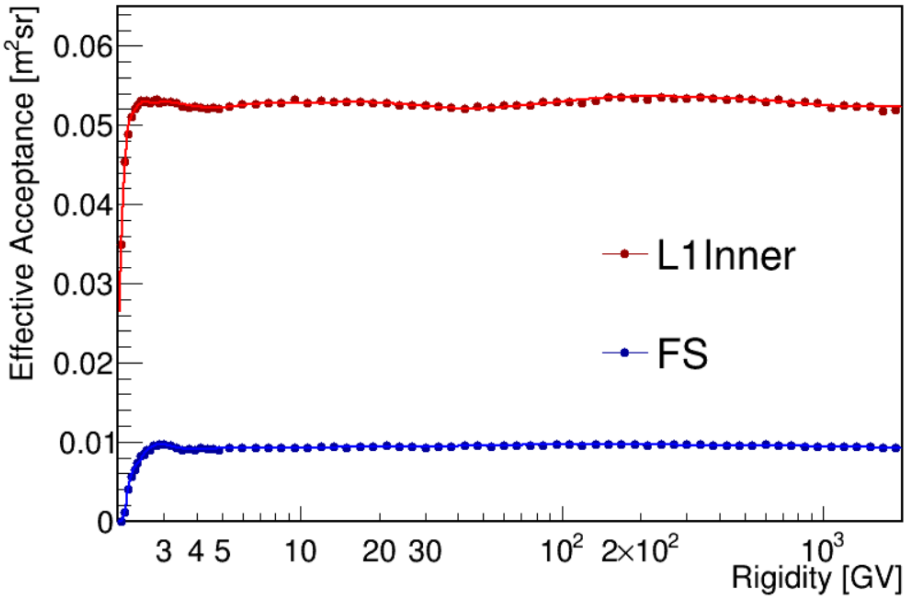

Fig. 4.7 Al MC effective acceptance as a function of rigidity for L1Inner (red points) and FS (blue points) geometries. The red and blue solid curves show the spline fit to L1Inner and FS results respectively.

- Inner tracker reconstruction efficiency evaluates the probability that the event has a well reconstructed Inner Tracker track. This efficiency is not affected by the contamination since it does not depend on the charge value.
- Inner tracker charge efficiency evaluates the probability that the event which has a well reconstructed Inner Tracker track has the charge measured by tracker compatible with the charge of a Al nucleus (Z=13). The charge efficiency is just a charge cut efficiency, and it is estimated on a clean sample obtained by requiring tight charge cuts on Tracker L1, the 4 layers of TOF and Tracker L9.

The inner tracker reconstruction efficiency is estimated on an Al sample selected by the following cuts:

- bad runs removal, SAA and RTI cut, requiring physical trigger
- TOF standalone built by requiring TRD Track matched with TOF Track
- good unbiased TOF β
- TOF and TRD track extrapolation within the Tracker L1-L9 fiducial volume
- unbiased X- and Y- side hits on Tracker L1 and L9 (for FS study)

- unbiased Tracker L1 charge cut Q[11.8,14.4], and good charge status
- tight charge cuts on the unbiased charge of 4 TOF layers
- unbiased Tracker L9 charge cut Q[12.2876 , 14.4674] (for FS)

The inner Tracker reconstruction efficiency is obtained requiring that the selected events have a well reconstructed track, matching the TOF track, and charge measured by Inner tracker greater than 10.5.

Figure 4.8 shows the Inner Tracker reconstruction efficiency where the TOF unbiased β and the rigidity cutoff R_c as rigidity estimators. The Data to MC efficiency ratio is calculated with β estimator for R<6.4 GV, and R_c estimator for rigidity between 6.4 GV and 20 GV. Since the estimator is only valid up to 20 GV, the ratio is assumed to be constant at higher rigidity, and the error band of the parametrization result is calculated from the slope of the MC efficiency function of the generated rigidity.

The Inner tracker charge efficiency is estimated on a sample of Al selected by the Al nuclei event selection without the Inner Tracker charge cut. To minimize the contamination, tight charge cuts on Tracker L1, the 4 layers of TOF and Tracker L9 have been required. The Inner tracker charge efficiency is obtained requiring that the selected events have the Inner tracker charge compatible with an Al nucleus.

Figure 4.9 shows the Inner Tracker charge efficiency, the discrepancy between Data and MC is smaller than 1%. The product of Inner tracker reconstruction and charge efficiencies gives the total Inner Tracker efficiency.

TOF charge efficiency

The sample of the TOF charge efficiency is selected by the Inner Tracker and the Tracker external layers including L1 and L9 (for FS study) with tighter charge cuts. The TOF charge efficiency is then evaluated counting the events that pass UTOF and LTOF (for FS study) charge cuts. Without requiring the charge cuts of 4 layers of TOF, the sample of Al TOF charge efficiency is contaminated by Si and Mg. The contamination can be estimated from MC by mixing Mg, Al and Si MC in a proportion similar to their natural abundance, that is Mg:Al:Si=5:1:4.55. Figure 4.10 shows the composition of TOF charge efficiency sample estimated form MC mixture, The contamination from Si contributes for around 30%.

Considering that the charge of Al nuclei is in between that of Mg and Si, it is reasonable to assume that the TOF charge efficiency for Al is also in between the values for Mg and Si. Therefore, Al TOF charge efficiency can be estimated as the average of Mg and Si TOF charge efficiencies. Mg TOF charge efficiency has been obtained in Section 3.5.4, and Si

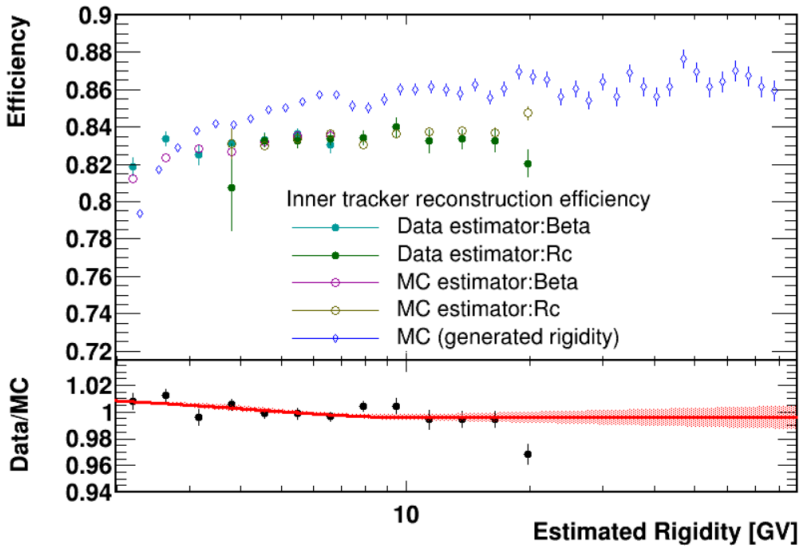

(a) L1Inner

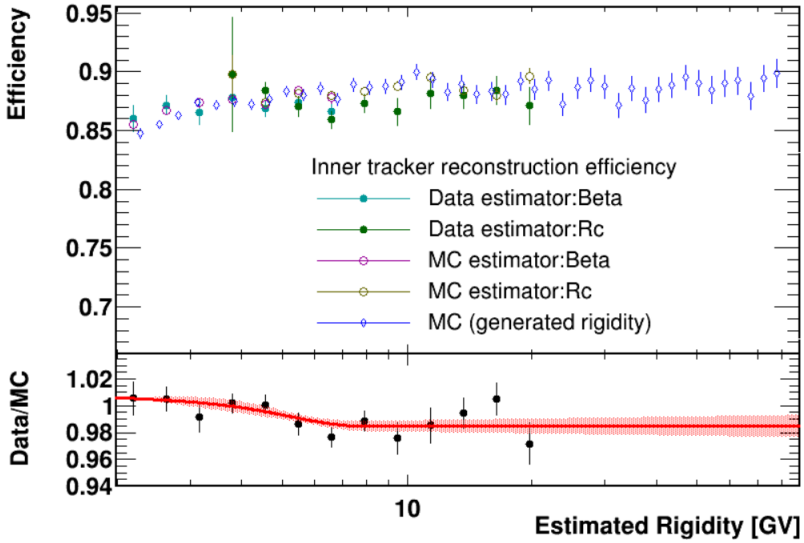

(b) FS

Fig. 4.8 Al Inner Tracker reconstruction efficiency as a function of rigidity for L1Inner (top) and FS (bottom) geometries. In the upper panel of the plots, The solid points show Data Inner Tracker efficiency as functions of estimated rigidity obtained from TOF β (cyan points) and R_c (green), open red and yellow points show the MC result with β and R_c estimator respectively. For reference, the blue points show the MC efficiency as a function of the generated rigidity. The lower panel shows the ratio between Data and MC efficiencies (black points) and the spline fit on the efficiency ratio of 68% C.L intervals. For rigidities above 20 GV, the error band of the spline fit is calculated from the slope of the MC generated efficiency. The ratio is calculated with β estimator for R$<$ 6.4 GV ,and R_c estimator for rigidity beteen 6.4 GV and 20 GV.

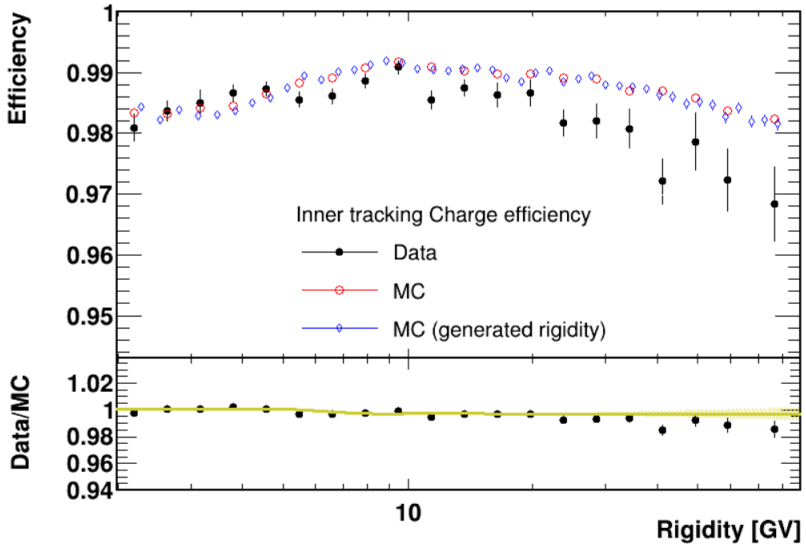

(a) L1Inner

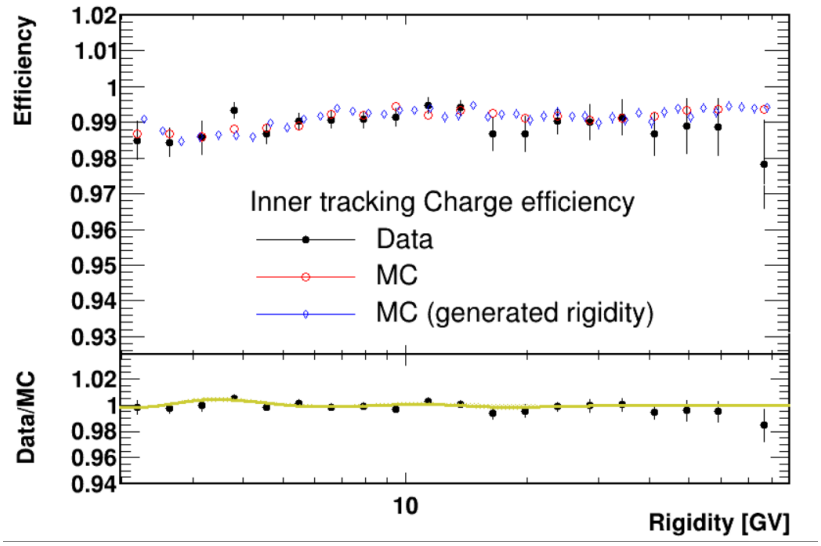

(b) FS

Fig. 4.9 Al Inner Tracker charge efficiency as a function of rigidity for L1Inner (top) and FS (bottom) geometries. In the upper panel of the plots, The black points show Data TOF charge efficiency, the red points show the MC result (function of reconstructed rigidity), and the blue points show the MC efficiency as function of the generated rigidity. The lower panel shows the ratio between Data and MC efficiencies (black points) and the spline fit on the efficiency ratio of 68% C.L intervals. For rigidities above $\sim$ 20 GV, the error band of the spline fit is calculated from the slope of the MC efficiency as a function of the generated rigidity.

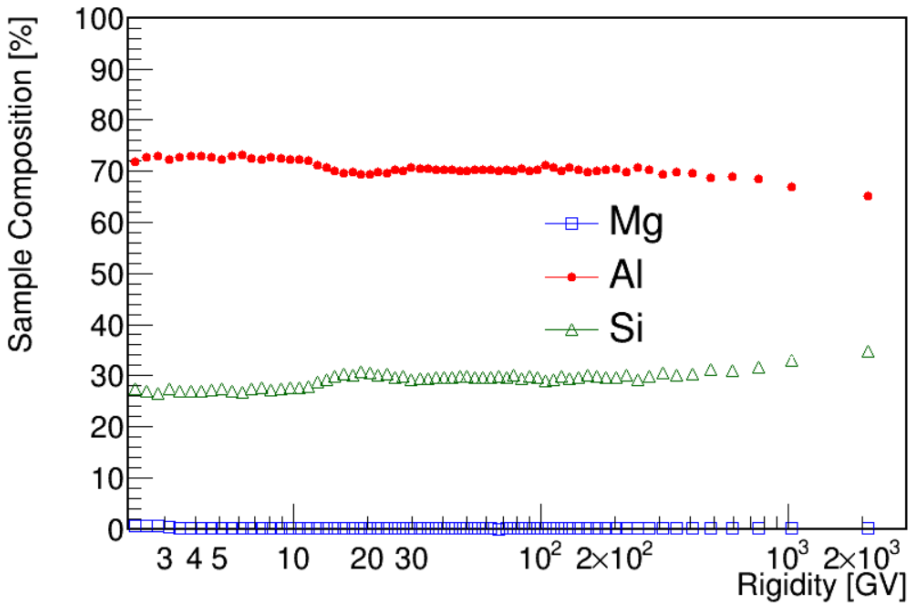

Fig. 4.10 Composition of the Z=13 sample selected by the Inner Tracker and the Tracker L1 with tighter charge cuts, estimated from MC by mixing Mg, Al and Si MC in a proportion reflecting their natural abundance, i.e. Mg:Al:Si=5:1:4.55. The Al signal (Red points) in the sample contributes for about 70%, and the contamination from Si (green points) amounts to 30%.

result can be evaluated the same way as Mg. Figure 4.11 shows Al TOF charge efficiency estimated with the average of Mg and Si results.

Trigger efficiency

Al trigger efficiency is estimated in the same way as TOF charge efficiency. Figure 4.12 shows Al trigger efficiency estimated as the average of Mg and Si results.

Overall correction

The other efficiencies including Tracker L1 BZ, Tracker L1 pick-up and Tracker L9 efficiencies are evaluated in the same way as for the Mg study.

Figure 4.13 shows the overall Al Data/MC efficiency correction. The overall corrections of Al for L1Inner and FS geometries are found to be $\sim$ 5% larger than those of Mg as discussed in Section 3.5 of Chapter 3, due to larger contamination in Al Data sample.

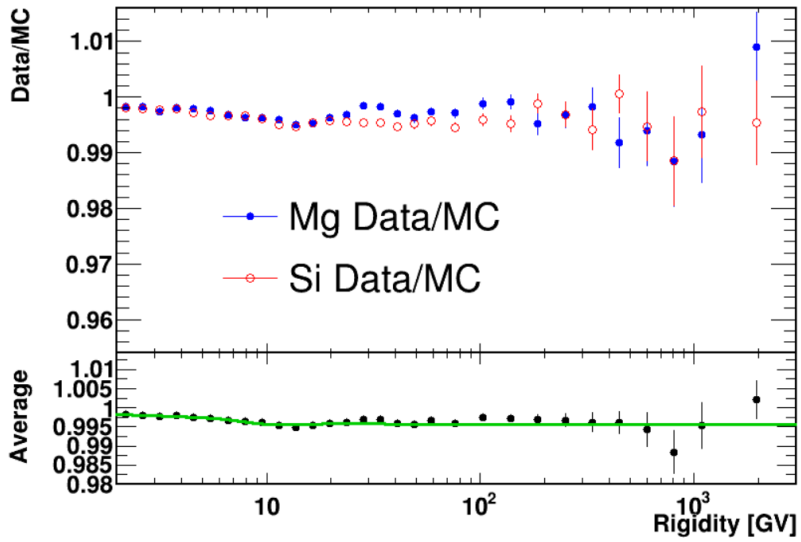

(a) L1Inner

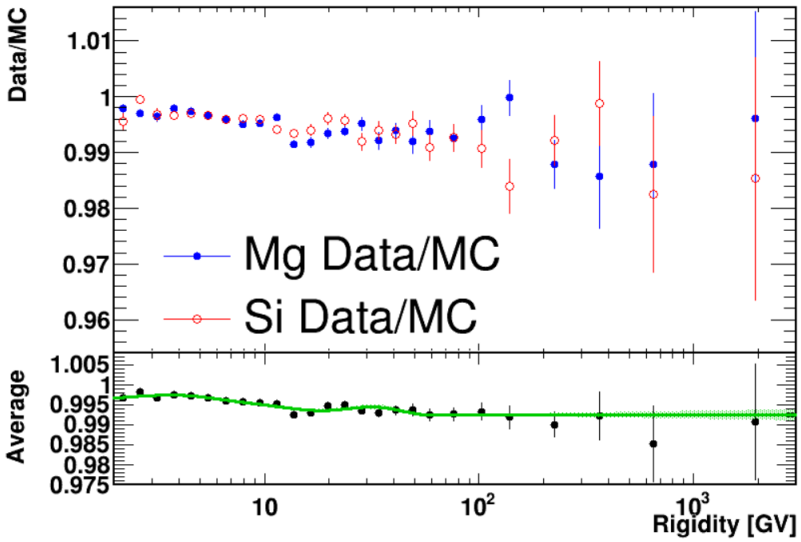

(b) FS

Fig. 4.11 Al TOF charge Data/MC efficiency ratio (bottom panel) evaluated as the average of Mg (blue points) and Si (red points) efficiencies as a function of rigidity for L1Inner (top) and FS (bottom) geometries. The lower panels show the Data/MC efficiency ratios, and the spline fit of the average of the Mg and Si efficiencies.

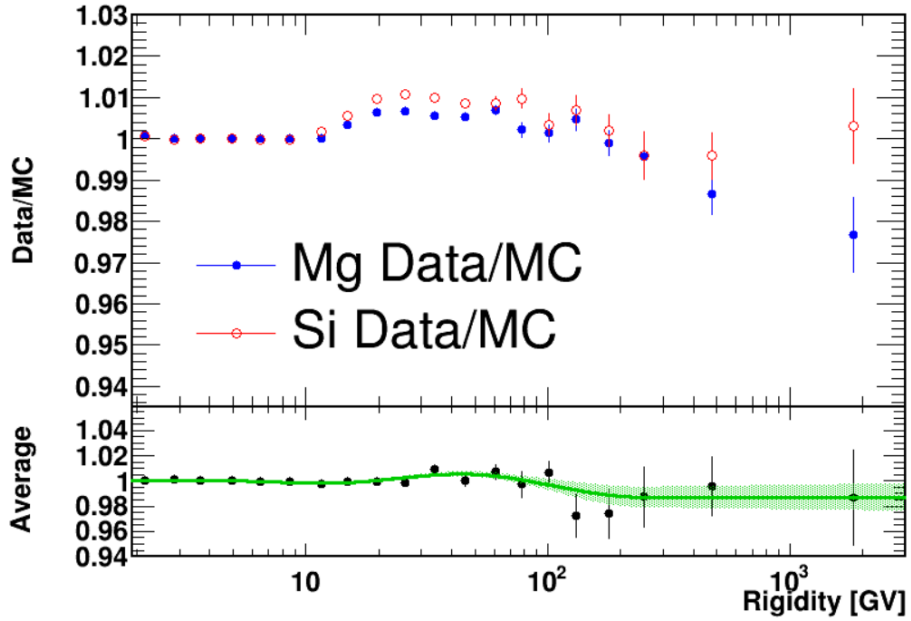

Fig. 4.12 Al trigger Data/MC efficiency ratio (bottom panel) evaluated as the average of Mg (blue points) and Si (red points) efficiencies as a function of rigidity. The green curve shows the spline fit to the average efficiencies.

4.3 Unfolding

The 2D rigidity resolution a function for Al nuclei is constructed following the same method described for Mg nuclei. Figure 4.14 shows the rigidity dependence of the σ of core Gaussian. The MDR for Al nuclei is 1.30 TV for L1Inner, and 2.86 TV for FS, similar to those found for Mg nuclei.

The unfolded Al L1Inner and FS fluxes are obtained by applying L1Inner and FS combined forward unfolding procedure. Figure 4.15 shows the Al unfolding factor, and Figure 4.16 shows the Al unfolded flux with statistical error.

Based on previous cross section and survival probability studies, the cross section has been well tuned according to the Data in the latest F, Na and Al MC, so that additional flux normalization correction is not needed for Al flux.

4.4 Flux error

The systematic error of Al flux includes errors from the absolute rigidity scale, the resolution function, the unfolding procedure, acceptance, DAQ efficiency, and L1 charge inefficiency.

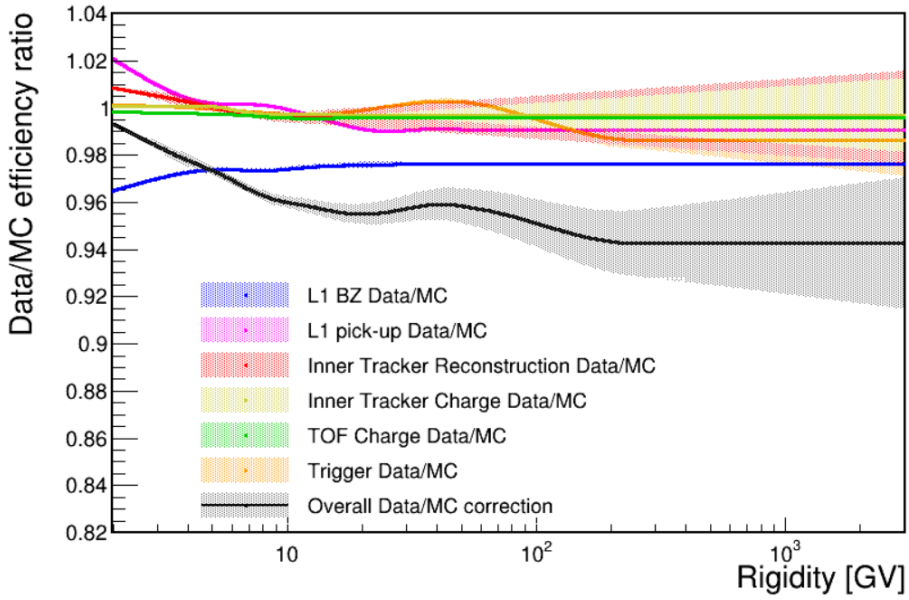

(a) L1Inner

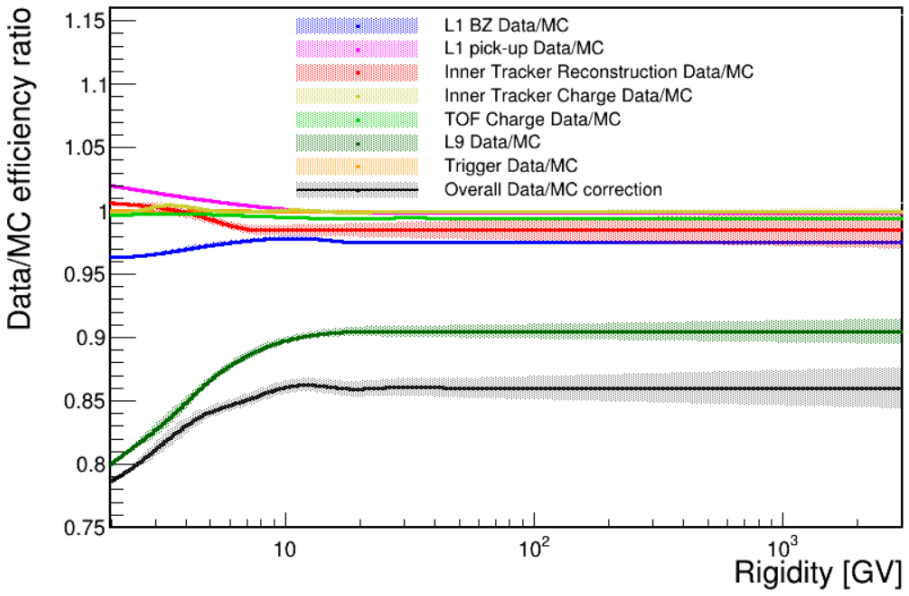

(b) FS

Fig. 4.13 Al overall Data/MC efficiency correction (black curve) as a function of rigidity for L1Inner (top) and FS (bottom,) geometries, together with the break-down of the overall correction including L1 BZ, L1 pick-up, Inner Tracker, TOF charge, and L9 (for FS) Data/MC efficiency ratios.

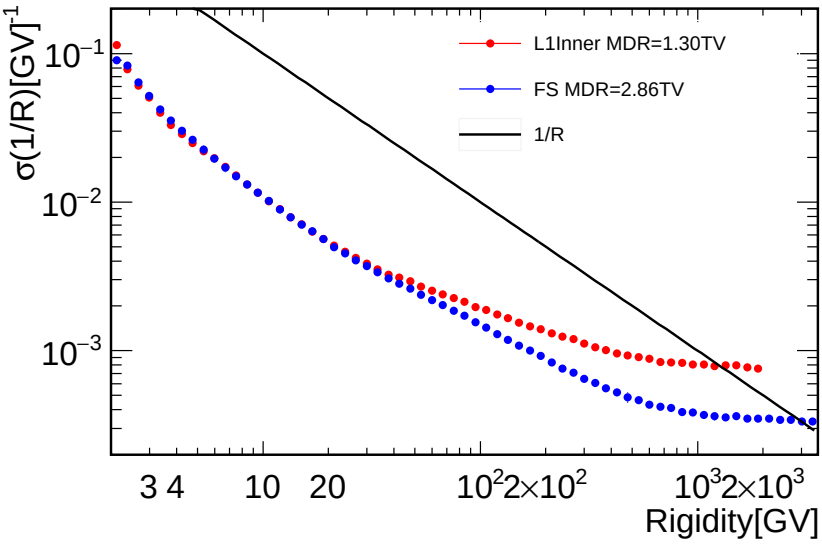

Fig. 4.14 Rigidity resolution for Al nuclei: σ_1 of core Gaussian as a function of the generated rigidity for L1Inner (red points) and FS (blue points). The black line shows the 1/R function. The MDR as the intercept between the σ_1 of the core Gaussian and 1/R, which is found to be 1.30 TV for L1Inner and 2.86 TV for FS.

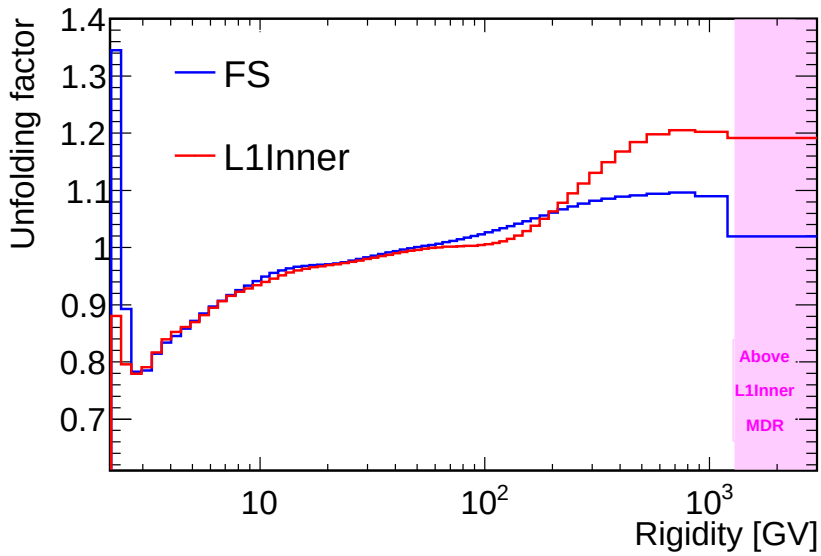

Fig. 4.15 Al unfolding factor as a function of the generated rigidity for L1Inner (red) and FS (blue). The shaded magenta area is the rigidity region above L1Inner MDR.

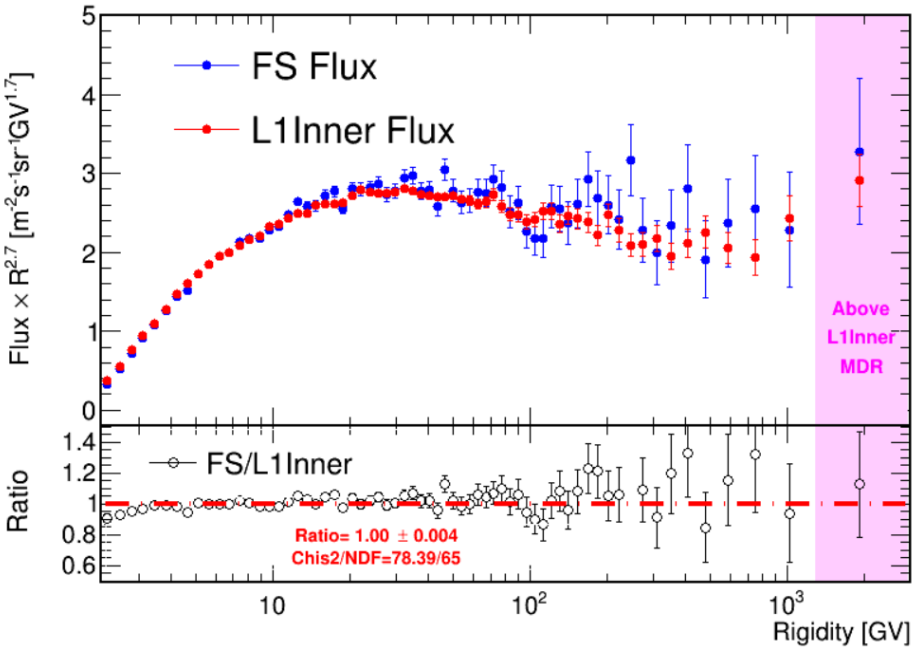

Fig. 4.16 Al unfolded flux with statistical error as functions of rigidity multiplied by $R^{2.7}$ for L1Inner (red points) and FS (blue points). The lower panel shows the ratio between FS and L1Inner unfolded flux (black points), and a fit to a constant value (red dashed line). The magenta shaded area is the rigidity region above L1Inner maximum detectable rigidity (MDR).

The contribution of individual sources of the systematic error have been evaluated and added in quadrature to obtain the total systematical error.

The flux value and associated error in the last rigidity bin is taken from the FS result, while below 1.2 TV, flux values and errors are taken form the L1Inner result. Figure 4.17 shows the total error of Al flux and its error break down. At 100 GV, Al flux has around 5% relative error.

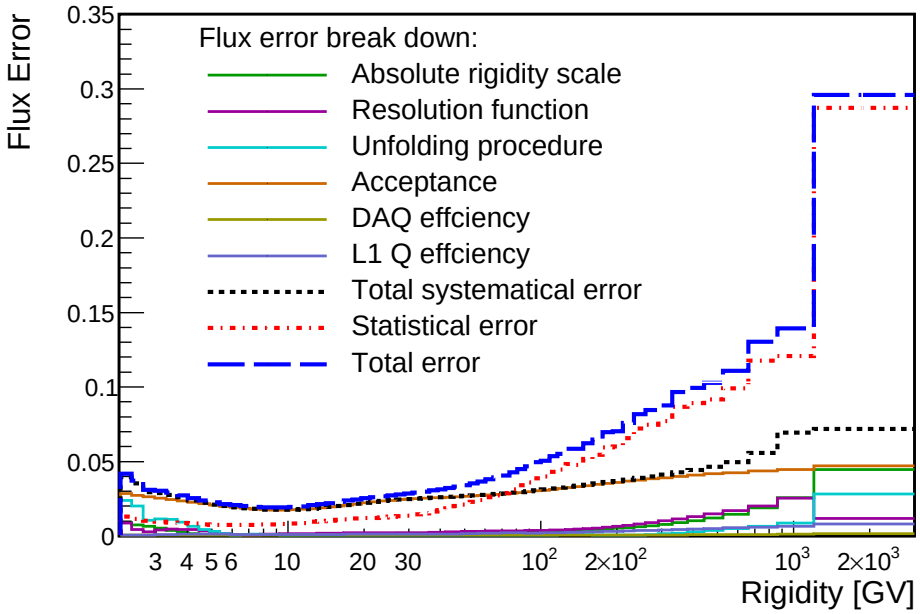

Fig. 4.17 Al flux error break down including total error (blue dashed line), statistical error (red dashed line), total systematic error (black dashed line), and the components of the systematic error (solid lines).

4.5 Al nuclei flux

4.5.1 8.5 years Al flux

The Al flux (multiplied by $R^{2.7}$) with total error and its spectral index in the rigidity range from 2.15 GV to 3 TV with 0.5 million Al nuclei events collected by AMS during the first 8.5 years operation from May 19, 2011 to October 30, 2019 are shown in Figure 4.18. The variation of the Al nuclei flux spectral indices with rigidity is obtained in a model independent way from $\gamma = \mathrm{d}[\log(\Phi)]/\mathrm{d}[\log(R)]$ over non-overlapping rigidity intervals bounded by 7.09, 12.0, 16.6, 28.8, 45.1, 80.5, 211.0, and 3000.0 GV. Similar to the Mg nuclei flux, the

Al flux deviates from a single power law, and the spectral index hardens with increasing rigidity above $\sim$ 200 GV.

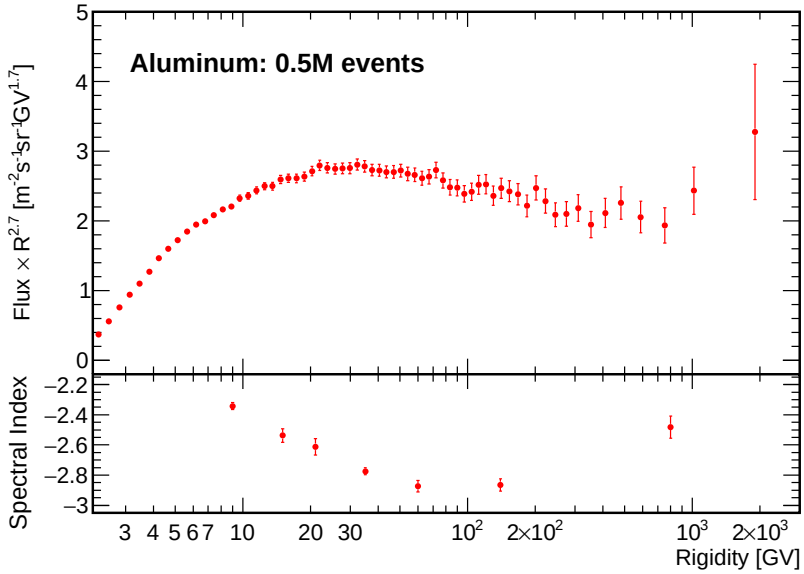

Fig. 4.18 Al nuclei flux with total error in the rigidity range from 2.15 GV to 3 TV with 0.5 million Al nuclei events collected by AMS during the first 8.5 years operation from May 19, 2011 to October 30, 2019. The upper panel shows the Al nuclei flux multiplied by $R^{2.7}$, the lower panel shows the spectral index.

Over the last 50 years, few cosmic ray experiments have measured the Al flux in kinetic energy up to $\sim$ 150 Gev/n [57, 58]. The measurements errors exceed 50% at 50 GeV/n. AMS Al flux is the first and the only measurement in rigidity. To compare with earlier measurements, the rigidity measured by AMS is converted to kinetic energy per nucleon by assuming Al nuclei in Al flux is mainly composed by $^{27}_{13}$Al [57, 58, 120].

Figure 4.19 shows the AMS Al nuclei flux as a function of kinetic energy per nucleon E_k multiplied $E_k^{2.7}$ together with earlier measurements [57, 58]. The total error of AMS 8.5 years Al flux is $\sim$ 5% at 100 GV ($\sim$ 50 Gev/n).

Four independent Al flux analyses were performed within the AMS Collaboration by groups from the University of Geneva (this work), MIT, INFN-Bologna and IHEP. As shown in Figure 4.20, the four results are compatible with each other. This work has contributed to the paper [121].

4.5.2 Discussion of the Al nuclei flux result

As mentioned in Section 1.4 of Chapter 1, previous AMS measurement [83] showed that the N nuclei flux is well described over the entire rigidity range by the sum of the primary

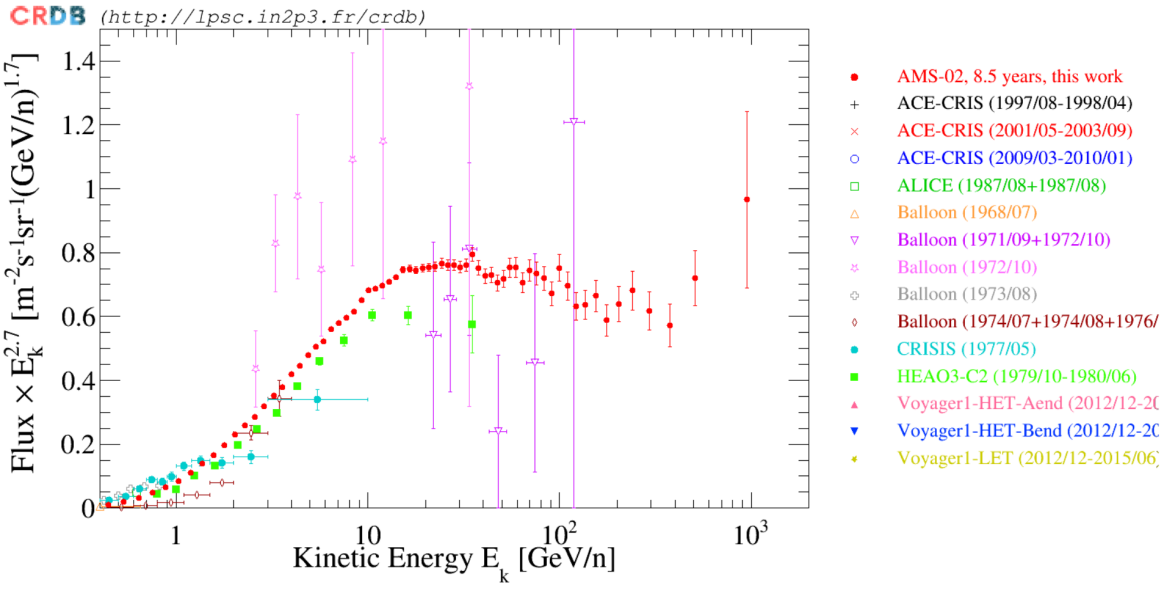

Fig. 4.19 Al flux as a function of kinetic energy per nucleon E_k multiplied $E_k^{2.7}$ together with earlier measurements [57, 58].

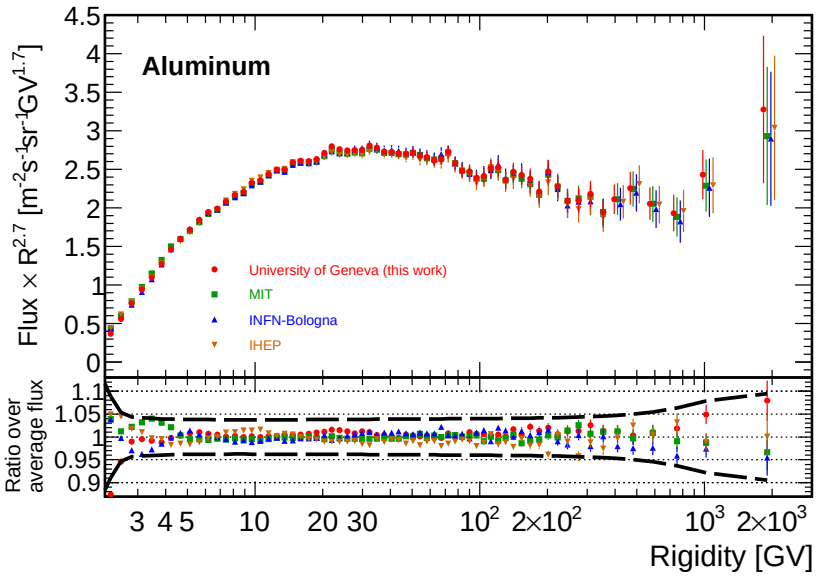

Fig. 4.20 Comparison of 8.5 years Al nuclei flux resulting from the independent analysis carried out at the University of Geneva (this work, red points), MIT (green squares), INFN-Bologna (blue up-triangles), and IHEP (orange down-triangles). The lower panel shows the ratio between each result and the average, together with the average of systematical error band.

flux and the secondary flux, and its fraction of primary component increases with rigidity. Similar to N, Al nuclei in cosmic rays are also thought to be produced both in astrophysical sources, and by the collisions of heavier nuclei with the interstellar medium.

To obtain the fractions of the primary Φ^P_{Al} and secondary Φ^S_{Al} components in Al nuclei flux $\Phi_{Al} = \Phi^P_{Al} + \Phi^S_{Al}$, a fit of Φ_{Al} to the weighted sum of a heavy primary cosmic ray flux and of a heavy secondary cosmic ray flux was performed above 5 GV. The Si flux (Φ_{Si}) and the F flux (Φ_F) are used as templates for the primary and secondary components respectively.

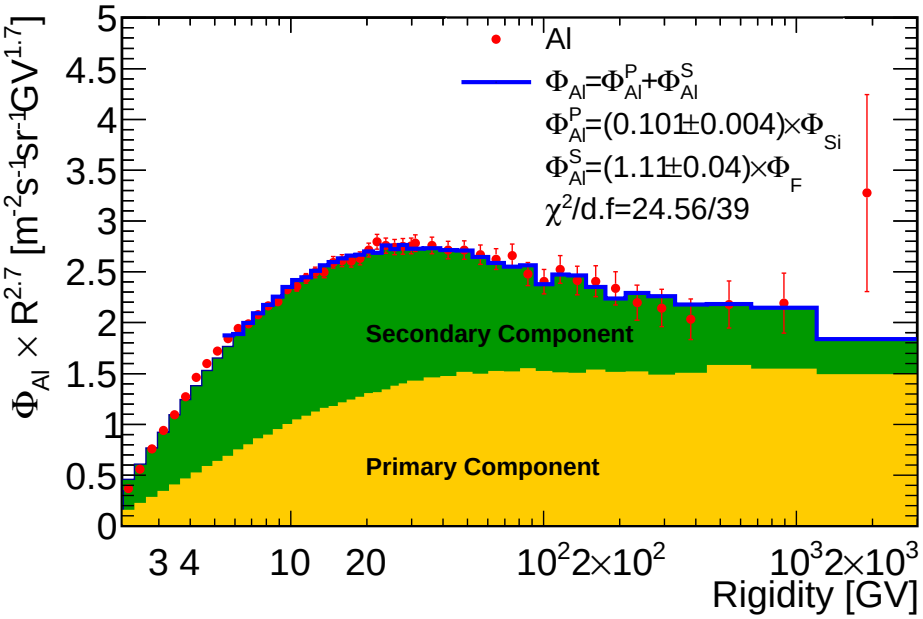

Fig. 4.21 Al flux Φ_{Al} fit to the weighted sum of Si flux Φ_{Si} and F flux Φ_F above 5 GV, i.e. $\Phi_{Al} = \Phi^P_{Al} + \Phi^S_{Al}$. The yellow shaded area shows the contribution of the primary component, the green area shows the contribution of the secondary component. To reduce statistical fluctuations, for rigidity above 28.8 GV, every two bins have been merged into one bin.

As shown in Figure 4.21, the fit yields $\Phi^P_{Al} = (0.101 \pm 0.004) \times \Phi_{Si}$ and $\Phi^S_{Al} = (1.11 \pm 0.04) \times \Phi_f$ with $\chi^2/d.f = 14.56/39$. Similar to what observed for N flux [83], the contribution of the secondary component in Al flux (Figure 4.22) decreases with increasing rigidity, while the contributions of the primary component increases with rigidity.

The latest measurement of Na flux observed the same behavior as N and Al. It can be concluded that N, Na, and Al belong to a distinct group and are combinations of primary and secondary cosmic rays [121].

Together with the measurement of light nuclei from He to F introduced in Chapter 1, and Ne Mg Si discussed in Chapter 3, AMS has measured the fluxes of cosmic nuclei as a

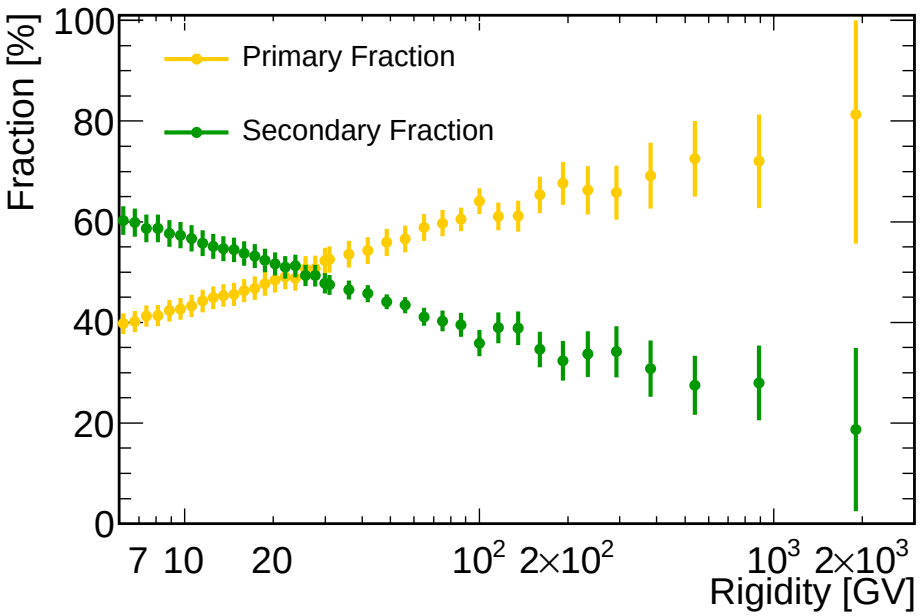

Fig. 4.22 The fractions of primary (yellow line) and secondary (green line) components of Al flux. The results are obtained by fitting Al flux Φ_{Al} to the weighted sum of Si flux Φ_{Si} and F flux Φ_F above 6 GV. To reduce statistical fluctuations, for rigidity above 28.8 GV, every two bins have been merged into one bin.

function of rigidity from $Z = 2$ to $Z = 14$. The observation shows that there are two classes of primary cosmic rays, He-C-O and Ne-Mg-Si, and two classes of secondary cosmic rays, Li-Be-B and F. Moreover, N, Na, and Al, belong to a distinct group and are combinations of primary and secondary cosmic rays.

Chapter 5

Cosmic ray age and Be/B and Al/Mg flux ratios: a feasibility study

5.1 Introduction

As mentioned in Section 1.3 of Chapter 1, the fluxes of radioactive secondary cosmic-ray isotopes such as ^{10}Be and ^{26}Al are the tools to study the cosmic-ray residence time t_{esc}. However, due to the limitation of experimental techniques, isotopes can only be measured up to $\sim$ 20 GV. AMS is able to measure charged nuclei fluxes up to the TV. The rigidity dependence of the cosmic-ray residence time t_{esc} can be extracted from the Be/B and Al/Mg decaying charge to decayed charge flux ratios.

In this work, t_{esc} is extracted in a model-independent approach based on several assumptions [122, 123], including secondary cosmic rays with the same rigidity propagate through the ISM in the same way, product nuclei have the same rigidity as primaries, and the relative composition of cosmic rays is uniform in time and space throughout the production process of secondaries. These assumptions yield that the ratio of local densities of two stable secondary cosmic-ray species approximately equal to the ratio of their net production rates:

$$\frac{n_a(R)}{n_b(R)} \approx \frac{Q_a(R)}{Q_b(R)} \tag{5.1}$$

where a and b denote two stable secondary cosmic-ray species, $n_a(R)$ is the rigidity dependent local densities of stable cosmic-ray species a, Q_a is the net production rate of species a, and same for species b. Note that the relation holds true in a wide context, and it is satisfied in many specific cosmic-ray propagation models such as the disc-halo diffusion models and the leaky-box model [123].

The cosmic-ray grammage

The local density $n_i(R)$ of a stable secondary cosmic-ray specie i such as B, F, and sub-Iron nuclei, can be retrieved from equation 5.1 with the following equation:

$$n_i(R) = Q_i(R) X_{esc}(R) \tag{5.2}$$

where $X_{esc}(R)$ is the cosmic-ray grammage which describes the column density of ISM traversed by the cosmic rays and has the unit of g/cm^2. $X_{esc}(R)$ is a key parameter to extract t_{esc}, and it is assumed to be independent of cosmic-ray specie.

The net production rate $Q_S(R)$ of a secondary cosmic-ray species is calculated by its production rate due to the spallation of its parent species P subtracted by the loss rate due to its own spallation with ISM:

$$Q_S = \sum_P \frac{\sigma_{P\to S}}{m} n_P - \frac{\sigma_S}{m} n_S \tag{5.3}$$

where n_P is the local density of the parent cosmic-ray specie P, $\sigma_{P\to S}$ is the spallation cross section of the parent nuclei P into the secondary nuclei S per ISM particle, σ_S is the total spallation cross section of S per ISM particle, m is the average ISM particle mass estimated to be $m \approx 1.3 m_p$, where $m_p \approx 0.938\,\mathrm{GeV}$ is the proton mass, by assuming the ISM is composed of 90% H and 10% He.

Combining equations 5.2 and 5.3 and expressing the local densities in terms of fluxes, the flux of a stable secondary cosmic-ray nuclei (S) can be calculated from the fluxes of parent nuclei (P) and the spallation cross sections:

$$\Phi_S = \frac{X_{esc} \sum_P \Phi_P \frac{\sigma_{P\to S}}{m}}{1 + X_{esc} \frac{\sigma_S}{m}} \tag{5.4}$$

From the above equation the cosmic-ray grammage X_{esc} can be extracted as

$$X_{esc} = \frac{\Phi_S}{\sum_P \Phi_P \frac{\sigma_{P\to S}}{m} - \Phi_S \frac{\sigma_S}{m}} \tag{5.5}$$

The ^{10}Be decay suppression factor f_{Be}

As shown in the Table 1.1 of Chapter 1, the radioactive secondary cosmic-ray ^{10}Be decays to ^{10}B. The decay suppression factor f_{Be} of ^{10}Be can be defined as:

$$f_{\mathrm{Be}} = \frac{\Phi_{^{10}\mathrm{Be}}}{\tilde{\Phi}_{^{10}\mathrm{Be}}} \tag{5.6}$$

where $\Phi_{^{10}\mathrm{Be}}$ is the observed ^{10}Be flux, and $\tilde{\Phi}_{^{10}\mathrm{Be}}$ is the ^{10}Be flux in the limit of infinite decay time, for which ^{10}Be are treated as stable nuclei.

By definition, the decay suppression factor f of a radioactive secondary cosmic-ray specie depends on the decay time of the nucleus t_d and the cosmic-ray residence time t_{esc}. It increases with the increasing t_d/t_{esc} and reaches the limit of $f = 1$ in the case of $t_d/t_{esc} \gg 1$. Since t_d is known, t_{esc} can be extracted from f.

Be is composed of the stable isotopes ^{7}Be and ^{9}Be and the radioactive isotope ^{10}Be. B is composed of two stable isotopes ^{10}B and ^{11}B, with part of ^{10}B coming from the decay of ^{10}Be. Using equation 5.6, the observed Be/B flux ratio can be expressed as:

$$\frac{\Phi_{\mathrm{Be}}}{\Phi_{\mathrm{B}}} = \frac{\Phi_{^{7}\mathrm{Be}} + \Phi_{^{9}\mathrm{Be}} + f\tilde{\Phi}_{^{10}\mathrm{Be}}}{\tilde{\Phi}_{^{10}\mathrm{B}} + \Phi_{^{11}\mathrm{B}} + (1 - f_{\mathrm{Be}})\xi\tilde{\Phi}_{^{10}\mathrm{Be}}} \tag{5.7}$$

where all fluxes are expressed as functions of rigidity. The correction factor ξ is applied to take into account that the daughter nuclei inherits the kinetic energy per nucleon of parent nuclei. For ^{10}Be decay, ξ is calculated by [122]

$$\xi = (5/4)^{1-\alpha_{^{10}\mathrm{Be}}} \tag{5.8}$$

where $\alpha_{^{10}\mathrm{Be}} = -\gamma_{^{10}\mathrm{Be}}$ with $\gamma_{^{10}\mathrm{Be}}$ the spectral index of ^{10}Be flux. Since the ^{10}Be flux is not available at high energy, $\alpha_{^{10}\mathrm{Be}}$ is estimated from the beryllium and boron nuclei fluxes with an iteration method [122]: $f^{(1)}$ is obtained by assuming $\alpha_{^{10}\mathrm{Be}}$ is equal to α_{Be}; then with α_{B} obtained from B nuclei flux, $\alpha_{^{10}\mathrm{Be}}$ is estimated to be $\alpha_{\mathrm{B}} - d\log f^{(1)}/d\log R$. Further iterations are not needed giving the fact that f is not sensitive to ξ, and ξ is not very sensitive to $\alpha_{^{10}\mathrm{Be}}$ neither.

Combining equation 5.4 and 5.7, the Be/B flux ratio can be written as [122]:

$$\frac{\Phi_{\mathrm{Be}}}{\Phi_{\mathrm{B}}} \approx \frac{\sum_P \Phi_P(\sigma^*_{P\to^{7,9}\mathrm{Be}}/m + f_{\mathrm{Be}}\sigma_{P\to^{10}\mathrm{Be}}/m)}{\sum_P \Phi_P(\sigma^*_{P\to\mathrm{B}}/m + (1 - f_{\mathrm{Be}})\xi\sigma_{P\to^{10}\mathrm{Be}}/m)} \tag{5.9}$$

where the cross section terms $\sigma^*_{P\to \mathrm{B}}/m$ and $\sigma^*_{P\to {}^{7,9}\mathrm{Be}}/m$ are calculated with the following formulas:

$$\frac{\sigma^*_{P\to \mathrm{B}}}{m} = \sum_{i=10,11} \frac{1 + X_{esc}\dfrac{\sigma_{^{10}\mathrm{Be}}}{m}}{1 + X_{esc}\dfrac{\sigma_{i\mathrm{B}}}{m}} \frac{\sigma_{i\mathrm{B}}}{m} \tag{5.10}$$

$$\frac{\sigma^*_{P\to {}^{7,9}\mathrm{Be}}}{m} = \sum_{i=7,9} \frac{1 + X_{esc}\dfrac{\sigma_{^{10}\mathrm{Be}}}{m}}{1 + X_{esc}\dfrac{\sigma_{i\mathrm{Be}}}{m}} \frac{\sigma_{i\mathrm{Be}}}{m} \tag{5.11}$$

with X_{esc} derived from the B flux using equation 5.5.

To obtain f_{Be}, the following two variables are defined from the cross sections and the fluxes:

$$\left(\frac{\Phi_{\mathrm{Be}}}{\Phi_{\mathrm{B}}}\right)_\infty = \frac{\sum_P \Phi_P \left(\dfrac{\sigma^*_{P\to {}^{7,9}\mathrm{Be}}}{m} + \dfrac{\sigma_{P\to {}^{10}\mathrm{Be}}}{m}\right)}{\sum_P \Phi_P \dfrac{\sigma^*_{P\to \mathrm{B}}}{m}} \tag{5.12}$$

$$\mathscr{K} = 1 + \frac{\sum_P \Phi_P \dfrac{\sigma^*_{P\to {}^{7,9}\mathrm{Be}}}{m}}{\sum_P \Phi_P \dfrac{\sigma_{P\to {}^{10}\mathrm{Be}}}{m}} \tag{5.13}$$

where $(\Phi_{\mathrm{Be}}/\Phi_{\mathrm{B}})_\infty$ is the Be/B flux ratio in the limit of infinite ^{10}Be decay time.

Finally, the decay suppression factor $f_{\mathrm{Be}} = \Phi_{^{10}\mathrm{Be}}/\tilde{\Phi}_{^{10}\mathrm{Be}}$ can be extracted from Be/B flux ratio (equations 5.5 to 5.13):

$$f_{\mathrm{Be}} \approx 1 - \frac{\mathscr{K}}{1 + \left(\dfrac{\Phi_{\mathrm{Be}}}{\Phi_{\mathrm{B}}}\right)\xi} \left[1 - \frac{\left(\dfrac{\Phi_{\mathrm{Be}}}{\Phi_{\mathrm{B}}}\right)}{\left(\dfrac{\Phi_{\mathrm{Be}}}{\Phi_{\mathrm{B}}}\right)_\infty}\right] \tag{5.14}$$

The ^{26}Al decay suppression factor f_{Al}

Similarly, the decay suppression factor of ^{26}Al, $f_{\mathrm{Al}} = \Phi_{^{26}\mathrm{Al}}/\tilde{\Phi}_{^{26}\mathrm{Al}}$, can be extracted from the Al/Mg flux ratio:

$$\frac{\Phi_{\mathrm{Al}}}{\Phi_{\mathrm{Mg}}} = \frac{f_{\mathrm{Al}}\tilde{\Phi}_{^{26}\mathrm{Al}} + \tilde{\Phi}_{^{27}\mathrm{Al}}}{\tilde{\Phi}_{^{24}\mathrm{Mg}} + \tilde{\Phi}_{^{25}\mathrm{Mg}} + \tilde{\Phi}_{^{26}\mathrm{Mg}} + (1 - f_{\mathrm{Al}})\xi\tilde{\Phi}_{^{26}\mathrm{Al}}} \tag{5.15}$$

where X_{esc} can be calculated from the stable secondary cosmic-ray nuclei B or from F, to check the assumption that X_{esc} does not depend on cosmic-ray specie

Ingredients to extract f from Be/B and Al/Mg

To extract f from Be/B and Al/Mg flux, many fluxes and cross sections data are needed:

1. Be, B and Al, F fluxes and their parent nuclei fluxes (up to Fe);
2. total spallation cross sections of Be, B, Al, F;
3. cross sections of Be, B, Al, F isotopes due to the spallation of their parent isotopes.

AMS has measured cosmic-ray nuclei fluxes from H (Z=1) to Si (Z=14) and Fe (Z=26) in the rigidity range from ~ 2 GV to ~ 3 TV with unprecedented accuracy [65, 124, 121, 125]. The S (Z=16) nuclei flux has also been measured by AMS, although not published yet. The parent nuclei fluxes of Be and B, especially for those having major contributions such as C and O, are well measured. While for F and Al, some of their parents nuclei fluxes (Z between 17 and 25) are still missing. The cross section data of light nuclei have been measured by many experiments, all the needed cross section for Be/B are available even though at low energies. While, for Al and F, many cross section measurements are still missing (Appendix B). Moreover, as shown in Appendix B, the cross sections are measured at low energies (typically below GeV/n). In this analysis, the cross section values are extrapolated to high energies by assuming they are constants.

The cosmic-ray residence time t_{esc} can be inferred from the decay suppression factor f_{Be} of ^{10}Be. And f_{Be} can be extracted from Be/B using AMS flux data and experimental cross section data. Ideally, with the similar calculation procedure, t_{esc} can also be obtained from the ^{26}Al decay suppression factor f_{Al} extracted from Al/Mg, which will provide an independent cross check. But due to missing data on parent nuclei fluxes and spallation cross section, a thorough calculation of f_{Al} from Al/Mg is not yet possible.

The result of f_{Be} from Be/B will be shown in the next section. A preliminary study of extracting f_{Al} from Al/Mg will be shown in the last section.

5.2 Extracting f from the Be/B flux ratio

5.2.1 Cosmic-ray grammage X_{esc}

To extract f_{Be} from the Be/B flux ratio, X_{esc} is deduced from the stable secondary cosmic-ray B. According to equation 5.5, X_{esc} is calculated as:

$$X_{esc} = \frac{\Phi_{\mathrm{B}}/\Phi_{\mathrm{C}}}{\sum_{P=C,N,O,Ne,Mg,Si,S,Fe} \Phi_P/\Phi_{\mathrm{C}} \frac{\sigma_{P\to B}}{m} - \Phi_{\mathrm{B}}/\Phi_{\mathrm{C}} \frac{\sigma_B}{m}} \tag{5.16}$$

where the parent nuclei of B include C, N, O, Ne, Mg, Si, S, and Fe. The contribution from ^{10}Be $\rightarrow^{10}$ B can be safely neglected [122].

Although ^{10}Be is radioactive, X_{esc} can also be calculated from Be as a cross-check, for which the ^{10}Be decay is expected to produce a deviation from X_{esc} calculated from B,

$$X_{esc} = \frac{\Phi_{\rm Be}/\Phi_{\rm C}}{\sum_{P=B,C,N,O,Ne,Mg,Si,S,Fe} \Phi_P/\Phi_{\rm C} \frac{\sigma_{P\rightarrow Be}}{m} - \Phi_{\rm Be}/\Phi_{\rm C} \frac{\sigma_{Be}}{m}} \tag{5.17}$$

AMS fluxes

Figure 5.1 shows the fluxes ratios of Be/C, B/C, N/C, O/C, Ne/C, Mg/C, Si/C, S/C, and Fe/C in the rigidity from 5 GV to 3 TV measured by AMS [65, 124, 125]. Data below rigidity 5 GV are not used to avoid solar modulation effect and non-relativistic effects.

Moreover, Figure 5.2 shows their spectral indices (γ) as a function of rigidity, defined in Section 3.9 and calculated using sliding windows over rigidity.

Total cross section

To evaluate X_{esc} with equation 5.16 and equation 5.17, the total cross section of B and Be per ISM unit mass σ_B/m and σ_{Be}/m are needed.

The total cross section of projectile A_p scattering on target A_t is estimated with the following energy independent phenomenological formula [126, 122]:

$$\sigma_{tot}(A_p, A_t) \approx \pi r_0^2 (A_p^{1/3} + A_t^{1/3} - b)^2 \,[\rm mb] \tag{5.18}$$

with $r_0 = 3.57$ and $b = 0.83$. The total cross section of cosmic-ray nuclei A scattering on H target ($A_t = 1$) can be calculated with:

$$\sigma_{tot}(H) \approx \pi 3.57^2 (A^{1/3} + 1 - 0.83)^2 \,[\rm mb] \tag{5.19}$$

The total cross section on He target can be obtained in the same way, and it can be written as $\sigma_{tot}(He) = \sigma_{tot}(H) \times \frac{\sigma_{tot}(He)}{\sigma_{tot}(H)}$.

As mentioned, ISM is assumed to be composed of 90% H and 10% He. Therefore σ_{tot}/m for cosmic-ray nuclei A_P can be estimated with:

$$\frac{\sigma_{tot}}{m} = \frac{0.9\sigma(H) + 0.1\sigma(He)}{0.9m_H + 0.1m_{He}} \approx \frac{0.9\sigma(H) + 0.1\sigma(H)\frac{\sigma_{tot}(A_P,4)}{\sigma_{tot}(A_P,1)}}{1.3m_p} \tag{5.20}$$

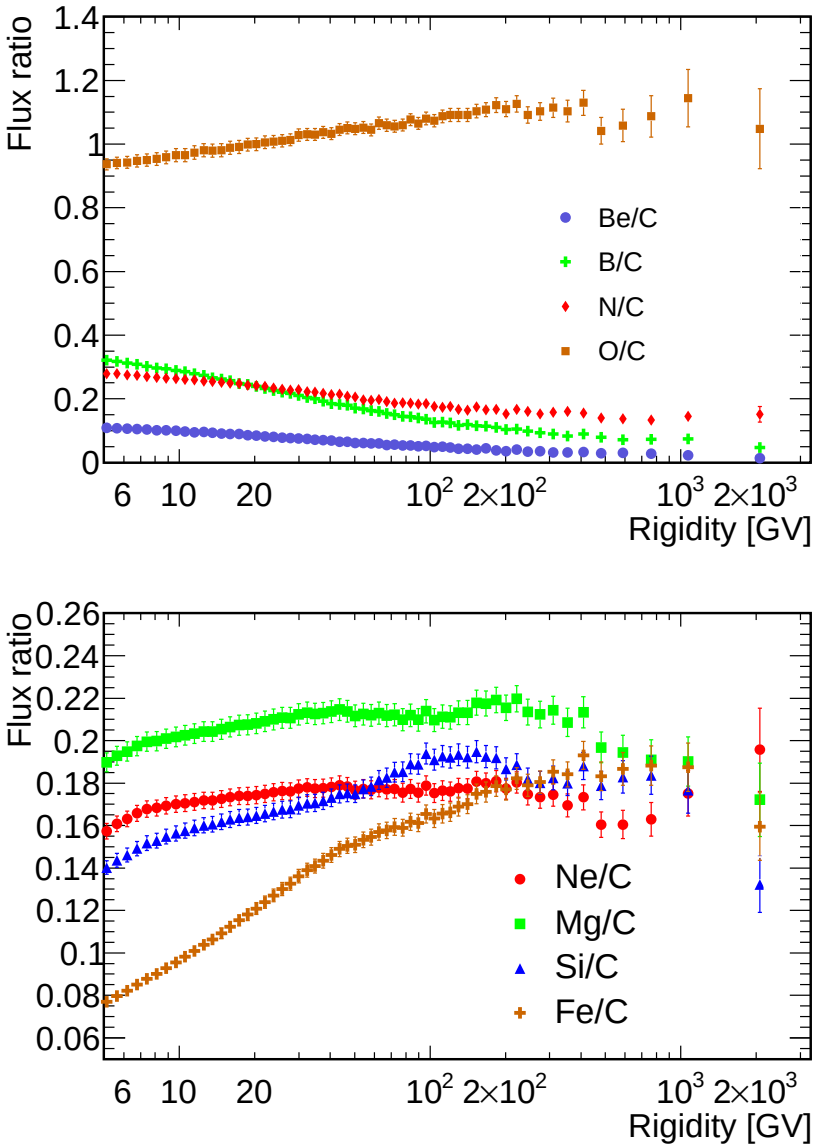

Fig. 5.1 The fluxes ratios of Be/C, B/C, N/C, O/C, Ne/C, Mg/C, Si/C, S/C, and Fe/C in the rigidity from 5 GV to 3 TV measured by AMS [65, 124, 125]. The Ne, Mg, Si, S and Fe fluxes have been rebinned to have the same binning of lighter nuclei fluxes. The correlations in the systematic errors from uncertainties in nuclear interaction cross sections, unfolding procedure and absolute rigidity scale have been subtracted.

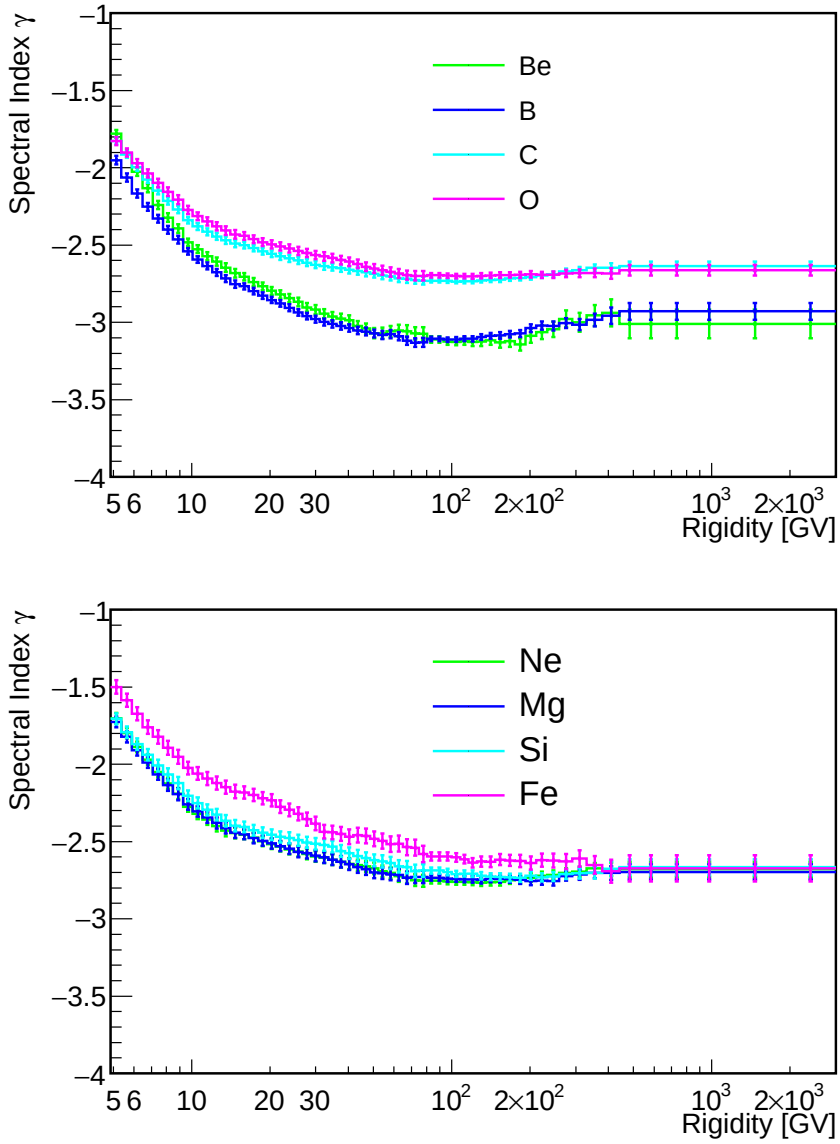

Fig. 5.2 The spectral index of AMS fluxes of Be, B, C, O, Ne, Mg, Si, S, and Fe in the rigidity from $\sim$ 5 GV to $\sim$ 3 TV. The spectral index γ are defined in Section 3.9 and calculated with the sliding windows over rigidity.

Combining the above formula, with the isotopic composition listed in Appendix A, the total cross sections for Be and B on ISM target per unit mass are:

$$\frac{\sigma_B}{m} \approx 194.492\,[\text{mb/GeV}]$$

$$\frac{\sigma_{Be}}{m} \approx 159.252\,[\text{mb/GeV}]$$

The relative errors on the total cross sections are estimated to be 15% by comparing some of the available cross section data on C target [102] with the predicted values from the phenomenological formula (equation 5.18).

Isotopic cross section

The isotopic fragmentation cross sections on H target are listed in Appendix A. And the cross sections on ISM target are then calculated with equation 5.20. Similar to equation 5.8, a rigidity correction factor ξ' needs to be applied to the cross sections to account for the effect of non-conserved rigidity between parent (P) and daughter (S), i.e.,

$$\hat{\sigma}_{P\to S} = \xi' \sigma_{P\to S} \tag{5.21}$$

with

$$\xi' = \left[\frac{(A/Z)_P}{(A/Z)_S}\right]^{1-\alpha_P} \tag{5.22}$$

where A is the mass number, Z is the charge and $\alpha_P = -\gamma_P$ is additive inverse of the rigidity dependent spectral index of the parent nucleus flux. In the cross section calculation, the spectral indices of isotopes are estimated from those of the corresponding nuclei fluxes.

In equation 5.16, to obtain the $P \to B$ spallation cross sections ($\sigma_{P\to B}$), the contributions from ghost nuclei channels must be included. The short-lived isotopes ^{10}C with the half life of 19.3 s and branching ratio $Br(^{10}\text{C} \to ^{10}\text{B}) = 1$, and ^{11}C with the half life of 20.36 min and branching ratio $Br(^{11}\text{C} \to ^{11}\text{B}) = 1$ contribute to $\sigma_{P\to B}$:

$$\sigma_{P\to B} = \sigma_{P\to ^{10}\text{B}} + \sigma_{P\to ^{10}\text{C}} \times Br(^{10}\text{C} \to ^{10}\text{B}) + \sigma_{P\to ^{11}\text{B}} + \sigma_{P\to ^{11}\text{C}} \times Br(^{11}\text{C} \to ^{11}\text{B}) \tag{5.23}$$

The cross sections of parent nuclei P fragmenting to each of the B isotopes are calculated taking into account the natural isotopic composition of the parent nuclei in cosmic rays. As an example, the cross section of C fragmenting to ^{10}B (i.e., $\sigma_{\text{C}\to^{10}\text{B}}$) is calculated as:

$$\sigma_{\text{C}\to^{10}\text{B}} = f_{12}\sigma_{^{12}\text{C}\to^{10}\text{B}} + f_{13}\sigma_{^{13}\text{C}\to^{10}\text{B}} + f_{14}\sigma_{^{14}\text{C}\to^{10}\text{B}} \tag{5.24}$$

where C is composed of ^{12}C, ^{13}C, and ^{14}C with relative abundances f_{12}, f_{13}, and f_{14}. The isotopic composition of cosmic-ray nuclei are listed in Table A.1 of Appendix A.

The correction factor in equation 5.22 introduces a rigidity dependence to the cross sections $\sigma_{P\to B}$ and $\sigma_{P\to Be}$.

X_{esc} results

With the fluxes and cross sections obtained, X_{esc} is independently derived from B and Be with Equations 5.16 and 5.17, respectively. As mentioned, Be contains the radioactive isotope ^{10}Be. The decay effect,which dependents on the rigidity, will be observed in X_{esc}.

- At high rigidity, considering the fact that the decay time is much longer than the escape time (i.e., $t_d \gg t_{esc}$), the ^{10}Be decay is negligible, and Be can be considered as a stable secondary nuclei. Therefore, in this framework, X_{esc} derived from Be should yield the same result as that derived from B.

- At low rigidity, in the case of $t_d \lesssim t_{esc}$, the effect of ^{10}Be decaying to ^{10}B is not negligible. As a result, X_{esc} derived from Be should be smaller than that derived from B.

Figure 5.3 shows X_{esc} derived independently from B and Be in rigidity ranging from 5 GV to 3.3 TV. As expected, the two results have a good agreement at high rigidity, which is a good consistency check of the framework. Result from B will be used to evaluate f_{Be}.

5.2.2 Decay suppression factor f_{Be}

Figure 5.4 shows the Be to B flux ratio $\Phi_{\mathrm{Be}}/\Phi_{\mathrm{B}}$ and the ratio in the limit of infinite decay time $(\Phi_{\mathrm{Be}}/\Phi_{\mathrm{B}})_{\infty}$. Similar to what is observed in Figure 5.3, at high rigidity $(\Phi_{\mathrm{Be}}/\Phi_{\mathrm{B}}) \approx (\Phi_{\mathrm{Be}}/\Phi_{\mathrm{B}})_{\infty}$, because the ^{10}Be decay time t_d is much longer than the escape time t_{esc}. While $(\Phi_{\mathrm{Be}}/\Phi_{\mathrm{B}}) < (\Phi_{\mathrm{Be}}/\Phi_{\mathrm{B}})_{\infty}$ at low rigidity, because the ^{10}Be decay depletes the numerator of the Be/B flux ratio.

With all the ingredients obtained, the decay suppression factor f_{Be} is finally extracted from data. Figure 5.5 shows f of ^{10}Be as a function of rigidity ranging from 5 GV to 1 TV. In the calculation of the error of f_{Be}, contribution from cross section uncertainties are not included. The cross section error are almost rigidity independent, their uncertainties will move the result of f_{Be} up or down by $\sim 10\%$. However this bias will have no effect because the value of f at high rigidity can be rescaled to its expected value of 1 [122].

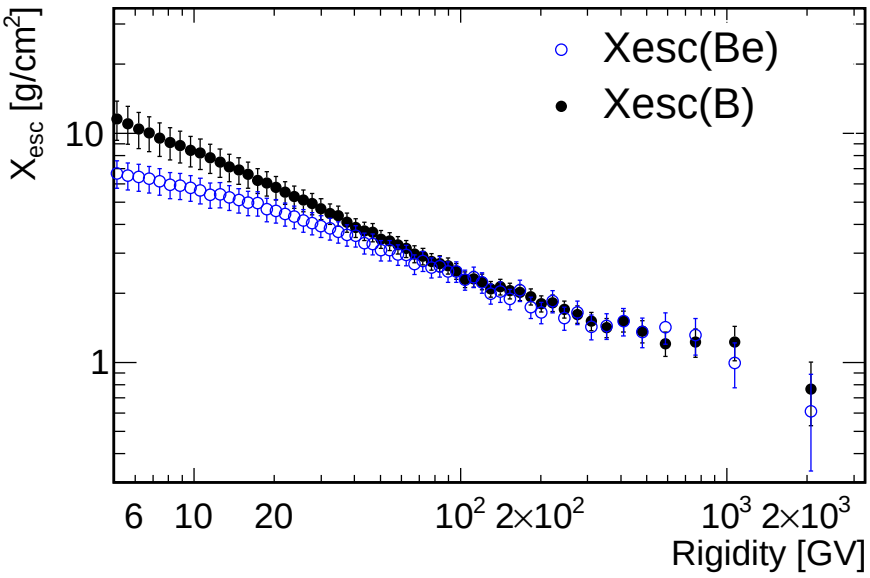

Fig. 5.3 X_{esc} derived independently from B (black points) and Be (blue points) as a function of rigidity ranging from 5 GV to 3.3 TV. The error includes the uncertainties of flux ratios and cross sections.

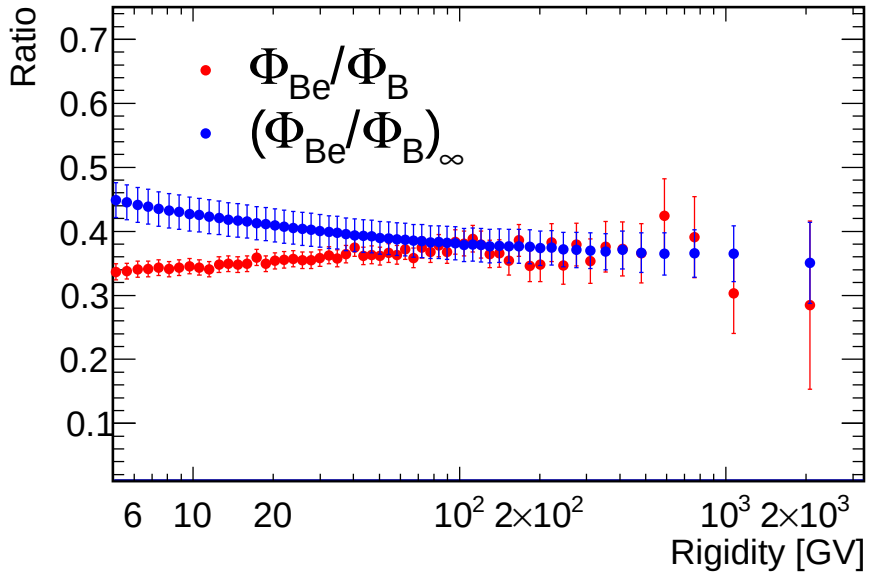

Fig. 5.4 Be to B flux ratio Φ_{Be}/Φ_B (red points) and the ratio in the limit of infinite decay time, $(\Phi_{Be}/\Phi_B)_\infty$ (blue points) as a function of rigidity ranging from 5 GV to 3.3 TV.

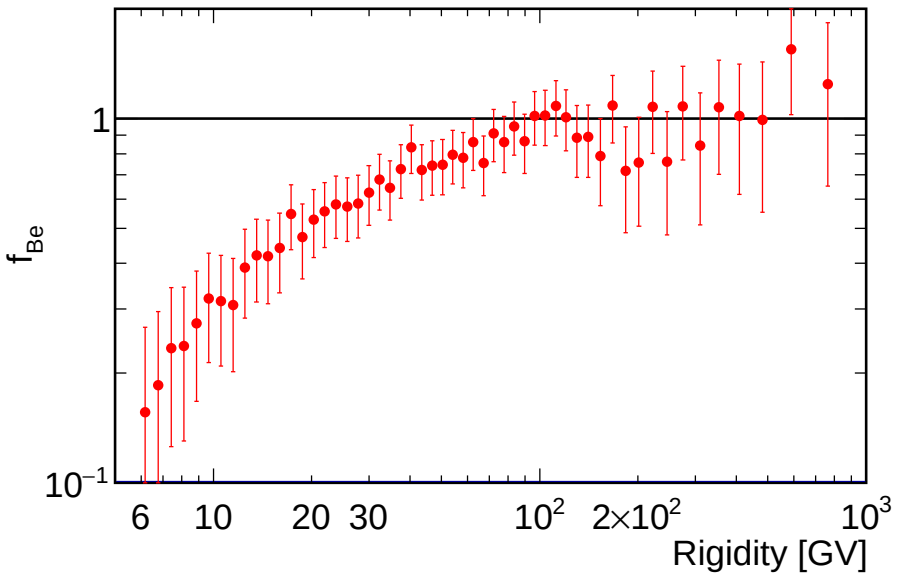

Fig. 5.5 The decay suppression factor of ^{10}Be, i.e., f_{Be}, as a function of rigidity ranging from 5 GV to 1 TV. The black solid line shows $f = 1$. The error of f_{Be} includes flux uncertainties and does not include systematic cross section uncertainties.

The surviving fractions f provide constraints on the cosmic-ray residence (or escape) time t_{esc} in the Galaxy, and allow to distinguish between different cosmic-ray propagation scenarios. In the framework introduced in Section 5.1, the relation between f and t_{esc} is [122, 60]:

$$f = \frac{1}{1 + \frac{t_{esc}}{t_d}} \tag{5.25}$$

, the same as the prediction from the leaky-box model.

The diffusion model predicts [122, 60]:

$$f = \sqrt{\frac{t_d}{t_{esc}}} \tanh \sqrt{\frac{t_{esc}}{t_d}} \tag{5.26}$$

The ^{10}Be decay time t_d is known, and the cosmic-ray residence time t_{esc} is assumed to follow a power law:

$$t_{esc} = t_0 \left(\frac{R}{10\,\mathrm{GV}} \right)^{-\delta} \tag{5.27}$$

Fitting f_{Be} with the predictions from models provides constraints on the two free parameters of t_{esc}, i.e., t_0 and δ. These results and their interpretation will be the subject of a future publication([122]).

5.3 A preliminary analysis of extracting the ^{26}Al decay suppression factor from the Al/Mg flux ratio

An independent study of extracting ^{26}Al decay suppression factor f_{Al} provides supplemental information to the study of the cosmic-ray propagation. However, the extraction of f_{Al} from Al/Mg flux ratio is not possible yet because of lack of measurements of some heavy nuclei fluxes and cross sections, moreover for some of the nuclei fluxes the existing measurements suffer from large uncertainties. Nevertheless, since the study of Be/B has paved the way to the study of Al/Mg, a preliminary analysis will be discussed in this section.

Similar to equation 5.9, f_{Al} can be extracted from the following formula:

$$\frac{\Phi_{\mathrm{Al}}}{\Phi_{\mathrm{Mg}}} \approx \frac{\sum_P \Phi_P \left(\frac{\sigma^*_{P\to^{27}\mathrm{Al}}}{m} + f_{\mathrm{Al}} \frac{\sigma_{P\to^{26}\mathrm{Al}}}{m} \right)}{\sum_P \Phi_P \left(\frac{\sigma^*_{P\to\mathrm{Mg}}}{m} + (1 - f_{\mathrm{Al}})\xi \frac{\sigma_{P\to^{26}\mathrm{Al}}}{m} \right)} \tag{5.28}$$

with

$$\xi = \left(\frac{12}{13}\right)^{1-\alpha_{^{26}\mathrm{Al}}} \tag{5.29}$$

$$\frac{\sigma^*_{P\to\mathrm{Mg}}}{m} = \sum_{i=24,25} \frac{1 + X_{esc}\frac{\sigma_{^{26}\mathrm{Al}}}{m}}{1 + X_{esc}\frac{\sigma_{^{i}\mathrm{Mg}}}{m}} \frac{\sigma_{^{i}\mathrm{Mg}}}{m} \tag{5.30}$$

$$\frac{\sigma^*_{P\to^{27}\mathrm{Al}}}{m} = \sum_{i=27} \frac{1 + X_{esc}\frac{\sigma_{^{26}\mathrm{Al}}}{m}}{1 + X_{esc}\frac{\sigma_{^{i}\mathrm{Al}}}{m}} \frac{\sigma_{^{i}\mathrm{Al}}}{m} \tag{5.31}$$

Again, to obtain $f_{\rm Al}$, $\left(\frac{\rm Al}{\rm Mg}\right)_\infty$ and $\mathscr{K}$ are defined from cross sections and fluxes:

$$\left(\frac{\Phi_{\rm Al}}{\Phi_{\rm Mg}}\right)_\infty = \frac{\sum_P \Phi_P \left(\frac{\sigma^*_{P\to^{27}{\rm Al}}}{m} + \frac{\sigma_{P\to^{26}{\rm Al}}}{m}\right)}{\sum_P \Phi_P \frac{\sigma^*_{P\to{\rm Mg}}}{m}} \tag{5.32}$$

$$\mathscr{K} = 1 + \frac{\sum_P \Phi_P \frac{\sigma^*_{P\to^{27}{\rm Al}}}{m}}{\sum_P \Phi_P \frac{\sigma_{P\to^{26}{\rm Al}}}{m}} \tag{5.33}$$

With the X_{esc} derived from B or from F, the decay suppression factor $f_{\rm Al} = \Phi_{^{26}{\rm Al}}/\tilde{\Phi}_{^{26}{\rm Al}}$ can be derived from available fluxes and cross sections data:

$$f_{\rm Al} \approx 1 - \frac{\mathscr{K}}{1 + \left(\frac{\Phi_{\rm Al}}{\Phi_{\rm Mg}}\right)\xi}\left[1 - \frac{\left(\frac{\Phi_{\rm Al}}{\Phi_{\rm Mg}}\right)}{\left(\frac{\Phi_{\rm Al}}{\Phi_{\rm Mg}}\right)_\infty}\right] \tag{5.34}$$

The availability of the ingredients

The following ingredients are needed to evaluate $f_{\rm Al}$ from Al/Mg:

1. The precise fluxes in rigidity from 5 GV up to $\sim$ TV, including Mg (Z=12) and Al (Z=13) fluxes, and their parent nuclei fluxes such as Si (Z=14), P (Z=15) and the even charged elemental nuclei from S (Z=16) to Fe (Z=26).

2. fragmentation cross sections to Al for nuclei heavier than Al $\sigma_{P\to{\rm Al}}$

3. fragmentation cross sections to Mg for nuclei heavier than Mg $\sigma_{P\to{\rm Mg}}$

The cross section data $\sigma_{P\to{\rm Al}}$ and $\sigma_{P\to{\rm Mg}}$ are listed in Table B.3 and B.4 of Appendix B, respectively. As shown in Table 5.1, the cross section data of P, Ar, Ca are also available. The Mg, Al, Si, S (preliminary), and Fe fluxes have been measured by AMS as a function of rigidity from $\sim$ 2 GV to 3 TV with unprecedented precision. The fluxes of P, Ar, Ca, Ti, Cr have not yet been released by AMS, so their corresponding fluxes in rigidity from 5 GV to 3 TV have been estimated from previous measurements performed by other experiments as a function of kinetic energy per nucleon extrapolated at high energy assuming that their spectral shape is similar to neighbor nuclei (such as S nuclei) fluxes measured by AMS.

Table 5.1 The availability of the ingredients for extracting f from Al/Mg

	$_{12}$Mg	$_{13}$Al	$_{14}$Si	$_{15}$P	$_{16}$S	$_{18}$Ar	$_{20}$Ca	$_{22}$Ti	$_{24}$Cr	$_{26}$Fe
Flux	✓ (AMS)	✓ (AMS)	✓(AMS)	✓	✓ (AMS)	✓	✓	✓ (∗)	✓ (∗)	✓ (AMS)
$\sigma_{P\to\mathrm{Al}}$	-	-	✓	✓	✓	✓	✓	×	×	✓
$\sigma_{P\to\mathrm{Mg}}$	-	✓	✓	✓	✓	✓	✓	×	×	✓

✓ data available (regardless of the quality of cross section data);
× data not available;
∗ flux data can't be used in this study because their corresponding fragmentation cross section data are not available and in the calculation, the parent nuclei flux always appears with the cross section.

Experiments such as HEAO3 [6], TRACER [127], CRISIS [128], etc, have measured the P, Ar, Ca nuclei fluxes in different regions of kinetic energy per nucleon E_k ranging from 0.5 GeV/n to 1 TeV/n. However, it is not possible to determine the flux shapes at high energies with these data, because the measurements errors exceed 50% at 50 GeV/n. Alternatively, the P, Ar, Ca nuclei fluxes can be estimated with the S nuclei flux measured by AMS by rescaling it according to the measurements of P, Ar, Ca fluxes. The preliminary AMS S nuclei flux was measured as a function of rigidity ranging from 2.15 GV to 3 TV. To compare with P, Ar, Ca nuclei fluxes, the rigidity measured by AMS is converted to kinetic energy per nucleon by assuming the cosmic-ray S nuclei are mainly composed of ^{32}S. Figure 5.6 and 5.7 show the P, Ar, Ca nuclei fluxes measured by other experiments together with the S nuclei flux measured by AMS rescaled by the factors of 0.15, 0.3 and 0.5 respectively. As seen, the P, Ar, Ca nuclei fluxes can be approximated as the rescaled AMS S nuclei flux. The bias due to the normalization of the fluxes and the description of shapes at high energies are negligible, because the P, Ar, Ca nuclei are more than 10 times less abundant than Si and their corresponding fragmentation cross sections to Al and Mg are around twice smaller than those of Si. Even without taking P, Ar, Ca nuclei fluxes into account, the bias in the evaluation of f_{Al} and X_{esc} from heavy nuclei is estimated to be smaller than 10%.

These estimated P, Ar, Ca fluxes and their corresponding cross section are injected into the calculation of f_{Al}. The contributions from Ti and Cr nuclei have been neglected because their fragmentation cross sections to Al and Mg have not been measured. However the abundance and fragmentation cross-sections of Ti, Ar and Cr relative to Si and Mg are much lower and hence they are not expected to contribute much. Figure 5.8 shows the fluxes ratios to Si for Mg, Al, P, S, Ar and Fe. As seen, P, Ar, Ca nuclei are less abundant than others.

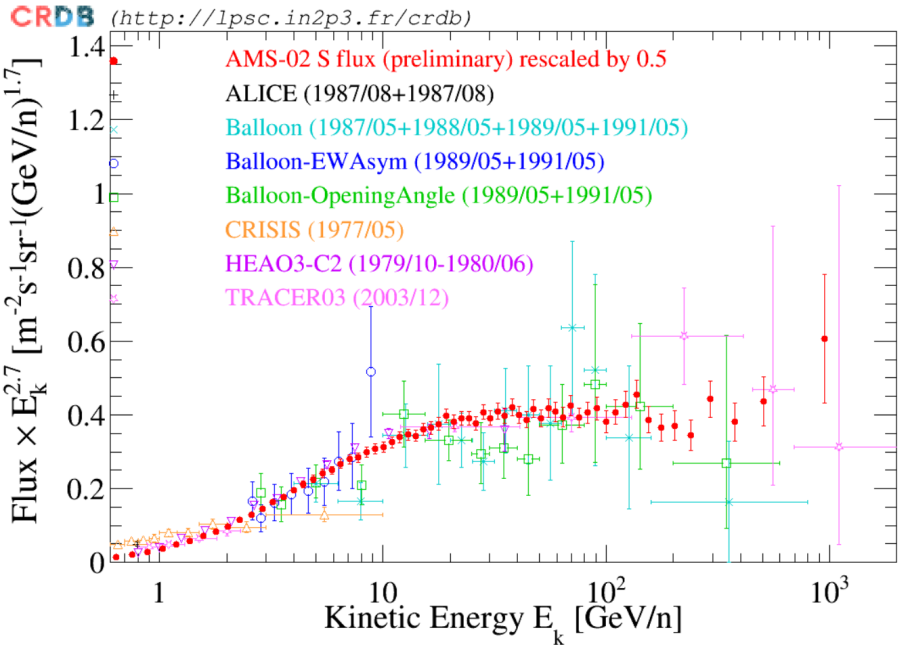

Fig. 5.6 The Ca nuclei fluxes multiply by $E_k^{2.7}$ in kinetic energy per nucleon E_k measured by other experiments together with the preliminary S nuclei flux measured by AMS (red points) rescaled by the factors of 0.5.

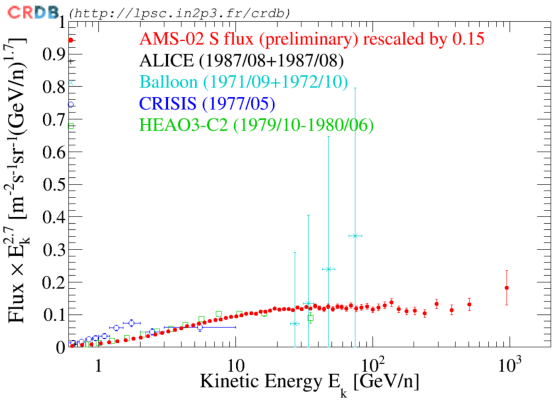

(a) P nuclei flux

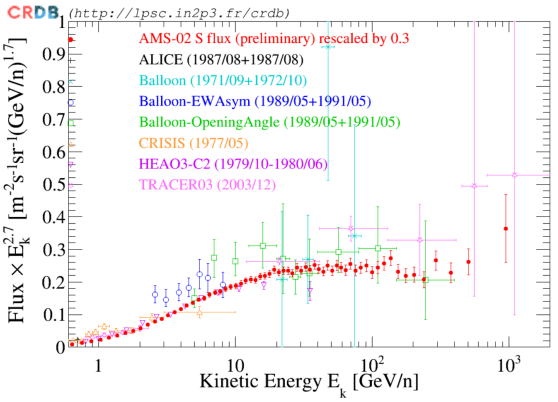

(b) Ar nuclei flux

Fig. 5.7 The P (left), Ar (right) nuclei fluxes multiply by $E_k^{2.7}$ in kinetic energy per nucleon E_k measured by other experiments together with the preliminary S nuclei flux measured by AMS (red points) rescaled by the factors of 0.15 and 0.3.

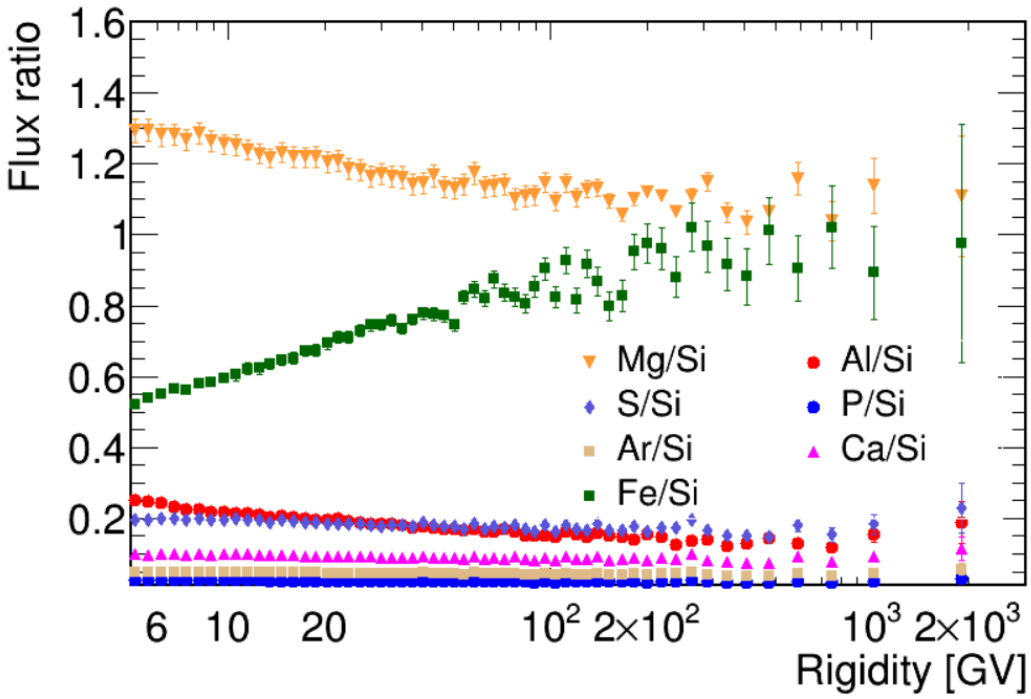

Fig. 5.8 Flux ratios to Si for Mg, Al, P, S (preliminary result), Ar, Ca and Fe as a function of rigidity in 5 GV to 3 GV. P, Ar, Ca fluxes are approximated as the rescaled AMS S nuclei flux (preliminary result) based on measurements of cosmic-ray P, Ar, Ca nuclei performed by other experiments.

The cosmic-ray grammage

As the heavy nuclei fluxes obtained, the cosmic-ray grammage X_{esc} can be derived from the heavy stable secondary cosmic-ray F. And the assumption that X_{esc} does not depend on the nuclei species is examined by comparing the X_{esc} evaluated from B and F.

With the Ne, Na, Mg, Al, Si, S and Fe nuclei fluxes from AMS and P, Ar, Ca from other experiments, and the experimental cross section data listed in the Table B.5 Appendix B, the F X_{esc} is calculated as

$$X_{esc} = \frac{\Phi_{\mathrm{F}}/\Phi_{\mathrm{Si}}}{\sum_{P=\mathrm{Ne,Na,Mg,Al,Si,P,S,Ar,Ca,Fe}} \Phi_P/\Phi_{\mathrm{Si}} \frac{\sigma_{P\to F}}{m} - \Phi_{\mathrm{F}}/\Phi_{\mathrm{Si}} \frac{\sigma_F}{m}} \tag{5.35}$$

Figure 5.9 shows X_{esc} derived from B and F. In rigidities above 60 GV, the X_{esc} result from F agrees with that from B, which confirms the expectation that X_{esc} does not depend on the nuclei species. At low rigidities, the estimation of X_{esc} from F becomes not valid because the denominator of equation 5.35 reaches its limit (close to 0).

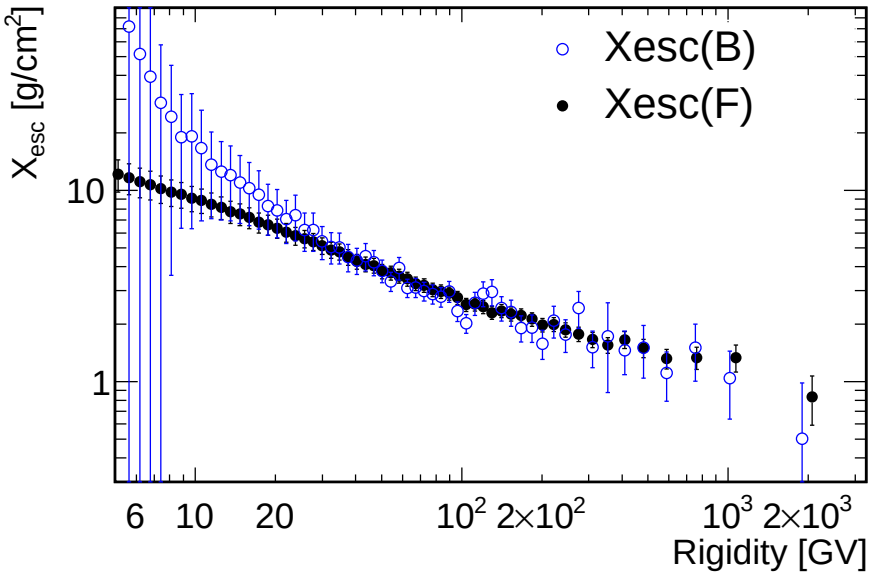

Fig. 5.9 X_{esc} derived independently from B (black points) and F (blue points) as functions of rigidity from 5 GV to 3 TV.

Al/Mg flux ratio

To evaluate the cosmic-ray Al to Mg nuclei flux ratio in the limit of infinite decay time $(\Phi_{\mathrm{Al}}/\Phi_{\mathrm{Mg}})_\infty$, the weighted cross sections $\sigma^*_{P\to\mathrm{Mg}}/m$ and $\sigma^*_{P\to{}^{17}\mathrm{Al}}/m$ are calculated with equa-

tion 5.3 and 5.31 using the weight factors defined by

$$r_S = \frac{1 + X_{esc}\frac{\sigma_{^{26}\mathrm{Al}}}{m}}{1 + X_{esc}\frac{\sigma_S}{m}} \tag{5.36}$$

where S stands for ^{27}Al, ^{24}Mg,^{25}Mg, and ^{26}Mg. X_{esc} is evaluated from B.

Figure 5.10 shows the rigidity dependent weight factors of ^{27}Al, ^{24}Mg,^{25}Mg, and ^{26}Mg.

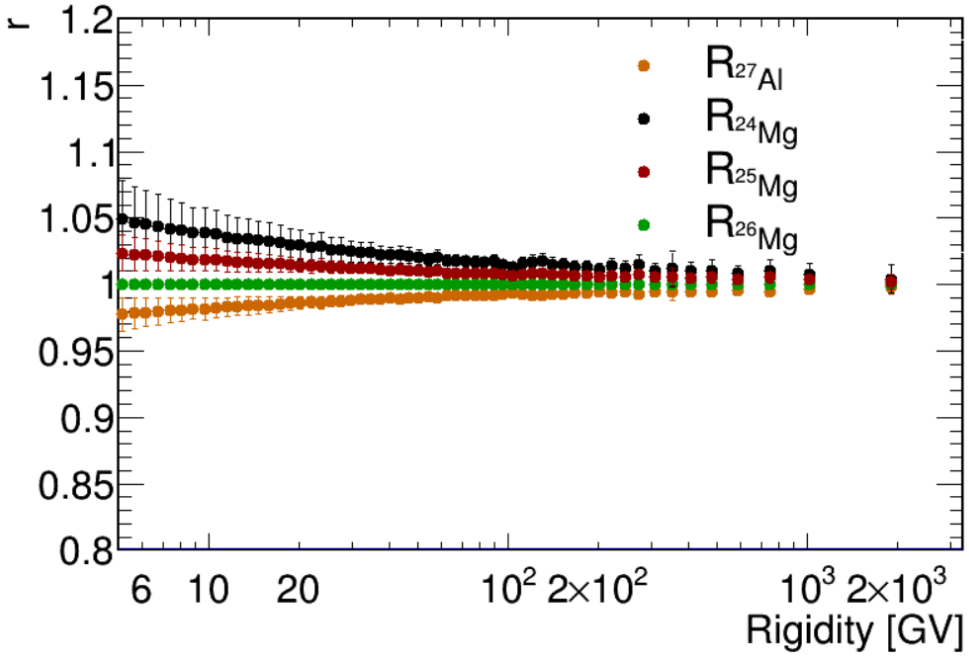

Fig. 5.10 The weight factors of ^{27}Al (orange), ^{24}Mg (black), ^{25}Mg (red), and ^{26}Mg (green) as functions of rigidity. The errors are obtained from the leading contribution channels Si→ S.

With the weighted cross sections calculated from the weight factors, the Al/Mg flux ratio in the limit of infinite decay time $(\Phi_{\mathrm{Al}}/\Phi_{\mathrm{Mg}})_\infty$ is evaluated with equation 5.32. As discussed in Section 4.5 of Chapter 4 for Al nuclei and Section 3.9 of Chapter 3 for Mg nuclei, different from cosmic-ray Be and B, Al and Mg nuclei have important primary contributions from astrophysical sources. The ratio of the secondary components of Al and Mg nuclei fluxes $\Phi^S_{\mathrm{Al}}/\Phi^S_{\mathrm{Mg}}$ can be obtained by subtracting the primary components of the Al and Mg nuclei fluxes measured by AMS.

Figure 5.11 shows $\Phi^S_{\mathrm{Al}}/\Phi^S_{\mathrm{Mg}}$ obtained from the secondary components of Al and Mg nuclei fluxe and $(\Phi_{\mathrm{Al}}/\Phi_{\mathrm{Mg}})_\infty$ obtained from the currently available fluxes and cross section data. Contrary to the expectation the two results show a large discrepancy over the entire

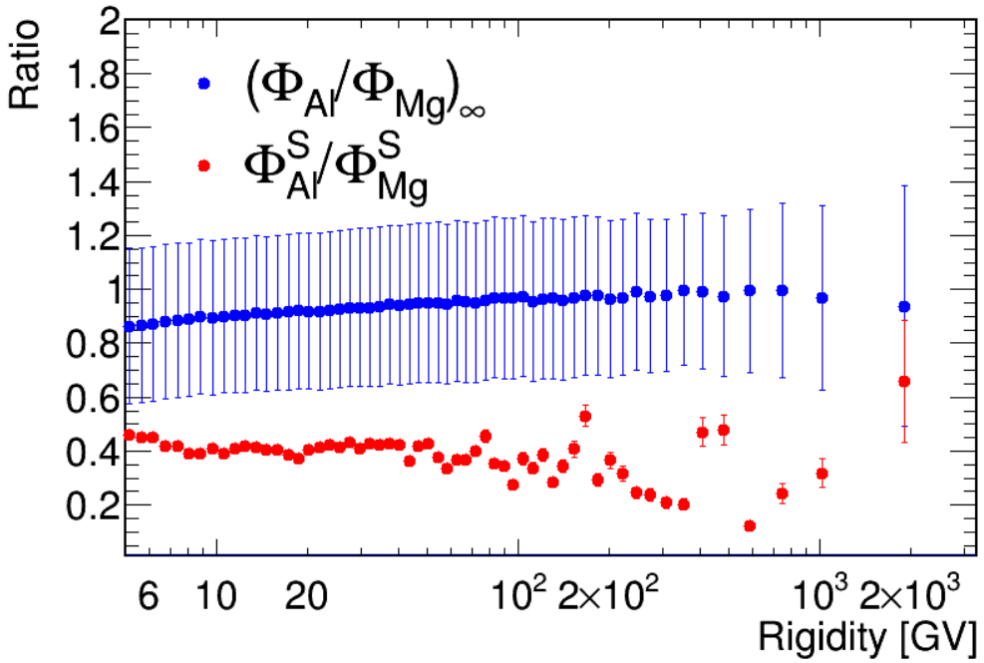

Fig. 5.11 The ratio of the secondary components of Al and Mg nuclei fluxes Φ^S_{Al}/Φ^S_{Mg} (red points) and the Al/Mg flux ratio in the limit of infinite decay time $(\Phi_{Al}/\Phi_{Mg})_\infty$ (blue points). Φ^S_{Al}/Φ^S_{Mg} is obtained by subtracting the primary components of the Al and Mg nuclei fluxes measured by AMS as discussed in Section 4.5 of Chapter 4 and Section 3.9 of Chapter 3 respectively. $(\Phi_{Al}/\Phi_{Mg})_\infty$ is calculated from the currently available fluxes and cross section data.

rigidity range hinting to an overestimation of $(\Phi_{\rm Al}/\Phi_{\rm Mg})_\infty$ caused by the quality of data and by the approximations made in the calculation, namely:

1. Ti and Cr fluxes have not been included in the calculation due to the lack of data of both fluxes and cross sections. The Ti and Cr nuclei in cosmic rays have abundance similar to S nuclei, and their fragmentation cross sections to Al and Mg are estimated to be smaller than S nuclei. Therefore the contribution of Ti and Cr nuclei is estimated to be smaller than 10%.;

2. P, Ar, Ca fluxes are approximated from the rescaled S flux measured by AMS. However, as discussed, the bias due to the approximation is negligible.

3. the quality of the cross section data give the largest bias. First, the values of fragmentation cross sections for heavier nuclei are underestimated. As shown in Table B.3 and B.4 of Appendix B, the available cross sections are all measured at very low energy (below 1 GeV/n). Second, the fragmentation cross sections data from the ghost nuclei ^{25}Si and ^{26}Na have not been measured yet, which would result in the underestimation of Mg fragmentation cross sections.

Moreover, the estimation of $\Phi^S_{\rm Al}/\Phi^S_{\rm Mg}$ can be biased. As mentioned, the secondary components of Al and Mg nuclei fluxes are estimated by fitting the measured fluxes with the weighted sum of the primary cosmic ray Si nuclei flux and of the secondary F nuclei flux under the assumption that the secondary component of Al follows the F flux. This assumption may be broken if the secondary component of Al mimic the primary component. This is checked expressing the Al/Si flux ratio from equation 5.4:

$$\frac{\Phi_{\rm Al}}{\Phi_{\rm Si}} = \frac{X_{esc}\sum_{P=\rm Si,P,S,Ar,Ca,Fe}\Phi_P/\Phi_{\rm Si}\frac{\sigma_{P\rightarrow \rm Al}}{m}}{1+X_{esc}\frac{\sigma_{\rm Al}}{m}} \tag{5.37}$$

In the limit of $X_{esc}\frac{\sigma_{Al}}{m} \gg 1$, the above reduces to

$$\frac{\Phi_{\rm Al}}{\Phi_{\rm Si}} = \frac{X_{esc}\sum_{P=\rm Si,P,S,Ar,Ca,Fe}\Phi_P/\Phi_{\rm Si}\frac{\sigma_{P\rightarrow \rm Al}}{m}}{X_{esc}\frac{\sigma_{\rm Al}}{m}} \tag{5.38}$$

which, simplifying X_{esc} and taking into account that Si is much more abundant than other primary nuclei producing Al by spallation, leads to:

$$\Phi_{\mathrm{Al}} \approx \Phi_{\mathrm{Si}} \frac{\sigma_{\mathrm{Si}\rightarrow\mathrm{Al}}}{\sigma_{\mathrm{Al}}} \tag{5.39}$$

the secondary component of Al nuclei will have same rigidity dependence of the primary (Si) nuclei flux. Similarly, Mg can be checked by comparing $X_{esc}\frac{\sigma_{Mg}}{m}$ with 1. Figure 5.12 shows the $X_{esc}\frac{\sigma_i}{m}$ with total fragmentation cross section σ_i for Al and Mg using X_{esc} calculated from B. As seen $X_{esc}\frac{\sigma_i}{m}$ is well below 1 for both Al and Mg nuclei at rigidities above 30 GV which indicates that the evaluation of the secondary components of Al and Mg nuclei fluxes is good.

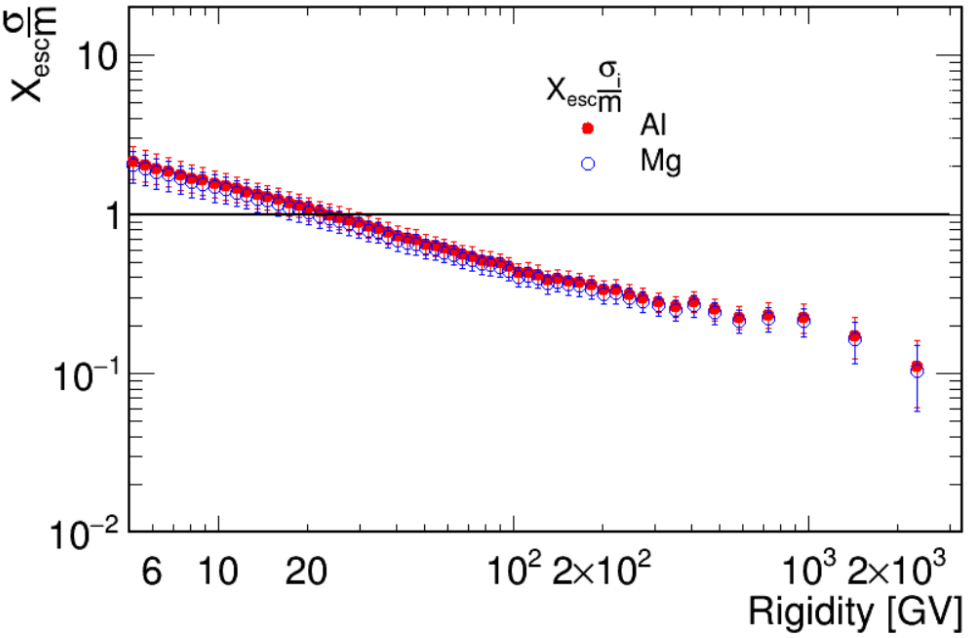

Fig. 5.12 $X_{esc}\frac{\sigma_i}{m}$ with total fragmentation cross section σ_i for Al (red points) and Mg (blue points) using X_{esc} calculated from the stable secondary cosmic-ray B. The black line indicates 1. The Al and Mg results cross 1 at ~20 GV.

The outlook for the analysis of extracting f_{Al} from the Al/Mg flux ratio

Some ingredients in the calculation of $(\Phi_{\mathrm{Al}}/\Phi_{\mathrm{Mg}})_{\infty}$, including fluxes and cross sections are still missing and some of the existing measurements have larger uncertainties than those used in the extracting f_{Be} from the Be/B flux ratio. Therefore the evaluation of f_{Al} from the Al/Mg

flux ratio is not possible yet although the procedure of the calculation is clear. With more heavier nuclei fluxes measured by AMS becoming available, and more fragmentation cross section data for heavier nuclei being released, extraction of f_{Al} from the Al/Mg flux ratio will be feasible, and thus providing complementary constraints to the cosmic-ray residence time.

Chapter 6

Conclusions and outlook

The primary cosmic rays Mg are thought to be mainly produced and accelerated in astrophysical sources. And the cosmic rays Al, as the combination of primary and secondary cosmic rays, are produced both in astrophysical sources and by the collisions of heavier nuclei with the interstellar medium. The precise knowledge of their spectra in the GV to TV rigidity region provides important information on the production, acceleration, and propagation mechanisms of cosmic rays in the Galaxy. The cosmic-ray residence time is a critical parameter of cosmic-ray propagation. The rigidity dependent survival fraction of cosmic-ray clocks such as ^{10}Be and ^{26}Al can be extracted from the decaying charge to the decayed charge ratios Be/B and Al/Mg with a model independent method, and allows to provide constraints on the cosmic-ray residence time.

In this thesis, the Mg and Al fluxes measured by AMS and the physical interpretation of Be/B and Al/Mg flux ratios are presented.

Mg and Al fluxes

The precision measurements of Mg and Al fluxes in the rigidity range from 2.15 GV to 3.0 TV based on 2.5 million Mg and 0.5 million Al nuclei collected by AMS during its first 8.5 years (May 19, 2011 to October 30, 2019) are presented.

The comparison with other primary cosmic rays fluxes measured by AMS in the same data-taking period shows:

- Ne, Mg, Si fluxes have identical rigidity dependence above 86.5 GV and deviate from a single power law above 200 GV.
- Above 86.5 GV, the rigidity dependence of Ne, Mg, and Si fluxes is different from that of He, C, and O fluxes.

It can be concluded that Ne, Mg, and Si and the lighter nuclei He, C, and O belong to two different classes of primary cosmic rays.

The Al flux is well described by the sum of a primary cosmic ray component and a secondary cosmic ray component. The fraction of the primary component increases with rigidity and becomes dominant at 20 GV. And N and Na are also a mixture of primary and secondary components. It can be concluded that N, Na, and Al belong to a distinct group and are the combinations of primary and secondary cosmic rays.

Physical interpretation of Be/B and Al/Mg flux ratios

With the precision measurement of cosmic-ray fluxes by AMS and the fragmentation cross section data available, the rigidity-dependent decay suppression factor of radioactive isotope ^{10}Be, f_{Be}, has been extracted from the Be/B flux ratio with a model independent method. f_{Be} constrains the cosmic-ray residence time predicted in different models, and thus allows to distinguish between different cosmic-ray propagation scenarios.

The study of Be/B has paved the way for the study of Al/Mg. Due to the limited heavy nuclei fluxes and fragmentation cross section data, extracting f_{Al} from Al/Mg is not possible yet. However, the feasibility of the study has been presented.

With more heavy nuclei fluxes measured by AMS becoming available, and more fragmentation cross section data for heavier nuclei being released, the extraction of f_{Al} from Al/Mg will be feasible, and thus providing complementary constraints to the cosmic-ray residence time.

References

[1] Viktor F Hess. About observations of penetrating radiation during seven free balloon flights. *phys. Time*, 13:1084–1091, 1912.

[2] AD Panov, JH Adams Jr, HS Ahn, GL Bashindzhagyan, KE Batkov, J Chang, M Christl, AR Fazely, O Ganel, RM Gunasingha, et al. The energy spectra of heavy nuclei measured by the atic experiment. *Advances in Space Research*, 37(10):1944–1949, 2006. doi: https://doi.org/10.1016/j.asr.2005.07.040.

[3] T Sanuki, M Motoki, H Matsumoto, ES Seo, JZ Wang, K Abe, K Anraku, Y Asaoka, M Fujikawa, M Imori, et al. Precise measurement of cosmic-ray proton and helium spectra with the bess spectrometer. *The Astrophysical Journal*, 545(2):1135, 2000. doi: https://doi.org/10.1086/317873.

[4] YS Yoon, HS Ahn, PS Allison, MG Bagliesi, JJ Beatty, G Bigongiari, PJ Boyle, JT Childers, NB Conklin, S Coutu, et al. Cosmic-ray proton and helium spectra from the first cream flight. *The Astrophysical Journal*, 728(2):122, 2011. doi: https://doi.org/10.1088/0004-637x/728/2/122.

[5] A Obermeier, M Ave, P Boyle, Ch Höppner, J Hörandel, and D Müller. Energy spectra of primary and secondary cosmic-ray nuclei measured with tracer. *The Astrophysical Journal*, 742(1):14, 2011. doi: https://doi.org/10.1088/0004-637x/742/1/14.

[6] JJ Engelmann, P Ferrando, A Soutoul, Ph Goret, E Juliusson, L Koch-Miramond, N Lund, P Masse, B Peters, N Petrou, et al. Charge composition and energy spectra of cosmic-ray nuclei for elements from be to ni-results from heao-3-c2. *Astronomy and Astrophysics*, 233:96–111, 1990.

[7] O Adriani, GC Barbarino, GA Bazilevskaya, R Bellotti, M Boezio, EA Bogomolov, M Bongi, V Bonvicini, S Bottai, A Bruno, et al. The pamela mission: Heralding a new era in precision cosmic ray physics. *Physics Reports*, 544(4):323–370, 2014. doi: https://doi.org/10.1016/j.physrep.2014.06.003.

[8] WB Atwood, Aous A Abdo, Markus Ackermann, W Althouse, B Anderson, M Axelsson, Luca Baldini, J Ballet, DL Band, Guido Barbiellini, et al. The large area telescope on the fermi gamma-ray space telescope mission. *The Astrophysical Journal*, 697(2):1071, 2009. doi: https://doi.org/10.1088/0004-637x/697/2/1071.

[9] G Ambrosi, Q An, R Asfandiyarov, P Azzarello, P Bernardini, B Bertucci, MS Cai, J Chang, DY Chen, HF Chen, et al. Direct detection of a break in the teraelectronvolt cosmic-ray spectrum of electrons and positrons. *Nature*, 552(7683):63, 2017. doi: https://doi.org/10.1038/nature24475.

[10] Dietrich Mueller, Simon P Swordy, Peter Meyer, Jacques L'Heureux, and John M Grunsfeld. Energy spectra and composition of primary cosmic rays. *The Astrophysical Journal*, 374:356–365, 1991.

[11] M. Aguilar, et al. (AMS Collaboration). The Alpha Magnetic Spectrometer (AMS) on the International Space Station: Part I – results from the test flight on the space shuttle. *Physics Reports*, 366(6):331–405, 2002. ISSN 0370-1573. doi: https://doi.org/10.1016/S0370-1573(02)00013-3.

[12] S Torii, CALET Collaboration, et al. The calet experiment on iss. *Nuclear Physics B-Proceedings Supplements*, 166:43–49, 2007. doi: https://doi.org/10.1016/j.nuclphysbps.2006.12.046.

[13] Gianpaolo Bellini, J Benziger, D Bick, S Bonetti, G Bonfini, M Buizza Avanzini, B Caccianiga, L Cadonati, Frank Calaprice, C Carraro, et al. Precision measurement of the be 7 solar neutrino interaction rate in borexino. *Physical Review Letters*, 107 (14):141302, 2011. doi: https://doi.org/10.1103/PhysRevLett.107.141302.

[14] Peter Anselmann, W Hampel, G Heusser, J Kiko, T Kirsten, M Laubenstein, E Pernicka, S Pezzoni, U Rönn, M Sann, et al. Gallex results from the first 30 solar neutrino runs. *Physics Letters B*, 327(3-4):377–385, 1994. doi: https://doi.org/10.1016/0370-2693(94)90744-7.

[15] D Kerszberg, M Kraus, D Kolitzus, K Egberts, S Funk, JP Lenain, O Reimer, and P Vincent. The cosmic-ray electron spectrum measured with hess. In *Talk at the 35th International Cosmic Ray Conference (ICRC), Busan, Korea*, 2017.

[16] AU Abeysekara, R Alfaro, C Alvarez, JD Álvarez, R Arceo, JC Arteaga-Velázquez, HA Ayala Solares, AS Barber, BM Baughman, N Bautista-Elivar, et al. Observation of small-scale anisotropy in the arrival direction distribution of tev cosmic rays with hawc. *The Astrophysical Journal*, 796(2):108, 2014. doi: https://doi.org/10.1088/0004-637x/796/2/108.

[17] Carl D Anderson. The positive electron. *Physical Review*, 43(6):491, 1933.

[18] Seth H Neddermeyer and Carl D Anderson. Note on the nature of cosmic-ray particles. *Physical Review*, 51(10):884, 1937.

[19] Cesare Mansueto Giulio Lattes, Hugh Muirhead, Giuseppe PS Occhialini, and Cecil Frank Powell. Processes involving charged mesons. *Nature*, 159(4047):694–697, 1947.

[20] GD ROCHESTERD and CC BUTLERD. Evidence for the existence of new unstable elementary particles. *Nature*, 160(4077):855–857, 1947.

[21] VD Hopper and S Biswas. Evidence concerning the existence of the new unstable elementary neutral particle. *Physical Review*, 80(6):1099, 1950.

[22] R Armenteros, KH Barker, CC Butler, A Cachon, and CM York. Lvi. the properties of charged v-particles. *The London, Edinburgh, and Dublin Philosophical Magazine and Journal of Science*, 43(341):597–611, 1952.

[23] G Di Sciascio, Lhaaso Collaboration, et al. The lhaaso experiment: from gamma-ray astronomy to cosmic rays. *Nuclear and particle physics proceedings*, 279:166–173, 2016. doi: https://doi.org/10.1016/j.nuclphysbps.2016.10.024.

[24] Pierre Auger Collaboration et al. The pierre auger cosmic ray observatory. *Nuclear Instruments and Methods in Physics Research Section A: Accelerators, Spectrometers, Detectors and Associated Equipment*, 798:172–213, 2015. doi: https://doi.org/10.1016/j.nima.2015.06.058.

[25] Carmelo Evoli. The cosmic-ray energy spectrum, December 2020.

[26] Domenico D'Urso. oscmic ray physics. *arXiv preprint arXiv:1411.4642*, 2014.

[27] Marius S Potgieter. Solar modulation of cosmic rays. *Living Reviews in Solar Physics*, 10(1):1–66, 2013. doi: https://doi.org/10.12942/lrsp-2013-3.

[28] Alexander Aab, Pedro Abreu, Marco Aglietta, Imen Al Samarai, IFM Albuquerque, Ingomar Allekotte, Alejandro Almela, J Alvarez Castillo, Jaime Alvarez-Muñiz, Gioacchino Alex Anastasi, et al. Observation of a large-scale anisotropy in the arrival directions of cosmic rays above 8× 1018 ev. *Science*, 357(6357):1266–1270, 2017. doi: 10.1126/science.aan4338.

[29] Thomas K Gaisser and Todor Stanev. High-energy cosmic rays. *Nuclear Physics A*, 777:98–110, 2006. doi: https://doi.org/10.1016/j.nuclphysa.2005.01.024.

[30] H. A. Bethe. Energy production in stars. *Phys. Rev.*, 55:434–456, Mar 1939. doi: 10.1103/PhysRev.55.434.

[31] Isabelle A. Grenier, John H. Black, and Andrew W. Strong. The nine lives of cosmic rays in galaxies. *Annual Review of Astronomy and Astrophysics*, 53(1):199–246, 2015. doi: 10.1146/annurev-astro-082214-122457.

[32] Jörg R Hörandel. Cosmic-ray composition and its relation to shock acceleration by supernova remnants. *Advances in Space Research*, 41(3):442–463, 2008. doi: https://doi.org/10.1016/j.asr.2007.06.008.

[33] AM Bykov, DC Ellison, A Marcowith, and SM Osipov. Cosmic ray production in supernovae. *Space Science Reviews*, 214(1):1–34, 2018. doi: https://doi.org/10.1007/s11214-018-0479-4.

[34] Stefano Gabici, Carmelo Evoli, Daniele Gaggero, Paolo Lipari, Philipp Mertsch, Elena Orlando, Andrew Strong, and Andrea Vittino. The origin of galactic cosmic rays: Challenges to the standard paradigm. *International Journal of Modern Physics D*, 28(15):1930022, 2019. doi: https://doi.org/10.1142/S0218271819300222.

[35] Pasquale Blasi. Recent results in cosmic ray physics and their interpretation. *Brazilian Journal of Physics*, 44(5):426–440, 2014. doi: 10.1007/s13538-014-0223-9.

[36] EA Helder, J Vink, AM Bykov, Y Ohira, JC Raymond, and R Terrier. Observational signatures of particle acceleration in supernova remnants. *Space Science Reviews*, 173(1-4):369–431, 2012. doi: https://doi.org/10.1007/s11214-012-9919-8.

[37] P. Slane, S.-H. Lee, D. C. Ellison, D. J. Patnaude, J. P. Hughes, K. A. Eriksen, D. Castro, and S. Nagataki. ERRATUM: "a CR-HYDRO-NEI MODEL OF THE STRUCTURE AND BROADBAND EMISSION FROMTYCHO's SUPERNOVA REMNANT" (2014, ApJ, 783, 33). *The Astrophysical Journal*, 799(2):238, feb 2015. doi: 10.1088/0004-637x/799/2/238.

[38] Markus Ackermann, Marco Ajello, A Allafort, Luca Baldini, Jean Ballet, Guido Barbiellini, MG Baring, D Bastieri, K Bechtol, R Bellazzini, et al. Detection of the characteristic pion-decay signature in supernova remnants. *Science*, 339(6121):807–811, 2013. doi: 10.1126/science.1231160.

[39] D Caprioli, E Amato, and P Blasi. The contribution of supernova remnants to the galactic cosmic ray spectrum. *Astroparticle Physics*, 33(3):160–168, 2010. doi: https://doi.org/10.1016/j.astropartphys.2010.01.002.

[40] L. Woltjer. Supernova remnants. *Annual Review of Astronomy and Astrophysics*, 10 (1):129–158, 1972. doi: https://doi.org/10.1146/annurev.aa.10.090172.001021.

[41] AR Bell. Cosmic ray acceleration. *Astroparticle Physics*, 43:56–70, 2013. doi: https://doi.org/10.1016/j.astropartphys.2012.05.022.

[42] Damiano Caprioli. Cosmic-ray acceleration and propagation. *arXiv preprint arXiv:1510.07042*, 2015.

[43] Elena Amato. The origin of galactic cosmic rays. *International Journal of Modern Physics D*, 23(07):1430013, 2014. doi: https://doi.org/10.1142/S0218271814300134.

[44] Vladimir Ptuskin. Cosmic ray transport in the galaxy. In *Journal of Physics: Conference Series*, volume 47, pages 113–119. Institute of Physics and IOP Publishing Limited, 2006.

[45] Andrew W Strong, Igor V Moskalenko, and Vladimir S Ptuskin. Cosmic-ray propagation and interactions in the galaxy. *Annu. Rev. Nucl. Part. Sci.*, 57:285–327, 2007. doi: https://doi.org/10.1146/annurev.nucl.57.090506.123011.

[46] VL Ginzburg, Ya M Khazan, and VS Ptuskin. Origin of cosmic rays: Galactic models with halo. *Astrophysics and Space Science*, 68(2):295–314, 1980. doi: https://doi.org/10.1007/BF00639701.

[47] VS Ptuskin, FC Jones, ES Seo, and R Sina. Effect of random nature of cosmic ray sources–supernova remnants–on cosmic ray intensity fluctuations, anisotropy, and electron energy spectrum. *Advances in Space Research*, 37(10):1909–1912, 2006. doi: https://doi.org/10.1016/j.asr.2005.08.036.

[48] Andrew W Strong and Igor V Moskalenko. Propagation of cosmic-ray nucleons in the galaxy. *The Astrophysical Journal*, 509(1):212, 1998. doi: https://doi.org/10.1086/306470.

[49] Carmelo Evoli, Daniele Gaggero, Andrea Vittino, Giuseppe Di Bernardo, Mattia Di Mauro, Arianna Ligorini, Piero Ullio, and Dario Grasso. Cosmic-ray propagation with dragon2: I. numerical solver and astrophysical ingredients. *Journal of Cosmology and Astroparticle Physics*, 2017(02):015, 2017. doi: https://doi.org/10.1088/1475-7516/2017/02/015.

[50] Ralf Kissmann. Picard: A novel code for the galactic cosmic ray propagation problem. *Astroparticle Physics*, 55:37–50, 2014. doi: https://doi.org/10.1016/j.astropartphys.2014.02.002.

[51] David Maurin. Usine: Semi-analytical models for galactic cosmic-ray propagation. *Computer Physics Communications*, 247:106942, 2020. doi: https://doi.org/10.1016/j.cpc.2019.106942.

[52] Elena Orlando, Gudlaugur Johannesson, Igor V Moskalenko, Troy A Porter, and Andrew Strong. Galprop cosmic-ray propagation code: recent results and updates. *Nuclear and Particle Physics Proceedings*, 297:129–134, 2018. doi: https://doi.org/10.1016/j.nuclphysbps.2018.07.020.

[53] WR Webber and A Soutoul. A study of the surviving fraction of the cosmic-ray radioactive decay isotopes 10be, 26al, 36cl and 54mn as a function of energy using the charge ratios be/b, al/mg, cl/ar, and mn/fe measured on heao 3. *The Astrophysical Journal*, 506(1):335, 1998. doi: https://doi.org/10.1086/306224.

[54] VS Ptuskin, ON Strelnikova, and LG Sveshnikova. On leaky-box approximation to galprop. *Astroparticle Physics*, 31(4):284–289, 2009. doi: https://doi.org/10.1016/j.astropartphys.2009.02.004.

[55] DW Sciama. On the interaction between cosmic rays and dark matter molecular clouds in the milky way—ii. the age distribution of cosmic ray electrons. *Monthly Notices of the Royal Astronomical Society*, 319(4):1001–1004, 2000. doi: https://doi.org/10.1046/j.1365-8711.2000.03586.x.

[56] Fiorenza Donato, David Maurin, and Richard Taillet. β–radioactive cosmic rays in a diffusion model: test for a local bubble? *Astronomy & Astrophysics*, 381(2):539–559, 2002.

[57] David Maurin, Hans Peter Dembinski, Javier Gonzalez, Ioana Codrina Mariş, and Frédéric Melot. Cosmic-Ray Database Update: Ultra-High Energy, Ultra-Heavy, and Antinuclei Cosmic-Ray Data (CRDB v4.0). *Universe*, 6(8), 2020. ISSN 2218-1997. doi: https://doi.org/10.3390/universe6080102.

[58] D Maurin, F Melot, and Richard Taillet. A database of charged cosmic rays. *Astronomy & Astrophysics*, 569:A32, 2014. doi: https://doi.org/10.1051/0004-6361/201321344.

[59] Nathan Eugene Yanasak, ME Wiedenbeck, RA Mewaldt, AJ Davis, AC Cummings, JS George, RA Leske, EC Stone, ER Christian, TT Von Rosenvinge, et al. Measurement of the secondary radionuclides 10be, 26al, 36cl, 54mn, and 14c and implications for the galactic cosmic-ray age. *The Astrophysical Journal*, 563(2):768, 2001. doi: https://doi.org/10.1086/323842.

[60] Kfir Blum. Cosmic ray propagation time scales: lessons from radioactive nuclei and positron data. *Journal of Cosmology and Astroparticle Physics*, 2011(11):037, 2011. doi: https://doi.org/10.1088/1475-7516/2011/11/037.

[61] M. Aguilar, et al. (AMS Collaboration). First Result from the Alpha Magnetic Spectrometer on the International Space Station: Precision Measurement of the Positron Fraction in Primary Cosmic Rays of 0.5–350 GeV. *Phys. Rev. Lett.*, 110:141102, Apr 2013. doi: https://doi.org/10.1103/PhysRevLett.110.141102.

[62] M. Aguilar, et al. (AMS Collaboration). Electron and Positron Fluxes in Primary Cosmic Rays Measured with the Alpha Magnetic Spectrometer on the International Space Station. *Phys. Rev. Lett.*, 113:121102, Sep 2014. doi: https://doi.org/10.1103/PhysRevLett.113.121102.

[63] M. Aguilar, et al. (AMS Collaboration). Antiproton Flux, Antiproton-to-Proton Flux Ratio, and Properties of Elementary Particle Fluxes in Primary Cosmic Rays Measured with the Alpha Magnetic Spectrometer on the International Space Station. *Phys. Rev. Lett.*, 117:091103, Aug 2016. doi: https://doi.org/10.1103/PhysRevLett.117.091103.

[64] M. Aguilar, et al. (AMS Collaboration). Towards Understanding the Origin of Cosmic-Ray Positrons. *Phys. Rev. Lett.*, 122:041102, Jan 2019. doi: https://doi.org/10.1103/PhysRevLett.122.041102.

[65] M. Aguilar, et al. (AMS Collaboration). The Alpha Magnetic Spectrometer (AMS) on the international space station: Part II — Results from the first seven years. *Physics Reports*, 894:1–116, 2021. ISSN 0370-1573. doi: https://doi.org/10.1016/j.physrep.2020.09.003.

[66] Mathieu Boudaud, Sandy Aupetit, Sami Caroff, Antje Putze, Genevieve Belanger, Yoann Genolini, Corrine Goy, Vincent Poireau, Vivian Poulin, S Rosier, et al. A new look at the cosmic ray positron fraction. *Astronomy & Astrophysics*, 575:A67, 2015. doi: https://doi.org/10.1051/0004-6361/201425197.

[67] DS Akerib, S Alsum, HM Araújo, X Bai, AJ Bailey, J Balajthy, P Beltrame, EP Bernard, A Bernstein, TP Biesiadzinski, et al. Results from a search for dark matter in the complete lux exposure. *Physical review letters*, 118(2):021303, 2017. doi: 10.1103/PhysRevLett.118.021303.

[68] Xiangyi Cui, Abdusalam Abdukerim, Wei Chen, Xun Chen, Yunhua Chen, Binbin Dong, Deqing Fang, Changbo Fu, Karl Giboni, Franco Giuliani, et al. Dark matter results from 54-ton-day exposure of pandax-ii experiment. *Physical review letters*, 119(18):181302, 2017. doi: 10.1103/PhysRevLett.119.181302.

[69] MG ea Aartsen, M Ackermann, J Adams, JA Aguilar, M Ahlers, M Ahrens, D Altmann, T Anderson, C Arguelles, TC Arlen, et al. Observation of high-energy astrophysical neutrinos in three years of icecube data. *Physical review letters*, 113(10):101101, 2014. doi: 10.1103/PhysRevLett.113.101101.

[70] S Desai, Y Ashie, S Fukuda, Y Fukuda, K Ishihara, Y Itow, Y Koshio, A Minamino, M Miura, S Moriyama, et al. Search for dark matter wimps using upward through-going muons in super-kamiokande. *Physical Review D*, 70(8):083523, 2004. doi: 10.1103/PhysRevD.70.083523.

[71] D. Grasso, S. Profumo, A.W. Strong, L. Baldini, R. Bellazzini, E.D. Bloom, J. Bregeon, G. Di Bernardo, D. Gaggero, N. Giglietto, T. Kamae, L. Latronico, F. Longo, M.N. Mazziotta, A.A. Moiseev, A. Morselli, J.F. Ormes, M. Pesce-Rollins, M. Pohl, M. Razzano, C. Sgro, G. Spandre, and T.E. Stephens. On possible interpretations of the high energy electron–positron spectrum measured by the fermi large area telescope. *Astroparticle Physics*, 32(2):140–151, 2009. ISSN 0927-6505. doi: https://doi.org/10.1016/j.astropartphys.2009.07.003.

[72] F Aharonian, AG Akhperjanian, G Anton, U Barres De Almeida, AR Bazer-Bachi, Yvonne Becherini, B Behera, K Bernlöhr, A Bochow, C Boisson, et al. Probing the atic peak in the cosmic-ray electron spectrum with hess. *Astronomy & Astrophysics*, 508(2):561–564, 2009. doi: https://doi.org/10.1051/0004-6361/200913323.

[73] Dan Hooper, Pasquale Blasi, and Pasquale Dario Serpico. Pulsars as the sources of high energy cosmic ray positrons. *Journal of Cosmology and Astroparticle Physics*, 2009(01):025, 2009. doi: https://doi.org/10.1088/1475-7516/2009/01/025.

[74] Hasan Yüksel, Matthew D Kistler, and Todor Stanev. Tev gamma rays from geminga and the origin of the gev positron excess. *Physical review letters*, 103(5):051101, 2009. doi: https://doi.org/10.1103/PhysRevLett.103.051101.

[75] Tim Linden and Stefano Profumo. Probing the pulsar origin of the anomalous positron fraction with ams-02 and atmospheric cherenkov telescopes. *The Astrophysical Journal*, 772(1):18, 2013. doi: https://doi.org/10.1088/0004-637x/772/1/18.

[76] AU Abeysekara, A Albert, R Alfaro, C Alvarez, JD Álvarez, R Arceo, JC Arteaga-Velázquez, D Avila Rojas, HA Ayala Solares, AS Barber, et al. Extended gamma-ray sources around pulsars constrain the origin of the positron flux at earth. *Science*, 358 (6365):911–914, 2017. doi: 10.1126/science.aan4880.

[77] J-F Glicenstein et al. The cherenkov telescope array, an advanced facility for ground based gamma-ray astronomy. *Nuclear Instruments and Methods in Physics Research Section A: Accelerators, Spectrometers, Detectors and Associated Equipment*, 639(1): 46–49, 2011. doi: https://doi.org/10.1016/j.nima.2010.10.056.

[78] Pasquale Blasi and Pasquale D Serpico. High-energy antiprotons from old supernova remnants. *Physical Review Letters*, 103(8):081103, 2009. doi: https://doi.org/10.1103/PhysRevLett.103.081103.

[79] V Bresci, E Amato, P Blasi, and G Morlino. Effects of re-acceleration and source grammage on secondary cosmic rays spectra. *Monthly Notices of the Royal Astronomical Society*, 488(2):2068–2078, 07 2019. ISSN 0035-8711. doi: 10.1093/mnras/stz1806.

[80] Kfir Blum, Boaz Katz, and Eli Waxman. Ams-02 results support the secondary origin of cosmic ray positrons. *Physical review letters*, 111(21):211101, 2013. doi: https://doi.org/10.1103/PhysRevLett.111.211101.

[81] M. Aguilar, et al. (AMS Collaboration). Observation of the identical rigidity dependence of He, C, and O cosmic rays at high rigidities by the Alpha Magnetic Spectrometer on the International Space Station. *Physical review letters*, 119(25):251101, 2017. doi: https://doi.org/10.1103/PhysRevLett.119.251101.

[82] M. Aguilar, et al. (AMS Collaboration). Observation of New Properties of Secondary Cosmic Rays Lithium, Beryllium, and Boron by the Alpha Magnetic Spectrometer on the International Space Station. *Phys. Rev. Lett.*, 120:021101, Jan 2018. doi: https://doi.org/10.1103/PhysRevLett.120.021101.

[83] M. Aguilar, et al. (AMS Collaboration). Precision Measurement of Cosmic-Ray Nitrogen and its Primary and Secondary Components with the Alpha Magnetic Spectrometer on the International Space Station. *Phys. Rev. Lett.*, 121:051103, Jul 2018. doi: https://doi.org/10.1103/PhysRevLett.121.051103.

[84] Pasquale Dario Serpico. Entering the cosmic ray precision era. *Journal of Astrophysics and Astronomy*, 39(4):1–8, 2018. doi: https://doi.org/10.1007/s12036-018-9532-7.

[85] K. Lübelsmeyer, A. Schultz von Dratzig, M. Wlochal, G. Ambrosi, P. Azzarello, R. Battiston, R. Becker, U. Becker, B. Bertucci, K. Bollweg, J.D. Burger, F. Cadoux, X.D. Cai, M. Capell, V. Choutko, M. Duranti, C. Gargiulo, C. Guandalini, S. Haino, M. Ionica, A. Koulemzine, A. Kounine, V. Koutsenko, G. Laurenti, A. Lebedev, T. Martin, A. Oliva, M. Paniccia, E. Perrin, D. Rapin, A. Rozhkov, St. Schael, H. Tholen, S.C.C. Ting, and P. Zuccon. Upgrade of the Alpha Magnetic Spectrometer (AMS-02) for long term operation on the International Space Station (ISS). *Nuclear Instruments and Methods in Physics Research Section A: Accelerators, Spectrometers, Detectors and Associated Equipment*, 654(1):639–648, 2011. ISSN 0168-9002. doi: https://doi.org/10.1016/j.nima.2011.06.051.

[86] K Lübelsmeyer, A Schultz von Dratzig, M Wlochal, G Ambrosi, P Azzarello, R Battiston, R Becker, U Becker, B Bertucci, K Bollweg, et al. Upgrade of the alpha magnetic spectrometer (ams-02) for long term operation on the international space station (iss). *Nuclear Instruments and Methods in Physics Research Section A: Accelerators, Spectrometers, Detectors and Associated Equipment*, 654(1):639–648, 2011. doi: https://doi.org/10.1016/j.nima.2011.06.051.

[87] J. Alcaraz, B. Alpat, G. Ambrosi, Ph. Azzarello, R. Battiston, B. Bertucci, J. Bolmont, et al. The alpha magnetic spectrometer silicon tracker: Performance results with protons and helium nuclei. *Nuclear Instruments and Methods in Physics Research Section A: Accelerators, Spectrometers, Detectors and Associated Equipment*, 593(3): 376–398, 2008. ISSN 0168-9002. doi: https://doi.org/10.1016/j.nima.2008.05.015.

[88] Y Jia, Q Yan, V Choutko, H Liu, and A Oliva. Nuclei charge measurement by the Alpha Magnetic Spectrometer silicon tracker. *Nuclear Instruments and Methods in Physics Research Section A: Accelerators, Spectrometers, Detectors and Associated Equipment*, 972:164169, 2020. doi: https://doi.org/10.1016/j.nima.2020.164169.

[89] G Ambrosi, V Choutko, C Delgado, A Oliva, Q Yan, and Yang Li. The spatial resolution of the silicon tracker of the Alpha Magnetic Spectrometer. *Nuclear Instruments and Methods in Physics Research Section A: Accelerators, Spectrometers, Detectors and Associated Equipment*, 869:29–37, 2017. doi: https://doi.org/10.1016/j.nima.2017.07.014.

[90] V. Bindi, G.M. Chen, H.S. Chen, E. Choumilov, V. Choutko, A. Contin, A. Lebedev, Y.S. Lu, N. Masi, A. Oliva, F. Palmonari, L. Quadrani, and Q. Yan. Calibration and

performance of the ams-02 time of flight detector in space. *Nuclear Instruments and Methods in Physics Research Section A: Accelerators, Spectrometers, Detectors and Associated Equipment*, 743:22–29, 2014. ISSN 0168-9002. doi: https://doi.org/10.1016/j.nima.2014.01.002.

[91] C. Adloff, L. Basara, G. Bigongiari, F. Bosi, P. Brun, F. Cadoux, F. Cervelli, V. Chambert, et al. The AMS-02 lead-scintillating fibres Electromagnetic Calorimeter. *Nuclear Instruments and Methods in Physics Research Section A: Accelerators, Spectrometers, Detectors and Associated Equipment*, 714:147–154, 2013. ISSN 0168-9002. doi: https://doi.org/10.1016/j.nima.2013.02.020.

[92] Ph von Doetinchem, W Karpinski, Th Kirn, K Lübelsmeyer, St Schael, and M Wlochal. The AMS-02 Anticoincidence Counter. *Nuclear Physics B Proceedings Supplements*, 197(1):15–18, 2009. doi: https://doi.org/10.1016/j.nuclphysbps.2009.10.025.

[93] C. Adloff, L. Basara, G. Bigongiari, F. Bosi, P. Brun, F. Cadoux, et al. The AMS-02 lead-scintillating fibres Electromagnetic Calorimeter. *Nuclear Instruments and Methods in Physics Research Section A: Accelerators, Spectrometers, Detectors and Associated Equipment*, 714:147–154, 2013. ISSN 0168-9002. doi: https://doi.org/10.1016/j.nima.2013.02.020.

[94] A. Basili, V. Bindi, D. Casadei, G. Castellini, A. Contin, A. Kounine, M. Lolli, F. Palmonari, and L. Quadrani. The TOF-ACC flight electronics for the fast trigger and time of flight of the AMS-02 cosmic ray spectrometer. *Nuclear Instruments and Methods in Physics Research Section A: Accelerators, Spectrometers, Detectors and Associated Equipment*, 707:99–113, 2013. ISSN 0168-9002. doi: https://doi.org/10.1016/j.nima.2012.12.089.

[95] Sadakazu Haino. Performance of the ams-02 silicon tracker in the iss mission. *Nuclear Instruments and Methods in Physics Research Section A: Accelerators, Spectrometers, Detectors and Associated Equipment*, 699:221–224, 2013. ISSN 0168-9002. doi: https://doi.org/10.1016/j.nima.2012.05.060. Proceedings of the 8th International "Hiroshima" Symposium on the Development and Application of Semiconductor Tracking Detectors.

[96] Christopher Charles Finlay, Stefan Maus, CD Beggan, TN Bondar, A Chambodut, TA Chernova, A Chulliat, VP Golovkov, B Hamilton, Mohamed Hamoudi, et al. International geomagnetic reference field: the eleventh generation. *Geophysical Journal International*, 183(3):1216–1230, 2010. doi: https://doi.org/10.1111/j.1365-246X.2010.04804.x.

[97] Erwan Thébault, Christopher C Finlay, Ciarán D Beggan, Patrick Alken, Julien Aubert, Olivier Barrois, Francois Bertrand, Tatiana Bondar, Axel Boness, Laura Brocco, et al. International geomagnetic reference field: the 12th generation. *Earth, Planets and Space*, 67(1):1–19, 2015. doi: https://doi.org/10.1186/s40623-015-0228-9.

[98] J Alcaraz, B Alpat, G Ambrosi, H Anderhub, L Ao, A Arefiev, P Azzarello, E Babucci, Luca Baldini, M Basile, et al. Leptons in near earth orbit. *Physics Letters B*, 484(1-2):10–22, 2000. doi: https://doi.org/10.1016/S0370-2693(00)00588-8.

[99] D Grandi, B Bertucci45, MJ Boschini13, M Crispoltoni45, S Della Torre, F Donnini45, M Duranti45, D D'Urso56, E Fiandrini45, V Formato, et al. Trajectory reconstruction in the earth magnetosphere using ts05 model and evaluation of geomagnetic cutoff in ams-02 data. In *34th International Cosmic Ray Conference (ICRC2015)*, volume 34, page 116, 2015.

[100] W. Li and M.K. Hudson. Earth's van allen radiation belts: From discovery to the van allen probes era. *Journal of Geophysical Research: Space Physics*, 124(11):8319–8351, 2019. doi: https://doi.org/10.1029/2018JA025940.

[101] M. Aguilar, et al. (AMS Collaboration). Precision measurement of the Helium flux in primary cosmic rays of rigidities 1.9 GV to 3 TV with the Alpha Magnetic Spectrometer on the International Space Station. *Physical review letters*, 115(21):211101, 2015. doi: https://doi.org/10.1103/PhysRevLett.115.211101.

[102] Q. Yan, V. Choutko, A. Oliva, and M. Paniccia. Measurements of nuclear interaction cross sections with the Alpha Magnetic Spectrometer on the International Space Station. *Nuclear Physics A*, 996:121712, 2020. ISSN 0375-9474. doi: https://doi.org/10.1016/j.nuclphysa.2020.121712.

[103] Sea Agostinelli, John Allison, K al Amako, John Apostolakis, H Araujo, P Arce, M Asai, D Axen, S Banerjee, G 2 Barrand, et al. Geant4—a simulation toolkit. *Nuclear instruments and methods in physics research section A: Accelerators, Spectrometers, Detectors and Associated Equipment*, 506(3):250–303, 2003. doi: https://doi.org/10.1016/S0168-9002(03)01368-8.

[104] John Allison, Katsuya Amako, JEA Apostolakis, HAAH Araujo, P Arce Dubois, MAAM Asai, GABG Barrand, RACR Capra, SACS Chauvie, RACR Chytracek, et al. Geant4 developments and applications. *IEEE Transactions on nuclear science*, 53(1):270–278, 2006. doi: 10.1109/TNS.2006.869826.

[105] J Allison, Katsuya Amako, John Apostolakis, Pedro Arce, M Asai, T Aso, E Bagli, A Bagulya, S Banerjee, GJNI Barrand, et al. Recent developments in geant4. *Nuclear Instruments and Methods in Physics Research Section A: Accelerators, Spectrometers, Detectors and Associated Equipment*, 835:186–225, 2016. doi: https://doi.org/10.1016/j.nima.2016.06.125.

[106] M. Aguilar, et al. (AMS Collaboration). Properties of Neon, Magnesium, and Silicon Primary Cosmic Rays Results from the Alpha Magnetic Spectrometer. *Phys. Rev. Lett.*, 124:211102, May 2020. doi: https://doi.org/10.1103/PhysRevLett.124.211102.

[107] M. Aguilar, et al. (AMS Collaboration). Precision Measurement of the Proton Flux in Primary Cosmic Rays from Rigidity 1 GV to 1.8 TV with the Alpha Magnetic Spectrometer on the International Space Station. *Phys. Rev. Lett.*, 114:171103, Apr 2015. doi: https://doi.org/10.1103/PhysRevLett.114.171103.

[108] M. Aguilar, et al. (AMS Collaboration). Precision measurement of the Boron to Carbon flux ratio in cosmic rays from 1.9 GV to 2.6 TV with the Alpha Magnetic Spectrometer on the International Space Station. *Physical Review Letters*, 117(23):231102, 2016. doi: https://doi.org/10.1103/PhysRevLett.117.231102.

[109] Wouter Verkerke and David Kirkby. The roofit toolkit for data modeling. In *Statistical Problems in Particle Physics, Astrophysics and Cosmology*, pages 186–189. World Scientific, 2006. doi: https://doi.org/10.1142/9781860948985_0039.

[110] Ilka Antcheva, Maarten Ballintijn, Bertrand Bellenot, Marek Biskup, Rene Brun, Nenad Buncic, Ph Canal, Diego Casadei, Olivier Couet, Valery Fine, et al. Root—a c++ framework for petabyte data storage, statistical analysis and visualization. *Computer Physics Communications*, 182(6):1384–1385, 2011. doi: https://doi.org/10.1016/j.cpc.2011.02.008.

[111] S. Purushothaman, S. Ayet San Andrés, J. Bergmann, T. Dickel, J. Ebert, H. Geissel, C. Hornung, W.R. Plaß, C. Rappold, C. Scheidenberger, Y.K. Tanaka, and M.I. Yavor. Hyper-emg: A new probability distribution function composed of exponentially modified gaussian distributions to analyze asymmetric peak shapes in high-resolution time-of-flight mass spectrometry. *International Journal of Mass Spectrometry*, 421: 245–254, 2017. ISSN 1387-3806. doi: https://doi.org/10.1016/j.ijms.2017.07.014.

[112] John Betteley Birks. *The theory and practice of scintillation counting: International series of monographs in electronics and instrumentation*, volume 27. Elsevier, 2013.

[113] V. Bindi, G.M. Chen, H.S. Chen, E. Choumilov, V. Choutko, A. Contin, A. Lebedev, Y.S. Lu, N. Masi, A. Oliva, F. Palmonari, L. Quadrani, and Q. Yan. Calibration and performance of the AMS-02 time of flight detector in space. *Nuclear Instruments and Methods in Physics Research Section A: Accelerators, Spectrometers, Detectors and Associated Equipment*, 743:22–29, 2014. ISSN 0168-9002. doi: https://doi.org/10.1016/j.nima.2014.01.002.

[114] Laurent Basara, Vitaly Choutko, and Qiang Li. Light nuclear charge measurement with Alpha Magnetic Spectrometer Electromagnetic Calorimeter. *Nuclear Instruments and Methods in Physics Research Section A: Accelerators, Spectrometers, Detectors and Associated Equipment*, 821:23–27, 2016. ISSN 0168-9002. doi: https://doi.org/10.1016/j.nima.2016.03.047.

[115] J. Berdugo, V. Choutko, C. Delgado, and Q. Yan. Determination of the rigidity scale of the Alpha Magnetic Spectrometer. *Nuclear Instruments and Methods in Physics Research Section A: Accelerators, Spectrometers, Detectors and Associated Equipment*, 869:10–14, 2017. ISSN 0168-9002. doi: https://doi.org/10.1016/j.nima.2017.07.012.

[116] G.D. Lafferty and T.R. Wyatt. Where to stick your data points: The treatment of measurements within wide bins. *Nuclear Instruments and Methods in Physics Research Section A: Accelerators, Spectrometers, Detectors and Associated Equipment*, 355 (2):541–547, 1995. ISSN 0168-9002. doi: https://doi.org/10.1016/0168-9002(94)01112-5.

[117] WR Webber, JC Kish, and DA Schrier. Cosmic ray isotope measurements with a new cerenkov x total energy telescope. In *19th International Cosmic Ray Conference (ICRC19), Volume 2*, volume 2, 1985.

[118] Isabelle A Grenier, John H Black, and Andrew W Strong. The nine lives of cosmic rays in galaxies. *Annual Review of Astronomy and Astrophysics*, 53, 2015. doi: https://doi.org/10.1146/annurev-astro-082214-122457.

[119] Pasquale Blasi. The origin of galactic cosmic rays. *The Astronomy and Astrophysics Review*, 21(1):70, 2013. doi: 10.1007/s00159-013-0070-7.

[120] WR Webber. The charge and isotopic composition of z= 6-14 cosmic ray nuclei at their source. *The Astrophysical Journal*, 252:386–392, 1982.

[121] M. Aguilar, et al. (AMS Collaboration). Properties of a new group of cosmic nuclei: Results from the alpha magnetic spectrometer on sodium, aluminum, and nitrogen. *Physical Review Letters*, 127:021101, Jul 2021. doi: https://link.aps.org/doi/10.1103/PhysRevLett.127.021101.

[122] Kfir Blum, Yao Chen, Zhen Liu, Mercedes Paniccia, and Jiahui Wei. Reading the time in cosmic ray clocks. unpublished, 2021.

[123] Boaz Katz, Kfir Blum, Jonathan Morag, and Eli Waxman. What can we really learn from positron flux 'anomalies'? *Monthly Notices of the Royal Astronomical Society*, 405(3):1458–1472, 06 2010. ISSN 0035-8711. doi: https://doi.org/10.1111/j.1365-2966.2010.16568.x.

[124] M. Aguilar, et al. (AMS Collaboration). Properties of Heavy Secondary Fluorine Cosmic Rays: Results from the Alpha Magnetic Spectrometer. *Phys. Rev. Lett.*, 126:081102, Feb 2021. doi: https://doi.org/10.1103/PhysRevLett.126.081102.

[125] M. Aguilar, et al. (AMS Collaboration). Properties of Iron Primary Cosmic Rays: Results from the Alpha Magnetic Spectrometer. *Physical Review Letters*, 126(4):041104, 2021. doi: https://doi.org/10.1103/PhysRevLett.126.041104.

[126] P Ferrando, WR Webber, P Goret, JC Kish, DA Schrier, A Soutoul, and O Testard. Measurement of c 12, o 16, and fe 56 charge changing cross sections in helium at high energy, comparison with cross sections in hydrogen, and application to cosmic-ray propagation. *Physical Review C*, 37(4):1490, 1988. doi: https://doi.org/10.1103/PhysRevC.37.1490.

[127] F. Gahbauer, G. Hermann, J. R. Horandel, D. Muller, and A. A. Radu. A new measurement of the intensities of the heavy primary cosmic-ray nuclei around 1 TeV amu-1. *The Astrophysical Journal*, 607(1):333–341, may 2004. doi: https://doi.org/10.1086/383304.

[128] J. Young, P. Freier, C. Waddington, N. Brewster, and R. Fickle. The elemental and isotopic composition of cosmic rays - silicon to nickel. *The Astrophysical Journal*, 246:1014–1030, June 1981. doi: 10.1086/158997.

[129] Yoann Génolini, David Maurin, Igor V Moskalenko, and Michael Unger. Current status and desired precision of the isotopic production cross sections relevant to astrophysics of cosmic rays: Li, be, b, c, and n. *Physical Review C*, 98(3):034611, 2018. doi: https://doi.org/10.1103/PhysRevC.98.034611.

[130] WR Webber, JC Kish, JM Rockstroh, Y Cassagnou, R Legrain, A Soutoul, O Testard, and C Tull. Production cross sections of fragments from beams of 400-650 mev per nucleon 9be, 11b, 12c, 14n, 15n, 16o, 20ne, 22ne, 56fe, and 58ni nuclei interacting in a liquid hydrogen target. ii. isotopic cross sections of fragments. *The Astrophysical Journal*, 508(2):949, 1998. doi: https://doi.org/10.1086/306446.

[131] A Korejwo, T Dzikowski, M Giller, J Wdowczyk, V V Perelygin, and A V Zarubin. The measurement of isotopic cross sections of12c beam fragmentation on liquid hydrogen at 3.66 GeV/nucleon. *Journal of Physics G: Nuclear and Particle Physics*, 26 (8):1171–1186, jun 2000. doi: https://doi.org/10.1088/0954-3899/26/8/306.

[132] WR Webber, JC Kish, and DA Schrier. Individual isotopic fragmentation cross sections of relativistic nuclei in hydrogen, helium, and carbon targets. *Physical Review C*, 41(2):547, 1990. doi: https://doi.org/10.1103/PhysRevC.41.547.

[133] Reuven Ramaty, Benzion Kozlovsky, Richard E. Lingenfelter, and Hubert Reeves. Light elements and cosmic rays in the early galaxy. *The Astrophysical Journal*, 488 (2):730–748, oct 1997. doi: https://doi.org/10.1086/304744.

[134] DL Olson, BL Berman, DE Greiner, HH Heckman, PJ Lindstrom, and HJ Crawford. Factorization of fragment-production cross sections in relativistic heavy-ion collisions. *Physical Review C*, 28(4):1602, 1983.

[135] Igor V Moskalenko and Andrew W Strong. Galprop code. https://galprop.stanford.edu/code.php, 2017.

[136] C-X Chen, S Albergo, Z Caccia, S Costa, HJ Crawford, M Cronqvist, J Engelage, L Greiner, TG Guzik, A Insolia, et al. Relativistic interaction of 22ne and 26mg in hydrogen and the cosmic-ray implications. *The Astrophysical Journal*, 479(1):504, 1997. doi: https://doi.org/10.1086/303881.

[137] P. Napolitani, K.-H. Schmidt, A. S. Botvina, F. Rejmund, L. Tassan-Got, and C. Villagrasa. High-resolution velocity measurements on fully identified light nuclides produced in ^{56}Fe + hydrogen and ^{56}Fe + titanium systems. *Phys. Rev. C*, 70:054607, Nov 2004. doi: 10.1103/PhysRevC.70.054607.

[138] GM Raisbeck, J Lestringuez, and F Yiou. Production of 7 be, 9 be and 10 be in the spallation of 13 c by protons of 150 and 600 mev. *Nature Physical Science*, 244(132): 28–30, 1973. doi: https://doi.org/10.1038/physci244028a0.

[139] Jonathan R Radin, Elie Gradsztajn, and Alan R Smith. Be 7 production cross sections in n, c, b 11, and b 10 with 740 mev protons. *Physical Review C*, 20(2):787, 1979. doi: https://doi.org/10.1103/PhysRevC.20.787.

[140] A.E. Vladimirov, S.W. Digel, G. Jóhannesson, P.F. Michelson, I.V. Moskalenko, P.L. Nolan, E. Orlando, T.A. Porter, and A.W. Strong. Galprop webrun: An internet-based service for calculating galactic cosmic ray propagation and associated photon emissions. *Computer Physics Communications*, 182(5):1156–1161, 2011. ISSN 0010-4655. doi: https://doi.org/10.1016/j.cpc.2011.01.017.

[141] WR Webber, A Soutoul, JC Kish, JM Rockstroh, Y Cassagnou, R Legrain, and O Testard. Measurement of charge changing and isotopic cross sections at 600 mev/nucleon from the interactions of 30 separate beams of relativistic nuclei from 10 b to 55 mn in a liquid hydrogen target. *Physical Review C*, 58(6):3539, 1998. doi: https://doi.org/10.1103/PhysRevC.58.3539.

[142] CN Knott, S Albergo, Z Caccia, C-X Chen, S Costa, HJ Crawford, M Cronqvist, J Engelage, L Greiner, TG Guzik, et al. Interactions of relativistic 36 ar and 40 ar nuclei in hydrogen: Isotopic production cross sections. *Physical Review C*, 56(1): 398, 1997. doi: https://doi.org/10.1103/PhysRevC.56.398.

[143] C-X Chen, S Albergo, Z Caccia, S Costa, HJ Crawford, M Cronqvist, J Engelage, L Greiner, TG Guzik, A Insolia, et al. Systematics of isotopic production cross sections from interactions of relativistic 40 ca in hydrogen. *Physical Review C*, 56(3): 1536, 1997. doi: https://doi.org/10.1103/PhysRevC.56.1536.

[144] C Villagrasa-Canton, A Boudard, J-E Ducret, B Fernandez, S Leray, C Volant, P Armbruster, Timo Enqvist, F Hammache, K Helariutta, et al. Spallation residues in the reaction fe 56+ p at 0.3 a, 0.5 a, 0.75 a, 1.0 a, and 1.5 a gev. *Physical Review C*, 75 (4):044603, 2007. doi: https://doi.org/10.1103/PhysRevC.75.044603.

Appendix A

Cosmic-ray isotopic composition data

The isotopic composition of cosmic-ray nuclei needed to compute the decay suppression factor of the radioactive isotopes ^{10}Be and ^{26}Al elements are listed in Table A.1. The data is taken from [129] and CRDB [57, 58] by choosing the data with the highest energy and/or from the most precise measurement. The errors on the isotopic compositions are typically $\sim 15\%$, which will result in $\sim 5\%$ rigidity independent errors on the cross sections.

Table A.1 Isotopic composition of the most abundant cosmic-ray nuclei from Be to Fe.

Element	**Isotopic composition**			
Be (Z=4)	63% ^{7}Be	30% ^{9}Be	6% ^{10}Be	
B (Z=5)	33% ^{10}B	67% ^{11}B		
C (Z=6)	90% ^{12}C	10% ^{13}C		
N (Z=7)	54% ^{15}N	46% ^{16}N		
O (Z=8)	94.4% ^{16}O	2.8% ^{17}O	2.6% ^{18}O	
F (Z=9)	100% ^{19}F			
Ne (Z=10)	54.7% ^{20}Ne	10.6% ^{21}Ne	34.7% ^{22}Ne	
Na (Z=11)	3.7% ^{22}Na	96.3% ^{23}Na		
Mg (Z=12)	64.8% ^{24}Mg	17.5% ^{25}Mg	17.7% ^{26}Mg	
Al (Z=13)	2.2% ^{26}Al	97.8% ^{27}Al		
Si (Z=14)	88.7% ^{28}Si	5.9% ^{29}Si	5.4% ^{30}Si	
P (Z=15)	100% ^{31}P			
S (Z=16)	69.9% ^{32}S	14.5% ^{33}S	15.6% ^{34}S	
Ar (Z=18)	63.7% ^{36}Ar	31.4% ^{38}Ar	2.2% ^{40}Ar	
Ca (Z=20)	46.9% ^{40}Ca	23.8% ^{42}Ca	14.3% ^{43}Ca	10.9% ^{44}Ca
Fe (Z=26)	6.9% ^{54}Fe	93.1% ^{56}Fe		

Appendix B

Nuclei fragmentation cross section data

The fragmentation cross sections for B, Be, Al and Mg are listed in Table B.1, Table B.2, Table B.3, Table B.4.

B.1 B (and ghost C) cross sections

Fragmentation cross sections for B production are listed in Table B.1. Short-lived radioisotopes ^{11}C, and ^{10}C contribute to the production cross sections of ^{11}B, and ^{10}B :

- $^{11}\mathrm{C} \rightarrow ^{11}$ B with the half-life $t_{1/2} = 20.36 min$ and branching ratio $Br = 1$
- $^{10}\mathrm{C} \rightarrow ^{10}$ B with the half-life $t_{1/2} = 19.3 s$ and branching ratio $Br = 1$

Table B.1 Fragmentation cross sections for B production.

reaction	σ [mb]	k $\left[\frac{\mathrm{GeV}}{\mathrm{nuc}}\right]$	Ref
$^{11}\mathrm{B}\rightarrow^{10}\mathrm{B}$	46.2 ± 9.24	0.365	[130]
$^{12}\mathrm{C}\rightarrow^{11}\mathrm{C}$	29.2 ± 2.5	3.66	[131]
$^{12}\mathrm{C}\rightarrow^{11}\mathrm{B}$	27.7 ± 0.7	3.66	[131]
$^{12}\mathrm{C}\rightarrow^{10}\mathrm{C}$	3.6 ± 0.5	3.66	[131]
$^{12}\mathrm{C}\rightarrow^{10}\mathrm{B}$	12.3 ± 3.0	3.66	[131]
$^{13}\mathrm{C}\rightarrow^{11}\mathrm{C}$	8.2 ± 0.8	10	[129]
$^{13}\mathrm{C}\rightarrow^{11}\mathrm{B}$	22.2 ± 3.86	10	[129]
$^{13}\mathrm{C}\rightarrow^{10}\mathrm{C}$			
$^{13}\mathrm{C}\rightarrow^{10}\mathrm{B}$	9 ± 1.6	10	[129]

Continued on next page

Table B.1 – continued from previous page

reaction	σ [mb]	k $\left[\frac{\text{GeV}}{\text{nuc}}\right]$	Ref
$^{14}N \rightarrow ^{11}C$	11.7 ± 0.35	0.6	[132]
$^{14}N \rightarrow ^{11}B$	17.5 ± 0.26	0.6	[132]
$^{14}N \rightarrow ^{10}C$	0.9 ± 0.09	0.6	[132]
$^{14}N \rightarrow ^{10}B$	9.9 ± 0.15	0.6	[132]
$^{15}N \rightarrow ^{11}C$	5.6 ± 0.56	0.373	[130]
$^{15}N \rightarrow ^{11}B$	26.9 ± 1.345	0.373	[130]
$^{15}N \rightarrow ^{10}C$			
$^{15}N \rightarrow ^{10}B$	13.6 ± 1.36	0.4	[133]
$^{16}O \rightarrow ^{11}C$	11.0 ± 1.1	2.1	[134]
$^{16}O \rightarrow ^{11}B$	15.4 ± 1.5	2.1	[134]
$^{16}O \rightarrow ^{10}C$	1.83 ± 0.21	2.1	[134]
$^{16}O \rightarrow ^{10}B$	8.9 ± 1.69	2.1	[134]
$^{20}Ne \rightarrow ^{11}C$	6.3 ± 0.32	0.6	[135, 132]
$^{20}Ne \rightarrow ^{11}B$	12 ± 0.12	10	[129]
$^{20}Ne \rightarrow ^{10}C$	0.3 ± 0.03	0.6	[135, 132]
$^{20}Ne \rightarrow ^{10}B$	6.75 ± 0.68	10	[129]
$^{22}Ne \rightarrow ^{11}B$	17 ± 1.7	10	[129]
$^{22}Ne \rightarrow ^{10}B$			
$^{24}Mg \rightarrow ^{11}C$	5.5 ± 0.55	10	[129]
$^{24}Mg \rightarrow ^{11}B$	10.4 ± 1.04	10	[129]
$^{24}Mg \rightarrow ^{10}C$			
$^{24}Mg \rightarrow ^{10}B$	6.2 ± 0.62	10	[129]
$^{25}Mg \rightarrow ^{11}B$			
$^{25}Mg \rightarrow ^{10}B$			
$^{26}Mg \rightarrow ^{11}C$	0.4 ± 0.3	0.576	[136]
$^{26}Mg \rightarrow ^{11}B$	8.6 ± 2.0	0.576	[136]
$^{26}Mg \rightarrow ^{10}B$	2.2 ± 0.8	0.576	[136]
$^{28}Si \rightarrow ^{11}C$	4.65 ± 1.85	10	[129]
$^{28}Si \rightarrow ^{11}B$	6.75 ± 2.75	10	[129]
$^{28}Si \rightarrow ^{10}C$			

Continued on next page

Table B.1 – continued from previous page

reaction	σ [mb]	$k\left[\frac{\text{GeV}}{\text{nuc}}\right]$	Ref
^{28}Si→^{10}B	4.25 ± 0.75	10	[129]
^{56}Fe→^{11}C	1.12 ± 0.1	1	[137]
^{56}Fe→^{11}B	3.82 ± 0.4	1	[137]
^{56}Fe→^{10}C			
^{56}Fe→^{10}B	2.03 ± 0.2	1	[137]

B.2 Be cross sections

Table B.2 Fragmentation cross sections for Be production.

reaction	σ [mb]	$k\left[\frac{\text{GeV}}{\text{nuc}}\right]$	Ref
^{9}Be→^{7}Be	10.6 ± 3.18	0.365	[130]
^{12}C→^{7}Be	10.1 ± 1.3	3.66	[131]
^{12}C→^{9}Be	6.7 ± 0.9	3.66	[131]
^{12}C→^{10}Be	4.2 ± 0.6	3.66	[131]
^{13}C→^{7}Be	4.9 ± 0.9	0.6	[138]
^{13}C→^{9}Be	7.2 ± 0.78	0.6	[138]
^{13}C→^{10}Be	5.99 ± 0.98	0.6	[138]
^{14}N→^{7}Be	10.9 ± 0.654	0.74	[139]
^{14}N→^{9}Be	2.0 ± 0.2	0.6	[132]
^{14}N→^{10}Be	1.6 ± 0.16	0.6	[132]
^{15}N→^{7}Be	5.4 ± 0.5	2.2	[135]
^{15}N→^{9}Be	7.5 ± 1.5	0.4	[135]
^{15}N→^{10}Be	2.03 ± 0.035	4	[135]
^{16}O→^{7}Be	10.1 ± 1.2	2.1	[134]
^{16}O→^{9}Be	4.17 ± 0.55	2.1	[134]
^{16}O→^{10}Be	2.05 ± 0.31	2.1	[134]
^{20}Ne→^{7}Be	8.55 ± 0.86	10	[129]
^{20}Ne→^{9}Be			

Continued on next page

Table B.2 – continued from previous page

reaction	σ [mb]	k $\left[\frac{\text{GeV}}{\text{nuc}}\right]$	Ref
^{20}Ne→^{10}Be			
^{22}Ne→^{7}Be	5.55 ± 0.56	10	[129]
^{22}Ne→^{9}Be			
^{22}Ne→^{10}Be			
^{24}Mg→^{7}Be	10 ± 1	10	[129]
^{24}Mg→^{9}Be	4.3 ± 0.43	10	[129]
^{24}Mg→^{10}Be	2.56 ± 0.16	2.6	[140]
^{25}Mg→^{7}Be	7.2 ± 1.6	10	[129]
^{25}Mg→^{9}Be			
^{25}Mg→^{10}Be			
^{26}Mg→^{7}Be	5.95 ± 1.25	10	[129]
^{26}Mg→^{9}Be			
^{26}Mg→^{10}Be			
^{28}Si→^{7}Be	10.8 ± 1.08	10	[129]
^{28}Si→^{9}Be	4.72 ± 0.81	23	[140]
^{28}Si→^{10}Be		10	
^{56}Fe→^{7}Be	3.09 ± 0.3	1	[137]
^{56}Fe→^{9}Be	2.11 ± 0.2	1	[137]
^{56}Fe→^{10}Be			
^{10}B→^{7}Be	6.28 ± 0.44	0.74	[139]
^{10}B→^{9}Be	N.A.		
^{10}B→^{10}Be			
^{11}B→^{7}Be	4.17 ± 0.29	0.74	[139]
^{11}B→^{9}Be	13.4 ± 1.34	0.365	[130]
^{11}B→^{10}Be	7.7 ± 1.54	0.365	[130]

B.3 Al (and ghost nuclei) cross sections

Fragmentation cross sections for Al production are listed in Table B.3.

Short-lived radioisotopes ^{27}Mg, ^{27}Si, and ^{26}Si contribute to the production cross sections of ^{27}Al, and ^{26}Al:

- ^{27}Mg $\rightarrow^{27}$ Al with the half-life $t_{1/2} = 9.44min$ and branching ratio $Br = 1$
- ^{27}Si $\rightarrow^{27}$ Al with $t_{1/2} = 4.15s$ and branch ratio $Br = 1$
- ^{26}Si $\rightarrow^{26}$ Al with $t_{1/2} = 2.25s$ and branch ratio $Br = 1$

Table B.3 Fragmentation cross sections for Al production

reaction	σ [mb]	$k\left[\frac{\text{GeV}}{\text{nuc}}\right]$	Ref
^{28}Si$\rightarrow^{26}$Al	30.5 ± 1.00	0.77	[132, 141]
^{28}Si$\rightarrow^{26}$Si	1.4 ± 0.42	0.77	[132]
^{28}Si$\rightarrow^{27}$Al	46.6 ± 0.42	0.77	[132, 141]
^{28}Si$\rightarrow^{27}$Mg			
^{28}Si$\rightarrow^{27}$Si	31.2 ± 1.56	0.77	[132]
^{29}Si$\rightarrow^{26}$Al	14.9 ± 1.78	0.51	[141]
^{29}Si$\rightarrow^{26}$Si			
^{29}Si$\rightarrow^{27}$Al	46.5 ± 0.37	0.51	[141]
^{29}Si$\rightarrow^{27}$Mg	10.5 ± 2.1	0.51	[141]
^{29}Si$\rightarrow^{27}$Si	1.8 ± 0.54	0.51	[141]
^{31}P$\rightarrow^{26}$Al	18.3 ± 1.00	0.51	[141]
^{31}P$\rightarrow^{26}$Si			
^{31}P$\rightarrow^{27}$Al	35.7 ± 1.79	0.51	[141]
^{31}P$\rightarrow^{27}$Mg			
^{31}P$\rightarrow^{27}$Si	2.4 ± 0.48	0.51	[141]
^{32}S$\rightarrow^{26}$Al	14.6 ± 1.46	0.65	[132]
^{32}S$\rightarrow^{26}$Si	0.9 ± 0.276	0.65	[132]
^{32}S$\rightarrow^{27}$Al	25.2 ± 1.27	0.65	[132]
^{32}S$\rightarrow^{27}$Mg	1 ± 0.3	0.65	[132]
^{32}S$\rightarrow^{27}$Si	8.9 ± 0.71	0.65	[132, 141]
^{36}Ar$\rightarrow^{26}$Al	10.9 ± 1.6	0.765	[142]
^{36}Ar$\rightarrow^{26}$Si	0.6 ± 0.4	0.765	[142]
^{36}Ar$\rightarrow^{27}$Al	25.2 ± 3	0.765	[142]

Continued on next page

Table B.3 – continued from previous page

reaction	σ [mb]	$k\left[\frac{\text{GeV}}{\text{nuc}}\right]$	Ref
^{36}Ar→^{27}Mg	1 ± 0.6	0.765	[142]
^{36}Ar→^{27}Si	5.5 ± 0.8	0.765	[142]
^{38}Ar→^{26}Al	7.2 ± 0.86	0.498	[141]
^{38}Ar→^{26}Si			
^{38}Ar→^{27}Al	14.6 ± 1.17	0.498	[141]
^{38}Ar→^{27}Mg	3.3 ± 0.66	0.498	[141]
^{38}Ar→^{27}Si	0.2 ± 0.06	0.498	[141]
^{40}Ar→^{26}Al	2.2 ± 0.66	0.656	[132]
^{40}Ar→^{26}Si			
^{40}Ar→^{27}Al	21.4 ± 1.07	0.656	[132]
^{40}Ar→^{27}Mg	2.3 ± 0.69	0.656	[132]
^{40}Ar→^{27}Si			
^{40}Ca→^{26}Al	8.4 ± 0.67	0.763	[143]
^{40}Ca→^{26}Si			
^{40}Ca→^{27}Al	21.2 ± 1.9	0.763	[143]
^{40}Ca→^{27}Mg	0.4 ± 0.3	0.763	[143]
^{40}Ca→^{27}Si	2.6 ± 0.4	0.763	[143]
^{56}Fe→^{26}Al	2.751 ± 0.331	1.5	[144]
^{56}Fe→^{26}Si			
^{56}Fe→^{27}Al	7.469 ± 0.886	1.5	[144]
^{56}Fe→^{27}Mg	1.185 ± 0.142	1.5	[144]
^{56}Fe→^{27}Si	0.453 ± 0.0547	1.5	[144]

B.4 Mg (and ghost Na) cross sections

Fragmentation cross sections for Mg production are listed in Table B.4. Short-lived radioisotopes ^{24}Na, ^{25}Na, and ^{26}Na contribute to the production cross sections of ^{24}Mg, ^{25}Mg, and ^{26}Mg:

- ^{24}Na →^{24} Mg with the half-life $t_{1/2} = 14.96h$ and branching ratio $Br = 1$
- ^{25}Na →^{25} Mg with $t_{1/2} = 39s$ and branch ratio $Br = 1$

- ^{26}Na $\rightarrow^{26}$ Mg with $t_{1/2} = 1.07s$ and branch ratio $Br = 1$

(note, ^{25}Si and ^{26}Na are also the ghost nuclei, but their cross sections have not been measured.)

Table B.4 Fragmentation cross sections for Mg production.

reaction	σ [mb]	$k\left[\frac{\text{GeV}}{\text{nuc}}\right]$	Ref
^{26}Al$\rightarrow^{24}$Mg			
^{26}Al$\rightarrow^{24}$Na	11.4(0.2)	0.508	[141]
^{26}Al$\rightarrow^{25}$Mg	74(0.08)	0.508	[141]
^{26}Al$\rightarrow^{25}$Na			
^{26}Al$\rightarrow^{26}$Mg			
^{27}Al$\rightarrow^{24}$Mg	27.2(0.05)	0.582	[132]
^{27}Al$\rightarrow^{24}$Na	11.4(0.1)	0.582	[132]
^{27}Al$\rightarrow^{25}$Mg	42.6(0.05)	0.582	[132]
^{27}Al$\rightarrow^{25}$Na	2.6(0.2)	0.582	[132]
^{27}Al$\rightarrow^{26}$Mg	40.1(0.05)	0.582	[132]
^{28}Si$\rightarrow^{24}$Mg	33(0.05)	0.77	[132]
^{28}Si$\rightarrow^{24}$Na	5.4(0.12)	0.77	[132, 141]
^{28}Si$\rightarrow^{25}$Mg	27.2(0.05)	0.77	[132]
^{28}Si$\rightarrow^{25}$Na	1.8(0.2)	0.77	[132, 141]
^{28}Si$\rightarrow^{26}$Mg	15.9(0.05)	0.77	[132]
^{29}Si$\rightarrow^{24}$Mg	18.4(0.12)	0.508	[141]
^{29}Si$\rightarrow^{24}$Na	14.3(0.12)	0.508	[141]
^{29}Si$\rightarrow^{25}$Mg	26.6(0.08)	0.508	[141]
^{29}Si$\rightarrow^{25}$Na	4.3(0.3)	0.508	[141]
^{29}Si$\rightarrow^{26}$Mg	33.3(0.08)	0.508	[141]
^{31}P$\rightarrow^{24}$Mg	32.3(0.08)	0.505	[141]
^{31}P$\rightarrow^{24}$Na			
^{31}P$\rightarrow^{25}$Mg	18.4(0.12)	0.505	[141]
^{31}P$\rightarrow^{25}$Na			
^{31}P$\rightarrow^{26}$Mg	2.7(0.3)	0.505	[141]
^{32}S$\rightarrow^{24}$Mg	27.3(0.05)	0.649	[132]

Continued on next page

Table B.4 – continued from previous page

reaction	σ [mb]	$k\left[\frac{\text{GeV}}{\text{nuc}}\right]$	Ref
^{32}S→^{24}Na	3.5(0.12)	0.649	[132, 141]
^{32}S→^{25}Mg	23.5(0.05)	0.649	[132]
^{32}S→^{25}Na	0.3 ± 0.2	0.77	[140]
^{32}S→^{26}Mg	11.8(0.1)	0.649	[132]
^{36}Ar→^{24}Mg	20 ± 2.2	0.765	[142]
^{36}Ar→^{24}Na	2.2 ± 0.8	0.765	[142]
^{36}Ar→^{25}Mg	19.8 ± 2.4	0.765	[142]
^{36}Ar→^{25}Na	1.6 ± 0.6	0.765	[142]
^{36}Ar→^{26}Mg	12.3 ± 1.9	0.765	[142]
^{38}Ar→^{24}Mg	8.7(0.12)	0.498	[141]
^{38}Ar→^{24}Na			
^{38}Ar→^{25}Mg	15.6(0.08)	0.498	[141]
^{38}Ar→^{25}Na			
^{38}Ar→^{26}Mg	9(0.08)	0.498	[141]
^{40}Ar→^{24}Mg	6.7(0.2)	0.656	[132]
^{40}Ar→^{24}Na	2.5 ± 0.7	0.352	[142]
^{40}Ar→^{25}Mg	14.2(0.1)	0.656	[132]
^{40}Ar→^{25}Na	0.5 ± 0.5	0.352	[142]
^{40}Ar→^{26}Mg	15.1(0.1)	0.656	[132]
^{40}Ca→^{24}Mg	14.5 ± 1.3	0.763	[143]
^{40}Ca→^{24}Na	2.5 ± 0.4	0.763	[143]
^{40}Ca→^{25}Mg	14.5 ± 1.3	0.763	[143]
^{40}Ca→^{25}Na	0.6 ± 0.2	0.763	[143]
^{40}Ca→^{26}Mg	6.9 ± 0.7	0.763	[143]
^{56}Fe→^{24}Mg	4.837 ± 0.589	1.5	[144]
^{56}Fe→^{24}Na	2.594 ± 0.319	1.5	[144]
^{56}Fe→^{25}Mg	5.600 ± 0.676	1.5	[144]
^{56}Fe→^{25}Na	4.813 ± 0.583	1.5	[144]
^{56}Fe→^{26}Mg			

B.5 F (and ghost O and Na) cross sections

Fragmentation cross sections for F production are listed in Table B.5. Short-lived radioisotopes ^{19}O, and ^{19}Ne contribute to the production cross sections of ^{19}F:

- $^{19}\text{O} \rightarrow ^{19}$ F with the half-life $t_{1/2} = 26.47$ s and branching ratio $Br = 1$
- $^{19}\text{Ne} \rightarrow ^{19}$ F with the half-life $t_{1/2} = 17.27$ s and branching ratio $Br = 1$

Table B.5 Fragmentation cross sections for F production.

reaction	σ [mb]	$k \left[\frac{\text{GeV}}{\text{nuc}}\right]$	Ref
^{20}Ne→^{19}O			
^{20}Ne→^{19}F	25.70(0.050)	0.534	[132]
^{20}Ne→^{19}Ne	28.00(0.050)	0.534	[132]
^{22}Ne→^{19}O	4.30 ± 0.5	0.894	[136]
^{22}Ne→^{19}F	24.1 ± 3.3	0.894	[136]
^{22}Ne→^{19}Ne	0.1 ± 0.3	0.894	[136]
^{22}Na→^{19}O			
^{22}Na→^{19}F	12.80(0.2)	0.52	[141]
^{22}Na→^{19}Ne	5.9(0.3)	0.52	[141]
^{23}Na→^{19}O			
^{23}Na→^{19}F	16.6(0.2)	0.517	[141]
^{23}Na→^{19}Ne	7.5(0.3)	0.517	[141]
^{24}Mg→^{19}O			
^{24}Mg→^{19}F	10.4 ± 1.04	0.61	[132]
^{24}Mg→^{19}Ne	4.1(0.2)	0.61	[132]
^{25}Mg→^{19}F	15.2(0.2)	0.514	[141]
^{26}Mg→^{19}O	2.0 ± 0.6	0.576	[136]
^{26}Mg→^{19}F	19.90 ± 2.2	0.576	[136]
^{26}Mg→^{19}Ne	0.5(0.2)	0.576	[136]
^{26}Al→^{19}O			
^{26}Al→^{19}F	13.60(0.2)	0.508	[141]
^{26}Al→^{19}Ne	4.1(0.3)	0.508	[141]

Continued on next page

Table B.5 – continued from previous page

reaction	σ [mb]	k $\left[\frac{\text{GeV}}{\text{nuc}}\right]$	Ref
^{27}Al→^{19}O			
^{27}Al→^{19}F	9.9(0.08)	0.582	[141]
^{27}Al→^{19}Ne	1.5(0.3)	0.582	[132]
^{28}Si→^{19}O			
^{28}Si→^{19}F	9.0(0.08)	0.506	[141]
^{28}Si→^{19}Ne	3.0(0.2)	0.77	[132]
^{31}P→^{19}O			
^{31}P→^{19}F			
^{31}P→^{19}Ne			
^{32}S→^{19}O			
^{32}S→^{19}F	7.7 ± 0.5	0.77	[129]
^{32}S→^{19}Ne	2.4 ± 0.6	0.77	[129]
^{36}Ar→^{19}O			
^{36}Ar→^{19}F	5.6 ± 2.9	0.765	[142]
^{36}Ar→^{19}Ne	1.2 ± 0.8	0.765	[142]
^{40}Ca→^{19}O			
^{40}Ca→^{19}F			
^{40}Ca→^{19}Ne	0.4 ± 0.1	0.565	[143]
^{56}Fe→^{19}O	0.285 ± 0.035	1.5	[144]
^{56}Fe→^{19}F	2.08 ± 0.3	1.5	[144]
^{56}Fe→^{19}Ne	0.253 ± 0.032	1.5	[144]